



TECHNISCHE
UNIVERSITÄT
WIEN
Vienna University of Technology

GEOWISSENSCHAFTLICHE MITTEILUNGEN

Heft Nr. 89, 2012

Dynamic and Reduced-Dynamic Precise Orbit Determination of Satellites in Low Earth Orbits

Paul Swatschina

Veröffentlichung des Departments für Geodäsie und Geoinformation
ISSN 1811-8380

Schriftenreihe der Studienrichtung VERMESSUNG UND GEOINFORMATION



TECHNISCHE
UNIVERSITÄT
WIEN
Vienna University of Technology

GEOWISSENSCHAFTLICHE MITTEILUNGEN

Heft Nr. 89, 2012

Dynamic and Reduced-Dynamic Precise Orbit Determination of Satellites in Low Earth Orbits

Paul Swatschina

Veröffentlichung des Departments für Geodäsie und Geoinformation
ISSN 1811-8380

Schriftenreihe der Studienrichtung VERMESSUNG UND GEOINFORMATION

2012

Published by the Department of Geodesy and Geoinformation
of the Vienna University of Technology
Gußhausstraße 27-29
1040 Vienna, Austria

Responsible for this issue: Prof. Dr. Johannes Böhm

Printed by: Grafisches Zentrum HTU GmbH

The digital version of the full document with colored figures is available online:
http://www.hg.tuwien.ac.at/Bibl_Docs/Theeses_phd/phd_full/2012_phd_pswatschina.pdf

Die Kosten für den Druck wurden vom Department für Geodäsie und Geoinformation übernommen.

Diese Arbeit wurde an der Fakultät für Mathematik und Geoinformation der Technischen Universität Wien zur Erlangung des akademischen Grades eines Doktors der technischen Wissenschaften eingereicht.

Begutachter:

A.o. Univ. Prof. Dipl.-Ing. Dr. techn. Robert Weber
Institut für Geodäsie und Geophysik
der Technischen Universität Wien
Gußhausstraße 27-29, 1040 Wien, Österreich

Univ. Prof. Dr. phil. nat. Markus Rothacher
Institut für Geodäsie und Photogrammetrie
der Eidgenössischen Technischen Hochschule Zürich
Schafmattstraße 34, 8093 Zürich, Schweiz

Tag der mündlichen Prüfung: 19.10.2009

Auflage: 60 Stück

ISSN 1811-8380

Danksagung

An dieser Stelle möchte ich mich herzlich bei meinem Betreuer Prof. Dr. Robert Weber für die überaus angenehme und anregende Zusammenarbeit bedanken.

Weiters danke ich Prof. Dr. Markus Rothacher sehr für die Begutachtung dieser Arbeit.

Spezial thanks goes to Dr. Pere Ramos-Bosch for his many helpful advices and for providing his orbit solutions.

I am also very thankful to Dražen Švehla for giving me access to his orbit solutions.

Abstract

The precise positioning of satellites in Low Earth Orbits (LEO) has become a key technology for advanced space missions. Dedicated satellite missions, such as CHAMP, GRACE and GOCE, that aim to map the Earth's gravity field and its variation over time with unprecedented accuracy, initiated the demand for highly precise orbit solutions of LEO satellites. Furthermore, a wide range of additional science opportunities opens up with the capability to generate accurate LEO orbits. For all considered satellite missions, the primary measurement system for navigation is a spaceborne GPS receiver. The goal of this thesis is to establish and implement methods for Precise Orbit Determination (POD) of LEO satellites using GPS. Striving for highest precision using yet efficient orbit generation strategies, the attained orbit solutions are aimed to be competitive with the most advanced solutions of other institutions.

Dynamic and reduced-dynamic orbit models provide the basic concepts of this work. These orbit models are subsequently adjusted to the highly accurate GPS measurements. The GPS measurements are introduced at the zero difference level in the ionosphere free linear combination. Appropriate procedures for GPS data screening and editing are established to detect erroneous data and to employ measurements of good quality only. For the dynamic orbit model a sophisticated force model, especially designed for LEO satellites, has been developed. In order to overcome the limitations that are induced by the deficiencies of the purely dynamical model, two different types of empirical parameters are introduced into the force model. These reduced-dynamic orbit models allow for the generation of much longer orbital arcs while preserving the spacecraft dynamics to the most possible extent. The two methods for reduced-dynamic orbit modeling are instantaneous velocity changes (pulses) or piecewise constant accelerations. For both techniques highly efficient modeling algorithms are presented. The additional parameters are estimated within the adjustment process. In order to regulate their impact on the dynamic solution, the empirical parameters are assigned statistical a priori information. This allows for a perfect synergy of the advanced knowledge of spacecraft dynamics and the high accuracy of the GPS measurements.

The developed routines have been implemented in a computer program and tested for CHAMP and GRACE. The applied strategies proved to be highly efficient, robust and flexible. The attained orbit solutions are validated against solutions of other well-established POD methods. It is shown, that dynamic POD delivers accuracies at the 1 dm level for orbital lengths of up to 90 minutes. Furthermore, employing an adequate number of pseudo-stochastic parameters with optimal weighting, reduced-dynamic orbit determination is a powerful strategy for LEO POD. Orbital arcs over a whole day can be generated with an accuracy of up to 4.5 cm RMS.

Kurzfassung

Die präzise Bahnbestimmung von Satelliten in niedrigen Erdumlaufbahnen (LEO für Low Earth Orbit) entwickelte sich zu einem zentralen Verfahren für moderne Weltraummissionen. Das Erfordernis hochgenauer Orbitlösungen wurde wesentlich durch dedizierte Satellitenmissionen, wie CHAMP, GRACE und GOCE, ausgelöst, mit dem Ziel das Schwerefeld der Erde und dessen zeitliche Variation mit bisher unerreichter Genauigkeit zu bestimmen. Durch die Möglichkeit, LEO Satellitenbahnen genau zu bestimmen, eröffnen sich zusätzlich weitreichende wissenschaftliche Möglichkeiten. Das zugrundeliegende Messsystem für die Navigation dieser Satellitenmissionen sind GPS-Empfänger. Es ist das Ziel dieser Arbeit, Methoden zur exakten Bahnbestimmung (POD für Precise Orbit Determination) mittels GPS von LEO Satelliten zu entwickeln und umzusetzen. Dabei wird ein Höchstmaß an Genauigkeit angestrebt, bei gleichzeitiger Achtung auf Effizienz und Schnelligkeit der zum Einsatz kommenden Verfahren. Die erstellten Bahnlösungen sollen die Qualität der Lösungen etablierter Methoden anderer Organisationen erreichen.

Dynamische und reduziert-dynamische Bahnmodelle bilden die Grundlage der hier verwendeten Verfahren. Diese Modelle werden an die hochgenauen GPS-Messungen angepasst. Dabei werden die GPS-Messungen undifferenziert in der ionosphärenfreien Linearkombination verwendet. Es werden geeignete Methoden entwickelt um fehlerhafte Beobachtungsdaten zu detektieren und herauszufiltern. Für das dynamische Bahnmodell wird ein hochentwickeltes Kraftfeld speziell für LEO Satelliten erarbeitet. Um die dennoch eingeschränkte Einsatzfähigkeit rein dynamischer Modelle auszugleichen, wird das Bahnmodell alternativ um zwei verschiedene Arten empirischer Parameter erweitert. Das resultierende reduziert-dynamische Orbitmodell erlaubt die Erstellung weit längerer Bahnbögen unter größtmöglicher Bewahrung der dynamischen Gesetzmäßigkeiten. Als reduziert-dynamische Methoden werden Geschwindigkeitssprünge an vorgegebenen Zeitpunkten (Pulse) oder abschnittsweise konstante Beschleunigungen eingesetzt. Für beide Techniken kommen hocheffiziente Algorithmen zur Anwendung. Die Bestimmung der zusätzlich eingeführten Parameter erfolgt während der Anpassung an die Messdaten. Dabei werden diesen Parametern statistische Eigenschaften vorgegeben um deren Einfluss auf die Bahnlösung zu kontrollieren. Hiermit wird ein ausgezeichnetes Zusammenwirken des fortgeschrittenen Kenntnisstandes über Bahnbewegung und der hohen Genauigkeit der GPS-Messungen erzielt.

Die entwickelten Verfahren wurden in einem Computerprogramm umgesetzt und für die Missionen CHAMP und GRACE getestet. Die verwendeten Verfahren erwiesen sich als überaus effizient, robust und flexibel. Im Vergleich zu Bahnlösungen anderer bewährter Verfahren erreichen dynamisch erstellte Lösungen, mit Bahnlängen bis zu 90 Minuten, Genauigkeiten im 1-Dezimeterbereich. Mit dem Einsatz einer angemessenen Anzahl pseudostochastischer Parameter mit entsprechender Gewichtung, eignet sich die reduziert-dynamische Bahnbestimmung hervorragend für LEO-POD-Anwendungen. Es werden Genauigkeiten von bis zu 4.5 cm RMS für Orbitlösungen über einen ganzen Tag erreicht.

Contents

List of Figures	viii
List of Tables	x
Acronyms	xi
1 Introduction	1
1.1 LEO Precise Orbit Determination in Geodesy	2
1.2 Outline	3
2 LEOs using GPS	4
2.1 CHAMP	7
2.2 GRACE	8
2.3 GOCE	10
3 Fundamentals of GPS	13
3.1 The Global Positioning System – an Overview	13
3.1.1 GPS Orbit and Clock Products	15
3.2 Modeling of GPS Observations	19
3.2.1 Code Observation Equation	21
3.2.2 Phase Observation Equation	23
3.2.3 Dual Frequency Observation Model	25
3.3 The Ionosphere free linear Combination	26
3.4 Linearization of the Observation Equations	27
3.5 GPS Data Quality of spaceborne Receivers	30
4 Precise LEO Satellite Orbit Determination	32
4.1 Prerequisites for POD	34
4.1.1 Principles of Least-Squares Estimation	34
4.1.2 Initial Orbit Determination	38
4.1.3 Reference Frame Transformations	39
4.2 Dynamic Orbit Modeling	44
4.2.1 The Dynamic Force Model	47
4.2.2 Variational Equations	57

4.3	Reduced-Dynamic Orbit Modelling	59
4.3.1	Instantaneous Velocity Changes	60
4.3.2	Piecewise Constant Accelerations	66
4.4	Dynamic and Reduced-dynamic Orbit Determination	71
4.5	Data Editing	80
5	The Software <i>ORBIT</i>	83
6	Results for CHAMP and GRACE POD	87
6.2	CHAMP POD	87
6.3	GRACE POD	98
7	Conclusion and Outlook	104
Appendix		107
A.1	The Light Time Equation	107
A.2	Keplerian Ephemeris Calculation	108
A.2.1	Keplerian Elements from the Position and Velocity Vectors	108
A.2.2	Position and Velocity Vectors from the Keplerian Elements	110
A.3	The partial Derivatives of the dynamic Force Model	112
A.4	User Interface of the Software <i>ORBIT</i>	117
Bibliography		125
Curriculum Vitae		135

List of Figures

Figure 2.1:	Orbit of a LEO satellite (CHAMP)	4
Figure 2.2:	The concept of satellite-to-satellite tracking	5
Figure 2.3:	An artist's impression of the CAHMP satellite in orbit	7
Figure 2.4:	An artist's impression of the GRACE satellites in orbit	9
Figure 2.5:	An artist's impression of the GOCE satellite in orbit	11
Figure 3.1:	Orbit of a GPS satellite over 10 hours	13
Figure 3.2:	The GPS space segment (Status as of 7 April 2008)	14
Figure 3.3:	The IGS Tracking Network	16
Figure 3.4:	RMS error of GPS clock interpolation for 5 and 15 minute sampling	18
Figure 3.5:	Number of GPS satellites operating cesium (Cs) and rubidium (Rb) clocks over time	19
Figure 4.1:	Kinematic orbit solution (epochwise positions)	38
Figure 4.2:	The accompanying Satellite Coordinate System (SCS)	41
Figure 4.3:	The S/C-Body Coordinate System related to the nominal attitude (example of CHAMP)	43
Figure 4.4:	The Keplerian (or classical) elements	45
Figure 4.5:	The third-body attraction acting on a satellite	51
Figure 4.6:	The relations between the dynamic, reduced-dynamic, highly reduced-dynamic (HRD) and kinematic orbit determination methods as a function of the number (# Par.) and a priori standard deviation (Sigma) of the introduced pseudo-stochastic parameters	60
Figure 4.7:	The concept of pseudo-stochastic pulses	61
Figure 4.8:	The concept of pseudo-stochastic piecewise constant accelerations	67
Figure 4.9:	Structure of the normal equation matrix for reduced-dynamic orbit determination (example)	77
Figure 5.1:	The processing scheme for LEO POD with the software <i>ORBIT</i>	86
Figure 6.1:	CHAMP dynamic orbit solution over 90 minutes (approx. one revolution) w.r.t UPC (6 cm RMS)	88
Figure 6.2:	CHAMP dynamic orbit solution over 24 Hours w.r.t UPC (5.6 m RMS)	89
Figure 6.3:	CHAMP reduced-dynamic orbit solution with piecewise constant accelerations over 24 hours w.r.t UPC (5 cm RMS)	90

Figure 6.4:	CHAMP reduced-dynamic orbit solution with piecewise constant accelerations over 24 hours w.r.t JPL (18 cm RMS)	91
Figure 6.5:	CHAMP reduced-dynamic orbit solution with piecewise constant accelerations over 24 hours w.r.t TUM (7.5 cm RMS)	92
Figure 6.6:	CHAMP reduced-dynamic Orbit Solution with instantaneous velocity changes w.r.t solution with piecewise constant accelerations (2 mm RMS)	93
Figure 6.7:	The estimated piecewise constant accelerations	94
Figure 6.8:	The estimated instantaneous velocity changes	94
Figure 6.9:	The impact of different GPS clock offset data (25 cm RMS)	95
Figure 6.10:	The impact of different GPS observation sampling rates (2 cm RMS)	96
Figure 6.11:	Orbit difference between using code plus phase data w.r.t. using code data only (23 cm RMS)	97
Figure 6.12:	GRACE A dynamic orbit solution over 90 minutes (approx. one revolution) w.r.t JPL (11 cm RMS)	98
Figure 6.13:	GRACE A reduced-dynamic orbit solution with piecewise constant accelerations over 24 hours w.r.t JPL (4.5 cm RMS)	100
Figure 6.14:	GRACE A reduced-dynamic orbit solution with piecewise constant accelerations over 24 hours w.r.t UPC (4.5 cm RMS)	101
Figure 6.15:	GRACE B reduced-dynamic orbit solution with piecewise constant accelerations over 24 hours w.r.t JPL (5.5 cm RMS)	102
Figure 6.16:	The residuals of an orbit solution employing piecewise constant accelerations over 100 seconds with respect to the solution with accelerations over 300 seconds (2.0 cm RMS)	103
Figure A.1:	The Keplerian (or classical) elements	108
Figure A.2:	Welcome screen of the software <i>ORBIT</i>	117
Figure A.3:	Definition of the collocation parameters with <i>ORBIT</i>	118
Figure A.4:	Definition of the force field with <i>ORBIT</i>	119
Figure A.5:	Import of GPS data with <i>ORBIT</i>	120
Figure A.6:	Propagation settings with <i>ORBIT</i>	121
Figure A.7:	Orbit determination settings with <i>ORBIT</i>	122
Figure A.8:	Definition of the reference Orbit solution with <i>ORBIT</i>	123
Figure A.9:	Display of the attained results with <i>ORBIT</i>	124

List of Tables

Table 2.1:	LEOs using geodetic-type GPS receivers	6
Table 3.1:	IGS orbit and clock products	16
Table 3.2:	Antenna phase center offsets for GPS satellites	17
Table 3.3:	Effects of the code observation equation for LEO satellites	23
Table 3.4:	Effects of the carrier phase observation equation for LEO satellites	25
Table 3.5:	Standard deviations for the ionosphere free GPS observations	31
Table 4.1:	Reference frame transformation models used for this research	40
Table 4.2:	GPS receiver phase center offsets in the body-fixed frame	44
Table 4.3:	Gravitational perturbations acting on a LEO satellite	47
Table 4.4:	Non-gravitational perturbations acting on a LEO satellite	48
Table 4.5:	Initial conditions for the variational equations	58
Table 5.1:	The dynamical model components employed	83
Table 5.2:	Selected gravity field models from the ICGEM	84
Table 5.3:	The reduced-dynamical model options with the software <i>ORBIT</i>	84
Table 6.1:	Parametrization, weighting settings and data products for CHAMP POD	89
Table 6.2:	Parametrization, weighting settings and data products for GRACE POD	99

Acronyms

ANTEX	Antenna Exchange Format
AC	Analysis Center
AS	Anti-spoofing
C/A	Coarse Aquisition
CHAMP	Challenging Mini Satellite Payload
CODE	Center for Orbit Determination in Europe
ESA	European Space Agency
FOC	Full Operational Capability
GNSS	Global Navigation Satellite System
GOCE	Gravity field and steady-state Ocean Circulation Explorer
GPS	Global Positioning System
GRACE	Gravity Recovery and Climate Experiment
ICGEM	International Centre for Global Earth Models
ICRF	International Celestial Reference System
IERS	International Earth Rotation Service
IF	Ionosphere-free
IGS	International GNSS Service
ITRF	International Terrestrial Reference Frame
JPL	Jet Propulsion Laboratoy
LEO	Low Earth Orbit/Orbiter
LSQ	Least-Squares
OD	Orbit determination
PCO	Phase Center Offset
POD	Precise Orbit Determination
PRN	Pseudo Random Noise
RINEX	Receiver-INdependent EXchange Format
RMS	Root Mean Square
S/C	Spacecraft
SLR	Satellite Laser Ranging
SNR	Signal to Noise Ratio
SST	Satellite-to-Satellite Tracking
UD	Undifferenced
ZD	Zero Difference

1 Introduction

The aim of this thesis is to develop and implement methods for the determination of the position and velocity of spacecraft in low Earth orbits with the most possible precision. The developed algorithms should deliver competitive results compared to orbit solutions of other highly accurate orbit determination technologies. In addition, it is intended that the established procedures are efficient, robust and yield very fast computation times.

The equipment of Low Earth Orbiters (LEOs) with spaceborne Global Positioning System (GPS) receivers offers a unique possibility for Precise Orbit Determination (POD). For satellites orbiting at altitudes of up to 1500 km the extremely precise GPS measurements can be collected globally, densely and with a good viewing geometry. In the last years several technologies have been developed to make use of the GPS to determine the orbits of LEOs with unprecedented accuracy.

The methods of dynamic and reduced-dynamic orbit modeling are chosen as the two basic concepts for this research. Dynamic orbit models allow for the incorporation of a priori knowledge of the motion of spacecraft to the highest possible extent. This is done by introducing the spacecraft dynamics especially relevant for low Earth orbits. Today, the models which describe the forces that govern the motion of a LEO satellite are mostly highly advanced. In recent years especially highly accurate Earth gravity field models have been developed. However, several uncertainties remain in the modeling of LEO dynamics. Predominantly the impact of the upper atmosphere cannot be modeled with satisfactory accuracy. Thus, the use of purely dynamic orbit solution is limited in terms of orbital lengths. Therefore, in this research the dynamic force model is augmented by two different types of empirical models to overcome the inflexibility of the dynamic model within the adjustment process. This will be achieved by either instantaneous velocity changes (pulses) at predefined epochs or by piecewise constant accelerations over predefined time intervals. By this means, the rigidity of the dynamics is reduced by the necessary extent to enable the trajectory to fit optimally to the measurements. The parameters of the empirical models are assigned statistical properties to allow for an adequate balance between the impact of the dynamic principles and the precision of the GPS observations. Thus, reduced-dynamic orbit solutions fully exploit the accuracy of the GPS measurements while retaining a maximum of information about orbital motion.

In this work, the GPS measurements are incorporated in the zero difference mode. Due to the availability of highly accurate GPS orbit and clock data, the direct introduction of undifferenced GPS observations yields an efficient and yet precise technique. In order to employ only GPS data of good quality, adequate data screening has been developed to reliably reject erroneous data and detect interruptions in the observation of the GPS carrier phases. The adjustment of the adopted orbit models to the cleaned measurements is performed in the batch mode. Here, the whole observation data over the concerned orbital

arc is processed in one step. This method promises to be very robust and to yield the most accurate and best fitting solution.

In the following chapters, the entire process of dynamic and reduced-dynamic orbit determination will be discussed in full detail. The described methods were implemented into a computer program and are tested with real LEO GPS data. The capabilities as well as the limitations of the established POD strategies will be assessed for various model and data configurations. It will be shown that the generated orbit solutions are of extremely good quality and the developed software may be used for many POD and POD related applications.

1.1 LEO Precise Orbit Determination in Geodesy

The motivation for precise orbit determination from a geodetic point of view is driven by the fact that from the very beginning of spaceflight artificial satellites of all kinds and orbits played a key role for all fundamental fields of research in geodesy. Satellites orbiting at high altitudes, like GPS or other Global Navigation Satellite System (GNSS) satellites, are and have been of vital importance for the determination of the size and shape of the Earth as well as of its rotational behavior.

The motion of artificial satellites orbiting the Earth is governed by a multitude of forces induced by various interactions between the satellites and the physical environment of the Earth. Satellites in LEO orbits are especially sensitive to geophysical properties like the Earth's gravity field and the atmosphere, which represent yet further areas of primary geodetic interest. The big advantage of satellite gravity field mapping is that a global and homogeneous coverage of the Earth is obtained. The exact knowledge of the motion of satellites, such as position and velocity, stability and variation of the orbit geometry, is therefore of great importance for these areas of research.

A series of dedicated missions, equipped with geodetic-type spaceborne GPS receivers, has been launched for the generation of high-fidelity gravity field models, GPS radio occultation to sound the atmosphere and radar or laser altimetry. LEO POD is therefore presently an important and evolving technology, under intensive development and research. In addition, new science opportunities emerge through the analysis of ground reflected GPS signals. The highly successful missions have already delivered extremely valuable data and products, and are continuing to do so. New missions of single or multiple spacecraft for geodetic research will certainly be deployed.

Thus, LEO POD in geodesy is driven by a continuous demand for ever increasing accuracy of orbital solutions of LEO satellites. This holds not only for the spacecraft position but also for its velocity and acceleration, primarily for the determination of Earth gravity field models. Therefore, advanced orbit modeling is required to most realistically represent the trajectory. Furthermore, real-time or near real-time orbit determination is especially required for atmospheric sounding. Thus, the underlying algorithms increasingly need to be efficient to yield a fast generation of orbit solutions.

1.2 Outline

This thesis provides a thorough treatment of the whole process of dynamic and reduced-dynamic orbit determination.

Chapter 2, *LEOs using GPS*, gives an introduction of the basic concept of LEO orbit determination using GPS measurements. An overview of the most dedicated geodetic LEO space missions is given, with the missions CHAMP, GRACE and GOCE being discussed in detail.

Chapter 3, *Fundamentals of GPS*, provides a short overview of the Global Positioning System. The applied GPS observational models are discussed in detail. In addition, a review of available GPS orbit and clock data as well as an assessment of the quality of the employed GPS data is given.

Chapter 4, *Precise LEO Orbit Determination*, gives a detailed description of the applied dynamic and reduced-dynamic orbit determination models. Highly efficient algorithms for reduced-dynamic orbit determination using either instantaneous velocity changes or piecewise constant accelerations are outlined. Furthermore, efficient procedures for data screening and editing, the principles of least-squares estimation, the necessary reference frame transformations and a method for initial orbit determination are explained.

Chapter 5, *The Software ORBIT*, gives an overview of the structure and features of the established software *ORBIT*.

Chapter 6, *Results for CHAMP and GRACE POD*, demonstrates the capabilities of the developed strategies using real LEO GPS data. The attained orbit solutions are compared to highly accurate solutions of other institutions to assess their quality.

Chapter 7, *Conclusion and Outlook*, finally sums up the achieved results and provides an outlook for POD applications related to this work.

2 LEOs using GPS

Satellites orbiting the Earth at altitudes below 1500 km are commonly classified as Low Earth Orbiters (LEOs) [Capderou, 2005]. The LEO segment is the most populated of all space segments [Wertz, 2001]. LEO satellites serve for almost the whole range of space applications comprising scientific, commercial and military missions. Figure 2.1 shows a typical LEO orbit (CHAMP over 1 hour in a height of approximately 400 km).

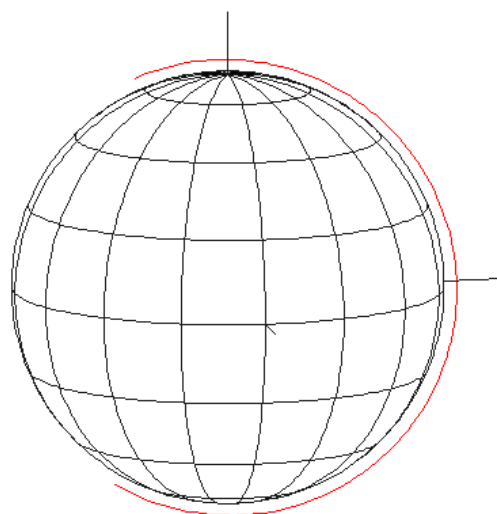


Figure 2.1: Orbit of a LEO satellite (CHAMP)

On the other hand, satellites of the Global Positioning System (GPS), as well as satellites of other global navigation satellite systems (GNSS), orbit at much higher altitudes of around 20000 km above the surface of the Earth in so-called medium Earth orbits (MEO) [Capderou, 2005]. The GPS satellites emit navigation signals within a cone of about 15 degrees aperture from the nadir direction [Švehla and Rothacher, 2005 and Wertz, 2001]. This makes GPS capable of serving as a spaceborne orbit navigation and control system for LEO satellites, following the concept of satellite-to-satellite tracking (SST). Figure 2.2 displays the concept of SST. Because these inter-satellite links are made between a high orbiting GPS satellite and a LEO satellite, the concept is more specifically referred to as high-low SST (hl-SST). For higher orbiting satellites the use GPS is usually not feasible, because of not enough GPS satellites in view, due to the limited emission section of 15 degrees [Wertz, 2001].

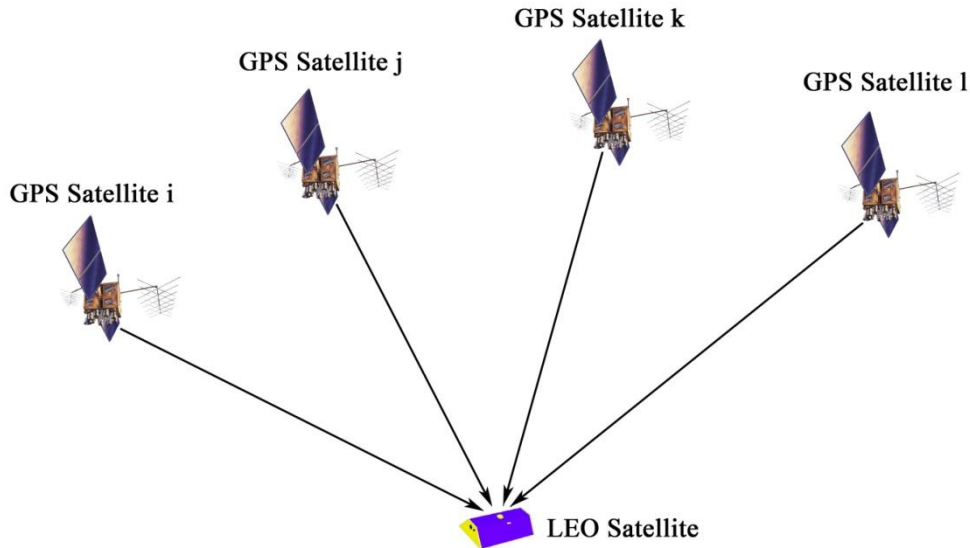


Figure 2.2: The concept of satellite-to-satellite tracking

The possibility of making use of the GPS for orbit determination (OD) of other spacecraft was demonstrated for the first time in 1984 reaching navigational accuracies of 50 m for the LANDSAT-4 satellite [Jäggi, 2006]. Since that time significant advancements in receiver technology and processing techniques made spaceborne GPS navigation a well established technology, delivering superb accuracies at very low costs. The achievable high accuracy, the global coverage and the three-dimensional nature of the GPS measurements are striking advantages over other traditional satellite tracking systems [Kroes, 2006].

Today GPS receivers are the primary navigation system for many satellite missions. A variety of manufacturers offer GPS receivers for spacecraft OD [Wertz, 2001]. In most cases, a medium navigational accuracy is sufficient. For this purpose commercial off-the-shelf receivers (mostly single-frequency receivers) are a cheap and well-established means for OD [Montenbruck *et al.*, 2007]. For LEO satellites equipped with single-frequency receivers orbital accuracies of 1 – 10 meters could be achieved [Gill and Montenbruck, 2004 and Montenbruck, 2003].

For scientific applications, especially for geodetic research, orbit accuracies of the best possible extent are of significant interest. Along with the appearance of dedicated LEO missions for geodetic and geophysical research precise orbit determination (POD) for LEOs became a key technology in recent years. It has to be mentioned that LEO POD crucially relies on POD of GPS satellites, which has reached an excellent quality over the last years [IGSCB, 2005].

To make the best use of the highly accurate GPS measurements, advanced dual-frequency receivers are necessary. Table 2.1 lists some important LEO missions carrying geodetic-type GPS receivers onboard [Jäggi, 2006]. All these missions demand highest orbit accuracies. Topex/Poseidon was the first space mission dedicated to the investigation of the circulation of the oceans [Fu *et al.*, 1994]. It carried the first spaceborne radar altimeter to map the ocean topography. Mocrolab-1 was the first mission to demonstrate the ability of GPS radio

occultation for atmosphere sounding [Rocken *et al.*, 1997]. It carried a GPS antenna which was pointed 90 degrees with respect to the zenith direction. This enables to analyze signals that propagate horizontally through the atmosphere. By sounding the atmosphere with GPS for each day a large amount of globally distributed atmospheric profiles, e.g. of temperature, can be obtained [Kursinski *et al.* 1997]. The mission Satelite de Aplicaciones Cientificas-C (SAC-C) carries, among several other scientific instruments, a GPS receiver which serves a total of four antennas [SAC-C, 2009]. The antennas are mounted zenith-viewing for POD, fore- and aft-viewing for atmosphere sounding and also nadir-viewing for GPS altimetry by means of GPS signals reflected by the Earth's oceans. JASON-1 is the follow-on mission of TOPEX/Poseidon [JASON-1, 2009]. It is equipped with an advanced instrument for dual-frequency radar altimetry, but also carries a BlackJack GPS receiver, a retro-reflector array for SLR and a Doris receiver for POD. For Jason-1 a record of 1 cm radial accuracy has been reached [Luthcke *et al.*, 2003 and Haines *et al.*, 2004]. This is mainly due to its altitude of over 1300 km, where atmospheric drag is at a very low level. For satellites at lower altitudes precise orbit determination becomes more difficult, because of the increasing influence of the atmosphere. The Ice, Cloud and Land Elevation Satellite (ICESat) was designed to measure the annual and long-term behavior of the cryosphere [Schutz *et al.*, 2005] using a dedicated laser altimetry system. As a crucial condition for altimetry, ICESat is equipped with a BlackJack receiver for precise orbit determination. Radial accuracies of 2 cm have been achieved for ICESat which orbits at about 600 km [Rim *et al.*, 2005]. The Formosat-3 mission, also referred to as Cosmic (Constellation Observing System for Meteorology, Ionosphere and Climate) mission, is a constellation of six microsatellites [Wu *et al.*, 2005]. Each satellite carries two GPS antennas for precise orbit determination and two GPS occultation limb antennas for atmosphere sounding.

However, geodetic missions for studying the Earth's gravity field require highest orbital accuracies at the lowest possible altitudes. In the following the three most important and most dedicated geodetic missions, namely CHAMP, GRACE and GOCE, are discussed in more detail.

Table 2.1: LEOs using geodetic-type GPS receivers [Jäggi, 2006]

Satellite	Apogee (km)	Perigee (km)	Inclination (°)	Launch date
TOPEX/Poseidon	1331	1317	66.1	10 Aug. 1992
MicroLab-1	749	733	70.0	3 Apr. 1995
CHAMP	477	416	87.3	15 Jul. 2000
SAC-C	707	687	98.2	21 Nov. 2000
JASON-1	1333	1318	66.1	7 Dec. 2001
GRACE 1,2	506/507	483/483	89.0	17 Mar. 2002
ICESat	598	595	94.0	13 Jan. 2003
Formosat 3A,B,D-F	524-543	496-508	72.0	15 Apr. 2006
Formosat 3C	828	776	72.0	15 Apr. 2006
GOCE	270	270	96.5	exp. Mar. 2009

2.1 CHAMP

The German CHAMP (CHAllenging Minisatellite Payload) mission marked the first of a series of dedicated LEO satellite missions to study the Earth's gravity field [Reigber *et al.*, 2003]. The mission is managed by the GeoForschungsZentrum (GFZ) Potsdam, Germany [CHAMP, 2008]. CHAMP was launched from Plesetsk, Russia on 15 July 2000 into a near polar orbit with an inclination of 87° to obtain an almost global orbit coverage of the Earth. The orbit is near circular and had an initial altitude of approximately 454 km. Atmospheric drag is continuously lowering the satellite. Depending mostly on the density of the upper atmosphere, the spacecraft loses between some 10 to almost 100 meters per day in height. However, the envisaged mission lifetime of five years could repeatedly be prolonged by orbit maneuvers [Jäggi, 2006].

The spacecraft (see Figure 2.3) is 8.333 m long, 1.621 m wide and has a height of 0.750 m. Its mass amounts 522 kg.

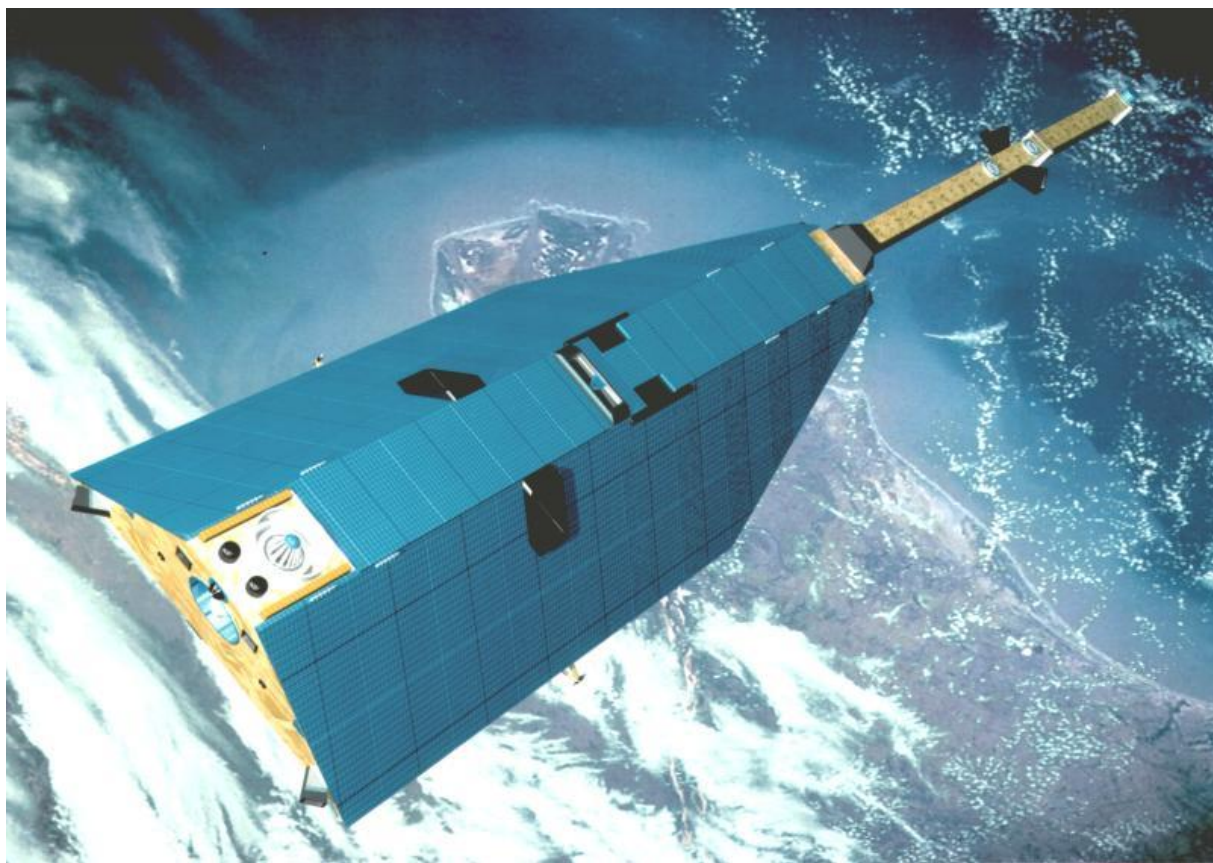


Figure 2.3: An artist's impression of the CAHMP satellite in orbit
[courtesy of Astrium GmbH]

The CHAMP mission aims to study the Earth's gravity field, its magnetic field and the physical properties of the troposphere and ionosphere [Reigber *et al.*, 2003]. In order to

achieve these goals, the spacecraft is equipped with several highly accurate scientific instruments. For the determination of the gravity field a GPS receiver, an accelerometer, SLR reflectors and star sensors are the most relevant instruments. For the other scientific research goals the satellite is additionally equipped with a magnetometer and an ion drift meter [*Reigber et al.*, 2003].

The satellite carries a BlackJack GPS receiver which was manufactured by the Jet Propulsion Laboratory (JPL) [*Kuang et al.*, 2001]. It is connected to a total of four GPS antennas and collects dual-frequency phase and pseudo-range measurements. The prime antenna is equipped with a choke ring and mounted on top of the satellite and serves for precise orbit determination [*Kroes*, 2006]. A backup antenna for POD is mounted right next to it. On the rear side of the spacecraft another antenna is placed for occultation measurements to sound the atmosphere [*Wickert et al.*, 2005]. The fourth antenna is positioned nadir-looking to be used for GPS altimetry.

To keep the spacecrafts attitude within a few degrees with respect to its nominal attitude cold gas thrusters are regularly fired (between 70 and 200 times per day) [*Jäggi*, 2006]. The spacecrafts attitude is autonomously determined by star sensors. The ASC (Advanced Stellar Compass) sensors provide attitude measurements with a precision of approximately 4 arcsec [*Jäggi*, 2006].

For the gravity field estimation the non-conservative forces acting on the satellite must be separated from the conservative forces. This task is performed by an accelerometer which is located within 2 mm from the center of mass. The STAR (Space Triaxial Accelerometer for Research missions) instrument measures the accelerations acting on the spacecraft along all three body axes with highest precision [*Reigber et al.*, 2003].

For an independent tracking of the satellite by Satellite Laser Ranging (SLR), CHAMP additionally carries a laser retro-reflector array on its bottom side. This allows for validation of the orbit solution derived purely from GPS measurements.

2.2 GRACE

The Gravity Recovery and Climate Experiment (GRACE) mission, see Figure 2.4, can be considered as the direct follow-on mission to CHAMP [*Tapley et al.*, 2004b]. It is a joint German - US mission conducted by the Deutsches Zentrum für Luft- und Raumfahrt (DLR) and the US National Aeronautics and Space Administration (NASA) [*GRACE*, 2008]. GRACE consists of two almost identical satellites flying in formation. The orbital characteristics are relatively similar to that of CHAMP, with the two satellites orbiting in the same trajectory with a nominal distance of approximately 220 km [*GRACE*, 2008]. The two satellites were launched on 17 March 2002 from Plesetsk, Russia. The orbit is near circular and near polar with an inclination of 89° and an initial altitude of 500 km. Orbital maneuvers are carried out at intervals of about 50 days to maintain the two spacecraft GRACE A and GRACE B within a distance of 170 and 270 km. GRACE A was initially the leading satellite of the formation. To avoid atmospheric surface erosion of the instruments a switch maneuver was conducted on 10 December 2005 making GRACE B the leading satellite [*Jäggi*, 2006].

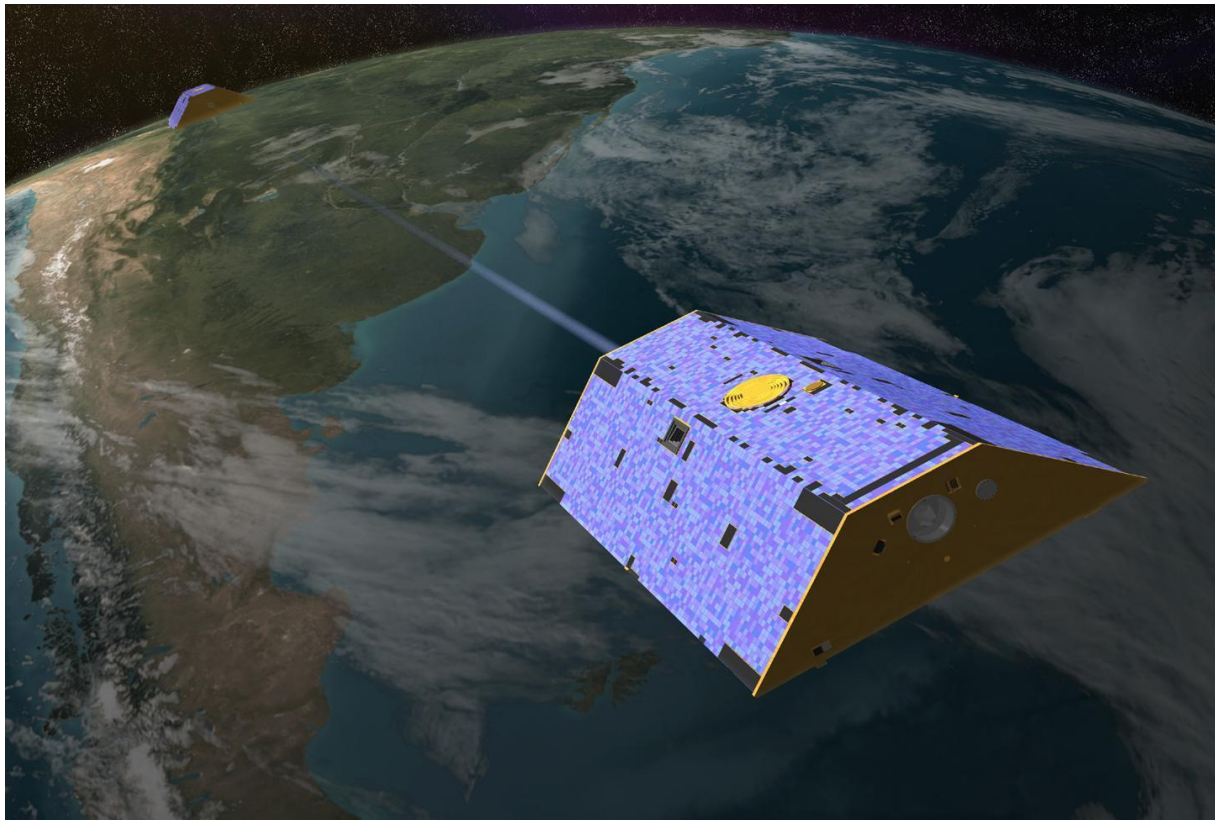


Figure 2.4: An artist's impression of the GRACE satellites in orbit
[courtesy of *University of Texas*]

The two GRACE spacecraft are of the same size with a length of 3.122 m, a width of 1.942 m and a height of 0.720 m [Jörggi, 2006]. The primary mission goal is to map the Earth's gravity field and its temporal variation with unprecedented accuracy [Tapley *et al.*, 2004b]. For this purpose, like for the CHAMP mission, the GRACE satellites themselves can be considered as the main scientific instruments. They are free falling proof masses that probe the Earth's gravity field. To accurately track the spacecrafats trajectory the satellites are equipped with several instruments for precise orbit determination. These comprise a JPL BlackJack receiver, a SuperSTAR accelerometer, autonomous star sensors and SLR reflectors. In addition, the two satellites are equipped with a ranging system to measure the (biased) distance between the two spacecraft [Kang *et al.*, 2006a]. This K/Ka-Band Ranging (KBR) system can be considered as the key instrument of the GRACE mission.

The GPS BlackJack receiver is a dual-frequency codeless type receiver which serves a total of three antennas mounted on the spacecraft. The main antenna for precise orbit determination is placed zenith-viewing and is equipped with a choke ring. The other two antennas are limb-viewing for atmosphere sounding.

The SuperSTAR accelerometer is a modified model of the STAR accelerometer as it is used for CHAMP. The accuracies of the measured accelerations are specified with 10^{-10} m/s^2 for the radial and along-track directions, and 10^{-9} m/s^2 for the cross-track component [Kang *et al.*, 2006b].

The orientation of the GRACE spacecraft is monitored by star camera assemblies (SCA) which measure the attitude of the satellites with a precision of approximately 25 arsec. This is a little bit less accurate than for CHAMP, because the vector measurements of the magnetosphere demand highest precision attitude data for CHAMP. However, accurate maintenance of the line-of-sight pointing of the K-band radar is necessary. Therefore the GRACE attitude control is very accurate and the actual attitude coincides with the nominal attitude model by less than 0.4° [Kirschner *et al.*, 2001]. It is therefore appropriate to use the nominal attitude model for the center of mass correction of the GPS signals, because the GPS antenna is separated from the center of mass of the satellite by 0.450 m which relates to an effect of incorrect attitude of only 0.1 mm [Kang *et al.*, 2006a].

The key instrument of the GRACE mission, however, is the K/Ka-Band inter-satellite ranging system. The two GRACE satellites form a gradiometer that is particularly sensitive to high-order harmonic components in the Earth's gravity field [Kirschner *et al.*, 2001]. The system delivers ultra-precise measurements of the change of distance between both spacecraft. The KBR system generates K- and Ka-band microwave signals at 24.5 GHz and 32.7 GHz for the generation of ionosphere free biased range measurements. The precision of these observations is of 10 μm at 1 Hz samples [Dunn *et al.*, 2003]. The concept of two LEO satellites measuring their mutual distance is generally denoted as low-low satellite-to-satellite tracking (ll-SST) [van Loon, 2008].

2.3 GOCE

The Gravity field and steady-state Ocean Circulation Explorer (GOCE) is so far the last of a series of dedicated gravity field satellite missions [GOCE, 2008]. It is managed by the European Space Agency (ESA) as part of its “Living Planet Program”. The project experienced several delays and the satellite was eventually launched on 17 March 2009. After the commissioning phase, it will be an ideal complement to the existing CHAMP and GRACE missions.

The GOCE satellite (see Figure 2.5) is the first satellite to carry a gradiometer onboard. Three pairs of accelerometers measure the gravity gradients in three orthogonal directions. The baselines between the accelerometers are approximately 0.5 m. The accelerometers will work with a precision of $10^{-12} \text{ m/s}^2/\sqrt{\text{Hz}}$ [Drinkwater *et al.*, 2007]. The difference of the respective accelerometer readings is the actual gradiometer measurement, and the half of the sum of the readings represents the total external acceleration acting on the satellite [Jäggi, 2006]. The data of the Electrostatic Gravity Gradiometer (EGG) will allow for a high resolution recovery of the static gravity field of homogeneous quality with unprecedented accuracy and resolution. The resulting products will eventually yield a remarkable step forward in ocean, solid Earth and sea-level modelling.

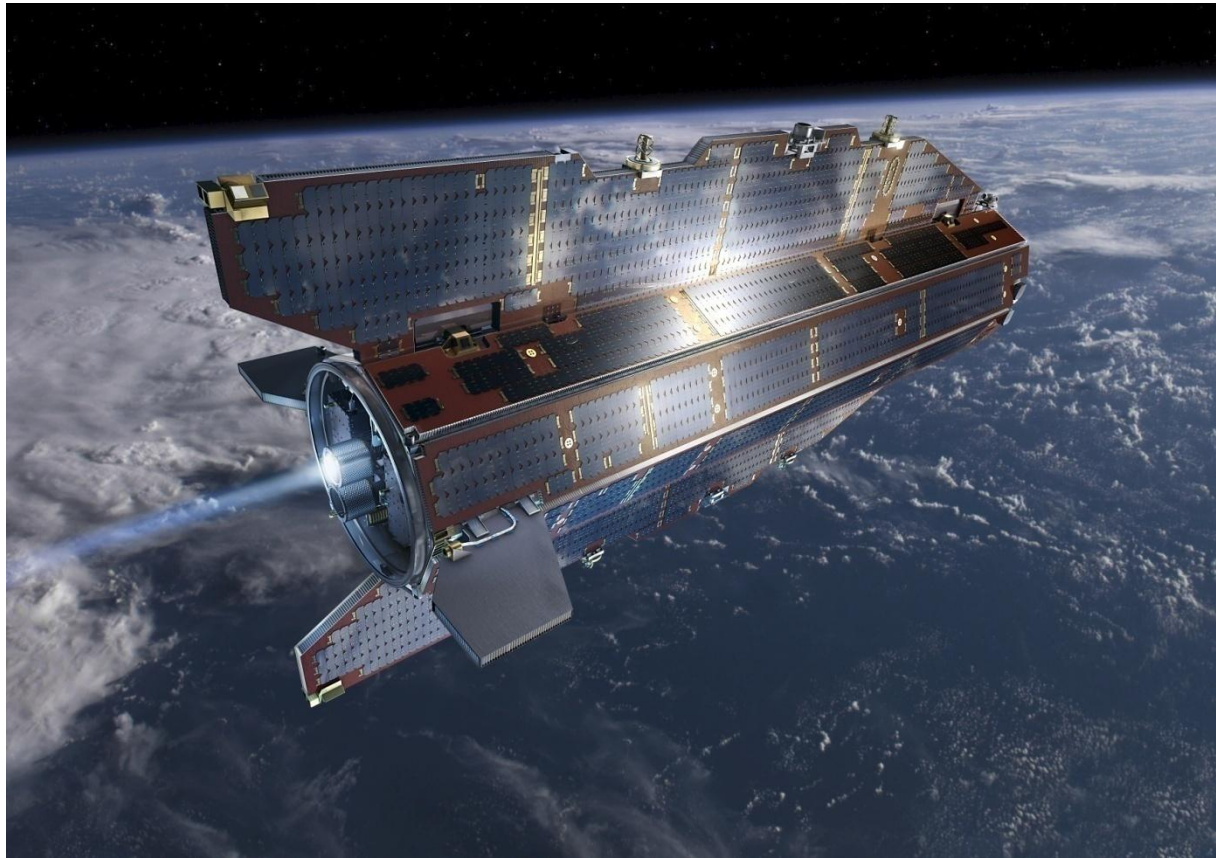


Figure 2.5: An artist's impression of the GOCE satellite in orbit [courtesy of *ESA*]

For a spaceborne gradiometer a very low orbit is preferable because it implies stronger signals and a better accuracy. Therefore, GOCE will start operation at an altitude of 250 km. This will allow for a mapping of the gravity field with a precision of 1 mgal which relates to a determination of the geoid with a precision of 1 to 2 cm [*Drinkwater et al.*, 2007]. The orbit will be inclined by 96.5° and almost circular for global coverage. The nominal mission duration is set to 20 month in a sun-synchronous dusk-dawn configuration. In contrast to the CHAMP and GRACE missions the GOCE satellite will orbit using drag-free control. An assembly of ion thrusters will work to overcome drag in the along-track direction. The drag-free attitude-control system comprises star trackers, Sun and Earth sensors [*Drinkwater et al.*, 2007]. The spacecraft propulsion for flying in drag-free mode is necessary to prevent the satellite from declining too rapidly due to atmospheric drag in its very low altitude. The mission duration is thus ultimately dependent on the lifetime of the ion thruster. In addition, to keep the effect of atmospheric drag low, the spacecraft is shaped like an arrowhead with a minimized cross-section of 0.8 m^2 in the direction of flight [*Drinkwater et al.*, 2007]. The satellite has a length of 5 m and a mass of 1100 kg.

It must be pointed out that for the GOCE mission the gradiometer is the main measurement system, and not the satellite body itself, like it is for the CHAMP and GRACE missions. Non-gravitational effects acting on a spacecraft's surface exhibit constant accelerations throughout the spacecraft's body. Thus, gradiometer measurements, acquired through forming the difference between two accelerometer measurements, are not affected from non-gravitational forces. Therefore, flying in drag-free mode is possible for gravity field recovery with gradiometry.

In order to locate its measurements with respect to the Earth, the satellite gradiometry will be complemented by instruments for precise orbit determination. The dual-frequency Lagrange GPS receiver is connected to two GPS antennas and can track up to twelve GPS satellites. The Lagrange receiver provides high precision GPS data at a sample rate of 1 Hz [*Drinkwater et al.*, 2007]. Like the CHAMP and GRACE satellites, a laser retro-reflector array is mounted on the bottom side of the GOCE satellite.

3 Fundamentals of GPS

Besides a wide range of terrestrial applications, GPS is also a highly capable means for spacebased applications like orbit navigation and control of LEO satellites. Compared to other orbit navigation systems, GPS has the striking advantage of remarkable accuracy with a global coverage. The relevant information and the mathematical framework about GPS, as needed for the POD applications applied in this research, will be provided in the following. The employed observation types, what affects them and how they are prepared for positioning will be outlined in detail.

3.1 The Global Positioning System – an Overview

As described in *Leick* [2004], the Global Positioning System is operated by the U.S. Department of Defense as a space-based radio navigation system. It nominally consists of 24 satellites distributed over six orbital planes. The planes are inclined by 55° with respect to the Earth's equator and equally spread by 60° on the equator. The orbits are near circular with a semi-major axis of about 26600 km. Figure 3.1 illustrates a GPS satellite orbit over a time intervall of 10 hours.

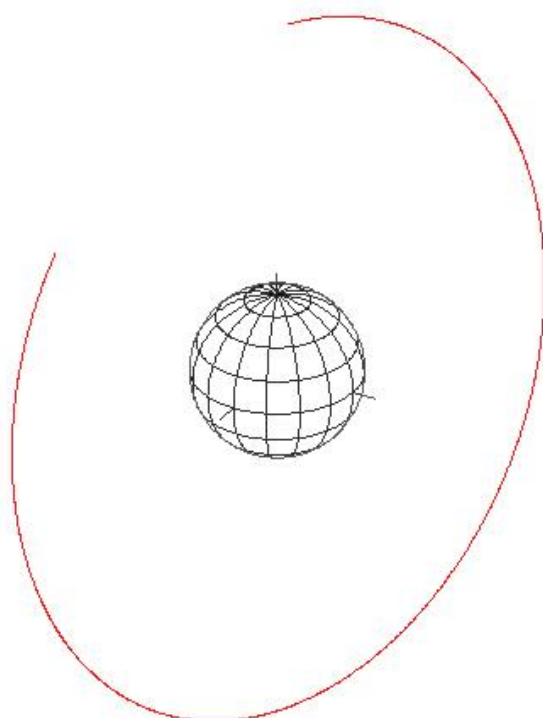


Figure 3.1: Orbit of a GPS satellite over 10 hours

The revolution period for GPS satellites is about 11 hours and 58 minutes atomic time, which corresponds to half a sidereal day. As a consequence, the ground track of each satellite repeats itself twice a day in an Earth-fixed reference system. The entire constellation of all the GPS satellites is denoted as the space segment. The full operational capability (FOC) of the space segment was declared in July 1995. FOC assures that there are permanently at least four or more GPS satellites in view for any location on the Earth and within its vicinity of about 1000 km elevation [Wertz, 2001]. However, the space segment gets continuously maintained and modernized, with satellites of newer generations replacing out-dated ones. GPS satellites are produced in always modernized tranches, denoted as Blocks. These are Block I, Block II, Block IIA ('A' denotes advanced), Block IIR ('R' denotes replenishment), Block IIR-M ('M' denotes modernized), Block IIF ('F' denotes follow on) and Block III [Hofmann-Wellenhof *et al.*, 2008]. As of April 2008, there are 32 active satellites in orbit ranging from Block IIA to Block IIR-M [Hugentobler, 2008]. Figure 3.2 displays the status of the space segment as of 7 April 2008. The modernization of GPS also includes new signals on additional frequencies, starting with Block IIR-M. The receivers that provide data for this research only make use of the initially provided signals. Therefore, only these initial signals and frequencies are discussed in the following chapters. Nevertheless, the types of the different GPS satellites must be distinguished for applying different corrections to the observations (see Section 3.1.1).

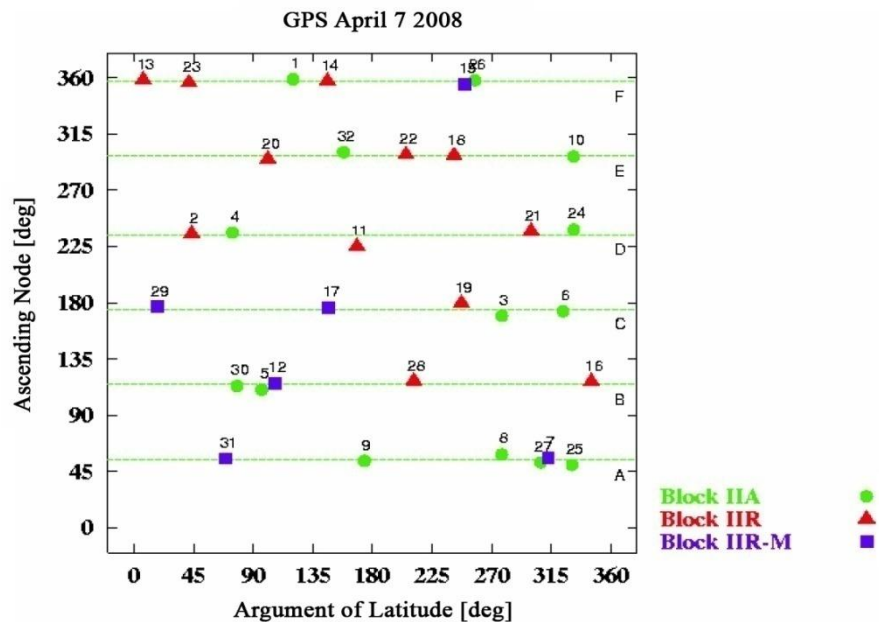


Figure 3.2: The GPS space segment (Status as of 7 April 2008)
[courtesy of Hugentobler, 2008]

Each satellite continuously emits data on two carriers, denoted as L_1 and L_2 , in the microwave L-band. As already mentioned, the emission of the signals covers the area of a cone around the nadir direction with an opening angle of approximately 15 degrees. The two frequencies, f_1 and f_2 , and their corresponding wavelengths, λ_1 and λ_2 , amount to [Hofmann-Wellenhof *et al.*, 2008]

$$\begin{aligned} f_1 &= 1575.42 \text{ MHz} & \lambda_1 &\approx 19.0 \text{ cm}, \\ f_2 &= 1227.60 \text{ MHz} & \lambda_2 &\approx 24.4 \text{ cm}. \end{aligned} \quad (3.1)$$

For the acquisition and tracking of the signals, so-called pseudo random noise (PRN) codes are generated and modulated onto the carriers. The coarse acquisition (C/A) code is modulated onto the first frequency only. It is freely accessible for all users. The more accurate precision (P) code is modulated on both of the frequencies. Direct observation of the P-code is usually restricted to authorized users by “anti-spoofing” (AS), which generates an encrypted version of the P-code, called P(Y)-code [Kroes, 2006].

As described later, the orbit determination methods used throughout this research are based on undifferenced observation data. An important precondition for this approach is that the intentional manipulation of GPS clocks and orbits, called selective availability (SA) remains turned off as it is the case since 2 May 2000 [Hofmann-Wellenhof *et al.*, 2008].

Besides the signals for navigation, GPS satellites additionally emit the broadcast message which contains information comprising the satellite’s orbit ephemeris data and clock offset estimations, the satellite’s health status, i.e. the satellite’s operational status, various correction data, such as ionospheric corrections, and other data messages [Hoffmann-Wellenhof, 2008]. However, for applications as presented in this work, the accuracy of the broadcast orbit and clock data is too coarse to reach the intended precision for LEO positioning [IGSCB, 2005]. Precise orbit and clock data of the GPS satellites must therefore be acquired from external sources.

3.1.1 GPS Orbit and Clock Products

Accurate orbit and clock information is of crucial importance for any precise GPS application, especially for the chosen zero difference approach of this research (see section 3.2). For post-processing applications, as it is the case in this research, other data than that contained in the broadcast message can easily be employed. For GPS and other Global Navigation Satellite Systems (GNSS) the International GNSS Service (IGS) is the primary provider of precise orbit and clock products. As a service of the International Association of Geodesy (IAG), the IGS is a well-established voluntary federation of more than 200 worldwide agencies that collect station data and contribute to the generation of highly accurate GNSS ephemerides [Dow *et al.*, 2005]. The number of contributors to the IGS and the achieved product quality is continuously increasing. Due to the worldwide participation of organizations to the IGS, one of its most decisive advantages is that it maintains a large and globally distributed network of over 300 tracking stations (see Figure 3.3). Furthermore, the IGS provides Earth orientation parameters (ERPs), coordinates and velocities of the tracking stations, global ionosphere maps and tracking station troposphere zenith wet delays [Dow *et al.*, 2005]. All data and products of the IGS are currently free of charge and will apparently stay freely available in the foreseeable future.

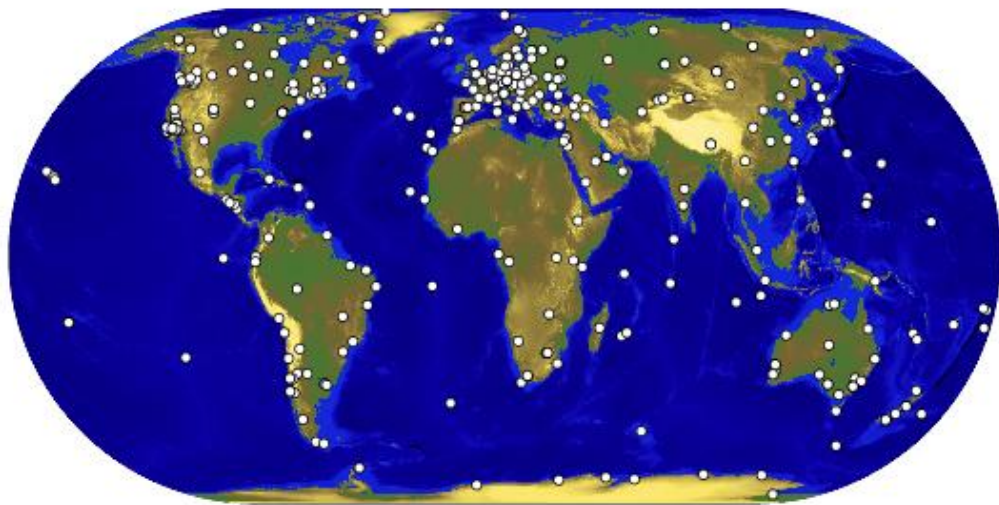


Figure 3.3: The IGS Tracking Network [courtesy of *IGS*]

Within the IGS, several analysis centers (ACs) produce independent orbit and clock data. These solutions are afterwards combined to a single IGS product by suitable weighting. Currently three types of ephemerides with different latencies are offered [*IGSCB*, 2008], namely the final, rapid and ultra-rapid products (see Table 3.1). The final orbits and clocks are published with a latency of about 13 days after each week. They are the most carefully processed and quality controlled solution with a reported orbital accuracy of better than 5 cm root mean square (RMS). The rapid solution is already made available approximately some 17 hours after the end of the day. Today the rapid solution already achieves an accuracy comparable to the final solution. The ultra-rapid solution contains an observed and a predicted part. It is updated four times daily, with the observed half even too reaching this high accuracy level of the other solutions, whereas the accuracy of the prediction decreases to about 10 cm RMS for the orbits. The ultra-rapid solution is especially intended for real-time applications.

Table 3.1: IGS orbit and clock products [*IGSCB*, 2008]

Solution	Product	Accuracy	Rate	Latency
Final	Orbits	< 5 cm	15 min	13 days
	Clocks	< 0.1 ns	5 min	
Rapid	Orbits	< 5 cm	15 min	17 hours
	Clocks	0.1 ns	5 min	
Ultra-Rapid (observed)	Orbits	< 5 cm	15 min	3 hours
	Clocks	~0.2 ns		
Ultra-Rapid (predicted)	Orbits	10 cm	15 min	real – time
	Clocks	5 ns		

The IGS uses a set of various standard formats for its data and products. The above described ephemerides are provided in the SP3 format [Hilla, 2007]. Therein, positions, velocities and also clock offsets of the GPS satellites are provided in a temporal resolution of 15 minutes. For high-precision applications the satellite clocks are additionally offered separately with a rate of 5 minutes or even 30 seconds, delivered in the clock-RINEX format [Ray and Gurtner, 2006].

The orbits are expressed in the International Terrestrial Reference Frame, i.e. an Earth-fixed reference frame (ITRF) [ITRF, 2009]. As recommended by the IGS, a Lagrange interpolation between the given positions may be employed to compute the position for each needed epoch [Hofmann-Wellenhof *et al.*, 2008]. An 8th-order Lagrange interpolation delivers positions of sufficient accuracy with 15 min spaced data points, and is therefore used within this work [Kroes, 2006]. Furthermore, the given positions relate to the center of mass of the spacecraft. To be used for precise positioning the actual position of the antenna phase center must be known. Therefore, the positions have to be corrected for the so-called antenna phase center offsets (PCO), following exact rules, stipulated by the IGS. The coordinates of the antenna phase center are defined in the GPS satellite body coordinate system. According to Kouba and Héroux [2001], the constant PCOs for the different satellite blocks, given in Table 3.2, are to be applied.

Table 3.2: Antenna phase center offsets for GPS satellites
in the body fixed coordinate system

	X [m]	Y [m]	Z [m]
Block II/IIA	0.279	0.000	1.023
Block IIR	0.000	0.000	0.000

However, this convention was only valid until 5 November 2006 (GPS week 1400). On 6 November 2006 a change from relative to absolute antenna phase center corrections has been accomplished [Schmid *et al.*, 2005 and Schmid *et al.*, 2007]. From this epoch on more elaborate models of the PCOs have to be used [Gendt, 2006]. The PCO coordinates are no longer considered identical for all satellites of a certain block. For the individual satellites (and also for the IGS ground stations) the PCOs are now published in the ANTEX format [Rothacher and Schmid, 2006]. It further accounts for the fact that besides the phase center offset, the GPS antennas additionally show nadir- and azimuth-dependent phase center variations (PCVs). As the PCVs are typically at the mm level [Schmid *et al.*, 2005], they are not taken into account for this research.

The transformation of the PCO correction from the body-fixed coordinate system requires the knowledge of the satellites orientation in space. For that, it can be assumed that the orientation of the GPS satellites is close enough to the nominal attitude. It is defined that the z-axis is pointed towards the center of the Earth, the y-axis is perpendicular to the vector between the Sun and the GPS satellite and the x-axis completes the right-handed system [Kouba, 2002 and Xu, 2003]. The vector of the Sun can be conveniently calculated with sufficient precision using analytical series expansions [Montenbruck and Gill, 2000].

As specified in Table 3.1, the clock estimates of the precise IGS products are at the 0.1 – 0.2 nanosecond level. This corresponds to 3-6 cm, which is compatible with the orbit precision [Kouba, 2001]. For the interpolation of the clock offsets a linear interpolation is more appropriate than any higher order interpolation [Kroes, 2006]. This yields a precision level for interpolated values of a few decimeters using 15 min sampled data, and is below the decimeter level with a 5 min data grid [Zumberge and Gendt, 2001].

Montenbruck et al. [2005a] carried out extensive testing and assessment of the errors resulting from interpolation of the different clock data. It revealed a dependency on the satellite block and further on the type of the atomic clock. In general the satellites using Rubidium clocks show a better performance, see Figure 3.4, which has also been confirmed by *Bröderbauer*, 2009. Because of the fact, that an increasing number of GPS satellites is equipped with Rubidium clocks, the overall interpolation error for the entire GPS constellation decreased to 6 cm for the 15 min interpolation and to 3 cm for the 5 min interpolation by the end of year 2004, see Figure 3.5 [*Montenbruck et al.*, 2005a].

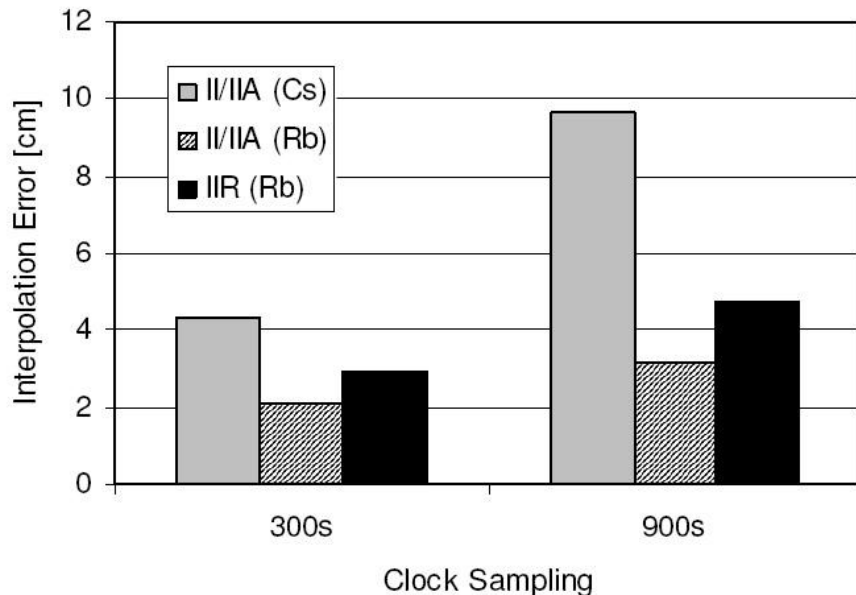


Figure 3.4: RMS error of GPS clock interpolation for 5 and 15 minute sampling [courtesy of *Montenbruck et al.*, 2005a]

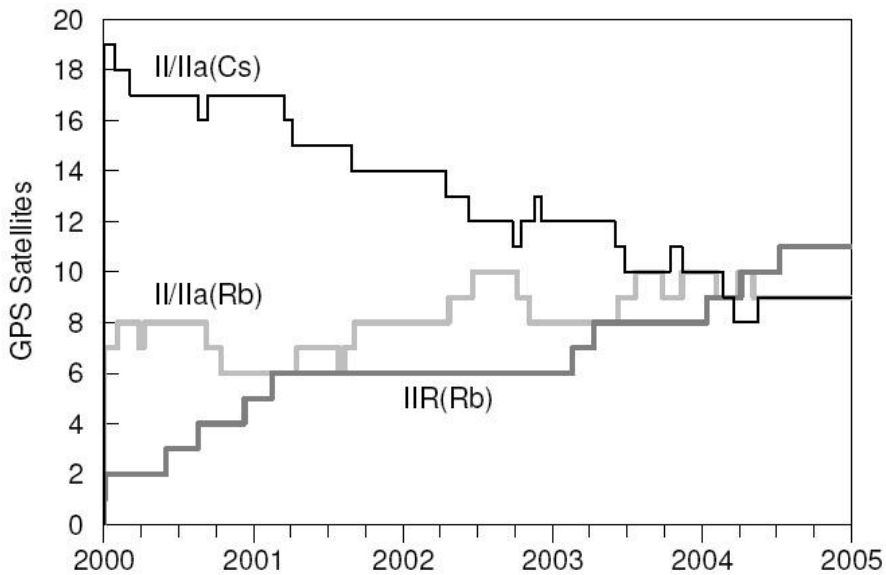


Figure 3.5: Number of GPS satellites operating cesium (Cs) and rubidium (Rb) clocks over time [courtesy of Montenbruck *et al.*, 2005a]

Besides the release of the combined solutions by the IGS, some of the contributing Analysis Centers make their own products available. Due to the increasing request for an even denser sampling rate, the Center for Orbit Determination in Europe (CODE) and the Jet Propulsion Laboratory (JPL) publish so-called high-rate orbit and clock data with a 30 seconds sampling rate [Hugentobler, 2004]. Within this research, the same antenna phase offsets and attitude model, as applied for IGS products, are also used for the high-rate data. For these products Zumberge and Gendt [2001] determined an interpolation error of only 4 mm.

However, the chosen approach for orbit determination of this thesis, which is based on zero difference GPS observations (see. section 3.2.3), fully relies on the quality of precise orbit and clock data. Especially in the radial direction, any error in these data, but also errors in the phase center correction, map into the observation equation and thus affects the LEO positioning. As described in chapter 4, this is particularly the case for kinematic orbit determination. Nevertheless, the chosen orbit model of reduced-dynamic orbit determination is also heavily affected due to the high relaxation by pseudo-stochastic parameters [Švehla and Rothacher, 2006].

3.2 Modeling of GPS Observations

GPS observables are ranges which are deduced from measured time or phase differences based on a comparison between received signals and receiver-generated signals [Hoffmann-Wellenhof *et al.*, 2008]. These measurements are categorized as “down-links” from the satellite down to the receiver. Employing the “one-way concept”, the obtained ranges are biased by the difference of the errors of the involved satellite and receiver clocks. As a consequence, these biased ranges are denoted as pseudoranges.

In general, there are three types of GPS observations, the code or pseudorange observation, the carrier phase or integrated Doppler observation, and the range-rate or instantaneous Doppler observation [Kroes, 2006]. Not every spaceborne receiver supports or records all of these observations. This section primarily deals with the GPS observation types that are used within this research.

Although the P(Y)-code is encrypted, several techniques, such as (semi-)codeless tracking, have been developed allowing P(Y)-code observations to be made without the decryption key and hardware, at the expense of the Signal to Noise Ratio (SNR), and thus a reduced precision [Woo, 1991]. The CHAMP and GRACE satellites are equipped with identical JPL Blackjack receivers, which record observations of all three GPS codes (C/A, P₁, P₂) and the two carrier phases (L₁, L₂).

All GPS signals are related to the time of the GPS system. The GPS time is defined as a common reference time, and has a constant offset of -19 seconds with respect to the international atomic time (TAI) [McCarthy, 1996 and McCarthy *et al.*, 2003]. To realize GPS time, the satellites are equipped with Cesium and/or Rubidium atomic clocks. Geodetic-type receivers mostly make use of temperature compensated crystal oscillators (TCXOs) [Kroes, 2006].

However, both the GPS satellite clock's time s and the receiver clock's time r experience a deviation (δs and δr) with respect to the GPS system time t . These clock offsets are not constant over time, but exhibit a drift. The internal times as well as their offsets can therefore be considered as functions of t :

$$\begin{aligned} s(t) &= t + \delta s(t) \\ r(t) &= t + \delta r(t). \end{aligned} \tag{3.2}$$

For each measurement the two relevant epochs are the emission time t_e and the reception time t_r . Accordingly, the received signal is the satellite signal s_e of emission time t_e and r_r is the receiver generated signal at reception time t_r :

$$\begin{aligned} s_e &= s(t_e) = t_e + \delta s(t_e) \\ r_r &= r(t_r) = t_r + \delta r(t_r) \end{aligned} \tag{3.3}$$

Because the clock offsets are not constant over time they are only valid for a certain epoch. This has to be taken into account when modelling the different observation types. Modern GPS receivers, such as those onboard the CHAMP and GRACE satellites, however, keep their clocks roughly synchronized with respect to GPS time within about one millisecond [Jäggi, 2006]. However, the epoch t_r , at which the observation is made, can be considered the same for all types of measurements and to all satellites. Of course, the corresponding emission times are different for each involved satellite.

In the following sections the GPS observation equations, linear combinations and further processing details that are relevant for the chosen approach for LEO POD will be discussed.

3.2.1 Code Observation Equation

PRN codes essentially realize a reference to the system time on the signal. A measure of signal travel time, and thus of the distance between receiver and satellite, can therefore be obtained by time correlation of the received and the internally generated code. The code observation $P(t_r)$, measured at time t_r , is thus the difference of $r_r - s_e$, multiplied by the speed of light c to obtain a measure in units of meters:

$$P(t_r) = (r_r - s_e) \cdot c. \quad (3.4)$$

Substitution of (3.3) into (3.4) yields

$$P(t_r) = (t_r + \delta r(t_r) - t_e - \delta s(t_e)) \cdot c. \quad (3.5)$$

Rearranging leads to

$$P(t_r) = (t_r - t_e) \cdot c + \delta r(t_r) \cdot c - \delta s(t_e) \cdot c. \quad (3.6)$$

The term $(t_r - t_e) \cdot c$ represents the true geometric range between the phase centers of the receiver and the satellite at the considered epochs. The true signal travelling time $(t_r - t_e)$ is denoted as $\tau(t_r)$ and the true geometric range is given by $\rho(t_r) = c\tau(t_r)$. Substitution of these expressions results in the basic pseudorange observation equation

$$P(t_r) = \rho(t_r) + \delta r(t_r) \cdot c - \delta s(t_r - \tau(t_r)) \cdot c. \quad (3.7)$$

Thus, the code observation is a direct but biased measure of the true range between the antenna phase centers of the GPS satellite and the receiver. Equation (3.7) is only parametrized with t_r . Although, τ as well as ρ are actually functions of the unknown epoch t_e , this fact can be dealt with using the light time equation [Blewitt, 1991]. A detailed description and derivation of the light time equation is given in Appendix A.1.

Equation (3.7) represents the fundamental concept of the code observation. The actual observation however is further affected by additional influences. Most relevant for this work are atmospheric effects, instrumental biases in both the satellite and the receiver, signal multipath and measurement noise [Kroes, 2006].

For GPS signals the relevant propagation regions in the atmosphere are the troposphere and the ionosphere. The troposphere's effective height is about 40 km [Leick, 2004]. Therefore it is of no relevance for the considered space applications because no ground based observations are involved.

Other than the troposphere, the ionosphere ranges from about 50 to 1000 km above the surface of the Earth [Hofmann-Wellenhof *et al.*, 2008]. It consists of ions and free electrons and is a dispersive medium with respect to GPS L-band radio signals. Thus, its effect on the signals is frequency dependent. According to Hofmann-Wellenhof *et al.* [2008] the ionosphere causes a delay of the modulated code signal. The so-called ionospheric path delay, $I(t, f)$, can be modeled for GPS code observations, given in units of meters, by

$$I(t, f) = \frac{40.3}{f^2} \text{TEC}(t), \quad (3.8)$$

where TEC is defined as the Total Electron Content along the signal path between the receiver and the respective GPS satellite. It has to be mentioned that (3.8) only covers the first order ionospheric effect. But it comprises the dominant part of the delay, i.e. more than 99.9% of the total effect, whereas higher order effects only cause influences up to the mm level on the measurements [Montenbruck and Gill, 2002].

The remaining relevant biases and errors can be grouped into one term [Leick, 2004],

$$M_P(t) = s_P(t) + m_P(t) + r_P(t), \quad (3.9)$$

where $s_P(t)$ covers the satellite hardware delay, $m_P(t)$ stands for the code multipath delay and the receiver hardware delay is given by $r_P(t)$.

Each observation underlies a thermal measurement noise $\varepsilon_P(t)$, which can be assumed purely random with a zero mean and is typically at the decimeter level for modern geodetic-type receivers [Kroes, 2006].

However, a rigorous consideration of GPS observations also requires to account for post-Newtonian effects. The (periodic) relativistic effects on the signal between a moving receiver and emitter are caused by variations of velocity and potential level in the Earth's gravity field, due to the eccentricity of the orbits. The effects induced by the receiver motion and by the motion of the GPS satellite are attained with sufficient accuracy through

$$\begin{aligned} \delta_{rel}(t_r) &= \delta rel_{LEO}(t_r) + \delta rel_{GPS}(t_r) = \\ &= \frac{-2 \cdot \mathbf{x}_{LEO}(t_r) \cdot \mathbf{v}_{LEO}(t_r)}{c} + \frac{2 \cdot \mathbf{x}_{GPS}(t_e) \cdot \mathbf{v}_{GPS}(t_e)}{c}, \end{aligned} \quad (3.10)$$

[McCarthy, 1996 and Ashby, 2007], where \mathbf{x} and \mathbf{v} are the positions and the velocities of the LEO spacecraft and of the GPS satellite, respectively.

Taking into account these additional effects, the final observation equation for code pseudoranges for each of the two frequencies yields

$$P(t_r) = \rho(t_r) + \delta r(t_r) \cdot c - \delta s(t_r - \tau(t_r)) \cdot c + I(t_r, f) + M_P(t_r) + \delta_{rel}(t_r) + \varepsilon_P(t_r). \quad (3.11)$$

A summary of all effects, and their amounts, that influence the pseudorange measurement is given in Table 3.3 [Ramos-Bosch, 2008a].

Table 3.3: Effects of the code observation equation for LEO satellites

Effect	Amount of influence
Geometric range	ρ ~20000 km
Receiver clock offset	$c\delta r$ < 300 km
GPS satellite clock offset	$c\delta s$ < 300 km
Ionospheric phase delay	$I(t_r, f)$ 2 – 5 m
Satellite and receiver hardware delays	$s_p \& r_p$ < 2 m
Multipath	m_p < 5 cm
Relativistic effects (for eccentricities $e \leq 0.01$)	δ_{rel} < 13 m
Thermal noise	ε_p < 1 m

The observation equation (3.11) relates the phase centers of the GPS satellite's antenna and of the LEO satellite's receiver. Center of mass corrections have to be applied for LEO positioning, see section 4.1.3. Furthermore, it has to be considered, that the epoch t_r of the measurement is initially unknown, due to the unknown clock offset $\delta r(t_r)$. The epoch has, therefore, to be updated within each iteration of positioning.

3.2.2 Phase Observation Equation

Similar to the measurement of the code, most GPS receivers additionally track the accompanying carrier onto which the code is modulated. For one of the frequencies the according carrier phases are here denoted as ψ for the satellite's phase and ϕ for the receiver's phase. The considered phases are:

$$\begin{aligned}\psi_e &= \psi(t_0) + f(t_e - t_0) + f(\delta s(t_e) - \delta s(t_0)), \\ \phi_r &= \phi(t_0) + f(t_r - t_0) + f(\delta r(t_r) - \delta r(t_0)),\end{aligned}\tag{3.12}$$

where $\psi(t_0)$ and $\phi(t_0)$ are the initial phases of the receiver and of the satellite at t_0 , and f is the frequency of the particular carrier. Correlation Φ of these phases is ambiguous because of an unknown integer number N of carrier cycles between the two signals. Thus the beat phase is given in units of cycles by

$$\Phi(t_r) = \phi_r - \psi_e + N.\tag{3.13}$$

Substitution of (3.12) into (3.13), rearrangement and the introduction of the signal travel time $\tau(t_r)$ yields

$$\Phi(t_r) = f\tau(t_r) + f\delta r(t_r) - f\delta s(t_r - \tau(t_r)) + A_L,\tag{3.14}$$

where the now real valued bias or ambiguity term

$$A_L = N + \phi(t_0) - f\delta r(t_0) - \psi(t_0) + f\delta s(t_0),\tag{3.15}$$

contains all parameters which are constant over a continuous tracking pass [Teunissen and Kleusberg, 1998]. The phase ambiguity parameter is the same for all observation epoches as long as the GPS satellite is above the horizon of the receiving antenna and phase-lock is maintained. If the receiver loses lock of the signal, a new bias term has to be introduced due to the discontinuity (phase break) in the accumulated carrier phase. Like for the code observation equation, the basic phase observation (3.14) is directly related to the true signal travelling time $\tau(t_r) = (t_r - t_e)$ between the phase centers of the satellite and the receiver, and only parametrized with t_r .

Also the phase observation underlies further influences, like the effect of the ionosphere, hardware delays, multipath and thermal noise [Kroes, 2006]. Like for the code observation, the troposphere does not affect the phase observation when the considered range is located in space.

The carrier phase experiences an advancement due to the ionosphere [Leick, 2004]. In a first order approximation it amounts the same as the delay of the modulated code, but with opposite sign [Leick, 2004].

Relativistic effects on the phase measurements occur in the same way as for the code measurements, see equation (3.10) [McCarthy, 1996 and Ashby, 2007].

Multiplication of equation (3.14) with the according signal wavelength λ yields an expression in units of meters. Introducing the necessary corrections, the final carrier phase observation equation, for any of the two frequencies, is given by

$$L(t_r) = \rho(t_r) + c\delta r(t_r) - c\delta s(t_r - \tau(t_r)) - I(t_r, f) + \lambda A_L + M_L(t_r) + \delta_{rel}(t_r) + \varepsilon_L(t_r). \quad (3.16)$$

The bias term

$$M_L(t) = s_L(t) + m_L(t) + r_L(t) + w_L(t), \quad (3.17)$$

comprises all systematic errors of the observation, where $s_L(t)$ covers the satellite hardware delay, $m_L(t)$ stands for the phase multipath delay and the receiver hardware delay is given by $r_L(t)$. In addition $w_L(t)$ accounts for the effect of phase wind-up. Because of the polarized GPS signal, phase wind-up occurs when the receiver is rotating around the line of sight towards the GPS satellite [Wu *et al.*, 1993]. Such a rotation is interpreted by the receiver as an apparent variation of distance relative to the GPS satellite. For spaceborne GPS applications this effect can increase to significant amounts when e.g. the satellite's attitude is not actively controlled [Kroes, 2004].

The measurement noise $\varepsilon_L(t_r)$ is again assumed to be purely random with a zero mean. The overall accuracy of phase observations is on the mm level, and thus much more accurate than of code measurements. Furthermore, multipath errors can be confined to a quarter of the signal wavelength [Braasch, 1995]. A summary of all effects, and their amounts, that influence the carrier phase signal is given in Table 3.4 [Ramos-Bosch, 2008a].

Table 3.4: Effects of the carrier phase observation equation for LEO satellites

Effect	Amount of influence
Geometric range	ρ ~20000 km
Receiver clock offset	$c\delta r$ < 300 km
GPS satellite clock offset	$c\delta s$ < 300 km
Ionospheric phase advance	$I(t_r, f)$ 2 – 5 m
Ambiguity term	λA_L ~20000 km
Satellite and receiver hardware delays	$s_L \& r_L$ < 2 m
Multipath	m_L < 2 cm
Phase wind-up	w_L < 20 cm
Relativistic effects (for eccentricities $e \leq 0.01$)	δ_{rel} < 13 m
Thermal noise	ε_L < 1 cm

The described carrier phase observation equation relates the phase centers of the GPS satellite's antenna and of the LEO satellite's receiver. Therefore, center of mass corrections have to be applied for LEO positioning, see section 4.1.3. Like for the code measurement, the epoch t_r has to be updated with a new estimate for the clock offset $\delta r(t_r)$ within each iteration of positioning.

3.2.3 Dual Frequency Observation Model

Modern GPS receivers generate pseudoranges and carrier phases to all satellites in view at the same nominal time t_r on both frequencies [Leick, 2004]. Therefore, the receiver clock error, but also hardware delays, can be considered the same for a single epoch. Without considering the comparatively imprecise C/A-code for this research, the overall dual frequency observation model for the P-code and the associated carrier phase measurements can be grouped as

$$\begin{aligned}
 P_1(t_r) &= \rho(t_r) + c\delta r(t_r) - c\delta s(t_r - \tau(t_r)) + I(t_r, f_1) + M_{P_1}(t_r) + \delta_{rel}(t_r) + \varepsilon_{P_1}(t_r) \\
 P_2(t_r) &= \rho(t_r) + c\delta r(t_r) - c\delta s(t_r - \tau(t_r)) + \frac{f_1^2}{f_2^2} I(t_r, f_1) + M_{P_2}(t_r) + \delta_{rel}(t_r) + \varepsilon_{P_2}(t_r) \\
 L_1(t_r) &= \rho(t_r) + c\delta r(t_r) - c\delta s(t_r - \tau(t_r)) - I(t_r, f_1) + \lambda_1 A_{L_1} + M_{L_1}(t_r) + \delta_{rel}(t_r) + \varepsilon_{L_1}(t_r) \\
 L_2(t_r) &= \rho(t_r) + c\delta r(t_r) - c\delta s(t_r - \tau(t_r)) - \frac{f_1^2}{f_2^2} I(t_r, f_1) + \lambda_2 A_{L_2} + M_{L_2}(t_r) + \delta_{rel}(t_r) + \varepsilon_{L_2}(t_r)
 \end{aligned} \tag{3.18}$$

with the phase ambiguity terms

$$\begin{aligned}
 A_{L_1} &= N_1 + \phi_1(t_0) - f_1 \delta r(t_0) - \psi_1(t_0) + f_1 \delta s(t_0), \\
 A_{L_2} &= N_2 + \phi_2(t_0) - f_2 \delta r(t_0) - \psi_2(t_0) + f_2 \delta s(t_0).
 \end{aligned} \tag{3.19}$$

The subscripts 1 and 2 correspond to the two frequencies, f_1 and f_2 . The set of observations (3.18) is attained for every tracked satellite per epoch. Furthermore, the ionospheric path delay for f_1 is mapped to f_2 , employing equation (3.8) [Kroes, 2006].

Within this thesis further assumptions are made concerning the true range $\rho(t_r)$ between the phase centers. For each set of observations as (3.18), it is assumed to be identical for all code and phase observations to the respective satellite at the particular epoch. In fact, the signal travelling time slightly differs between the two frequencies, but within less than $0.1 \mu\text{s}$, which results in sub-mm differences for positioning [Kroes, 2006].

The stochastic part of the observation equation is captured in the thermal noise terms $\varepsilon(t_r)$. As described earlier it is considered purely random with a zero mean. Furthermore, it is assumed to be completely uncorrelated between the frequencies and observation types, between all satellites and between consecutive epochs. Thus, the stochastic model of the observation vector

$$\mathbf{zD}(t_r) = \begin{pmatrix} P_1(t_r) \\ P_2(t_r) \\ L_1(t_r) \\ L_2(t_r) \end{pmatrix}, \quad (3.20)$$

is given by the covariance matrix

$$Q_{\mathbf{zD}}(t_r) = \begin{pmatrix} (\varepsilon_{P_1}(t_r))^2 & 0 & 0 & 0 \\ 0 & (\varepsilon_{P_2}(t_r))^2 & 0 & 0 \\ 0 & 0 & (\varepsilon_{L_1}(t_r))^2 & 0 \\ 0 & 0 & 0 & (\varepsilon_{L_2}(t_r))^2 \end{pmatrix}. \quad (3.21)$$

The above described observation model is the basis for several differencing techniques, used extensively for the wide range of GPS applications. The resulting differenced observation models are referred to as single difference (SD), double difference (DD) or triple difference (TD) observation models. Within this context the model described in equation (3.20) is often denoted as undifferenced (UD) or zero difference (ZD) model.

3.3 The Ionosphere free linear Combination

The ZD dual frequency observation model, as described in equation (3.20), can not, or not easily, be used for positioning applications. But several linear combinations can be derived from the original measurements which make positioning possible. One of the most applicable linear combinations is the ionosphere free linear combination which eliminates (or at least drastically reduces) the first order ionospheric effect [Hofmann-Wellenhof *et al.*, 2008]. As the ionospheric effect is frequency dependent, it can be eliminated by

$$\begin{aligned} P_{IF}(t_r) &= \frac{f_1^2}{f_1^2 - f_2^2} P_1(t_r) - \frac{f_2^2}{f_1^2 - f_2^2} P_2(t_r) \approx 2.546 P_1(t_r) - 1.546 P_2(t_r), \\ L_{IF}(t_r) &= \frac{f_1^2}{f_1^2 - f_2^2} L_1(t_r) - \frac{f_2^2}{f_1^2 - f_2^2} L_2(t_r) \approx 2.546 L_1(t_r) - 1.546 L_2(t_r), \end{aligned} \quad (3.22)$$

yielding the ionosphere free (IF) observation model

$$\begin{aligned} P_{IF}(t_r) &= \rho(t_r) + c\delta r(t_r) - \delta s(t_r - \tau(t_r)) + M_{P_{IF}}(t_r) + \delta_{rel}(t_r) + \varepsilon_{P_{IF}}(t_r), \\ L_{IF}(t_r) &= \rho(t_r) + c\delta r(t_r) - \delta s(t_r - \tau(t_r)) + \lambda_{IF} A_{IF} + M_{L_{IF}}(t_r) + \delta_{rel}(t_r) + \varepsilon_{L_{IF}}(t_r). \end{aligned} \quad (3.23)$$

The ZD ionosphere free linear combination will be used for POD throughout this work. It must be noted, that because of the non-integer multiplication the integer nature of the ambiguities N_1 and N_2 , contained in the ambiguity term A_{IF} , is lost. The resulting wavelength λ_{IF} amounts approximately to 10.7 cm.

The covariance matrix for the ionosphere free model is still uncorrelated. But the noise is about a factor 3 higher than for the individual measurements, due to the propagation of the covariances. Furthermore, within this research the thermal noise will be assumed constant over time and identical for all GPS satellites, resulting in the following overall covariance matrix

$$\mathbf{Q}_{IF}(t) = \begin{pmatrix} (\varepsilon_{P_{IF}})^2 & 0 \\ 0 & (\varepsilon_{L_{IF}})^2 \end{pmatrix}, \quad (3.24)$$

with only receiver specific values for $\varepsilon_{P_{IF}}$ and $\varepsilon_{L_{IF}}$.

The ionosphere free observation model has the striking advantage that it can be used for absolute positioning.

3.4 Linearization of the Observation Equations

The described ionosphere free observation model (3.23), parametrized with the unknown range ρ , is formally linear. But for positioning applications the observation has to be related to the phase center position of the receiver. The geometric range

$$\rho(t_r) = \|\mathbf{x}_r(t_r) - \mathbf{x}_s(t_r - \tau(t_r))\|, \quad (3.25)$$

is the norm of the vector from the position of the GPS satellite's antenna phase center $\mathbf{x}_s(t_r - \tau(t_r))$ at emission time to the position of the receiver's antenna phase center $\mathbf{x}_r(t_r)$ at reception time. Introducing (3.25) into (3.23), results in a non-linear observation equation.

The unknowns, now contained in the observation model, are the three coordinates of the receivers phase center $\mathbf{x}_r(t_r)$, the receiver clock offset $\delta r(t_r)$, the ionosphere free carrier phase ambiguity term A_{IF} and the biases and errors captured in the terms $M_{P_{IF}}(t_r)$ and $M_{L_{IF}}(t_r)$.

Within this work the bias terms $M_{P_{IF}}(t_r)$ and $M_{L_{IF}}(t_r)$ are not taken into account in the estimation process. The terms comprise hardware delays of the satellite and of the receiver, multipath effects and phase wind-up. The effects of multipath are assumed to be eliminated by adequate data editing procedures prior to the estimation process. The mean value of all receiver-dependent delays, to all satellites in view, cannot be separated from the receiver clock offset. The estimated receiver clock offset will therefore be biased. This can be accepted, because it does not affect the position of the receiver. Similarly, the mean value of the hardware delays of the GPS satellite, over a continuous tracking pass, is mapped into the respective phase ambiguity term. This is also the case for constant phase channel biases. Again, this has no effect on the positioning. The variations of these hardware delays however, do well affect the position, but are considered to be negligible. The same holds for the effects of phase wind-up.

The remaining parameters of the observation equations, the position of the GPS satellite's phase center $\mathbf{x}_s(t_r - \tau(t_r))$ and the clock offset of the GPS satellite $\delta s(t_r - \tau(t_r))$, are obtained from external sources (see chapter 3.1.1) for each epoch. Thus, they are not estimated within this research. Nevertheless, the errors of these ephemerides (Table 3.1) introduce an additional uncertainty into the observation model. The error of the adopted value of the GPS satellite clock offset fully maps into the observation. The error of the GPS satellite's position is propagated into the observation equation depending on the line of sight towards the receiver. Thus, mainly the radial error component of the GPS satellite position affects LEO positioning.

As already mentioned, the signal travelling time $\tau(t_r)$ (and consequently also the emission epoch t_e) are strictly determined by a priori values for the unknown position and clock offset of the receiver and the known ephemerides and clock offset data of the GPS satellite. A detailed derivation of the light time equation is given in Appendix A.1.

However, the least squares estimation process for orbit determination, as outlined in chapter 4, requires linear observation equations with respect to the unknowns. Linearization of the ionosphere free code observation equation with respect to the unknown coordinates of the receivers phase center position yields

$$\frac{\partial P_{IF}}{\partial x_{r_i}(t_r)} = \frac{\partial \rho(t_r)}{\partial x_{r_i}(t_r)} = \frac{(x_{r_i}(t_r) - x_{s_i}(t_r - \tau(t_r)))}{\| \mathbf{x}_r(t_r) - \mathbf{x}_s(t_r - \tau(t_r)) \|} ; \quad i = 1, 2, 3. \quad (3.26)$$

Here, x_{r_i} and x_{s_i} represent the coordinates of the phase center of the receiver and of the GPS satellite respectively. Although the relativistic correction in the observation equation actually also contains the unknown coordinates x_{r_i} , its contribution to the derivations is negligible.

Furthermore, the observation equation has to be linearized with respect to the unknown receiver clock offset $\delta r(t_r)$, which simply yields

$$\frac{\partial P_{IF}}{\partial \delta r(t_r)} = c . \quad (3.27)$$

The above developed derivations have to be applied in the same way for the carrier phase observation. Additionally, the carrier phase observation depends on the ionosphere free carrier phase ambiguity term A_{IF} . The linearization for this term yields

$$\frac{\partial L_{IF}}{\partial A_{IF}} = \lambda_{IF} . \quad (3.28)$$

Thus, the linearized ionosphere free zero difference observation equations for code and phase reads

$$\begin{aligned} \Delta P_{IF}(t_r) &= \sum_{i=1}^3 \frac{(x_{r_i}(t_r) - x_{s_i}(t_r - \tau(t_r)))}{\|x_r(t_r) - x_s(t_r - \tau(t_r))\|} \cdot \Delta x_{r_i} + c \cdot \Delta \delta r(t_r) , \\ \Delta L_{IF}(t_r) &= \sum_{i=1}^3 \frac{(x_{r_i}(t_r) - x_{s_i}(t_r - \tau(t_r)))}{\|x_r(t_r) - x_s(t_r - \tau(t_r))\|} \cdot \Delta x_{r_i} + c \cdot \Delta \delta r(t_r) + \lambda_{IF} \cdot \Delta A_{IF} . \end{aligned} \quad (3.29)$$

Equation (3.29) can be readily applied for kinematic orbit determination where the receiver coordinates at every epoch are to be directly estimated (see section 4). Care must be taken in the case of dynamic and reduced-dynamic orbit determination (see sections 4.2 and 4.3), where an orbit model is introduced, which replaces the epoch-wise coordinates by state, dynamic and pseudo-stochastic parameters $P_j, j = 1, \dots, n$, of the trajectory as unknowns. Applying the chain rule for derivation, the linearized code observation equation with respect to these parameters yields

$$\frac{\partial P_{IF}}{\partial P_j} = \sum_{i=1}^3 \frac{\partial \rho(t)}{\partial x_{r_i}(t)} \cdot \left. \frac{\partial x_{r_i}(t)}{\partial P_j} \right|_{t_r} = \mathbf{e}(t_r) \cdot \left. \frac{\partial \mathbf{x}_r(t)}{\partial P_j} \right|_{t_r} , \quad (3.30)$$

where

$$\mathbf{e}(t_r) = \frac{x_r(t_r) - x_s(t_r - \tau(t_r))}{\|x_r(t_r) - x_s(t_r - \tau(t_r))\|} , \quad (3.31)$$

is the line of sight unit vector from the GPS satellite to the receiver. The term

$$\frac{\partial \mathbf{x}_r(t)}{\partial P_j} , \quad (3.32)$$

describes the dependency of the orbit solution $\mathbf{x}_r(t)$ on the parameters P_j , which is calculated through the variational equations, described in section 4.2.2.

Together with a priori values for all unknown parameters the above developed linearized observation equations can be applied for the adjustment processes of the various orbit determination strategies. The principles of the least squares adjustment are outlined in chapter 4.1.1.

3.5 GPS Data Quality of spaceborne Receivers

The quality of GPS data is of fundamental importance for any positioning application. Naturally, highly accurate measurements are desirable, which is the case for the employed geodetic-type BlackJack receivers. For the use in a least-squares estimation application the measurements are preferably randomly distributed around a zero mean. As already indicated, several known systematic effects, like hardware delays, channel biases or multipath effects, are not taken into account in the functional model in the LSQ process. Because these influences are extremely hard to model or require a priori knowledge from pre-flight calibration, these effects have to be accounted for in the stochastic part or systematically affected data has to be eliminated by proper data editing.

The mean value of all receiver-dependent systematic effects to all satellites in view are absorbed by the clock offset for every measurement epoch. On the other hand, the mean systematic effects of any particular GPS satellite is mapped into the phase ambiguity bias for every continuous tracking pass. Accepting the solutions of the clock offsets and of the ambiguity parameters to be biased does not influence the positioning of the spacecraft. For this research, all remaining variational effects are, if not detected and eliminated within the data screening procedures, still assumed to be random with a zero mean and uncorrelated. As a consequence, the according a priori standard deviation has to be given a higher value than for thermal noise only. For the mitigation of multipath effects the GPS antennas on board the satellites are equipped with choke rings.

For the assessment of the variance level of the different observation types, intensive in-flight validation was carried out, see *Montenbruck and Kroes [2003]* and *Kroes [2006]*. The validation was done by analyzing post-fit residuals dependent on the azimuth and elevation of the incoming signal with respect to the spacecraft body-fixed reference frame. Code observation data of the BlackJack receiver onboard CHAMP showed maximum values of 0.8 m for the ionosphere free combination. These errors are not caused by multipath effects but are induced by cross-talk interference between the GPS POD and GPS occultation antennas of the receiver. The residuals of the pseudorange observations of the GRACE satellites were generally at the sub-dm level with maximum values of 0.2 m. The reason of the different noise levels for the two missions is that during the validation of the GRACE observations the occultation antenna was not activated. In addition, the physical separation of the occultation antenna from the main POD antenna is larger for GRACE than for CHAMP.

Analyzing the residuals of the ionosphere free carrier phase measurements is a bit more difficult. Due to the fact that these residuals are at the mm to cm level, observational errors can not precisely be separated from errors in the dynamic model or GPS clock offsets [*Kroes, 2006*]. However, these errors can be assumed to be at the mm level with maximum values of about 1 cm.

All observation types show dependencies on the elevation and also on the azimuth. The use of an elevation mask to discard observations obtained below a defined elevation, e.g. 5 degrees, might be advisable. However, no correlations between any observation types have been discovered [Montenbruck and Kroes, 2003]. In the presence of still undetected multipath and other systematic errors, as well as errors introduced by the GPS ephemerides, it is recommendable to use spacecraft and observation type specific but constant a priori standard deviations [Kroes, 2006]. The adopted values for this research are given in Table 3.5.

Table 3.5: Standard deviations for the ionosphere free GPS observations

	CHAMP	GRACE A	GRACE B
$\sigma_{P_{IF}}$ [cm]	50.0	40.0	40.0
$\sigma_{L_{IF}}$ [cm]	3.0	2.0	2.0

However, the BlackJack GPS receivers are top quality spaceborne dual-frequency receivers which deliver extremely accurate measurements. This is especially remarkable considering the high velocity of the receivers. LEO satellites at approximately 400 km orbit at about 7 km per second which results in a complete different viewing geometry compared to receivers at the surface of the Earth. A particular GPS satellite is typically tracked 14 times per day. Each pass lasts generally over 30 to 40 minutes. Due to the polar orbit of the considered missions, these passes appear as straight and vertical lines in a skyplot. It also has to be mentioned that the BlackJack receiver usually manages to lock the signal when the GPS satellite has ascended to an elevation of about 10 degrees. Descending satellites are usually being tracked down to 0 degrees or even some degrees below [Jäggi, 2006].

4 Precise LEO Satellite Orbit Determination

Orbit determination (OD) of human-made objects has been an important and challenging discipline since the first space flight of a satellite in 1957. Since that time orbit tracking and determination became a key operation with a continuous demand for increasing accuracy of the spacecrafts position and velocity. The range of concepts, techniques and models, developed during the last decades, is manifold. The introduction of several highly accurate tracking systems, along with enhanced computational resources allowed for constantly upgraded approaches to orbit modeling with improved accuracy. Today, at least under permissive conditions, the trajectory of a spacecraft can be reliably determined reaching the sub-decimeter level. Scientific satellite missions hold the most stringent accuracy requirements. The associated techniques are commonly referred to as precise orbit determination (POD).

LEO satellites have always been of special interest for geodetic research. However, especially the accurate determination of trajectories of LEO spacecraft has been extremely difficult for a long time. This has changed dramatically with the implementation of satellite based navigation systems, such as the GPS. Extracting the orbit of a LEO satellite from GPS observations became a key research area in recent years. A wide range of concepts and techniques has been developed for accurate and efficient orbit determination. This holds for the trajectory models, the observational models and for the estimation methods.

For all applications within this research GPS measurements are introduced in the zero difference mode using the ionosphere free linear combination, see chapter 3.3. The ZD observational model requires highly precise ephemerides and clock data of the GPS satellites. Since the beginning of operation of the IGS in 1994, ephemerides and clock data are publicly available with ever increasing accuracy, see section 3.1.1. An alternative to ZD observations would be the use of doubly differenced (DD) observations. By using DD observations errors in the GPS ephemeris and clock data are eliminated by the formation of baselines between the LEO satellite and ground stations [*Hofmann-Wellenhof et al.*, 2008]. This approach requires the processing of a huge amount of GPS observations of a large global network of GPS receivers [*Švehla and Rothacher*, 2002]. CPU times are significantly longer because of the big amount of data to be handled. Furthermore, the use of triply differenced GPS observations has been demonstrated for LEO POD [*Byun*, 2003]. The ZD approach was chosen, because of its comparatively simple and efficient data handling. The resulting orbit accuracies are by no means worse as for POD using DD or TD GPS data. It is especially attractive for the positioning of a single LEO spacecraft. For the estimation of baselines between two or more spacecraft in a formation, the DD mode would be more adequate [*Kroes*, 2006]. This work concentrates on the use of ionosphere free linearly combined observations of dual-frequency GPS data, obtained from most accurate GPS receivers onboard CHAMP and GRACE. It is referred to *Montenbruck* [2003] and *Gill and Montenbruck* [2004] for appropriate observation modeling of single-frequency spaceborne GPS data.

Concerning the trajectory, several models have been established, which in turn are adjusted to the observations within an estimation procedure. Kinematic approaches to orbit determination are comparatively simple and do not require any external models. The trajectory is represented as a time series of positions [Bock *et al.*, 2005]. Thus, kinematic POD is highly usable for many mission scenarios. On the other hand, kinematic orbit determination is particularly sensitive to erroneous measurements, inappropriate viewing geometry and data gaps. These disadvantages are widely removed by dynamical orbit modeling [Gill and Montenbruck, 2004]. Here, use is made out of a priori knowledge of the motion of the spacecraft. Physical models for the trajectory are introduced to constrain the estimate of the orbit. Bad observation data can be detected and eliminated easierly or attenuated by an averaging effect of measurements over different epochs. In addition, data outages can be overcome by simply propagating the current state vector according to the dynamic model. Thus, dynamic orbit solutions are continuous and have no gaps, which makes them preferable for a large portion of applications. Nevertheless, due to insufficient knowledge of spacecraft dynamics, especially for LEOs, dynamic solutions diverge with increasing lengths of data arcs. Over long data arcs, trajectories, which strictly fulfil the dynamics of a given model, can not be fitted to the measurements in a way that the residuals are kept at a constant level. In order to retain the advantages of dynamic solutions while fully exploiting the geometrical accuracy of the GPS observations, the concept of reduced-dynamic orbit modeling has been established [Montenbruck *et al.*, 2005b]. Hereby, the dynamic model is given additional flexibility to allow for a consistent adjustment to the measurements. This is achieved by introducing empirical parameters, which are co-determined in the estimation process. Although the total number of estimation parameters in the dynamic and reduced-dynamic cases is less than for the kinematic case, the numerical integration of the trajectory and of the variational equations, as well as usually more iterations, result in longer computation times.

Two concepts of reduced-dynamic orbit modeling, which are subsequently employed for precise orbit determination, will be discussed. The first concept introduces impulsive shots into the trajectory model, commonly referred to as pulses. This enables the trajectory to be flexibly fitted to the measurements, yielding satisfying results for positioning. The resulting jumps in the velocity are, however, undesirable in some respects. The second concept employs empirical constant accelerations over consecutive intervals. This results in a continuous, smoother and generally more accurate solution of the satellite orbit. The jumps now occur at the acceleration level, which is somewhat more realistic. It will be shown that the solution of the variational equations with respect to pseudo-stochastic parameters can be achieved very efficiently. Furthermore, the corresponding normal equation system can be rapidly set up for the adjustment process. Thus, precise reduced-dynamic orbit determination is a powerful alternative to any other approach for POD.

This chapter provides the mathematical framework of dynamic and reduced-dynamic orbit modeling. In the subsequent process of orbit determination, the chosen orbit models are adjusted to the GPS measurements. An efficient orbit estimation method will be outlined and applied with zero difference GPS observations. Antecedant, important prerequisites for orbit determination will be discussed. Additionally, applicable data screening and editing procedures, in order to attain clean observational data, will be presented.

4.1 Prerequisites for POD

In the following the fundamentals of batch least-squares estimation, the required coordinate transformations and initial orbit determination, which yields an a priori trajectory for the estimation, will be discussed.

4.1.1 Principles of Least-Squares Estimation

Within this work, the concept of least-squares estimation is used for the adjustment of the orbit models to the observations. This method follows the principle, that the sum of squares of the observation residuals is minimized. The technique outlined here processes all measurements in one step which is referred to as batch least-squares processing. The observation data over the whole time span must be available. Thus, the batch mode is only applicable for post-processing applications.

For real-time applications a filter technique, which processes the observations sequentially, might be preferable. The mathematical framework for various filter techniques can be found in *Rogers* [2007] and *Tapley et al.* [2004a]. For results attained from real-time processing of the considered LEO satellites it is referred to *Montenbruck and Ramos-Bosch* [2007].

The batch least-squares estimation however is a quite robust adjustment technique, which potentially delivers the best possible results. In the following a brief discussion of the batch least-squares algorithm is given, as far as applied in this research.

Following *Montenbruck and Gill* [2000], the observations L_i , $i = 1, \dots, n$ are grouped in the observation vector \mathbf{z} . The model function \mathbf{F} covers the observation equations, which relate the estimation parameters X_j , $j = 1, \dots, u$, contained in the vector \mathbf{X} , with the observations by

$$\mathbf{z} + \boldsymbol{\epsilon} = \mathbf{F}(\mathbf{X}). \quad (4.1)$$

Here, the vector $\boldsymbol{\epsilon}$ contains the resulting residuals ϵ_i . In general, the vector \mathbf{F} comprises non-linear functions. The adjustment can only employ linear model functions. Linearization about a reference solution with a priori values for the unknowns leads to

$$\mathbf{z} + \boldsymbol{\epsilon} = \mathbf{F}(\mathbf{X}_0) + \mathbf{A}\mathbf{x}, \quad (4.2)$$

where

\mathbf{X}_0 is the vector of a priori values for the unknown parameters,

\mathbf{A} is the model matrix or design matrix, and

\mathbf{x} is the vector containing the corrections of the a priori values \mathbf{X}_0 .

The design matrix \mathbf{A} is the Jacobian matrix of \mathbf{F} , defined by

$$\mathbf{A} = \left. \frac{\partial \mathbf{F}(\mathbf{X})}{\partial \mathbf{X}} \right|_{\mathbf{X}=\mathbf{X}_0} . \quad (4.3)$$

Introducing a priori values for all estimation parameters makes the corrections of these values the actual unknowns. Expressing the residual vector yields the system of correction equations

$$\boldsymbol{\epsilon} = \mathbf{Ax} - (\mathbf{z} - \mathbf{F}(\mathbf{X}_0)) = \mathbf{Ax} - \mathbf{y}. \quad (4.4)$$

Here,

$$\mathbf{y} = \mathbf{z} - \mathbf{F}(\mathbf{X}_0), \quad (4.5)$$

denotes the differences between the actual observations and the observation equations evaluated for the reference solution. The computation regime for \mathbf{y} is often denoted as “observed minus computed”.

The stochastic model of the observations is described by the covariance matrix of the observations \mathbf{Q}_{zz} containing the variances σ_i of the observations. The weighting matrix is described by

$$\mathbf{W} = \mathbf{C}_{zz}^{-1} = \sigma_0^2 \mathbf{Q}_{zz}^{-1}, \quad (4.6)$$

where

σ_0 is the a priori standard deviation, and

\mathbf{C}_{zz} is the cofactor matrix of the observations.

Now the correction equations (4.4) can be solved by requiring the cost function

$$J = \boldsymbol{\epsilon}^T \mathbf{W} \boldsymbol{\epsilon} = (\mathbf{Ax} - \mathbf{y})^T \mathbf{W} (\mathbf{Ax} - \mathbf{y}), \quad (4.7)$$

to be minimized. The minimum is determined by using the method of Lagrange multipliers, which yields the so-called normal equation system

$$\mathbf{A}^T \mathbf{WAx} - \mathbf{A}^T \mathbf{Wy} = \mathbf{0}. \quad (4.8)$$

The solution is finally given by

$$\mathbf{x} = (\mathbf{A}^T \mathbf{WA})^{-1} \mathbf{A}^T \mathbf{Wy} = \mathbf{N}^{-1} \mathbf{n}, \quad (4.9)$$

where $\mathbf{N} = \mathbf{A}^T \mathbf{WA}$ is the normal equation matrix and $\mathbf{n} = \mathbf{A}^T \mathbf{Wy}$.

The adjusted model parameters are now attained by

$$\mathbf{X}_1 = \mathbf{X}_0 + \mathbf{x}. \quad (4.10)$$

This process can be repeated iteratively until sufficient convergence of the reference is reached with model parameters \mathbf{X}_k .

In addition, the stochastic properties of the adjusted parameters can be assessed. Therefore, the a posteriori standard deviation is given by

$$s_0 = \sqrt{\frac{\boldsymbol{\epsilon}^T \mathbf{W} \boldsymbol{\epsilon}}{n - u}}. \quad (4.11)$$

The covariance and cofactor matrices, \mathbf{Q}_{xx} and \mathbf{C}_{xx} , containing the cofactors and variances of the adjusted model parameters can be calculated by

$$\mathbf{Q}_{xx} = s_0^2 \mathbf{C}_{xx} = s_0^2 \mathbf{N}^{-1}. \quad (4.12)$$

A Priori Values and Weighting of Parameters

For many orbit determination procedures it is desirable to constrain specific model parameters to pre-defined a priori values within the adjustment process. Especially for reduced-dynamic orbit determination, pseudo-stochastic parameters are often constrained to a priori expectation values with a priori variances. By this means a smoother, and thus more plausible, behavior of the estimated parameters can be achieved, which prevents the solution from adjusting too heavily to the measurements.

Therefore, artificial measurements are introduced which directly “observe” the parameters with the values $\bar{\mathbf{z}}$ and the associated weighting matrix $\bar{\mathbf{W}}$. Introducing these observations to the normal equation system (4.9) yields

$$\mathbf{x} = (\mathbf{A}^T \mathbf{W} \mathbf{A} + \bar{\mathbf{W}})^{-1} (\mathbf{A}^T \mathbf{W} \mathbf{y} + \bar{\mathbf{W}} \bar{\mathbf{y}}) = \mathbf{N}^{-1} \mathbf{n}, \quad (4.13)$$

where

$$\bar{\mathbf{y}} = \bar{\mathbf{z}} - \bar{\mathbf{F}}(\mathbf{X}_0). \quad (4.14)$$

It has to be mentioned, that for further iterations, \mathbf{X}_0 has to be replaced by the current state \mathbf{X}_l , which is usually non-zero for all elements.

The calculation of the covariances (4.12) remains unchanged, but the calculation of the a posteriori standard deviation (4.11) has to be modified to

$$s_0 = \sqrt{\frac{\boldsymbol{\epsilon}^T \mathbf{W} \boldsymbol{\epsilon}}{n + \bar{n} - u}}, \quad (4.15)$$

in order to account for the number of artificial measurements \bar{n} .

Parameter Pre-Elimination and Back-Substitution

The solution of the normal equation system (4.9) requires the inversion of the matrix \mathbf{N} of dimension $u \times u$, with u being the number of the estimation parameters. For applications like orbit determination this number can easily reach up to several thousands which results in severe numerical problems and long calculation times.

As will be described in section 4.4, a proper sequence of the unknowns within the normal equation matrix can yield submatrices being diagonal matrices. Thus, the uncomplex inversion of a diagonal matrix should be exploited for solving the whole normal equation system.

Therefore the normal equation system (4.9) is subdivided into

$$\begin{pmatrix} \mathbf{N}_{11} & \mathbf{N}_{12} \\ \mathbf{N}_{21} & \mathbf{N}_{22} \end{pmatrix} \begin{pmatrix} \mathbf{x}_1 \\ \mathbf{x}_2 \end{pmatrix} = \begin{pmatrix} \mathbf{n}_1 \\ \mathbf{n}_2 \end{pmatrix}. \quad (4.16)$$

where \mathbf{N}_{22} is assumed to be a diagonal matrix. The first group of unknowns \mathbf{x}_1 can be pre-eliminated by

$$\mathbf{x}_1 = (\mathbf{N}_{11} - \mathbf{N}_{12}\mathbf{N}_{22}^{-1}\mathbf{N}_{21})^{-1}(\mathbf{n}_1 - \mathbf{N}_{12}\mathbf{N}_{22}^{-1}\mathbf{n}_2), \quad (4.17)$$

[Dach et al., 2007]. Subsequently the solution is back-substituted to obtain the second part of the unknowns by

$$\mathbf{x}_2 = \mathbf{N}_{22}^{-1}(\mathbf{n}_2 - \mathbf{N}_{21}\mathbf{x}_1). \quad (4.18)$$

Thus, the inversion of the whole normal equation matrix is replaced by the simple inversion of a diagonal matrix and a general inversion of a usually much smaller matrix.

The related cofactors and covariances are given by

$$\mathbf{Q}_{11} = s_0^2 \mathbf{C}_{11} = s_0^2 (\mathbf{N}_{11} - \mathbf{N}_{12}\mathbf{N}_{22}^{-1}\mathbf{N}_{21})^{-1}, \quad (4.19)$$

and

$$\mathbf{Q}_{22} = s_0^2 \mathbf{C}_{11} = s_0^2 (\mathbf{N}_{22}^{-1} + (\mathbf{N}_{22}^{-1}\mathbf{N}_{21})\mathbf{C}_{11}(\mathbf{N}_{22}^{-1}\mathbf{N}_{21})^T). \quad (4.20)$$

Further exploitation of the special structure of the normal equation system for inversion will be described in section 4.4.

4.1.2 Initial Orbit Determination

As described in chapter 4.1.1, in order to attain the best estimate of the model parameters, the least-squares adjustment procedure requires a priori model parameters X_0 . With these parameters a reference trajectory is established and subsequently fitted to the measurements.

Within this work, initial orbit determination is done by determination of positions for every epoch using only code measurements, which is referred to as single point positioning (SPP). This yields a kinematic orbit solution, see Figure 4.1. From these low precision positions initial conditions are taken for a first dynamic orbit integration. In order to get a dynamic solution of similar precision as of the kinematic solution, the integrated trajectory is first fitted to the kinematic solution, taking the positions as pseudo-measurements. The resulting orbit and the corresponding solution of the variational equations are now at disposal to be further improvements within the adjustment process. The epoch-wise clock offsets, attained as a by-product of kinematic positioning, are also taken as a priori values for the adjustment. It is advisable to generate the best possible initial solution in order to avoid many iterations in the least-squares estimation and thus save computation time.

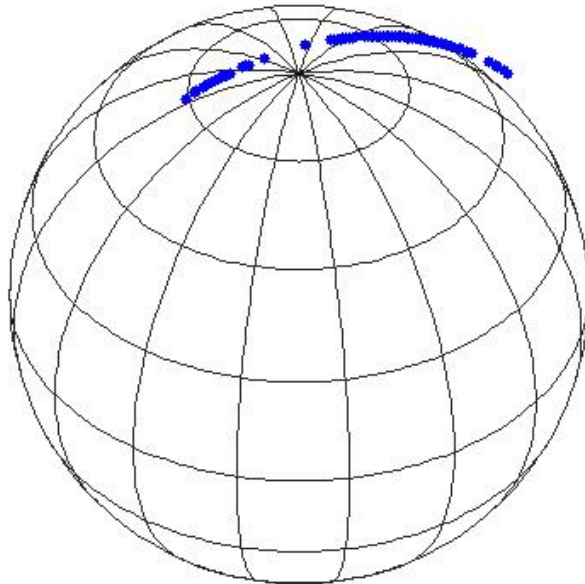


Figure 4.1: Kinematic orbit solution (epochwise positions)

Additionally, already for initial orbit determination a coarse code data screening is necessary to detect outliers. Therefore, the quality of the position solution is examined at every epoch. Whenever the RMS of the associated residuals exceeds a predefined threshold, the code observation that contributes the dominating error is identified and removed from the set of observations. This procedure is repeated until all remaining observations fulfil that requirement. As a consequence, not every epoch yields a position, especially at polar regions, as seen in Figure 4.1.

4.1.3 Reference Frame Transformations

The process of orbit determination involves that position coordinates and vectors are expressed in different coordinate systems. Within this research a total of four different coordinate systems are being used. The principal calculations, i.e. the integration of the trajectory and its adjustment to the measurements, are most conveniently accomplished in an inertial reference frame. Therefore the International Celestial Reference Frame (ICRF) is employed [McCarthy, 1996 and McCarthy and Petit, 2004]. The ephemeris data of the GPS satellites provided by the IGS is related to the International Terrestrial Reference Frame (ITRF) [ITRF, 2009]. Thus, transformations between these coordinate systems are necessary. In addition, measures related to the spacecraft, e.g. the offset of the receiver position with respect to the center of mass, are given in the satellite body-fixed coordinate frame. In order to process the observations, these quantities also have to be transformed into the inertial system. Furthermore, for applications like orbit validation the residuals related to an other orbit solution are most representatively expressed in the accompanying satellite coordinate system. For the considered CHAMP and GRACE missions the accompanying satellite system is closely related to the body-fixed frame due to attitude control. In the following the required coordinate transformations are briefly summarized.

ICRF – ITRF Transformation

The transformation of a position vector \mathbf{r}_{ICRF} , given in the ICRF, to the ITRF is accomplished by

$$\mathbf{r}_{ITRF} = \mathbf{U}(t) \cdot \mathbf{r}_{ICRF}, \quad (4.21)$$

where $\mathbf{U}(t)$ is a time-varying 3×3 orthogonal matrix. It consists of a series of successive rotations, defined by

$$\mathbf{U}(t) = \mathbf{P}_x^T(t) \cdot \mathbf{P}_y^T(t) \cdot \mathbf{E}(t) \cdot \mathbf{N}(t) \cdot \mathbf{\Pi}(t), \quad (4.22)$$

where

$\mathbf{P}_x^T, \mathbf{P}_y^T$ are the matrices describing the polar motion, i.e. the separation between the third axis of the terrestrial system (Conventional Terrestrial Pole) and the Celestial Ephemeris Pole,

\mathbf{E} describes the Earth rotation as a function of the Greenwich apparent sidereal time,

\mathbf{N} is the matrix accounting for the nutation, and

$\mathbf{\Pi}$ is the matrix which accounts for the precession.

The exact calculation of each of these matrices is defined by the International Astronomical Union (IAU). The algorithms are outlined in the IERS 1996 conventions [McCarthy, 1996] or in the later adopted and slightly improved IERS 2000 conventions [McCarthy, 2003]. However, the differences of these transformation algorithms are negligible for the

considered applications. For this work the IERS conventions 1996 are used. The particular models used for this transformation are summarized in Table 4.1.

Table 4.1: Reference frame transformation models used for this research

Transformation	Model Description
$\boldsymbol{P}(t)$	IAU 1976 Precession
$\boldsymbol{N}(t)$	IAU 1980 Nutation
$\boldsymbol{E}(t)$	IAU 1982 Sidereal Time
$\boldsymbol{P}_x^T, \boldsymbol{P}_y^T$	IERS EOPs

The Earth orientation parameters (EOPs), such as the polar motion parameters and the time offset $UT1 - UTC$, are required as input values for the models mentioned in Table 4.1. For this research, these parameters are obtained from the International Earth Rotation and Reference Systems Service (IERS) [IERS, 2009].

For the ITRF the convention used is the IGS realization of ITRF2000, also called IGS00, which is implied by the IGS or CODE GPS ephemerides. The transformation models described in Table 4.1 then yield the ICRF realization of Earth mean equator and equinox of J2000 (EME2000), also referred to as the J2000 inertial system.

The transformation of a position vector from the ICRF to the ITRF can be carried out using equation (4.21). The inverse transformation is simply given by the transpose $\boldsymbol{U}^T(t)$ of the matrix $\boldsymbol{U}(t)$, due to its orthogonality, yielding

$$\boldsymbol{r}_{ICRF} = \boldsymbol{U}^T(t) \cdot \boldsymbol{r}_{ITRF} . \quad (4.23)$$

For the practical computation of various perturbing forces the transformations of accelerations is additionally required. Therefore, the second derivative of equation (4.21) is given with sufficient accuracy by [Seeber, 2003]

$$\begin{aligned} \ddot{\boldsymbol{r}}_{ITRF} &= \boldsymbol{U}(t) \cdot \ddot{\boldsymbol{r}}_{ICRF} , \\ \ddot{\boldsymbol{r}}_{ICRF} &= \boldsymbol{U}^T(t) \cdot \ddot{\boldsymbol{r}}_{ITRF} . \end{aligned} \quad (4.24)$$

Here, the assumption was made, that the occurring products $\ddot{\boldsymbol{U}} \cdot \boldsymbol{r}$ and $\ddot{\boldsymbol{U}} \cdot \dot{\boldsymbol{r}}$ are always negligible due to the relatively small values of $\ddot{\boldsymbol{U}}$ and $\dot{\boldsymbol{r}}$ [Seeber, 2003]. Furthermore, the employed method for integrating the spacecrafts trajectory within the force model and the computation of the variational equations requires the transformation of the Jacobian matrices of the accelerations between the ITRF and ICRF systems. This is achieved by

$$\begin{aligned} \boldsymbol{J}_{ITRF} &= \boldsymbol{U}(t) \cdot \boldsymbol{J}_{ICRF} \cdot \boldsymbol{U}^T(t) , \\ \boldsymbol{J}_{ICRF} &= \boldsymbol{U}^T(t) \cdot \boldsymbol{J}_{ITRF} \cdot \boldsymbol{U}(t) , \end{aligned} \quad (4.25)$$

with the Jacobian matrices defined by

$$\begin{aligned} \mathbf{J}_{ITRF} &= \left(\frac{\partial \ddot{\mathbf{r}}_{ITRF}}{\partial x_{ITRF}} \quad \frac{\partial \ddot{\mathbf{r}}_{ITRF}}{\partial y_{ITRF}} \quad \frac{\partial \ddot{\mathbf{r}}_{ITRF}}{\partial z_{ITRF}} \right) , \\ \mathbf{J}_{ICRF} &= \left(\frac{\partial \ddot{\mathbf{r}}_{ICRF}}{\partial x_{ICRF}} \quad \frac{\partial \ddot{\mathbf{r}}_{ICRF}}{\partial y_{ICRF}} \quad \frac{\partial \ddot{\mathbf{r}}_{ICRF}}{\partial z_{ICRF}} \right) . \end{aligned} \quad (4.26)$$

SCS – ICRS Transformation

As already mentioned, in order to compare different orbit solutions the position difference can be expressed in the time-varying satellite coordinate system (SCS). The SCS has its origin in the spacecraft's center of mass (COM). The three coordinate axes are defined as, see Figure 4.2,

- $\mathbf{r}(t)$ is the unit vector pointing from the geocenter to the satellite's center of mass (radial),
- $\mathbf{a}(t)$ is the unit vector pointing in the flight direction of the satellite (along-track), and
- $\mathbf{c}(t)$ is the unit vector completing the right-handed coordinate system (cross-track).

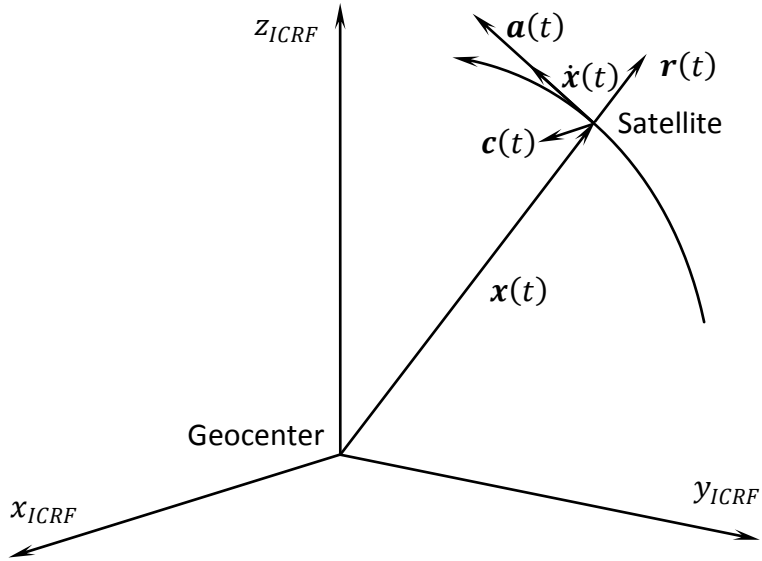


Figure 4.2: The accompanying Satellite Coordinate System (SCS)

The instantaneous axes are attained from the position $\mathbf{x}(t)$ and velocity $\dot{\mathbf{x}}(t)$ vectors of the satellite by

$$\begin{aligned} \mathbf{r}(t) &= \frac{\mathbf{x}(t)}{|\mathbf{x}(t)|} , \\ \mathbf{a}(t) &= \frac{\dot{\mathbf{x}}(t)}{|\dot{\mathbf{x}}(t)|} , \\ \mathbf{c}(t) &= \frac{\mathbf{x}(t) \times \dot{\mathbf{x}}(t)}{|\mathbf{x}(t) \times \dot{\mathbf{x}}(t)|} . \end{aligned} \quad (4.27)$$

The satellite coordinate system is a time-varying, non-orthogonal and right-handed system. The transformation of a direction vector in the SCS system to the inertial system is carried out by

$$\mathbf{r}_{ICRF} = \mathbf{D}(t) \cdot \mathbf{r}_{SCS}, \quad (4.28)$$

with the transformation matrix

$$\mathbf{D}(t) = (\mathbf{r}(t) \quad \mathbf{a}(t) \quad \mathbf{c}(t)) . \quad (4.29)$$

For the inverse transformation the matrix has to be inverted due to its non-orthogonality, yielding

$$\mathbf{r}_{SCS} = \mathbf{D}^{-1}(t) \cdot \mathbf{r}_{ICRF} . \quad (4.30)$$

If required, the transformation between the SCS and the ITRF is given by

$$\begin{aligned} \mathbf{r}_{ITRF} &= \mathbf{U}(t) \cdot \mathbf{D}(t) \cdot \mathbf{r}_{SCS} , \\ \mathbf{r}_{SCS} &= \mathbf{D}^{-1}(t) \cdot \mathbf{U}^T(t) \cdot \mathbf{r}_{ITRF} . \end{aligned} \quad (4.31)$$

S/C-Body – ICRS Transformation

The spacecraft body system is a body-fixed reference system. It is used for the description of the locations of the instruments with respect to the structure of the spacecraft. Its alignment to the inertial reference system is determined by the actual attitude of the spacecraft. In the case of CHAMP and GRACE a specified nominal attitude model is very accurately maintained. Thus, the nominal attitude model can be used as an approximation of the body-fixed frame. The unit vectors of the nominal orientation for both missions are defined as, see Figure 4.3,

- $\mathbf{x}_{Body}(t)$ is perpendicular to the \mathbf{z}_{Body} -axis and lies in the orbital plane towards the flight direction,
- $\mathbf{y}_{Body}(t)$ is perpendicular to the orbital plane, and
- $\mathbf{z}_{Body}(t)$ is pointing in nadir direction towards the Earth.

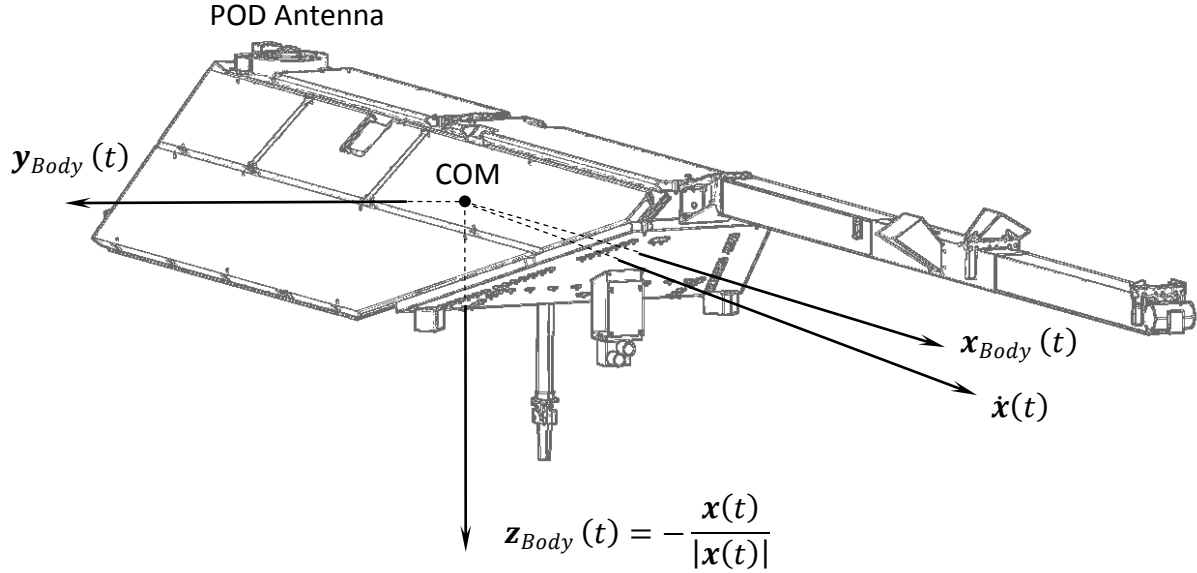


Figure 4.3: The S/C-Body Coordinate System related to the nominal attitude (example of CHAMP)

The origin of the body-fixed frame is located in the center of mass (COM) of the respective satellite. The orthogonal axes are calculated by

$$\begin{aligned} \mathbf{x}_{Body}(t) &= \mathbf{y}_{Body}(t) \times \mathbf{z}_{Body}(t) , \\ \mathbf{y}_{Body}(t) &= -\frac{\mathbf{x}(t) \times \dot{\mathbf{x}}(t)}{|\mathbf{x}(t) \times \dot{\mathbf{x}}(t)|} , \\ \mathbf{z}_{Body}(t) &= -\frac{\mathbf{x}(t)}{|\mathbf{x}(t)|} . \end{aligned} \quad (4.32)$$

The body-fixed coordinate system is a time-varying, orthogonal and right-handed system. The transformation of a direction vector from the Body-fixed system to the inertial system is given by

$$\begin{aligned} \mathbf{r}_{ICRF} &= \mathbf{C}(t) \cdot \mathbf{r}_{Body} , \\ \mathbf{r}_{Body} &= \mathbf{C}^T(t) \cdot \mathbf{r}_{ICRF} , \end{aligned} \quad (4.33)$$

with the transformation matrix

$$\mathbf{C}(t) = (\mathbf{x}_{Body}(t) \quad \mathbf{y}_{Body}(t) \quad \mathbf{z}_{Body}(t)) . \quad (4.34)$$

Preferably, for a rigorous transformation the actual attitude may be obtained from the precise attitude data, which is determined from the star camera observations. The attitude information is commonly provided as quaternions [Montenbruck, 2000]. However, the nominal attitude model is accurate to about 3 degrees with respect to the actual orientation [Kang et al., 2006a und Jäggi, 2006]. Thus, the use of the nominal attitude model is largely justifiable. This is even more the case for GRACE due to the closer distance of the GPS receiver from the center of mass.

The exact coordinates of the main GPS receivers for CHAMP [Schwintzer *et al.*, 2002] and GRACE [Case *et al.*, 2004 and Bettadpur, 2007], given in the body-fixed system are listed in Table 4.2. It has to be mentioned, that on 10 December 2005 the signs of the components have to be changed for the two GRACE spacecraft due to a switch maneuver. The offsets are assumed to be constant, implying that possible phase center variations are ignored. This also holds for variations of the spacecraft's center of mass, which can be caused by the expulsion of propellant.

Table 4.2: GPS receiver phase center offsets in the body-fixed frame

Satellite	$X_{Body}[\text{m}]$	$Y_{Body}[\text{m}]$	$Z_{Body}[\text{m}]$
CHAMP	-1.4880	0.0000	-0.3928
GRACE A	-0.0004	-0.0004	-0.4514
GRACE B	0.0006	0.0007	-0.4514

For GPS signal processing the center of mass correction must also be applied for the GPS satellites. The nominal attitude model and antenna phase center offsets of the GPS satellites are outlined in section 3.1.1.

4.2 Dynamic Orbit Modeling

As already outlined, the chosen approaches of orbit modeling are the dynamic and reduced-dynamic models. In this chapter the concept of dynamic orbit modeling, which is also the basis for reduced-dynamic orbit modeling, will be discussed in detail.

The motion of artificial satellites orbiting the Earth is governed by a multitude of forces induced by various interactions between the satellites and their physical environment. The mathematical framework describing the orbit is referred to as the equations of motion. They are built up successively, based on the gravitational force of a pointlike Earth, resulting in a linear differential equation system of second order. This equation represents the combination of Newton's second law with his law of gravitation for point masses, given by

$$\ddot{\mathbf{x}}(t) = -\frac{GM}{r^3} \cdot \mathbf{x}(t), \quad (4.35)$$

where $\mathbf{x}(t)$ represents the position of the spacecraft related to the center of the Earth as a function of time, $\ddot{\mathbf{x}}(t)$ is the second derivation of $\mathbf{x}(t)$ and represents the acceleration, r is the norm of $\mathbf{x}(t)$, M stands for the mass of the Earth and G is the gravitational constant [Schneider, 1988]. Equation (4.35) assumes the Earth's gravity field to be pointlike or spherically symmetric. It further assumes the mass of the satellite to be negligible compared to the mass of the Earth. The formula holds for the center of mass of the spacecraft. It is expressed in an inertial system. As will be shown later, additional corrections have to be introduced, if the orbit of the spacecraft is considered in an Earth-centered quasi-inertial system.

Equation (4.35) is the basic approximation of the equation of motion for artificial Earth satellites. It is the fundamental basis for any more advanced modeling of the equations of motion. Any solution of equation (4.35) represents a particular orbit. It can be solved analytically, revealing that all solutions have the shape of conic sections, also referred to as Keplerian orbits [Vallado, 2007]. For a three-dimensional differential equation of second order six constants of integration need to be defined in order to identify a particular trajectory. This set of constants of integration, denoted as the state of the orbit, can be arranged using initial values for position and velocity at epoch t_0

$$\begin{aligned}\mathbf{r}_0 &= \mathbf{x}(t_0) ; \\ \mathbf{v}_0 &= \dot{\mathbf{x}}(t_0) ,\end{aligned}\tag{4.36}$$

or using two boundary (position) values at epochs t_1 and t_2

$$\begin{aligned}\mathbf{r}_1 &= \mathbf{x}(t_1) ; \\ \mathbf{r}_2 &= \mathbf{x}(t_2) .\end{aligned}\tag{4.37}$$

For many practical applications, such as orbit propagation, the use of the (also more illustrative) six Keplerian Elements is preferable [Vallado, 2007]. With these elements the orbit is strictly defined, and position and velocity of the spacecraft can easily be calculated for any epoch. Figure 4.4 illustrates the concept of the Keplerian elements and the mathematical algorithms for Keplerian ephemeris calculation are given in Appendix A.2. The six elements are the semimajor axis a , the eccentricity e , the inclination i , the right ascension of the ascending node Ω , the argument of perigee ω and the true anomaly v [Vallado, 2007].

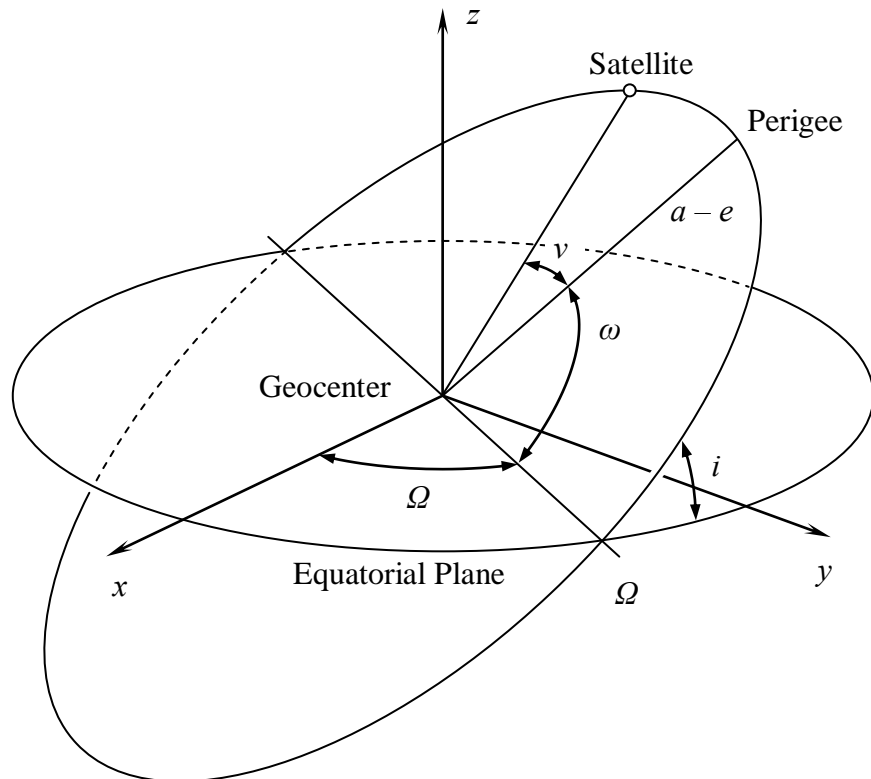


Figure 4.4: The Keplerian (or classical) elements

However, any satellite is affected by a virtually vast number of additional forces, perturbing the orbital motion (4.35). In this context, the above described model is denoted the unperturbed orbit model. To establish the perturbed orbit model, the accelerations $\ddot{x}(t)_{perturb,i}$, which are implied by the additionally considered forces, are subsequently added into equation (4.35), which can be written as

$$\ddot{x}(t) = -\frac{GM}{r^3} \cdot x(t) + \ddot{x}(t)_{perturb}, \quad (4.38)$$

with

$$\ddot{x}(t)_{perturb} = \sum_i \ddot{x}(t)_{perturb,i}. \quad (4.39)$$

Equation (4.38) is a non-linear differential equation of second order. The particular perturbational forces actually can depend on the position x , the velocity \dot{x} , the time t and on additional force model parameters q_1, \dots, q_d

$$\ddot{x}(t)_{perturb,i} = \ddot{x}(t, x, \dot{x}, q_1, \dots, q_d)_{perturb,i}. \quad (4.40)$$

These parameters are referred to as dynamical parameters [Montenbruck, 2000]. Dynamical parameters are either considered to be known or estimated together with the initial conditions within an adjustment process. In the case dynamical parameters relate to analytical models of accelerations they are also referred to as deterministic parameters [Bertiger et al., 1994]. Dynamic orbit modeling only involves deterministic parameters.

Equation (4.38) can formally be written as

$$\ddot{x}(t) \doteq f(t, x, \dot{x}, q_1, \dots, q_d) = f(t, p_1, p_2, \dots, p_6, q_1, \dots, q_d), \quad (4.41)$$

with p_1, p_2, \dots, p_6 representing the six initial parameters. It is generally too complex to be solved analytically. Therefore it has to be solved numerically. A wide range of methods has been developed for solving the differential equations efficiently and accurately [Beutler, 2005 and Vallado, 2007].

For this research the so-called collocation method was chosen [Beutler, 1990, Beutler, 2005 and Swatschina, 2004]. It can be considered as the most accurate and flexible numerical integrator for orbit propagation. It directly yields a polynomial function of time instead of a table of positions. The accumulated error of integration is at a remarkable low level due to the high orders of integration. Only limited by computational precision, orders of up to 12 can be employed [Beutler, 2005]. Test runs with the developed software (see section 5) showed that the integration of an unperturbed orbit coincides with the actual elliptic orbit within one millimeter even after several revolutions. In addition, with the collocation method also the boundary value problem is directly solvable. A detailed description of the collocation method as well as techniques to further improve its efficiency can be found in Beutler [1990], Beutler [2005] and Swatschina [2004].

4.2.1 The Dynamic Force Model

In this chapter, the modeling of the dynamic force field for LEO satellites will be discussed. The perturbational influences can generally be divided into gravitational and non-gravitational forces or accelerations. As the name suggests, gravitational perturbations are forces induced by mass attractions apart from the pointlike Earth model. Forces of gravitational nature are also denoted as conservative forces. Accordingly, non-gravitational forces are referred to as non-conservative forces.

Gravitational accelerations are fully determined by the position of the satellite. Therefore, the choice of which perturbations are included must be considered depending on the orbital characteristics of the respective mission. On the other hand, non-gravitational accelerations may additionally depend on a variety of other parameters. These parameters might describe the physical environment of the spacecraft, e.g. the density of the surrounding atmosphere, but also the properties of the spacecraft itself like its mass, shape and material. Thus, dynamic orbit modeling has to be treated spacecraft- and orbit-specific in order to achieve most precise results.

Table 4.3 lists the most relevant conservative accelerations acting on a typical LEO satellite in about 400 km altitude.

Table 4.3: Gravitational perturbations acting on a LEO satellite [Bock, 2003]

Perturbation	Acceleration [m/s ²]
1/r ² -Term	8.6
Inhomogeneous Earth Gravity Field	1.5·10 ⁻²
Lunar Attraction	5.5·10 ⁻⁶
Solar Attraction	5.0·10 ⁻⁷
Attraction of other Planets (Jupiter, Venus)	1.0·10 ⁻¹⁰
Solid Earth Tides	1.5·10 ⁻⁷
Polar Tides	1.0·10 ⁻⁸
Oceanic Tides	5.0·10 ⁻⁸
General Relativity	5.0·10 ⁻⁹

Non-gravitational perturbations can be globally categorized as frictional. The amplitude of the force component is directly proportional to the surface area of the spacecraft seen from a certain direction (e.g. the flight-direction or the direction towards the Sun) [Feltens, 1991]. Due to the mechanical inertia, the resulting force is indirectly proportional to the mass of the space vehicle. Besides other parameters, the effect of non-conservative perturbations depends essentially on the area-to-mass ratio A/m . Table 4.4 gives an overview of the most relevant non-gravitational perturbational forces for a spacecraft like CHAMP or GRACE in a LEO orbit.

Table 4.4: Non-gravitational perturbations acting on a LEO satellite [Bock, 2003]

Perturbation	Acceleration [m/s ²]
Atmospheric Drag	$5.0 \cdot 10^{-7}$
Direct Radiation Pressure	$3.0 \cdot 10^{-8}$
Albedo	$4.0 \cdot 10^{-9}$
Orbit Maneuvers	-

Dynamic orbit modeling crucially relies on the quality of the employed force field and on the accuracy of the integrator. As already mentioned, the integration can be performed delivering by far sufficient accuracy. In fact, purely dynamical orbit modeling is always limited by the deficiencies of the most dominant force among those forces that could not be satisfactorily modeled. In the case described in Tables 4.3 and 4.4, this holds for the modeling of the atmospheric drag. Due to the lack of the required knowledge of the atmospheric density and its variation with time and location, atmospheric drag modeling is much more uncertain than models for other, more dominant perturbations. Therefore, accurate dynamic orbits are always limited to rather short time intervals. With growing orbital length, the deficiencies of the dynamic model add up and force the orbit solution to diverge. As will be discussed later, the deficiencies of the dynamic model can be widely overcome by adding empirical forces to the dynamic model. Trajectories of much longer time intervals can be computed. The orbital length of such reduced-dynamic orbits is not limited any more by the underlying model, but rather by numerical problems of solving for too many parameters. For many applications, this even allows for disregarding the dynamics to some extent, which in turn yields shorter computation times. For scientific interest it is nevertheless reasonable to model the dynamics to the best possible extent. Thereby, the empirical part of the orbit model is reduced to a minimum, making the solution most plausible. This holds not only for the position, but also for the velocity and acceleration levels.

Below, an introduction of the modeling techniques for the listed gravitational and non-gravitational perturbations is given. The partial derivatives of most of the presented force model components with respect to the position and velocity coordinates are given in Appendix A.3. The derivatives are required for the orbit propagation with the collocation method and for the solution of the variational equations.

Gravitational Perturbations

The inhomogeneous Earth Gravity Field

The inhomogeneous Earth gravity field, that deviates from the gravitation of a point mass or a spherically symmetric mass, is commonly represented by spherical harmonic functions [Hofmann-Wellenhof and Moritz, 2006]. Using Legendre polynomials, the perturbing gravitational potential T can be modeled as

$$T = \frac{\mu}{r} \sum_{n=2}^{n_{\max}} \left(\frac{a}{r}\right)^n \sum_{m=0}^n (C_{nm} \cos m\lambda + S_{nm} \sin m\lambda) \cdot P_{nm}(\cos \theta), \quad (4.42)$$

where

μ is the gravitation parameter (product of the gravitational constant G and the mass of the Earth M),

a is the equatorial radius of the Earth,

r is the norm of the spacecraft's position,

λ is the geocentric longitude of the spacecraft,

θ is the polar distance of the spacecraft,

P_{nm} are the associated Legendre polynomials,

C_{nm}, S_{nm} are the coefficients of spherical harmonics, and

n, m are the degree and order of the spherical harmonics expansion.

To avoid numerical problems, normalized Legendre polynomials are usually employed [Hofmann-Wellenhof and Moritz, 2006]. The Earth-fixed cartesian coordinates x_e , y_e and z_e are related to the spherical coordinates by

$$\begin{aligned} r &= \sqrt{x_e^2 + y_e^2 + z_e^2}, \\ \theta &= \arctan\left(\frac{\sqrt{x_e^2 + y_e^2}}{z_e}\right), \\ \lambda &= \arctan\left(\frac{y_e}{x_e}\right). \end{aligned} \quad (4.43)$$

The perturbing acceleration of the inhomogeneous gravity field $\ddot{\mathbf{x}}_{T_i}$ is the gradient vector of the potential T . It has to be transformed into the inertial system from the Earth-fixed system where it is given by

$$\ddot{\mathbf{x}}_{T_e} = \nabla_{cartes} T = D \cdot \nabla_{sphere} T, \quad (4.44)$$

where

$$\begin{aligned} \nabla_{cartes} T &= \begin{pmatrix} \frac{\partial T}{\partial x_e} \\ \frac{\partial T}{\partial y_e} \\ \frac{\partial T}{\partial z_e} \end{pmatrix}, \\ D &= \begin{pmatrix} \frac{\partial r}{\partial x_e} & \frac{\partial \theta}{\partial x_e} & \frac{\partial \lambda}{\partial x_e} \\ \frac{\partial r}{\partial y_e} & \frac{\partial \theta}{\partial y_e} & \frac{\partial \lambda}{\partial y_e} \\ \frac{\partial r}{\partial z_e} & \frac{\partial \theta}{\partial z_e} & \frac{\partial \lambda}{\partial z_e} \end{pmatrix}, \\ \nabla_{sphere} T &= \begin{pmatrix} \frac{\partial T}{\partial r} \\ \frac{\partial T}{\partial \theta} \\ \frac{\partial T}{\partial \lambda} \end{pmatrix}. \end{aligned} \quad (4.45)$$

The partial derivatives of T with respect to the spherical coordinates are given by

$$\begin{aligned} \frac{\partial T}{\partial r} &= \frac{\mu}{r} \sum_{n=2}^{n_{max}} (1-n) \frac{a^n}{r^{n+1}} \sum_{m=0}^n (C_{nm} \cos m\lambda + S_{nm} \sin m\lambda) \cdot P_{nm}(\cos \theta), \\ \frac{\partial T}{\partial \theta} &= \frac{\mu}{r} \sum_{n=2}^{n_{max}} \left(\frac{a}{r}\right)^n \sum_{m=0}^n (C_{nm} \cos m\lambda + S_{nm} \sin m\lambda) \cdot \frac{\partial P_{nm}(\cos \theta)}{\partial \theta}, \\ \frac{\partial T}{\partial \lambda} &= \frac{\mu}{r} \sum_{n=2}^{n_{max}} \left(\frac{a}{r}\right)^n \sum_{m=0}^n m \cdot (-C_{nm} \cos m\lambda + S_{nm} \sin m\lambda) \cdot P_{nm}(\cos \theta). \end{aligned} \quad (4.46)$$

The derivation of the associated Legendre polynomials and their derivatives can be found in *Swatschka [2004]* *Hofmann-Wellenhof and Moritz [2006]*.

Satellites in lower orbit regions are much more sensitive to higher order terms of the inhomogeneous gravity field. On the other hand, with increasing distance from the Earth the gravity field becomes increasingly pointlike.

Today, an increasing number of high quality gravity field models, with degree and order reaching up to 360 or more, are available. The employed gravity field models will be described in section 5.

Third-Body Perturbations

The second largest perturbation on the spacecraft's trajectory is caused by third-body attractions of the Moon and the Sun. The Earth-centered quasi-inertial coordinate system underlies no rotations, but is still subject to the translative accelerations of the Earth's center of mass. The forces that act on the Earth's center of mass and govern its motion differ at all other positions outside the Earth's center of mass. Thus, this difference appears as an apparent force acting on a satellite, when considered in the quasi-inertial system. Figure 4.5 illustrates the third-body perturbation as a differential force. These tidal forces, caused by the celestial body C , can be described by

$$\ddot{\mathbf{x}}_C = GM_C \cdot \left(\frac{\mathbf{x}_c - \mathbf{x}}{|\mathbf{x}_c - \mathbf{x}|^3} - \frac{\mathbf{x}_c}{|\mathbf{x}_c|^3} \right), \quad (4.47)$$

where

GM_C is the gravitational constant of the celestial body C ,

\mathbf{x}_c is the geocentric position of C , and

\mathbf{x} is the geocentric position of the satellite.

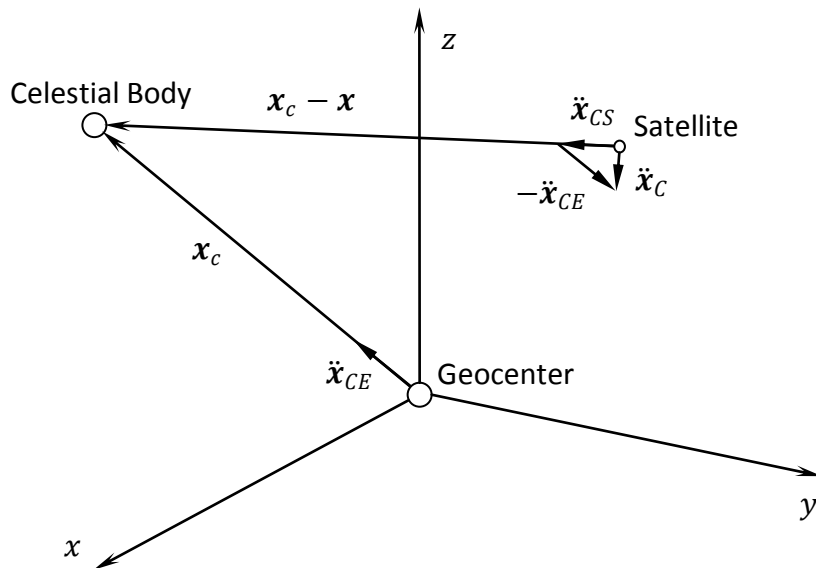


Figure 4.5: The third-body attraction acting on a satellite

It can be shown that the acceleration increases linearly with the satellite's distance from the center of the Earth, while it decreases with the third power of the distance of the perturbing body [Vallado, 2007].

As already mentioned, the third-body attractions have to be accounted only for the Moon and the Sun. These bodies can be treated as point masses and their coordinates need not to

be known to the highest precision. Low-precision formulas for Solar and Lunar coordinates, which are accurate to about 0.1 – 1%, can be found in *Montenbruck and Gill* [2000], and are employed in this research.

Solid Earth tides

Under the direct impact of the tidal forces the solid Earth itself experiences a deformation. The resulting change in the gravitational potential of the Earth causes additional forces that act on the satellite. This can be considered as an indirect gravitational effect of the Sun and the Moon. The acceleration caused by solid Earth tides is given by

$$\ddot{\mathbf{x}}_{ST,C} = \frac{k_2}{2} \frac{GM_C}{|\mathbf{x}_C|^3} \frac{a^5}{|\mathbf{x}|^5} \cdot \left(-15 \frac{(\mathbf{x} \cdot \mathbf{x}_C)^2}{|\mathbf{x}|^2 |\mathbf{x}_C|^2} \cdot \mathbf{x} + 6 \cdot \frac{(\mathbf{x} \cdot \mathbf{x}_C)}{|\mathbf{x}_C|^2} \cdot \mathbf{x}_C + 3\mathbf{x} \right), \quad (4.48)$$

where k_2 is the Love number, providing a measure for the elasticity of the Earth [Seeber, 2003].

The value of 0.29525 for the Love number k_2 represents the mean and frequency-independent part of the solid earth tides [McCarthy, 1996]. To account for the effects that are dependent on the frequencies of the tides, the tidal potential is developed in spherical harmonics. Then the time-dependent correction terms ΔC_{nm}^{ST} and ΔS_{nm}^{ST} are simply added to the geopotential coefficients C_{nm} and S_{nm} . A detailed description of the calculation of ΔC_{nm}^{ST} and ΔS_{nm}^{ST} can be found in McCarthy [1996]. A revised model is given in McCarthy and Petit [2004].

Satellites in LEOs orbit are much more sensitive to indirect Earth tide effects than higher orbiting satellites like GNSS or geostationary satellites due to the rapid attenuation of the gravity inhomogeneities with increasing distance.

Polar Tides

The centrifugal effect of the polar motion generates a perturbation in the external potential of the Earth, referred to as pole tide. It can be calculated as changes in the geopotential coefficients C_{21} and S_{21} , depending on the polar motion variables x_p and y_p [McCarthy, 1996 and McCarthy and Petit, 2004].

Ocean Tides

The direct tidal forces also affect the oceans causing mass redistributions. Similar to the treatment of solid Earth tides, the effect of ocean tides can be modeled using time variable spherical harmonics coefficients ΔC_{nm}^{OT} and ΔS_{nm}^{OT} [McCarthy and Petit, 2004]. However, the effect of ocean tides is rather small and their amplitudes are about one order of magnitude smaller than that of solid Earth tides.

Relativistic Effects

For a rigorous treatment of the orbital motion, the theory of general relativity has to be taken into account. The post-Newtonian effects can be very effectively handled by adding a correction term to the Newtonian acceleration (4.35), which is given by

$$\begin{aligned}\ddot{\mathbf{x}}_{Rel} = & \frac{\mu}{c^2|\mathbf{x}|^3} \cdot \left(\left(4 \frac{\mu}{|\mathbf{x}|} - \dot{\mathbf{x}}^2 \right) \cdot \mathbf{x} + 4 \cdot (\mathbf{x} \cdot \dot{\mathbf{x}}) \cdot \dot{\mathbf{x}} \right) + \\ & + 2 \frac{\mu}{c^2|\mathbf{x}|^3} \cdot \left(\frac{3}{|\mathbf{x}|^2} (\mathbf{x} \times \dot{\mathbf{x}})(\mathbf{x} \cdot \mathbf{J}) + (\dot{\mathbf{x}} \cdot \mathbf{J}) \right) + \\ & + 3 \left(\dot{\mathbf{R}} \times \left(\frac{-GM_S \mathbf{R}}{c^2 |\mathbf{R}|^3} \right) \times \dot{\mathbf{x}} \right),\end{aligned}\quad (4.49)$$

[*McCarthy and Petit*, 2004], where

c is the speed of light,

\mathbf{R} is the position of the Earth with respect to the Sun,

\mathbf{J} is the Earth's angular momentum per unit mass ($|\mathbf{J}| \cong 9.8 \cdot 10^8 \text{ m}^2/\text{s}$), and

M_S is the mass of the Sun.

The first term of equation (4.49) is the relativistic correction to the Newtonian acceleration for the Schwarzschild metric due to the central gravitational term [*Ashby and Bertotti*, 1984]. The second and third terms describe the Lense-Thirring precession and the de Sitter precession, respectively [*Ashby and Bertotti*, 1984 and *Ashby*, 2007]. However, the relativistic effect of the inhomogeneous mass distribution of the Earth can be ignored.

The Schwarzschild field of the Earth causes the main part of the relativistic effects on a near-Earth satellite. It acts like a small scaling factor to the classical Newtonian equations of motion. The relativistic acceleration is a linear combination of the position and velocity and thus lies in the orbital plane. For close Earth satellites the relativistic perturbation amounts to the order of 10^{-9} of the central term.

The relativistic effects caused by other celestial bodies, like the Sun, lead to distance variations at the sub-mm level for Earth satellites and thus can also be neglected [*Montenbruck and Gill*, 2004].

Concerning the classification of the relativistic perturbation it is remarkable that (4.49) does not fulfil the criteria for conservative forces, i.e. the rotation of (4.49) does not vanish

$$rot(\ddot{\mathbf{x}}_{Rel}) = \nabla \times \ddot{\mathbf{x}}_{Rel} \neq \mathbf{0}, \quad (4.50)$$

where ∇ is the Nabla-Operator which is defined by

$$\nabla = \begin{pmatrix} \frac{\partial}{\partial x} \\ \frac{\partial}{\partial y} \\ \frac{\partial}{\partial z} \end{pmatrix}. \quad (4.51)$$

Thus, the relativistic correction term is non-conservative, but undeniably not non-gravitational.

Non-gravitational Perturbations

Atmospheric Drag

As already pointed out, the atmospheric forces represent the largest non-gravitational perturbations acting on satellites at low altitudes. Accurate atmospheric drag modeling is difficult in many respects. In the first place, the physical properties of the upper atmosphere, especially the density which depends in a complex way on a variety of different parameters, are not known with sufficient accuracy. Furthermore, an exact knowledge of the aerodynamic impact of neutral gas and charged particles of the spacecraft with its complex structure and different surfaces would be necessary. Moreover, precise determination of the (often) varying attitude of the satellite towards the flight direction and atmospheric particle flux is required.

However, for many applications drag modeling can yet be done with admissible precision. A range of models for atmospheric densities at satellite heights, like the widely used Harris-Priester model [*Harris and Priester, 1962* or *Montenbruck and Gill, 2000*] or the Jacchia 1971 density model [*Jacchia, 1971* or *Montenbruck and Gill, 2000*], yield acceptable results. If a spacecraft is attitude controlled with a constant alignment with respect to the flight direction, then atmospheric drag can be modeled appropriately by

$$\ddot{\mathbf{x}}_D = -\frac{1}{2} C_D \frac{A}{m} \rho \cdot |\dot{\mathbf{x}}|^2 \cdot \frac{\dot{\mathbf{x}}}{|\dot{\mathbf{x}}|}, \quad (4.52)$$

[*Montenbruck and Gill, 2000*], where

C_D is the dimensionless drag coefficient,

A is the satellite's cross sectional area of the satellite in flight direction,

m is the mass of the satellite, and

ρ is the atmospheric density at the satellite's location.

The drag coefficient describes the aerodynamic interaction of the atmosphere with the surface material of the spacecraft. The a priori knowledge of C_D is usually very imprecise.

Thus, it has to be estimated within the orbit determination process. Typical values range from 1.5 to 3.0 [Montenbruck and Gill, 2000].

However, the modeling of the atmospheric impact does not reach the precision as it is attained for the previously discussed gravitational perturbations. This holds especially for non-spherical spacecraft because the “cannonball”-model described by (4.52) neglects any lift forces and binormal forces, acting perpendicular to the velocity of the spacecraft.

Direct Solar Radiation Pressure

The incoming radiation of the Sun exerts a force on the satellite. The effect of the direct radiation pressure is not related to the altitude of a satellite. Because the amplitude of the atmospheric drag decreases exponentially with height, the radiation pressure usually is the dominating non-gravitational perturbation for satellites above 600 km [Beutler, 2004].

The difficulties of radiation pressure modeling are similar as for atmospheric drag modeling. The entire process involves determining the location of the Sun, the satellite’s attitude, the effective cross-sectional area exposed to radiation and the correct modeling of the (usually time-varying) coefficients of the satellite’s reflectivity as well as the time-varying solar radiation.

For a spherically shaped satellite the resulting acceleration can be modeled by

$$\ddot{\mathbf{x}}_{SR} = -\frac{C_{SR}}{2} \frac{A_e^2}{|\mathbf{x} - \mathbf{x}_S|^2} \frac{S}{c m} \frac{\mathbf{x} - \mathbf{x}_S}{|\mathbf{x} - \mathbf{x}_S|}, \quad (4.53)$$

[Beutler, 2004], where

C_{SR} is the coefficient describing the reflective properties of the satellite’s surface,

A_e is the astronomical unit, $A_e = 149\,597\,870\,610\,m$,

S is the Solar constant, $S = 1\,368 \frac{W}{m^2}$,

c is the speed of light,

A is the cross-sectional area of the satellite in direction towards the Sun,

m is the mass of the satellite,

\mathbf{x} is the geocentric position of the satellite, and

\mathbf{x}_S is the geocentric position of the Sun.

In practice, this model can be employed efficiently as a first order approximation for radiation pressure.

A more refined empirical radiation pressure model , which is widely used for GPS satellites, decomposes the perturbing acceleration in three directions [Springer *et al.*, 1999]. For GPS satellites these directions are defined that the d -axis is pointing towards the Sun, the y -axis is perpendicular to the vectors between the Sun and the GPS satellite and between the geocenter and the GPS satellite and the x -axis completes the right-handed system [Bock, 2003]. The parametrization comprises constant parameters, D_0 , Y_0 and X_0 , and once-per-revolution cosine- and sine-terms, D_C , D_S , Y_C , Y_S , X_C and X_S , which depend on the latitude u of the spacecraft. The parameters are empirically estimated for the individual satellite and the model is given by

$$\begin{pmatrix} a_d \\ a_y \\ a_x \end{pmatrix} = \begin{pmatrix} D_0 + D_C \cdot \cos u + D_S \cdot \sin u \\ Y_0 + Y_C \cdot \cos u + Y_S \cdot \sin u \\ X_0 + X_C \cdot \cos u + X_S \cdot \sin u \end{pmatrix}, \quad (4.54)$$

An analogous empirical modeling of radiation pressure may be performed in the orbit-fixed reference frame, using the directions in along-track, radial and cross-track [Bock, 2003].

Additionally, the modeling of Solar radiation pressure has to account for shadowing effects, caused by either the Earth or the Moon. For satellites in LEO orbit a simple shadow cylinder casted by the Earth is usually sufficient. More elaborate shadow modeling accounts for the totally eclipsed umbra and the partially obscured penumbra regions of both the Earth and the Moon [Feltens, 1991 and Vallado, 2007].

Earth Albedo

In addition to the direct solar radiation pressure, the radiation reflected or re-emitted by the Earth, called albedo, yields a small pressure on the satellite. It decreases with height and can amount 10 – 35% of the direct radiation pressure for low Earth orbiters [Montenbruck and Gill, 2000]. The albedo radiation varies significantly due to surface characteristics and cloud coverage. Accurate modeling of albedo pressure is difficult. However, adequate modeling can be achieved by dividing the Earth's surface in a number of surface elements. Using the Lambertian reflection law the radiation of each element is calculated employing the same model as it is used for the direct radiation pressure (4.53).

Thrust

Aside from natural forces, onboard thrusters intentionally exert forces on the spacecraft for orbit control. The procedure of maintaining a nominally defined orbit is referred to as station keeping [Wertz, 2001]. Due to atmospheric drag, a LEO spacecraft is permanently decelerated, which leads to a loss in altitude. In order to prolong the mission lifetimes of the CHAMP and the GRACE missions, some major orbit maneuvers were carried out to transfer the spacecraft back into higher orbits. Furthermore, the two spacecraft of the GRACE mission have to be kept within a distance of 220 ± 50 km [Ramos-Bosch, 2008a]. Apart from these maneuvers the satellites can be widely considered as freely falling.

In addition, the mentioned spacecraft are also continuously attitude controlled. Due to the misalignments of the pointing of the thruster pairs, the attitude maneuvers can also exert a

residual translative force on the satellite. Any modeling of these residual forces is extremely difficult. However, besides the rare orbit maneuvers, the effects of thrust can easily be captured by empirical orbit models, as described in section 4.3. Thus, thrust is not included in the dynamical models for CHAMP and GRACE.

As already mentioned, the GOCE satellite is permanently propelled by an ion engine to overcome drag. In this case, it is well appropriate to model the propulsion dynamically.

4.2.2 Variational Equations

Dynamic orbit modeling describes the trajectory of a spacecraft as a particular solution of the equations of motion, set up in (4.41). As already mentioned, a particular solution is determined by its initial and dynamical parameters. Within the orbit determination process the trajectory that is best fitting to the observations is estimated. This requires the partial derivatives of the a priori orbit solution $\mathbf{x}(t)$ with respect to the initial and selected dynamical parameters P_i

$$\mathbf{z}_{P_i}(t) \doteq \frac{\partial \mathbf{x}(t)}{\partial P_i}, \quad (4.55)$$

with

$$P_i \in \{p_1, p_2, \dots, p_6, q_1, \dots, q_d\}. \quad (4.56)$$

The equations of motion (4.41) are not solvable analytically. Thus, the functional relations between the particular orbit and the orbit parameters P_i are not known. However, the differential equation system (4.41), which rigorously describes the relationship between the accelerations and the orbit parameters, can be differentiated with respect to these parameters. The resulting differential equations are referred to as variational equations, given by

$$\ddot{\mathbf{z}}_{P_i} = \mathbf{A}_0 \cdot \mathbf{z}_{P_i} + \mathbf{A}_1 \cdot \dot{\mathbf{z}}_{P_i} + \frac{\partial \ddot{\mathbf{x}}_{perturb}}{\partial P_i}, \quad (4.57)$$

with the Jacobian matrices A_0 and A_1 , defined by

$$\mathbf{A}_{0,jk} = \mathbf{A}_{0,jk}(t, \mathbf{x}, \dot{\mathbf{x}}) = \frac{\partial \mathbf{f}_j}{\partial \mathbf{x}_{,k}}, \quad j, k = 1, 2, 3, \quad (4.58)$$

and

$$\mathbf{A}_{1,jk} = \mathbf{A}_{1,jk}(t, \mathbf{x}, \dot{\mathbf{x}}) = \frac{\partial \mathbf{f}_j}{\partial \dot{\mathbf{x}}_{,k}}, \quad j, k = 1, 2, 3. \quad (4.59)$$

The last term of equation (4.57) is non-zero only for dynamical parameters $P_i \in \{q_1, \dots, q_d\}$. Thus, for initial values $P_i \in \{p_1, p_2, \dots, p_6\}$ the variational equation system becomes a linear and homogeneous differential equation system of second order. It is the same equation system for all initial parameters with different initial values for the derivatives \mathbf{z}_{p_i} . Whereas

for dynamical parameters the equation system is inhomogeneous and different for each parameter, but the initial values for the derivatives \mathbf{z}_{q_i} are always zero. Table 4.5 shows the initial values for the variational equations with respect to the parameters P_i .

Table 4.5: Initial conditions for the variational equations

P_i	$\mathbf{z}_{P_i,1}(t_0)$	$\mathbf{z}_{P_i,2}(t_0)$	$\mathbf{z}_{P_i,3}(t_0)$	$\dot{\mathbf{z}}_{P_i,1}(t_0)$	$\dot{\mathbf{z}}_{P_i,2}(t_0)$	$\dot{\mathbf{z}}_{P_i,3}(t_0)$
$x_1 = p_1$	1	0	0	0	0	0
$x_2 = p_2$	0	1	0	0	0	0
$x_3 = p_3$	0	0	1	0	0	0
$\dot{x}_1 = p_4$	0	0	0	1	0	0
$\dot{x}_2 = p_5$	0	0	0	0	1	0
$\dot{x}_3 = p_6$	0	0	0	0	0	1
q_i	0	0	0	0	0	0

To solve the variational equations according to a given (numerical) solution \mathbf{x}_0 of the primary equations (4.41), the Jacobian matrices and the last term of equation (4.57) have to be evaluated at \mathbf{x}_0 , yielding

$$\ddot{\mathbf{z}}_{P_i} = \mathbf{A}_0(t, \mathbf{x}, \dot{\mathbf{x}}) \Big|_{\mathbf{x}=\mathbf{x}_0} \cdot \mathbf{z}_{P_i} + \mathbf{A}_1(t, \mathbf{x}, \dot{\mathbf{x}}) \Big|_{\mathbf{x}=\mathbf{x}_0} \cdot \dot{\mathbf{z}}_{P_i} + \frac{\partial \ddot{\mathbf{x}}_{perturb} (t, \mathbf{x}, \dot{\mathbf{x}})}{\partial P_i} \Big|_{\mathbf{x}=\mathbf{x}_0} . \quad (4.60)$$

For this thesis the collocation method is employed for solving all the primary and variational differential equations [Beutler 1990, Beutler, 2005 and Swatschka 2004]. This method requires linear differential equations. Therefore, the primary equations have to be linearized and solved iteratively. The linearization implies that the Jacobian matrices are available when solving the primary equations. They simply have to be taken from the converged solution and are identical for all variational equation systems (4.60). Thus, using the collocation method, the variational equation systems can be set up very efficiently with little additional computation effort only for dynamical parameters.

4.3 Reduced Dynamic Orbit Modelling

The quality of dynamical orbit solutions relies on the one hand on the quality of the dynamic force model and on the other hand on the quality of the measurements tracking the spacecraft. Spaceborne GPS measurements continuously yield highly accurate observation data. For short arcs, e.g. over one hour, state-of-the-art dynamic models, adjusted to GPS measurements, achieve excellent results. But with increasing orbital length, e.g. several hours to a whole day, the accuracy of purely dynamic models decrease rapidly due to its deficiencies which add up exponentially. This is especially the case for LEO satellite dynamics. Thus, the advantage of the dynamic approach over the kinematic approach, due to the averaging effect of the measurements over successive epochs, is only beneficial for rather short time intervals.

To overcome this drawback the concept of reduced-dynamic orbit determination has been established [Wu *et al.*, 1991]. Hereby the deterministic orbit model (4.41) is augmented by appropriate parametrization, which reads as

$$\ddot{x}(t) \doteq f(t, p_1, p_2, \dots, p_6, q_1, \dots, q_d) + f_1(a_1, \dots, a_n). \quad (4.61)$$

The introduced parameters a_1, \dots, a_n , are determined empirically within the adjustment process. With the additional parametrization the deficiencies of the imperfectly known force model can be overcome, and the accuracy and geometrical strength of the GPS measurements can be fully exploited. This means that the trajectory can be adjusted to the observation data with the essential flexibility while retaining the highest possible amount of dynamical information.

The empirical parameters are usually assigned a priori stochastic properties like expectation values and weighting [Montenbruck *et al.*, 2005b]. Therefore these parameters are commonly referred to as pseudo-stochastic parameters. Realistic a priori constraints have to be applied in order to prevent the estimated trajectory from divergence.

The relaxation of the dynamic orbit model depends on the amount of the introduced pseudo-stochastic parameters, as well as on the constraints that are imposed on these parameters. The dynamics are attenuated with an increasing number of parameters, whereas an increase in weighting preserves the influence of the dynamics. At least theoretically, introducing a maximum of parameters with no constraints, the solution matches that of the kinematic model, because the whole dynamic restraint is removed. In this context reduced-dynamic models approaching this condition are referred to as highly reduced-dynamic (HRD) orbit models. Figure 4.6 illustrates the classification of the different orbit models with respect to the number and a priori standard deviation of the introduced pseudo-stochastic parameters.

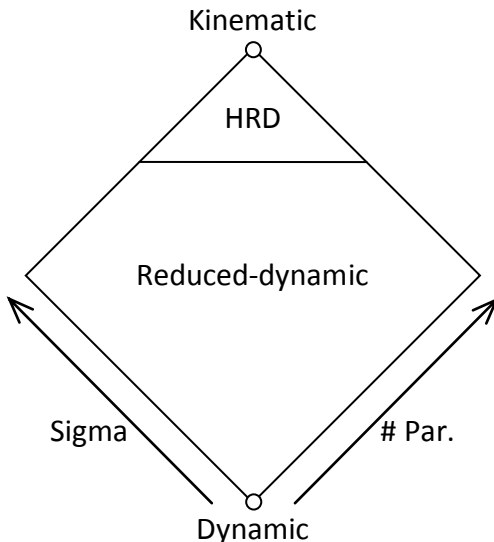


Figure 4.6: The relations between the dynamic, reduced-dynamic, highly reduced-dynamic (HRD) and kinematic orbit determination methods as a function of the number (# Par.) and a priori standard deviation (Sigma) of the introduced pseudo-stochastic parameters [Jäggi, 2006, slightly modified].

Several pseudo-stochastic force models, that are added to the deterministic force model, have been developed [Jäggi *et al.*, 2006]. Pseudo-stochastic parameters reduce the influence of the force field deficiencies only to a certain extent due to discretization effects, which depend on the type and spacing of pseudo-stochastic parameters. In the following, the concept of pseudo-stochastic pulses and piecewise constant accelerations, which are used in this work, are discussed. As will be demonstrated, these types of empirical parameters are highly adequate for compensating for the deficiencies of the deterministic force model. The difference of the pseudo-stochastic concepts presented below, become more pronounced at the velocity level. Velocities derived from the pulse solution show discontinuities. Thus, piecewise constant accelerations, which exhibit the discontinuities at the acceleration level, are much more realistic from a physical point of view.

For the adjustment process the partial derivatives of the orbit with respect to the empirical parameters are required. It will be shown that the solution of the variational equations of these parameters as well as the composition of the normal equation matrix can be accomplished very efficiently.

4.3.1 Instantaneous Velocity Changes

Instantaneous changes in the amount and direction of the spacecraft's velocity at particular epochs very effectively compensate for the imperfect modeling of the dynamics by continuously correcting the course of the satellite [Beutler *et al.*, 1994]. These instantaneous changes appear as discontinuities in the velocity function, which result in Dirac delta functions in the acceleration. Therefore, the parameters describing the velocity changes are commonly referred to as pseudo-stochastic pulses.

Pseudo-stochastic pulses are used routinely for the orbit determination of GPS and GLONASS satellites to overcome the difficulties in solar radiation pressure modeling, which is the limiting factor for modeling high altitude satellites. Here, the changes in velocity are set up once per revolution. To compensate for atmospheric drag a far higher number of pulses at much smaller time intervals is required. However, this method is also attractive for LEO orbit determination, because the huge amount of parameters can be processed very efficiently.

The characteristics of pseudo-stochastic pulses imply that the resulting trajectory is continuous and at pre-defined epochs the velocity of the orbit exhibits discontinuities [Bock, 2003]. In between the pulses the orbit is represented piecewise by a conventional ordinary differential equation of motion, i.e. the deterministic equation of motion. The pseudo-stochastic parameters are estimated conventionally within a classical least squares adjustment process, and are given a priori variances. Figure 4.7 illustrates the concept of pseudo-stochastic orbit modeling with pulses.

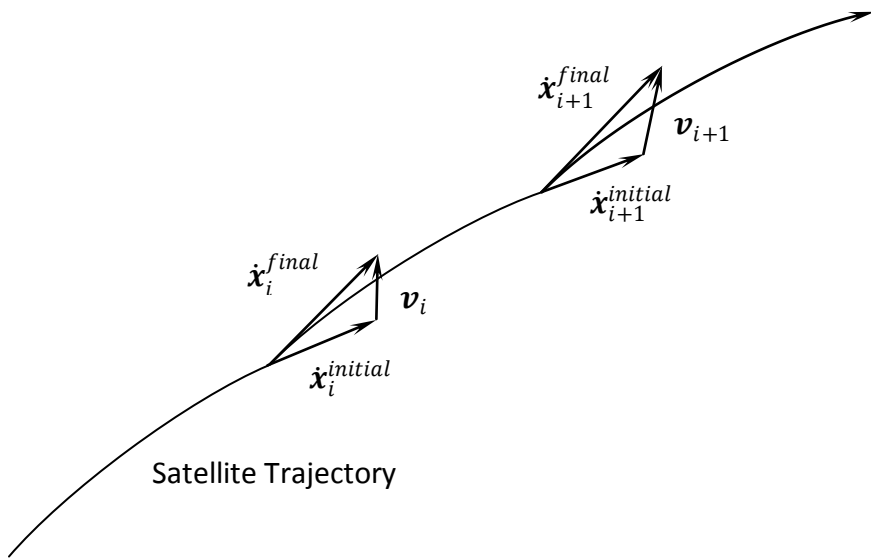


Figure 4.7: The concept of pseudo-stochastic pulses

Setting up three pulses $v_{i,j}, i = 1, \dots, n-1, j = 1, 2, 3$, at predefined epochs t_i in preset directions $e_j(t_i)$ (e.g. in the radial, along-track and cross-track directions) yields the equation of motion which can formally be written as

$$\ddot{\mathbf{x}}(t) \doteq \mathbf{f}(t, p_1, p_2, \dots, p_6, q_1, \dots, q_d) + \sum_{i=1}^{n-1} \sum_{j=1}^3 v_{i,j} \cdot \delta(t - t_i) \cdot e_j(t_i), \quad (4.62)$$

where $\delta(t)$ denotes the Dirac delta distribution [Jäggi et al., 2005]. The complete time interval considered is assumed to be $T = [t_0, t_n]$, with $t_0 < t_1$ and $t_{n-1} < t_n$. The corresponding variational equation for a particular component of one particular pulse can be written as

$$\ddot{\mathbf{z}}_{v_{i,j}} = A_0 \cdot \mathbf{z}_{v_{i,j}} + A_1 \cdot \dot{\mathbf{z}}_{v_{i,j}} + \delta(t - t_i) \cdot e_j(t_i). \quad (4.63)$$

However, it can be shown that the solution of the variational equations with respect to any pulse $v_{i,j}$ may be written as a linear combination (with constant coefficients) of the six solutions $\mathbf{z}_{p_k}, k = 1, \dots, 6$, referring to the six initial conditions p_k [Beutler et al., 2006]. The solution of the variational equation system (4.63) can be written in the form

$$\mathbf{z}_{v_{i,j}}(t) = \begin{cases} \mathbf{0} & ; t < t_i \\ \sum_{k=1}^6 \beta_{ij,k} \cdot \mathbf{z}_{p_k}(t) & ; t \geq t_i \end{cases} . \quad (4.64)$$

Thus, for the computation of all partial derivatives $\mathbf{z}_{v_{i,j}}$ only the variational equations with respect to the initial conditions have to be solved. The coefficients $\beta_{ij,k}$ are obtained from the condition equations

$$\begin{aligned} \mathbf{z}_{v_{i,j}}(t_i) &= \mathbf{0}, \\ \dot{\mathbf{z}}_{v_{i,j}}(t_i) &= \mathbf{e}_j(t_i), \end{aligned} \quad (4.65)$$

leading to the equation system

$$\begin{pmatrix} \mathbf{z}_{p_1} & \mathbf{z}_{p_2} & \mathbf{z}_{p_3} & \mathbf{z}_{p_4} & \mathbf{z}_{p_5} & \mathbf{z}_{p_6} \\ \dot{\mathbf{z}}_{p_1} & \dot{\mathbf{z}}_{p_2} & \dot{\mathbf{z}}_{p_3} & \dot{\mathbf{z}}_{p_4} & \dot{\mathbf{z}}_{p_5} & \dot{\mathbf{z}}_{p_6} \end{pmatrix} \cdot \begin{pmatrix} \beta_{i1,1} & \beta_{i2,1} & \beta_{i3,1} \\ \beta_{i1,2} & \beta_{i2,2} & \beta_{i3,2} \\ \beta_{i1,3} & \beta_{i2,3} & \beta_{i3,3} \\ \beta_{i1,4} & \beta_{i2,4} & \beta_{i3,4} \\ \beta_{i1,5} & \beta_{i2,5} & \beta_{i3,5} \\ \beta_{i1,6} & \beta_{i2,6} & \beta_{i3,6} \end{pmatrix} = \begin{pmatrix} \mathbf{0} & \mathbf{0} & \mathbf{0} \\ \mathbf{e}_1 & \mathbf{e}_2 & \mathbf{e}_3 \end{pmatrix}; \quad (4.66)$$

to be evaluated for epoch t_i .

The above described process for determining the partial derivatives $\mathbf{z}_{v_{i,j}}(t)$ is extremely time-saving and requires far less storage when setting up a large number of pulses with $3(n - 1)$ parameters to be determined.

However, further use can be made of the fact that the partial derivatives of the pulses are linear combinations of the partial derivatives of the initial conditions, when assembling the normal equation system. Linearizing the observation equation φ_l of a particular observation l with respect to the initial conditions and all preceding pulses leads to the correction equation

$$\sum_{k=1}^6 \frac{\partial \varphi_l}{\partial p_k} \cdot \Delta p_k + \sum_{m=1}^i \sum_{j=1}^3 \frac{\partial \varphi}{\partial v_{m,j}} \cdot \Delta v_{m,j} - y_l = \epsilon_l , \quad (4.67)$$

where the assumption was made that $t_l \in [t_i, t_{i+1})$ and that three pulses were set up per epoch. Here y_l denotes the difference between the measurement and the computed value and ϵ_l is the residual of the observation. Now the partial derivatives related to p_k are directly introduced and the partial derivatives related to $v_{i,j}$ are introduced using the representation (4.64), which yields

$$\begin{aligned} & \sum_{k=1}^6 \left(\nabla \varphi_l^T \cdot \mathbf{z}_{p_k}(t_l) \right) \cdot \Delta p_k \\ & + \sum_{k=1}^6 \left(\nabla \varphi_l^T \cdot \mathbf{z}_{p_k}(t_l) \right) \cdot \sum_{m=1}^i \sum_{j=1}^3 \beta_{mj,k} \cdot \Delta v_{m,j} - y_l = \epsilon_l . \end{aligned} \quad (4.68)$$

By grouping all observations of the subinterval $[t_i, t_{i+1})$, the correction equations can be written

$$\mathbf{A}_i \cdot \Delta \mathbf{p} + \mathbf{A}_i \cdot \sum_{m=1}^i \mathbf{B}_m \cdot \Delta \mathbf{v}_m - \mathbf{y}_i = \boldsymbol{\epsilon}_i , \quad (4.69)$$

[Beutler et al., 2006], where \mathbf{A}_i is the design matrix of the involved observations concerning the initial conditions $\mathbf{p} = (p_1, p_2, \dots, p_6)^T$, \mathbf{B}_m covers the coefficients $\beta_{mj,k}$

$$\mathbf{B}_m = \begin{pmatrix} \beta_{m1,1} & \beta_{m2,1} & \beta_{m3,1} \\ \beta_{m1,2} & \beta_{m2,2} & \beta_{m3,2} \\ \beta_{m1,3} & \beta_{m2,3} & \beta_{m3,3} \\ \beta_{m1,4} & \beta_{m2,4} & \beta_{m3,4} \\ \beta_{m1,5} & \beta_{m2,5} & \beta_{m3,5} \\ \beta_{m1,6} & \beta_{m2,6} & \beta_{m3,6} \end{pmatrix} , \quad (4.70)$$

and the correction vector of the three pulses of the corresponding epoch reads

$$\Delta \mathbf{v}_m = \begin{pmatrix} \Delta v_{m,1} \\ \Delta v_{m,2} \\ \Delta v_{m,3} \end{pmatrix} . \quad (4.71)$$

The correction equations for the whole observation data, where all observations are devided into the according subintervals $[t_i, t_{i+1}), i = 0, \dots, n-1$, can now be written in submatrix notation as

$$\begin{pmatrix} \mathbf{A}_0 & \mathbf{0} & \mathbf{0} & \cdots & \mathbf{0} \\ \mathbf{A}_1 & \mathbf{A}_1 \mathbf{B}_1 & \mathbf{0} & \cdots & \mathbf{0} \\ \mathbf{A}_2 & \mathbf{A}_2 \mathbf{B}_1 & \mathbf{A}_2 \mathbf{B}_2 & \cdots & \mathbf{0} \\ \vdots & \vdots & \vdots & \ddots & \vdots \\ \mathbf{A}_{n-1} & \mathbf{A}_{n-1} \mathbf{B}_1 & \mathbf{A}_{n-1} \mathbf{B}_2 & \cdots & \mathbf{A}_{n-1} \mathbf{B}_{n-1} \end{pmatrix} \cdot \begin{pmatrix} \Delta \mathbf{p} \\ \Delta \mathbf{v}_1 \\ \Delta \mathbf{v}_2 \\ \vdots \\ \Delta \mathbf{v}_{n-1} \end{pmatrix} - \mathbf{y} = \boldsymbol{\epsilon} . \quad (4.72)$$

Finally, the entire normal equation system can be established, reading

$$\begin{pmatrix} \sum_{i=0}^{n-1} \mathbf{N}_i & \sum_{i=1}^{n-1} \mathbf{N}_i \mathbf{B}_1 & \sum_{i=2}^{n-1} \mathbf{N}_i \mathbf{B}_2 & \cdots & \sum_{i=n-1}^{n-1} \mathbf{N}_i \mathbf{B}_{n-1} \\ \mathbf{B}_1^T \sum_{i=1}^{n-1} \mathbf{N}_i & \mathbf{B}_1^T \sum_{i=1}^{n-1} \mathbf{N}_i \mathbf{B}_1 & \mathbf{B}_1^T \sum_{i=2}^{n-1} \mathbf{N}_i \mathbf{B}_2 & \cdots & \mathbf{B}_1^T \sum_{i=n-1}^{n-1} \mathbf{N}_i \mathbf{B}_{n-1} \\ \mathbf{B}_2^T \sum_{i=2}^{n-1} \mathbf{N}_i & \mathbf{B}_2^T \sum_{i=2}^{n-1} \mathbf{N}_i \mathbf{B}_1 & \mathbf{B}_2^T \sum_{i=2}^{n-1} \mathbf{N}_i \mathbf{B}_2 & \cdots & \mathbf{B}_2^T \sum_{i=n-1}^{n-1} \mathbf{N}_i \mathbf{B}_{n-1} \\ \vdots & \vdots & \vdots & \ddots & \vdots \\ \mathbf{B}_{n-1}^T \sum_{i=n-1}^{n-1} \mathbf{N}_i & \mathbf{B}_{n-1}^T \sum_{i=n-1}^{n-1} \mathbf{N}_i \mathbf{B}_1 & \mathbf{B}_{n-1}^T \sum_{i=n-1}^{n-1} \mathbf{N}_i \mathbf{B}_2 & \cdots & \mathbf{B}_{n-1}^T \sum_{i=n-1}^{n-1} \mathbf{N}_i \mathbf{B}_{n-1} \end{pmatrix} \cdot \begin{pmatrix} \Delta \mathbf{p} \\ \Delta \mathbf{v}_1 \\ \Delta \mathbf{v}_2 \\ \vdots \\ \Delta \mathbf{v}_{n-1} \end{pmatrix} = \begin{pmatrix} \sum_{i=0}^{n-1} \mathbf{A}_i^T \mathbf{W}_i \cdot \mathbf{y}_i \\ \mathbf{B}_1^T \sum_{i=1}^{n-1} \mathbf{A}_i^T \mathbf{W}_i \cdot \mathbf{y}_i \\ \mathbf{B}_2^T \sum_{i=2}^{n-1} \mathbf{A}_i^T \mathbf{W}_i \cdot \mathbf{y}_i \\ \vdots \\ \mathbf{B}_{n-1}^T \sum_{i=n-1}^{n-1} \mathbf{A}_i^T \mathbf{W}_i \cdot \mathbf{y}_i \end{pmatrix}, \quad (4.73)$$

[Beutler et al., 2006], where $\mathbf{N}_i = \mathbf{A}_i^T \mathbf{W}_i \mathbf{A}_i$ is the normal equation matrix of the subinterval $[t_i, t_{i+1})$ related to the six initial conditions, with \mathbf{W}_i being the weighting matrix pertaining to the according subinterval.

As can be seen from the structure of the full normal equation system (4.73), no large submatrices have to be set up and an appropriate computation sequence allows for a minimum of multiplications to attain the full equation system. It should also be mentioned, that the normal equation matrix is by definition symmetric. This method of setting up the normal equation system is extremely timesaving compared to conventionally setting up the system. Nevertheless, a matrix of dimension $d = 6 + 3 \cdot (n - 1)$ has to be inverted.

The empirical parameters may be constrained to predefined expectation values. Within this work the pseudo-stochastic pulses are constrained individually to zero with an a priori set standard deviation. The characteristics of this stochastic model resemble that of a white noise sequence [Beutler et al., 2006]. Therefore, artificial observations directly measure the pulses, given by

$$\mathbf{v}_i = \mathbf{0}; \quad i = 0, \dots, n - 1. \quad (4.74)$$

The associated weighting matrix is defined as the inverse of the covariance matrix for these parameters

$$\bar{\mathbf{W}}_i = \sigma_0^2 \mathbf{Q}_{\mathbf{v}_i}^{-1} = \begin{pmatrix} \frac{\sigma_0^2}{\sigma_1^2} & 0 & 0 \\ 0 & \frac{\sigma_0^2}{\sigma_2^2} & 0 \\ 0 & 0 & \frac{\sigma_0^2}{\sigma_3^2} \end{pmatrix}; \quad i = 0, \dots, n-1, \quad (4.75)$$

where

σ_0 is the a priori standard deviation,

$\mathbf{Q}_{\mathbf{v}_i}$ is the covariance matrix of the parameters \mathbf{v}_i , and

$\sigma_k ; k = 1, 2, 3$ are the predefined standard deviations of the three components of \mathbf{v}_i .

For this thesis the same a priori weighting is applied to all triples of pulses, yielding $\bar{\mathbf{W}}_i \doteq \bar{\mathbf{W}}$. It has to be mentioned, that also relative constraints can be applied to the empirical parameters. This concept of a random walk sequence for the stochastic model is described in *Montenbruck et al.* [2005b]. In the case of another stochastic model for the empirical parameters, however, only the values of the weighting matrix and of the artificial observations are different. The computation algorithm remains unchanged.

Now the normal equation system including the constraints is attained as described in section 4.1.1. This is done by taking the normal equation matrix of (4.73) and adding the weighting matrix $\bar{\mathbf{W}}$ to all submatrices of the diagonal except for the first one, given by

$$\mathbf{B}_i^T \sum_{l=1}^{n-1} \mathbf{N}_l \mathbf{B}_i + \bar{\mathbf{W}}; \quad i = 1, \dots, n-1. \quad (4.76)$$

The adjustment of the orbit model to the observations within the least-squares method usually requires several iterations. For reduced-dynamic orbit determination the a priori solution for the first iteration may be a dynamic solution where all pulses are considered to be set to zero. For any further iteration I the pulses will usually be assigned non-zero values. Thus, the computation of observed minus computed for the artificial observations yields

$$\bar{\mathbf{y}}_i = \mathbf{0} - \mathbf{v}_i^I; \quad i = 1, \dots, n-1. \quad (4.77)$$

This has to be accounted for in the right-hand side of the normal equation system (4.73) in all subvectors except for the first one, by

$$\mathbf{B}_i^T \sum_{l=1}^{n-1} \mathbf{A}_l^T \mathbf{W}_l \cdot \mathbf{y}_l + \bar{\mathbf{W}} \cdot \bar{\mathbf{y}}_i; \quad i = 1, \dots, n-1. \quad (4.78)$$

Finally, the a posteriori standard deviation has to be computed by

$$m_0 = \sqrt{\frac{\sum_{i=0}^{n-1} \epsilon_i^T W_i \epsilon_i}{n_{real} + n_{art} - u_{dyn} - u_{red}}}, \quad (4.79)$$

where n_{real} and n_{art} are the numbers of the real and artificial observations, respectively, u_{dyn} is the number of deterministic unknowns and u_{red} is the numbers of the empirical parameters. Using the above notation yields

$$u_{red} = n_{art} = 3 \cdot (n - 1). \quad (4.80)$$

It has to be mentioned, that if enough measurements per subinterval are present, no constraints on the pulses have to be set in order to get a non-singular normal equation matrix.

Up to now the normal equation system accounts for the initial conditions and the pseudo-stochastic pulses. The introduction of further dynamical parameters and parameters of the observation model, like clock offsets and ambiguity biases, that also have to estimated, will be discussed in section 4.4.

4.3.2 Piecewise Constant Accelerations

The above presented technique of introducing pseudo-stochastic pulses is highly capable of overcoming the deficiencies of an imperfectly modeled force field. However, the artificial jumps in the velocity of the spacecraft at the epochs $t_i, i = 1, \dots, n - 1$, are disadvantageous for certain applications. From the physical point of view, the pulses cause discontinuities and undifferentiabilities at the velocity level. For applications like gravity field recovery, which is very sensitive to velocity errors, an improvement in the velocities would be very much appreciated [Gerlach et al., 2003].

Therefore, a refined concept of empirical parametrization, namely piecewise constant accelerations, may be introduced [Jäggi et al., 2005]. This method yields much more plausible and realistic orbit solutions. As will be shown, just one additional parameter in each coordinate component has to be introduced in order to upgrade the pseudo-stochastic model from instantaneous pulses to piecewise constant accelerations.

Piecewise constant accelerations compensate for the deficiencies of the dynamics more continuously than pulses at discrete epochs. The resulting trajectory as well as the velocity is continuous over the entire orbital arc. Empirical constant accelerations are introduced over predefined intervals in predefined directions. Just like for the pulses these directions may be assigned to the radial, along-track and cross-track component of the trajectory. Thus, the discontinuities at the velocity level at the epochs t_i are shifted to the next derivative. The discontinuities now occur at the acceleration level. Figure 4.8 illustrates the concept of pseudo-stochastic orbit modeling with piecewise constant accelerations.

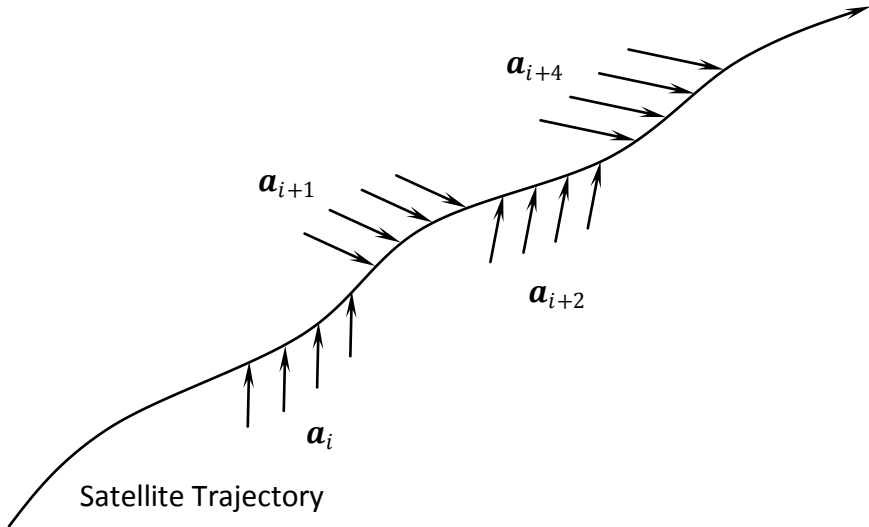


Figure 4.8: The concept of pseudo-stochastic piecewise constant accelerations

In the following, the mathematical framework for piecewise constant accelerations, which is closely related to that of pulses, will be elaborated. Three constant accelerations $a_{i,j}, i = 0, \dots, n - 1, j = 1, 2, 3$, are set up within each time interval $[t_i, t_{i+1})$ in three predefined directions $\mathbf{e}_j(t)$ [Jäggi et al., 2005]. In the case of the proposed radial, along-track and cross-track directions, these directions are time-dependent in the inertial coordinate system. The time interval is assumed to be $T = [t_0, t_n]$, assuring that the whole time span is covered with empirical parameters.

The according equation of motion may be written

$$\ddot{\mathbf{x}}(t) \doteq \mathbf{f}(t, p_1, p_2, \dots, p_6, q_1, \dots, q_d) + \sum_{i=0}^{n-1} \sum_{j=1}^3 a_{i,j} \cdot \xi_i(t) \cdot \mathbf{e}_j(t), \quad (4.81)$$

with ξ_i being defined as

$$\xi_i(t) = \begin{cases} 0 & ; t < t_i \\ 1 & ; t_i \leq t < t_{i+1} \\ 0 & ; t_{i+1} \leq t \end{cases} . \quad (4.82)$$

The variational equations corresponding to a certain acceleration $a_{i,j}$ reads

$$\ddot{\mathbf{z}}_{a_{i,j}} = \mathbf{A}_0 \cdot \mathbf{z}_{a_{i,j}} + \mathbf{A}_1 \cdot \dot{\mathbf{z}}_{a_{i,j}} + \xi_i(t) \cdot \mathbf{e}_j(t). \quad (4.83)$$

Again, it can be shown that the solution of the variational equations with respect to any acceleration $a_{i,j}$ may be written as a linear combination (now with constant and time-varying coefficients) of the six solutions $\mathbf{z}_{p_k}, k = 1, \dots, 6$, referring to the six initial conditions p_k [Beutler et al., 2006]. The partial derivates solving equation (4.83) take the form

$$\mathbf{z}_{a_{i,j}} = \begin{cases} \mathbf{0} & ; t < t_i \\ \sum_{k=1}^6 \beta_{ij,k}(t) \cdot \mathbf{z}_{p_k}(t) = \tilde{\mathbf{z}}_{a_{i,j}} & ; t_i \leq t < t_{i+1} \\ \sum_{k=1}^6 \beta_{ij,k}(t_i) \cdot \mathbf{z}_{p_k}(t) = \sum_{k=1}^6 \beta_{ij,k} \cdot \mathbf{z}_{p_k}(t) & ; t_{i+1} \leq t \end{cases} . \quad (4.84)$$

The coefficients of the linear combination are zero for the time prior to the respective interval, time-dependent during the interval and constant afterwards. However, an efficient solution for the parameters $\beta_{ij,k}$ requires the additional computation of the partial derivatives of the trajectory with respect to constant accelerations $\bar{a}_j, j = 1,2,3$, over the entire arc [Jäggi *et al.*, 2005]. The three accelerations \bar{a}_j must be set in the same directions as for the piecewise constant accelerations, which in this case are the radial, along-track and cross-track directions. The variational equations for these accelerations are

$$\ddot{\mathbf{z}}_{\bar{a}_j} = \mathbf{A}_0 \cdot \mathbf{z}_{\bar{a}_j} + \mathbf{e}_j(t), \quad (4.85)$$

which have to be solved conventionally for $j = 1,2,3$.

It now can be shown that the partial derivative $\tilde{\mathbf{z}}_{a_{i,j}}$ can be written as yet another linear combination of the partial derivatives \mathbf{z}_{p_k} plus $\mathbf{z}_{\bar{a}_j}$, but now with constant coefficients $\alpha_{ij,k}$, over the designated time interval $t_i \leq t < t_{i+1}$, given by

$$\tilde{\mathbf{z}}_{a_{i,j}}^{(r)}(t) = \mathbf{z}_{\bar{a}_j}^{(r)}(t) - \sum_{k=1}^6 \alpha_{ij,k} \cdot \mathbf{z}_{p_k}^{(r)}(t) ; \quad r = 0,1 , \quad (4.86)$$

where r denotes the order of the derivative [Jäggi *et al.*, 2005]. Evaluating equation (4.86) at epoch t_i and considering that, according to equation (4.84), $\tilde{\mathbf{z}}_{a_{i,j}}(t_i) = \mathbf{0}$, yields the following condition equations for the coefficients $\alpha_{ij,k}$

$$\begin{aligned} \sum_{k=1}^6 \alpha_{ij,k} \cdot \mathbf{z}_{p_k}(t_i) &= \mathbf{z}_{\bar{a}_j}(t_i) ; \\ \sum_{k=1}^6 \alpha_{ij,k} \cdot \dot{\mathbf{z}}_{p_k}(t_i) &= \dot{\mathbf{z}}_{\bar{a}_j}(t_i) . \end{aligned} \quad (4.87)$$

After determination of the coefficients $\alpha_{ij,k}$ the partial derivatives $\tilde{\mathbf{z}}_{a_{i,j}}(t)$ can be computed at every epoch using expression (4.86).

Finally the constant coefficients $\beta_{ij,k}$ for $\mathbf{z}_{a_{i,j}}$ for $t_{i+1} \leq t$ can be obtained by computing $\mathbf{z}_{\bar{a}_j}$ at epoch t_{i+1}

$$\sum_{k=1}^6 \beta_{ij,k} \cdot \mathbf{z}_{p_k}(t_{i+1}) = \tilde{\mathbf{z}}_{a_{ij}}(t_{i+1}); \quad (4.88)$$

$$\sum_{k=1}^6 \beta_{ij,k} \cdot \dot{\mathbf{z}}_{p_k}(t_{i+1}) = \dot{\tilde{\mathbf{z}}}_{a_{ij}}(t_{i+1}).$$

All condition equations can be solved in analogy to equation (4.66). Now all $3n$ partial derivatives with respect to the piecewise constant accelerations are efficiently determined.

Analogously to orbit determination using pseudo-stochastic pulses, the composition of the normal equation system for piecewise constant accelerations can be done efficiently using the above relationships between the partial derivatives.

Therefore the observations are grouped into the subintervals $[t_i, t_{i+1}), i = 0, \dots, n - 1$. The correction equations for the subinterval i reads

$$\mathbf{A}_i \cdot \Delta \mathbf{p} + \mathbf{A}_i \cdot \sum_{m=0}^{i-1} \mathbf{B}_{m+1} \cdot \Delta \mathbf{a}_m + \tilde{\mathbf{A}}_i \cdot \Delta \mathbf{a}_i - \mathbf{y}_i = \boldsymbol{\epsilon}_i, \quad (4.89)$$

[Beutler et al., 2006], where the matrix $\tilde{\mathbf{A}}_i$ contains the partial derivatives of the observations with respect to the piecewise constant accelerations pertaining to the subinterval $[t_i, t_{i+1})$. The matrix \mathbf{B}_i contains the constant parameters $\beta_{ij,k}$ attained from equation (4.88), but resulting from the subinterval $[t_{i-1}, t_i)$. It should be noted, that these parameters are not identical to the parameters for pulses.

The full set of correction equations is now given by

$$\left(\begin{array}{cccccc} \mathbf{A}_0 & \tilde{\mathbf{A}}_0 & \mathbf{0} & \cdots & \mathbf{0} & \mathbf{0} \\ \mathbf{A}_1 & \mathbf{A}_1 \mathbf{B}_1 & \tilde{\mathbf{A}}_1 & \cdots & \mathbf{0} & \mathbf{0} \\ \mathbf{A}_2 & \mathbf{A}_2 \mathbf{B}_1 & \mathbf{A}_2 \mathbf{B}_2 & \cdots & \mathbf{0} & \mathbf{0} \\ \vdots & \vdots & \vdots & \ddots & \vdots & \vdots \\ \mathbf{A}_{n-2} & \mathbf{A}_{n-2} \mathbf{B}_1 & \mathbf{A}_{n-2} \mathbf{B}_2 & \cdots & \tilde{\mathbf{A}}_{n-2} & \mathbf{0} \\ \mathbf{A}_{n-1} & \mathbf{A}_{n-1} \mathbf{B}_1 & \mathbf{A}_{n-1} \mathbf{B}_2 & \cdots & \mathbf{A}_{n-1} \mathbf{B}_{n-1} & \tilde{\mathbf{A}}_{n-1} \end{array} \right) \cdot \begin{pmatrix} \Delta \mathbf{p} \\ \Delta \mathbf{a}_0 \\ \Delta \mathbf{a}_1 \\ \Delta \mathbf{a}_2 \\ \vdots \\ \Delta \mathbf{a}_{n-1} \end{pmatrix} - \mathbf{y} = \boldsymbol{\epsilon}. \quad (4.90)$$

Accordingly, the full normal equation system is written as

$$\begin{aligned}
 & \left(\begin{pmatrix} \sum_{i=0}^{n-1} \mathbf{N}_i & \sum_{i=1}^{n-1} \mathbf{N}_i \mathbf{B}_1 & \cdots & \sum_{i=n-1}^{n-1} \mathbf{N}_i \mathbf{B}_{n-1} & \mathbf{0} \\ \mathbf{B}_1^T \sum_{i=1}^{n-1} \mathbf{N}_i & \mathbf{B}_1^T \sum_{i=1}^{n-1} \mathbf{N}_i \mathbf{B}_1 & \cdots & \mathbf{B}_1^T \sum_{i=n-1}^{n-1} \mathbf{N}_i \mathbf{B}_{n-1} & \mathbf{0} \\ \vdots & \vdots & \ddots & \vdots & \vdots \\ \mathbf{B}_{n-1}^T \sum_{i=n-1}^{n-1} \mathbf{N}_i & \mathbf{B}_{n-1}^T \sum_{i=n-1}^{n-1} \mathbf{N}_i \mathbf{B}_1 & \cdots & \mathbf{B}_{n-1}^T \sum_{i=n-1}^{n-1} \mathbf{N}_i \mathbf{B}_{n-1} & \mathbf{0} \\ \mathbf{0} & \mathbf{0} & \mathbf{0} & \mathbf{0} & \mathbf{0} \end{pmatrix} + \right. \\
 & \left. \begin{pmatrix} \mathbf{0} & \mathbf{A}_0^T \mathbf{W}_0 \tilde{\mathbf{A}}_0 & \mathbf{A}_1^T \mathbf{W}_1 \tilde{\mathbf{A}}_1 & \cdots & \mathbf{A}_{n-1}^T \mathbf{W}_{n-1} \tilde{\mathbf{A}}_{n-1} \\ \tilde{\mathbf{A}}_0^T \mathbf{W}_0 \mathbf{A}_0 & \tilde{\mathbf{A}}_0^T \mathbf{W}_0 \tilde{\mathbf{A}}_0 & \mathbf{B}_1^T \mathbf{A}_1^T \mathbf{W}_1 \tilde{\mathbf{A}}_1 & \cdots & \mathbf{B}_1^T \mathbf{A}_{n-1}^T \mathbf{W}_{n-1} \tilde{\mathbf{A}}_{n-1} \\ \tilde{\mathbf{A}}_1^T \mathbf{W}_1 \mathbf{A}_1 & \tilde{\mathbf{A}}_1^T \mathbf{W}_1 \mathbf{A}_1 \mathbf{B}_1 & \tilde{\mathbf{A}}_1^T \mathbf{W}_1 \tilde{\mathbf{A}}_1 & \cdots & \mathbf{B}_2^T \mathbf{A}_{n-1}^T \mathbf{W}_{n-1} \tilde{\mathbf{A}}_{n-1} \\ \vdots & \vdots & \vdots & \ddots & \vdots \\ \tilde{\mathbf{A}}_{n-1}^T \mathbf{W}_{n-1} \mathbf{A}_{n-1} & \tilde{\mathbf{A}}_{n-1}^T \mathbf{W}_{n-1} \mathbf{A}_{n-1} \mathbf{B}_1 & \tilde{\mathbf{A}}_{n-1}^T \mathbf{W}_{n-1} \mathbf{A}_{n-1} \mathbf{B}_2 & \cdots & \tilde{\mathbf{A}}_{n-1}^T \mathbf{W}_{n-1} \tilde{\mathbf{A}}_{n-1} \end{pmatrix} \right) \cdot \\
 & \cdot \begin{pmatrix} \Delta \mathbf{p} \\ \Delta \mathbf{a}_0 \\ \Delta \mathbf{a}_1 \\ \Delta \mathbf{a}_2 \\ \vdots \\ \Delta \mathbf{a}_{n-1} \end{pmatrix} = \begin{pmatrix} \sum_{i=0}^{n-1} \mathbf{A}_i^T \mathbf{W}_i \cdot \mathbf{y}_i \\ \mathbf{B}_1^T \sum_{i=1}^{n-1} \mathbf{A}_i^T \mathbf{W}_i \cdot \mathbf{y}_i \\ \mathbf{B}_2^T \sum_{i=2}^{n-1} \mathbf{A}_i^T \mathbf{W}_i \cdot \mathbf{y}_i \\ \vdots \\ \mathbf{B}_{n-1}^T \sum_{i=n-1}^{n-1} \mathbf{A}_i^T \mathbf{W}_i \cdot \mathbf{y}_i \\ \mathbf{0} \end{pmatrix} + \begin{pmatrix} \mathbf{0} \\ \tilde{\mathbf{A}}_0^T \mathbf{W}_0 \cdot \mathbf{y}_0 \\ \tilde{\mathbf{A}}_1^T \mathbf{W}_1 \cdot \mathbf{y}_1 \\ \vdots \\ \tilde{\mathbf{A}}_{n-2}^T \mathbf{W}_{n-2} \cdot \mathbf{y}_{n-2} \\ \tilde{\mathbf{A}}_{n-1}^T \mathbf{W}_{n-1} \cdot \mathbf{y}_{n-1} \end{pmatrix}, \tag{4.91}
 \end{aligned}$$

where $\mathbf{N}_i = \mathbf{A}_i^T \mathbf{W}_i \mathbf{A}_i$.

It can be seen that the structure and thus the efficiency is similar as for the pulses. The additional contributions require only little computational effort. It also has to be noted, that compared to pulses, for the same division into subintervals only three additional accelerations, i.e. $\Delta \mathbf{a}_0$, have to be set up. This yields a normal equation matrix of dimension $d = 6 + 3 \cdot n$.

Constraints for the piecewise constant accelerations may be imposed in exactly the same way as for the pulses. In principle, the accelerations can also be estimated without being given any a priori weighting. For the presented method of computing the partial derivatives with respect to the piecewise accelerations the solution for the partial derivatives with respect to accelerations over the whole time span is required. However, these permanent accelerations \bar{a}_j are not yet included for estimation in the normal equation system (4.91). Nevertheless, accelerations over the entire orbital arc are usually estimated together with all other parameters. In this case, unconstrained piecewise constant accelerations would lead to a linear dependence of the unknowns and thus a singular normal equation matrix.

So far, equation (4.91) contains only the initial conditions and pseudo-stochastic piecewise constant accelerations. In the next chapter, the introduction of additional parameters into the normal equation system will be discussed.

4.4 Dynamic and Reduced-dynamic Orbit Determination

In the two preceding chapters the concepts of dynamical and reduced-dynamical orbit modeling has been described in detail. The actual process of dynamical and reduced-dynamical orbit determination, however, comprises the adjustment of these models to observations. The observations imply a reference between the position of the satellite and a priori known positions of other satellites or ground stations. In this process the best fitting trajectory is determined according to the measurements.

Within this research, the adjustment is accomplished by a weighted batch least-squares (LSQ) estimation. The principles of the LSQ estimation have been outlined in section 4.1.1. Processing in the batch mode means that all code and phase measurements collected over the considered data arc are incorporated at once. As already stated, the measurements are introduced at the zero difference (ZD) level and in the ionosphere free (IF) linear combination (3.23). Thus, the measurements yield a reference between the spacecraft's GPS receiver position to the positions of the antennas of the GPS satellites in the form of biased ranges. The choice of employing zero differenced GPS observation data was primarily driven by the deactivation of Selective Availability (SA). As a consequence, highly precise ephemeris and clock data of the GPS satellites is available nowadays, see section 3.1.1. This allows to avoid making use of doubly or triply differenced GPS observations, which has to incorporate GPS data from a large network of GPS ground stations [*Švehla and Rothacher, 2003* and *van den IJssel et al., 2003*]. Thus, the associated complex data handling is avoided in the ZD mode.

Within the adjustment process all orbital parameters of interest are estimated. This is definitely the case for the initial values (or boundary values) of the trajectory, for both the dynamical and the reduced-dynamical POD strategies. In addition, a number of dynamical orbit parameters, describing the force field, may be added to the estimation parameters. In the case of reduced-dynamic orbit determination the empirical parameters are estimated along with the orbital parameters as well.

The required partial derivatives of the respective trajectory model with respect to the various orbital parameters are attained through the solution of the variational equations. The computation and efficient solution of all required variational equations has been elaborated in chapters 4.2 and 4.3. In addition, the structure and an efficient strategy to set up the normal equation system with respect to all orbital parameters has been presented.

However, the use of GPS based dynamic and reduced-dynamic orbit determination introduces additional estimation parameters. In the case of ZD observations, the observation model also contains the unknown receiver clock offset and the ionosphere free ambiguity bias. In this chapter, the necessary adaptations of the LSQ adjustment for processing zero difference observations will be outlined in detail. The following algorithms will always include both the code and the phase measurement types. It is, however, possible to use pseudoranges only, which simplifies the computation to some extent at the expense of the accuracy.

The observation model (3.23), as well as its linearized form (3.29), is parametrized for every measurement with the phase center position of the GPS receiver and the GPS receiver clock offset, which here may be denoted $\mathbf{x}_i = (x_1, y_2, z_3)_i^T$ and δt_i , for all epochs $i = 1, \dots, n_T$. These parameters are the same for all measurements at one particular epoch, but vary for different epochs. Additionally, the ionosphere free ambiguity or bias parameter A_{IFj} appears in the carrier phase measurement model, where $j = 1, \dots, n_B$. In contrast to the receiver clock offset, different ambiguity parameters are set up for all measurements at a single epoch, but they are kept constant over several epochs within an uninterrupted tracking pass of a particular GPS satellite, i.e. when the GPS satellite is above the horizon of the receiving antenna and phase-lock is maintained [Teunissen and Kleusberg, 1998]. For numerical reasons the clock offset, as well as the ambiguity parameters, might be estimated in metric units, given by $c\delta t_i$ and $b_j = (\lambda_{IF} A_{IF})_j$.

Thus, if no data gaps occur, a typical one day (24 hours) data arc yields $n_X = 8640$ epochs for a 10 second data sampling, or $n_T = 2880$ when the measurements are given at 30 seconds intervals. Due to the rapid motion of the considered spaceborne receivers, GPS satellites are in view for a maximum of about 40 minutes. This usually results in about 15 phase connected tracking passes to a single GPS satellite per day. The total number of independent ambiguity parameters, that have to be introduced over a one day arc, is approximately $n_B \approx 700 - 800$ for LEO satellites. The resulting total number of parameters to estimate is therefore $4n_T + n_B \approx 35000$ for 10s GPS data, or 12000 for 30s data. This number of parameters has to be solved for in the kinematic approach where epoch-wise LEO positions are determined. With the respective spaceborne receivers, delivering on average about 6 code and phase measurements of good quality per epoch, the number of observations is about 105000 or 35000 for 10s or 30s GPS data, respectively [Švehla and Rothacher, 2003]. Thus, for spaceborne scenarios, the estimation system is overdetermined for the kinematic strategy.

In this research, however, the dynamic and reduced-dynamic strategies for POD were chosen. The major difference of these techniques to the kinematic approach is that the epoch-wise position coordinates of the spacecraft are replaced by the orbital parameters of the trajectory model. Now, this implies that the (linearized) observational equations have to be related to the according estimation parameters in order to set up the design matrix. As

already mentioned briefly in section 3.4, this is achieved by applying the chain rule for derivation. The partial derivation of observation function φ_l with respect to the orbital parameter P_i is given by

$$\frac{\partial \varphi_l}{\partial P_i} = \sum_{k=1}^3 \frac{\partial \varphi_l}{\partial x_{k,l}} \cdot \frac{\partial x_{k,l}}{\partial P_i} = \nabla \varphi_l^T \cdot \frac{\partial \mathbf{x}_l}{\partial P_i}, \quad (4.92)$$

which yields for both code and phase observations in the IF ZD mode

$$\frac{\partial \varphi_l}{\partial P_i} = \mathbf{e}_l \cdot \mathbf{z}_{P_i}(t_l), \quad (4.93)$$

where \mathbf{e}_l is the line of sight unit vector from the antenna phase center of the GPS satellite to the phase center of the LEO receiver, and \mathbf{z}_{P_i} is the partial derivative of the trajectory with respect to any orbital parameter P_i . The orbital estimation parameter $P_i \in \{p_1, \dots, p_6, q_1, \dots, q_{n_Q}, a_1, \dots, a_{n_A-1}\}$ is either an initial value p_i or (possibly) a dynamical parameter q_i or (in the case of reduced-dynamical orbit determination) an empirical parameter a_i . The computation of all necessary partial derivatives \mathbf{z}_{P_i} has been described in sections 4.2.2, 4.3.1 and 4.3.2. Equation (4.93) has to be evaluated for the actual time t_l of the measurement. Here, it has to be considered, that the exact epochs of the observations are initially unknown, due to the unknown clock offset. The epoch when the observation is introduced, is, thus, updated for every iteration, according to the improved estimate of the clock offset.

The partial derivatives of the estimation parameters, arising from the observational model, i.e. the clock offsets δt_k and the ambiguity parameters b_j , are given by

$$\frac{\partial \varphi_l}{\partial c\delta t_k} = \begin{cases} 1 & ; \quad \delta t_k \text{ active in } \varphi_l \\ 0 & ; \quad \text{else} \end{cases}, \quad (4.94)$$

and

$$\frac{\partial \varphi_l}{\partial b_j} = \begin{cases} 1 & ; \quad b_j \text{ active in } \varphi_l \\ 0 & ; \quad \text{else} \end{cases}. \quad (4.95)$$

Now, these partial derivatives are inserted into the design matrix and the adjustment can be started. However, an appropriate order of the estimation parameters may lead to a normal equation matrix, of a certain structure, that can be inverted with considerable efficiency. In addition, for both the pulses or piecewise constant accelerations, the partial derivatives may be expressed as linear combinations of the derivatives with respect to the initial conditions. Therefore the entire orbital arc was divided into subintervals, with the matrices \mathbf{A}_i containing the partial derivatives with respect to the initial conditions $\mathbf{p} = (p_1, \dots, p_6)^T$ and the matrices \mathbf{B}_i containing the coefficients of the linear combinations. Additional estimation parameters can be added to the overall design matrix separately or they may be introduced directly into the matrices \mathbf{A}_i . In the following, the clock offsets and bias parameters will be added separately and the dynamical parameters will be introduced into the matrices \mathbf{A}_i .

Therefore, the estimation parameters are grouped into a $(6 + n_Q + n_A - 1)$ – dimensional vector

$$\mathbf{X} = (\mathbf{p}, \mathbf{q}, \mathbf{a}), \quad (4.96)$$

with $\mathbf{q} = (q_1, \dots, q_{n_Q})^T$ and $\mathbf{a} = (a_1, \dots, a_{n_A-1})^T$, which stands either for the pulses or for piecewise constant accelerations, a (n_B) – dimensional vector

$$\mathbf{C} = (b_1, \dots, b_{n_B}), \quad (4.97)$$

containing the ambiguity parameters, and a (n_T) – dimensional vector

$$\mathbf{T} = (c\delta t_1, \dots, c\delta t_{n_T}), \quad (4.98)$$

with the epoch-wise clock offsets.

Accordingly, a linearization about initial values for the estimation parameters yields

$$\begin{aligned} \mathbf{X} &= \mathbf{X}_0 + \Delta \mathbf{X}, \\ \mathbf{C} &= \mathbf{C}_0 + \Delta \mathbf{C}, \\ \mathbf{T} &= \mathbf{T}_0 + \Delta \mathbf{T}. \end{aligned} \quad (4.99)$$

The normal equation system is given by

$$\begin{aligned} \left(\frac{\partial \Phi}{\partial (\mathbf{X}_0, \mathbf{C}_0, \mathbf{T}_0)} \right)^T \mathbf{W} \left(\frac{\partial \Phi}{\partial (\mathbf{X}_0, \mathbf{C}_0, \mathbf{T}_0)} \right) \begin{pmatrix} \Delta \mathbf{X} \\ \Delta \mathbf{C} \\ \Delta \mathbf{T} \end{pmatrix} = \\ = \left(\frac{\partial \Phi}{\partial (\mathbf{X}_0, \mathbf{C}_0, \mathbf{T}_0)} \right)^T \mathbf{W} (\mathbf{z} - \Phi(\mathbf{X}_0, \mathbf{C}_0, \mathbf{T}_0)), \end{aligned} \quad (4.100)$$

where the vector Φ contains the functions φ_l and the actual measurements are captured in \mathbf{z} . The entire design matrix is split up into

$$\left(\frac{\partial \Phi}{\partial (\mathbf{X}_0, \mathbf{C}_0, \mathbf{T}_0)} \right) = (\mathbf{A}_X, \mathbf{A}_C, \mathbf{A}_T). \quad (4.101)$$

According to (4.94) a particular line of matrix \mathbf{A}_T pertaining to the observation φ_l of epoch k reads

$$\frac{\partial \varphi_l}{\partial \mathbf{T}} = (0_{(1)}, \dots, 0_{(k-1)}, 1_{(k)}, 0_{(k+1)}, \dots, 0_{(n_T)}), \quad (4.102)$$

where only the element related to the active clock offset is non-zero. Here no difference is made between the code or carrier phase measurements. In a similar way the corresponding line of the matrix \mathbf{A}_C is set up for the carrier phases, according to (4.95),

$$\frac{\partial \varphi_l}{\partial \mathbf{C}} = (0_{(1)}, \dots, 0_{(j-1)}, 1_{(j)}, 0_{(j+1)}, \dots, 0_{(n_B)}). \quad (4.103)$$

For all code observations the lines of \mathbf{A}_C are becoming n_B – dimensional null vectors because of no ambiguity bias being involved. And finally, the elements of a line in matrix \mathbf{A}_X related to observation φ_l is written as

$$\frac{\partial \varphi_l}{\partial \mathbf{X}} = \left(\frac{\partial \varphi_l}{\partial p_1}, \dots, \frac{\partial \varphi_l}{\partial p_6}, \frac{\partial \varphi_l}{\partial q_1}, \dots, \frac{\partial \varphi_l}{\partial q_{n_Q}}, \frac{\partial \varphi_l}{\partial a_1}, \dots, \frac{\partial \varphi_l}{\partial a_i}, 0_{(i+1)}, \dots, 0_{(n_A-1)} \right). \quad (4.104)$$

Here, the assumption was made, that φ_l was measured during the time interval i , as specified in sections 4.3.1 or 4.3.2.

In order to set up the matrix \mathbf{N}_{XX} efficiently and exploit the linear dependencies of the partials $\frac{\partial \varphi_l}{\partial a_i}$ on the partials $\frac{\partial \varphi_l}{\partial p_j}$, as described in sections 4.3.1 or 4.3.2, all submatrices \mathbf{A}_i have to be expanded by n_Q columns for the partial derivatives with respect to the dynamical parameters, which is written

$$\mathbf{A}_i^+ \doteq \begin{pmatrix} \frac{\partial \Phi_i}{\partial \mathbf{p}} & \frac{\partial \Phi_i}{\partial q_1} & \dots & \frac{\partial \Phi_i}{\partial q_{n_Q}} \end{pmatrix} = \begin{pmatrix} \mathbf{A}_i & \frac{\partial \Phi_i}{\partial q_1} & \dots & \frac{\partial \Phi_i}{\partial q_{n_Q}} \end{pmatrix}, \quad (4.105)$$

[Beutler *et al.*, 2005] where the Φ_i contains the observations pertaining to the subinterval i . The matrices \mathbf{B}_i have to be expanded by n_Q lines, yielding

$$\mathbf{B}_i^+ \doteq \begin{pmatrix} \mathbf{B}_i \\ \mathbf{0}^T \\ \vdots \\ \mathbf{0}^T_{(n_Q)} \end{pmatrix} = \begin{pmatrix} \beta_{i1,1} & \beta_{i2,1} & \beta_{i3,1} \\ \beta_{i1,2} & \beta_{i2,2} & \beta_{i3,2} \\ \beta_{i1,3} & \beta_{i2,3} & \beta_{i3,3} \\ \beta_{i1,4} & \beta_{i2,4} & \beta_{i3,4} \\ \beta_{i1,5} & \beta_{i2,5} & \beta_{i3,5} \\ \beta_{i1,6} & \beta_{i2,6} & \beta_{i3,6} \\ 0_{(1)} & 0_{(1)} & 0_{(1)} \\ \vdots & \vdots & \vdots \\ 0_{(n_Q)} & 0_{(n_Q)} & 0_{(n_Q)} \end{pmatrix}. \quad (4.106)$$

In the case of piecewise constant accelerations the matrices $\tilde{\mathbf{A}}_i$ do not have to be changed. The introduction of dynamical orbit parameters is completed by exchanging the matrices \mathbf{A}_i and \mathbf{B}_i in sections 4.3.1 or 4.3.2 by the matrices \mathbf{A}_i^+ and \mathbf{B}_i^+ . By way of example, the matrix \mathbf{A}_X in the case of piecewise constant accelerations reads, according to equation (4.90),

$$\mathbf{A}_X = \begin{pmatrix} \mathbf{A}_0^+ & \tilde{\mathbf{A}}_0 & \mathbf{0} & \dots & \mathbf{0} & \mathbf{0} \\ \mathbf{A}_1^+ & \mathbf{A}_1^+ \mathbf{B}_1^+ & \tilde{\mathbf{A}}_1 & \dots & \mathbf{0} & \mathbf{0} \\ \mathbf{A}_2^+ & \mathbf{A}_2^+ \mathbf{B}_1^+ & \mathbf{A}_2^+ \mathbf{B}_2^+ & \dots & \mathbf{0} & \mathbf{0} \\ \vdots & \vdots & \vdots & \ddots & \vdots & \vdots \\ \mathbf{A}_{n-2}^+ & \mathbf{A}_{n-2}^+ \mathbf{B}_1^+ & \mathbf{A}_{n-2}^+ \mathbf{B}_2^+ & \dots & \tilde{\mathbf{A}}_{n-2} & \mathbf{0} \\ \mathbf{A}_{n-1}^+ & \mathbf{A}_{n-1}^+ \mathbf{B}_1^+ & \mathbf{A}_{n-1}^+ \mathbf{B}_2^+ & \dots & \mathbf{A}_{n-1}^+ \mathbf{B}_{n-1}^+ & \tilde{\mathbf{A}}_{n-1} \end{pmatrix}. \quad (4.107)$$

Now, the design matrices \mathbf{A}_C and \mathbf{A}_T , related to the ambiguity biases and clock offsets, are included according to (4.101), yielding the final normal equation system

$$\begin{pmatrix} \mathbf{A}_X^T \mathbf{W} \mathbf{A}_X & \mathbf{A}_X^T \mathbf{W} \mathbf{A}_C & \mathbf{A}_X^T \mathbf{W} \mathbf{A}_T \\ \mathbf{A}_C^T \mathbf{W} \mathbf{A}_X & \mathbf{A}_C^T \mathbf{W} \mathbf{A}_C & \mathbf{A}_C^T \mathbf{W} \mathbf{A}_T \\ \mathbf{A}_T^T \mathbf{W} \mathbf{A}_X & \mathbf{A}_T^T \mathbf{W} \mathbf{A}_C & \mathbf{A}_T^T \mathbf{W} \mathbf{A}_T \end{pmatrix} \begin{pmatrix} \Delta \mathbf{X} \\ \Delta \mathbf{C} \\ \Delta \mathbf{T} \end{pmatrix} = \begin{pmatrix} \mathbf{A}_X^T \mathbf{W} \mathbf{y} \\ \mathbf{A}_C^T \mathbf{W} \mathbf{y} \\ \mathbf{A}_T^T \mathbf{W} \mathbf{y} \end{pmatrix}. \quad (4.108)$$

The terms $\mathbf{A}_X^T \mathbf{W} \mathbf{A}_X$ and $\mathbf{A}_X^T \mathbf{W} \mathbf{y}$ are computed in exactly the same way as described in (4.73) for the case of pulses, or as (4.91), if piecewise constant accelerations are employed. All remaining terms where the matrices \mathbf{A}_C and \mathbf{A}_T are involved, can be set up very easily because these matrices only contain the elements 0 or 1. Thus, only particular lines or columns have to be taken from the intermediate products which occur when setting up $\mathbf{A}_X^T \mathbf{W} \mathbf{A}_X$ and $\mathbf{A}_X^T \mathbf{W} \mathbf{y}$ with the efficient algorithms. Furthermore, constraints for the empirical parameters may be imposed, as described in sections 4.3.1 or 4.3.2, by adding the weights $\overline{\mathbf{W}}_i$ and the artificial observations $\overline{\mathbf{y}}_i$ to the terms $\mathbf{A}_X^T \mathbf{W} \mathbf{A}_X$ and $\mathbf{A}_X^T \mathbf{W} \mathbf{y}$.

In this context, dynamical modeling represents a special case of reduced-dynamic orbit modeling, i.e. when no pseudo-stochastic parameters are set up. In this case, the first subinterval can be considered as the only, overall, subinterval. No matrices \mathbf{B}_i^+ and $\tilde{\mathbf{A}}_i$ occur, and the matrix \mathbf{A}_X results in

$$\mathbf{A}_X = \mathbf{A}_0^+. \quad (4.109)$$

The final system (4.108) can formally be written in reduced form, as

$$\begin{pmatrix} \mathbf{N}_{XX} & \mathbf{N}_{XC} & \mathbf{N}_{XT} \\ \mathbf{N}_{CX} & \mathbf{N}_{CC} & \mathbf{N}_{CT} \\ \mathbf{N}_{TX} & \mathbf{N}_{TC} & \mathbf{N}_{TT} \end{pmatrix} \begin{pmatrix} \Delta \mathbf{X} \\ \Delta \mathbf{C} \\ \Delta \mathbf{T} \end{pmatrix} = \begin{pmatrix} \mathbf{n}_X \\ \mathbf{n}_C \\ \mathbf{n}_T \end{pmatrix}. \quad (4.110)$$

The structure of the resulting normal equation system now contains the diagonal matrices \mathbf{N}_{CC} and \mathbf{N}_{TT} , see Figure 4.9, and the matrices \mathbf{N}_{XC} , \mathbf{N}_{XT} , \mathbf{N}_{CT} , which are rather sparse matrices, populated to a large extent with zeros.

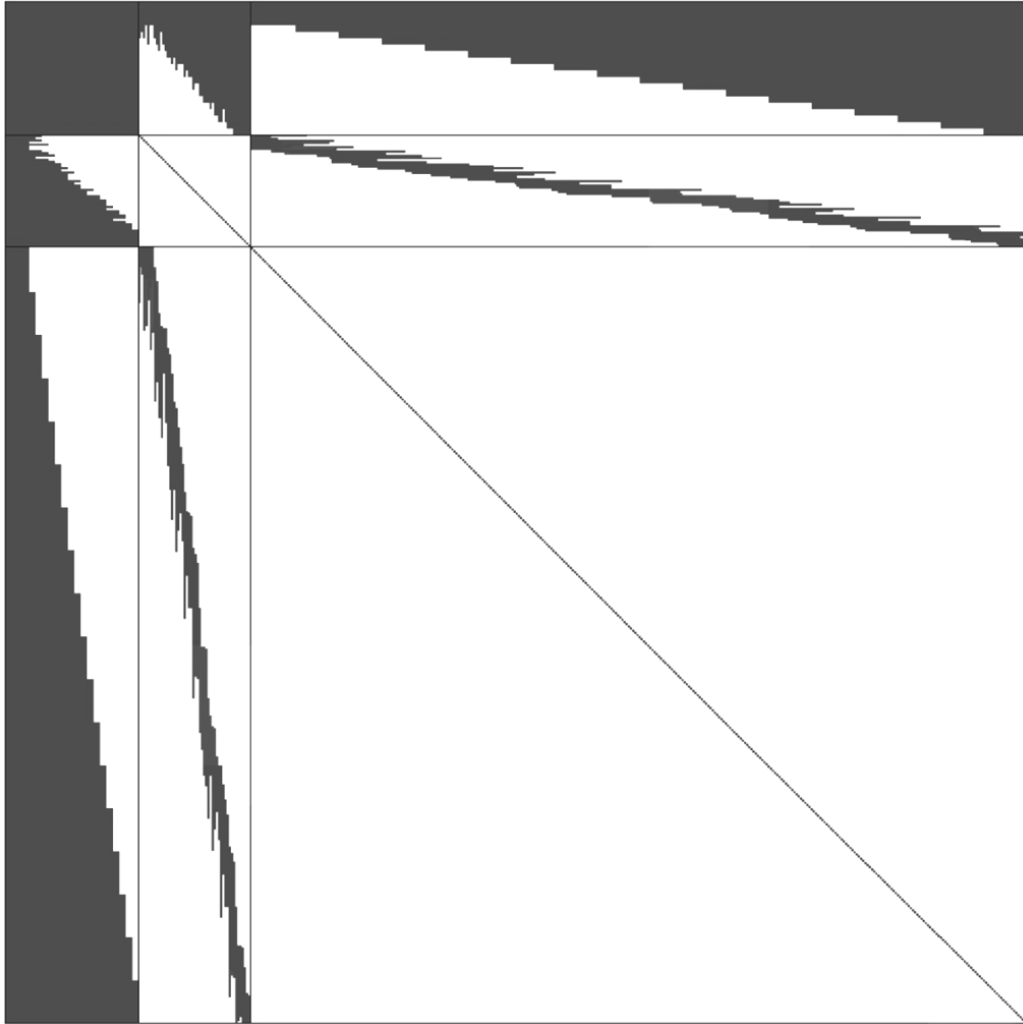


Figure 4.9: Structure of the normal equation matrix for reduced-dynamic orbit determination (example)

The matrices \mathbf{N}_{XC} , \mathbf{N}_{XT} , \mathbf{N}_{CT} clearly show the correlations between the estimation parameters. Matrix \mathbf{N}_{XX} is fully populated, therefore it was justified to introduce the dynamical estimation parameters directly into \mathbf{A}_X .

The solution of the normal equation system (4.110) can be achieved most efficiently by exploiting the simple invertibility of the diagonal matrix \mathbf{N}_{TT} . Therefore, the parameters \mathbf{X} and \mathbf{C} are grouped together as

$$\mathbf{Y} = \begin{pmatrix} \mathbf{X} \\ \mathbf{C} \end{pmatrix}, \quad (4.111)$$

[Kroes, 2006], and the system is rewritten accordingly in the form

$$\begin{pmatrix} \mathbf{N}_{YY} & \mathbf{N}_{YT} \\ \mathbf{N}_{TY} & \mathbf{N}_{TT} \end{pmatrix} \begin{pmatrix} \Delta \mathbf{Y} \\ \Delta \mathbf{T} \end{pmatrix} = \begin{pmatrix} \mathbf{n}_Y \\ \mathbf{n}_T \end{pmatrix}. \quad (4.112)$$

According to equation (4.17), pre-elimination of $\Delta \mathbf{Y}$ yields

$$\Delta \mathbf{Y} = (\mathbf{N}_{YY} - \mathbf{N}_{YT}\mathbf{N}_{TT}^{-1}\mathbf{N}_{TY})^{-1}(\mathbf{n}_Y - \mathbf{N}_{YT}\mathbf{N}_{TT}^{-1}\mathbf{n}_T). \quad (4.113)$$

The solution $\Delta \mathbf{Y}$ is subsequently back-substituted to obtain the corrections $\Delta \mathbf{T}$ of the clock offsets, given by

$$\Delta \mathbf{T} = \mathbf{N}_{TT}^{-1}(\mathbf{n}_T - \mathbf{N}_{TY}\mathbf{n}_Y). \quad (4.114)$$

However, yet another part of the arising calculations can be performed more efficiently. Therefore, the submatrices of the term $\mathbf{N}_{YY} - \mathbf{N}_{YT}\mathbf{N}_{TT}^{-1}\mathbf{N}_{TY}$ in (4.113) which has to be inverted is considered in detail,

$$\begin{aligned} & \begin{pmatrix} \mathbf{N}_{XX} & \mathbf{N}_{XC} \\ \mathbf{N}_{CX} & \mathbf{N}_{CC} \end{pmatrix} - \begin{pmatrix} \mathbf{N}_{XT} \\ \mathbf{N}_{CT} \end{pmatrix} \mathbf{N}_{TT}^{-1} (\mathbf{N}_{TX} \quad \mathbf{N}_{TC}) = \\ & = \begin{pmatrix} \mathbf{N}_{XX} - \mathbf{N}_{XT}\mathbf{N}_{TT}^{-1}\mathbf{N}_{TX} & \mathbf{N}_{XC} - \mathbf{N}_{XT}\mathbf{N}_{TT}^{-1}\mathbf{N}_{TC} \\ \mathbf{N}_{CX} - \mathbf{N}_{CT}\mathbf{N}_{TT}^{-1}\mathbf{N}_{TX} & \mathbf{N}_{CC} - \mathbf{N}_{CT}\mathbf{N}_{TT}^{-1}\mathbf{N}_{TC} \end{pmatrix} \doteq \begin{pmatrix} \mathbf{P} & \mathbf{Q} \\ \mathbf{Q}^T & \mathbf{S} \end{pmatrix}. \end{aligned} \quad (4.115)$$

It can be seen that the matrix \mathbf{S} attains the structure of a band matrix, with the size of the band being determined by the number of simultaneously active ambiguity parameters. Several algorithms for matrix inversion, such as the LU-decomposition, can be adapted for band matrices [Press *et al.*, 1989]. In the case of the band being very small compared to the dimension of the matrix \mathbf{S} , i.e. the orbit is estimated over a long time interval, the band-inversion is much more efficient and faster. The band-inversion of \mathbf{S} can be exploited by inverting the whole system as

$$\begin{pmatrix} \mathbf{P} & \mathbf{Q} \\ \mathbf{Q}^T & \mathbf{S} \end{pmatrix}^{-1} = \begin{pmatrix} \tilde{\mathbf{P}} & \tilde{\mathbf{Q}} \\ \tilde{\mathbf{Q}}^T & \tilde{\mathbf{S}} \end{pmatrix}, \quad (4.116)$$

[Staudinger, 2003], with

$$\begin{aligned} \tilde{\mathbf{P}} &= (\mathbf{P} - \mathbf{Q}\mathbf{S}^{-1}\mathbf{Q}^T)^{-1}, \\ \tilde{\mathbf{Q}} &= -(\mathbf{P} - \mathbf{Q}\mathbf{S}^{-1}\mathbf{Q}^T)^{-1}(\mathbf{Q}\mathbf{S}^{-1}), \\ \tilde{\mathbf{S}} &= \mathbf{S}^{-1} + (\mathbf{S}^{-1}\mathbf{Q}^T)(\mathbf{P} - \mathbf{Q}\mathbf{S}^{-1}\mathbf{Q}^T)^{-1}(\mathbf{Q}\mathbf{S}^{-1}), \\ \tilde{\mathbf{Q}}^T &= (\tilde{\mathbf{Q}})^T. \end{aligned} \quad (4.117)$$

Usually, a continuous tracking pass, with a constant ambiguity parameter, overlaps with about 20 other bias parameters while being active. Hence, only about $n_B \times 20$ elements of \mathbf{S} are non-zero. Thus, in the case of long data arcs, e.g. 24 hours with a typical number of $n_B = 500$ phase biases, the inversion of the band matrix is by far more efficient.

The total number of parameters, that are estimated in the dynamic or reduced-dynamic approaches, are usually much less than for kinematic orbit determination. If pseudo-stochastic parameters are set up every ten minutes, the number of these parameters over a one day arc results in 435. With six initial conditions, and only three dynamical parameters to be estimated, i.e. the constant accelerations in radial, along and cross-track direction, the total number of estimation parameters amounts to about 3800 or 9600, in the cases of 10

or 30 seconds data sampling, respectively. This is more than three times less than for the kinematic strategy.

The estimation process is iteratively repeated until convergence yields the final trajectory and the final estimations of all involved parameters. This is usually achieved after 3 iterations.

For the sake of completeness, the stochastic properties of all estimated parameters are captured in the covariance matrices, as described in section 4.1.1. For the covariances of \mathbf{Y} , which are given by

$$\mathbf{Q}_{YY} = s_0^2 (\mathbf{N}_{YY} - \mathbf{N}_{YT} \mathbf{N}_{TT}^{-1} \mathbf{N}_{TY})^{-1}, \quad (4.118)$$

the inversion has already been performed. The covariances of the clock offset estimates are easily calculated by

$$\mathbf{Q}_{TT} = s_0^2 (\mathbf{N}_{TT}^{-1} + (\mathbf{N}_{TT}^{-1} \mathbf{N}_{TY}) \mathbf{Q}_{YY} (\mathbf{N}_{TT}^{-1} \mathbf{N}_{TY})^T). \quad (4.119)$$

Finally, it has to be stated, that the elaborated procedure for orbit determination can also be performed with code observations only. This can be motivated by the faster computation times, if a loss in accuracy resembles acceptable. In this case, all terms that are related to the ambiguity parameters are omitted. This is possible, because the phase observations only contribute to the small-scale shape of the orbit. Due to the ambiguity biases, the phase measurements only imply position differences and do not determine the absolute position and orientation of the trajectory. The positioning is accomplished by the pseudoranges, which makes the estimation system non-singular. Using only phase data, would lead to a singular normal equation matrix, where the clock offsets can not be separated from the ambiguity biases. In order to extract the maximum information from the highly accurate carrier phases, the phase data should be given much weight for the estimation. By this means, the determination of the shape of the orbit is widely left to the phase measurements. Whereas the absolute positioning and orientation of the trajectory can still be accurately achieved by the weak, but numerous, code observations, due to the averaging effect.

An alternative to the use of raw code and carrier phase data would be posed by using code-smoothed data [Dach et al., 2007]. Here, the ambiguity parameters are pre-eliminated over each continuous tracking pass, by fitting the phase observations to the mean of the code ranges. The difference of code-smoothing to the combined data processing is, that in the first case the ambiguity parameters are (pre-)determined by only the pseudoranges of the according pass, whereas in the second case, the biases are estimated using the whole code data set. The combined use of code and phase data, thus, preserves the utmost information from the measurements and is much more robust. In this context, the combined use of zero differenced code and carrier phase data for the estimation of the ambiguity parameters is often referred to as float ambiguity resolution.

4.5 Data Editing

The quality of the GPS data is of crucial relevance for precise orbit determination. The data used for this research is obtained from high quality geodetic-type spaceborne receivers. Yet, the data can be subject to systematic errors, like multipath. Therefore, adequate data screening is necessary to detect possible outliers and bad measurements. In addition, when the receiver loses lock of the signal, a new ambiguity parameter has to be introduced for the phase measurement. For this purpose, the carrier phase observations have to be scanned for sudden “phase-breaks” or “phase-jumps”. Furthermore, a minimum signal strength for the accepted observations can be set, as well as the elevation angle of the incoming signal with respect to the receiver horizon might be evaluated to exclude measurements below a predefined cut-off angle. In the following the data editing procedures that are used for this research are described.

Prior to the search for erroneous data, measurements that are taken below a user-defined elevation are excluded. Hereby, the position and attitude of the spacecraft is determined from the intermediate trajectory solution. Because the concerned receivers might even track GPS satellites below the instant horizon, a minimum cut-off angle of 0 degrees should be used for POD. However, an elevation mask of 5 degrees is usually advisable to discard bad measurements.

In addition, the Signal to Noise Ratio (SNR) can be used as an indicator for observations with a high noise level. The SNR is provided for all measurements in the data files of the employed BlackJack receivers [Gurtner, 1994]. For these receivers, the carrier to noise density ratio C/N_0 is related to the SNR by [Montenbruck and Kroes, 2003],

$$C/N_0 = 20 \cdot \log_{10} \left(\frac{SNR}{\sqrt{2}} \right). \quad (4.120)$$

An SNR value of 5 corresponds to a C/N_0 of about 11 dB-Hz. This value has been found as an appropriate limit to exclude measurements with a high noise level of about 1 m for the P-codes and 3 mm for the carrier phases [Montenbruck and Kroes, 2003]. After the SNR and elevation-based data screening the remaining observations are scanned for outliers and phase-breaks.

In order to detect erroneous observation data, the post-fit residuals with respect to the current orbit solution and receiver clock offsets are calculated for all code and carrier phase measurements. It can be assumed, that the intermediate trajectory is always smooth enough, so that the residuals can reliably be used as an indicator of the data quality. The residuals are obtained by forming the differences between the observed values and the calculated quantities, given by

$$\begin{aligned} \Delta P_{IF}(t_r) &= P_{IF}(t_r) - P_{IF_0}(t_r), \\ \Delta L_{IF}(t_r) &= L_{IF}(t_r) - L_{IF_0}(t_r). \end{aligned} \quad (4.121)$$

In this research, erroneous code data is detected by absolute and relative limit checks. In a first run, measurements with residuals exceeding an absolute value are excluded. In a second run, the residuals of all measurements of each tracking pass are taken and their mean value $\bar{\Delta}P_{IF}$ and standard deviation $\sigma_{\Delta P_{IF}}$ is determined by

$$\bar{\Delta}P_{IF} = \frac{1}{n} \sum_{Pass} \Delta P_{IF}, \quad (4.122)$$

and

$$\sigma_{\Delta P_{IF}} = \sqrt{\frac{1}{n-1} \sum_{Pass} (\Delta P_{IF} - \bar{\Delta}P_{IF})^2}. \quad (4.123)$$

Here, the tracking pass comprises all pseudoranges that are obtained while the GPS satellite is in view. This tracking pass is not interrupted by data gaps of some epochs and is independent from phase-lock. It ranges from the ascension of a GPS satellite to its setting. The standard deviation of the involved residuals is required to fall below a user-defined threshold. If it exceeds the threshold, the measurement whose residual shows the largest deviation from the mean is excluded. This procedure is repeated until the standard deviation does not exceed the given threshold. This code data screening method quite effectively eliminates outliers, which are mainly caused by multipath effects. In order to achieve a statistical significance to some extent, only tracking passes with a minimum length of five minutes are accepted.

The data editing of the carrier phase measurements is achieved by a rather simple procedure. It is intended to search for outliers and also phase breaks. The detection of phase breaks is necessary for the correct introduction of the ambiguity parameters. Therefore, phase residuals of continuous tracking passes are investigated for sudden jumps. If the difference of consecutive phase residuals surpasses a certain limit L_ε , a phase break is assumed to be encountered,

$$|\Delta L_{IF}(t_{r-1}) - \Delta L_{IF}(t_r)| \begin{cases} < L_\varepsilon & \text{pass;} \\ > L_\varepsilon & \text{break.} \end{cases} \quad (4.124)$$

The threshold L_ε must be set very low to make sure that all jumps are detected. This is possible because of the low noise of the carrier phase measurements. In contrast to the code data screening, the carrier phase data screening accepts the residuals to exhibit a trend. This can occur, if in the iteration process the intermediate trajectory is not yet very accurate. Thus, statistical tests, like the standard deviation of the residuals, resembled not appropriate for the screening of carrier phase data.

In addition, a continuous tracking pass must consist of more than one phase measurement, because the ZD carrier phase measurements only imply relative information between consecutive epochs. Therefore, such single phase measurements have to be excluded. By this requirement, also outliers are widely removed. This is due to the fact, that, unless several consecutive measurements are affected by a constant systematic effect, a phase break is detected immediately before and afterwards, and thus isolating the observation.

And if a series of measurements is biased by a constant error, this is largely compensated by the pertaining ambiguity parameter.

After editing the data the measurements are introduced to the next iteration of the adjustment process. The whole data editing process has to be repeated prior to every iteration. Every time the whole data set has to be screened. Previously excluded measurements are possibly accepted in the next data screening run, where an updated trajectory is used. This holds for the code and carrier phase data screening as well as for the elevation cut-off. As the orbit solution becomes more and more accurate with each iteration, the thresholds can be set smaller for each screening run. This ensures, that for the final orbit solution the data editing is performed with the most possible sensibility, eliminating a maximum of outliers and detecting all phase-jumps. As already mentioned, even for the initial orbit determination a coarse data screening is performed, to keep the number of iterations low.

5 The Software *ORBIT*

In order to apply the previously elaborated techniques for precise orbit determination, a dedicated software has been developed for LEO POD. Subsequently, the structure and all relevant features of the software are explained.

To establish a software for dynamic and reduced-dynamic orbit determination, at first, the core feature of any orbit computing program, a propagator for a spacecraft within a force field, was implemented. The propagation is based on the numerical integration of the established force model. As an integrator the highly accurate collocation method has been implemented. It achieves the best possible numerical solution of the equations of motion. For all applications and results presented here, the order of integration is 12 and the step size for integration, i.e. the length of the polynomials, is 60 seconds. This holds for the solution of the trajectory and of all variational equations. The integration involves an inversion of a 15×15 matrix, which is achieved using either the Gauss-Jordan algorithm or the LU decomposition [Press *et al.*, 1989].

The dynamical force model is especially designed for LEOs, see section 4.2.1. The implemented forces are listed in Table 5.1. Each of the given perturbations can individually be switched off, so that its impact on the dynamical trajectory can be assessed.

Table 5.1: The dynamical model components employed
in the software *ORBIT* for LEOs

Perturbation	Model
Earth Gravity Field	Selectable model from ICGEM (degree/order selectable) [ICGEM, 2009]
Lunar Attraction	Analytical series expansion [Montenbruck and Gill, 2000]
Solar Attraction	Analytical series expansion [Montenbruck and Gill, 2000]
Solid Earth Tides	IERS Conventions 1996 [McCarthy, 1996]
Polar Tides	IERS Conventions 1996 [McCarthy, 1996]
General Relativity	IERS Conventions 2003 [McCarthy and Petit, 2004]
Atmospheric Drag	Canonball model in along-track direction (adjustable)
Radiation Pressure	Canonball model in direction towards the Sun (adjustable)

For the Earth gravity field several models, i.e. lists of geopotential coefficients, are available. The models are publicly available at the International Centre for Global Earth Models (ICGEM) [ICGEM, 2009] in a common data format [Barthelmes and Förste, 2006]. Thus, any of these models can be downloaded and readily be used for POD. The software allows for the truncation of the spherical harmonics expansion at a user-defined degree and order. By

truncating the expansion of the inhomogeneous Earth gravity field the influences of higher order terms on a satellite's orbit can be investigated. If the terms higher than a given degree and order are considered to be negligible, the truncation enables to save computation time significantly. Table 5.2 lists some notable models that can be obtained from the ICGEM.

Table 5.2: Selected gravity field models from the ICGEM

Gravity field model	Year	Degree	Reference
GGM03C	2009	360	[Tapley et al., 2007]
EIGEN-5C	2008	360	[Förste et al., 2008]
EGM2008	2008	2190	[Pavlis et al., 2008]
EIGEN-GL04C	2006	360	[Förste et al., 2006]
GGM02C	2004	200	[Tapley et al., 2005]
EIGEN-CHAMP03S	2004	140	[Reigber et al., 2004]
EIGEN-GRACE02S	2004	150	[Reigber et al., 2005]
GGM01S	2003	120	[Tapley et al., 2003]
EGM96	1996	360	[Lemoine et al., 1998]

In addition to the deterministic dynamical model, up to four constant forces (and, accordingly, accelerations) in designated directions can be estimated, see Table 5.3. These empirical forces are offered in the radial, along-track and cross-track directions and in the direction towards the Sun. The forces in along-track and Sun direction can be regarded as canonball models for atmospheric drag and radiation pressure. Nevertheless, these constant empirical forces are a first step towards reduced-dynamic orbit modeling.

However, for reduced-dynamic orbit determination the software offers two different types of pseudo-stochastic orbit models, see Table 5.3. The concepts of pseudo-stochastic pulses and piecewise constant accelerations are implemented. For both techniques the highly efficient algorithms, as outlined in sections 4.3.1 and 4.3.2, are implemented. The pulses and piecewise constant accelerations are set in the radial, along-track and cross-track directions. The number of empirical parameters, and thus the subinterval length, can be freely chosen. Individual a priori weighting of the three components is possible. The parameters are constrained to zero, which yields white noise characteristics for the parameter sequence. With these features the software is capable to execute the whole range from dynamic to highly reduced-dynamic orbit determination.

Table 5.3: The reduced-dynamical model options with the software *ORBIT*

Constant empirical forces (accelerations)	radial along-track cross-track Sun direction
Pseudo-Stochastic orbit models	Instantaneous velocity changes (pulses) Piecewise constant accelerations

The GPS measurements are introduced in the undifferenced mode. The underlying observational model is described in section 3.3. For the CHAMP and GRACE missions, the measurement data is publicly provided in the Receiver-Independent Exchange (RINEX) format [Gurtner, 1994]. It contains both the pseudorange and carrier phase measurements on the two frequencies, L1 and L2, as well as the respective SNR values. The software uses the data editing and screening procedures as outlined in section 4.5. All orbit determination approaches can be carried out using pseudorange and carrier phase data, or using pseudorange data only.

For the processing of the GPS data the required GPS ephemeris and clock data is obtained from various sources, as described in section 3.1.1. The GPS satellite orbits are given in the Standard Product 3 orbit format (SP3) [Remondi, 1991 and Hilla, 2007]. This data format also contains GPS clock offsets at the given epochs. If the clock offsets are required at a higher sample rate, separate data in the clock RINEX format can be introduced [Ray and Gurtner, 2006].

The least-squares adjustment is accomplished in the batch mode. This method was chosen because it delivers the most accurate estimation and is most robust. Thus, the computation of the orbits has to be accomplished ex post. Real-time applications are not of special interest for this research. However, the observations are processed sequentially and are directly mapped into the normal equation system. This is done still in accordance with the highly efficient methods of sections 4.3.1 and 4.3.2. By this means, the CPU memory is kept low and consequently very long arcs can be solved for. Additionally, the processing speed is significantly improved. For the inversion of the normal equation matrix, or its submatrices, the LU-decomposition algorithm has been implemented for fully populated matrices and for band matrices [Press *et al.*, 1989].

The produced orbit solutions can be evaluated with respect to external solutions. These orbit solutions are provided in various data formats. In the following, all comparisons will show the residuals split up in the components of the accompanying satellite system. The display of the residuals in this system is usually most conclusive. The residuals are always computed following the calculated minus external regime. This kind of validation assesses the quality of the absolute orbit position.

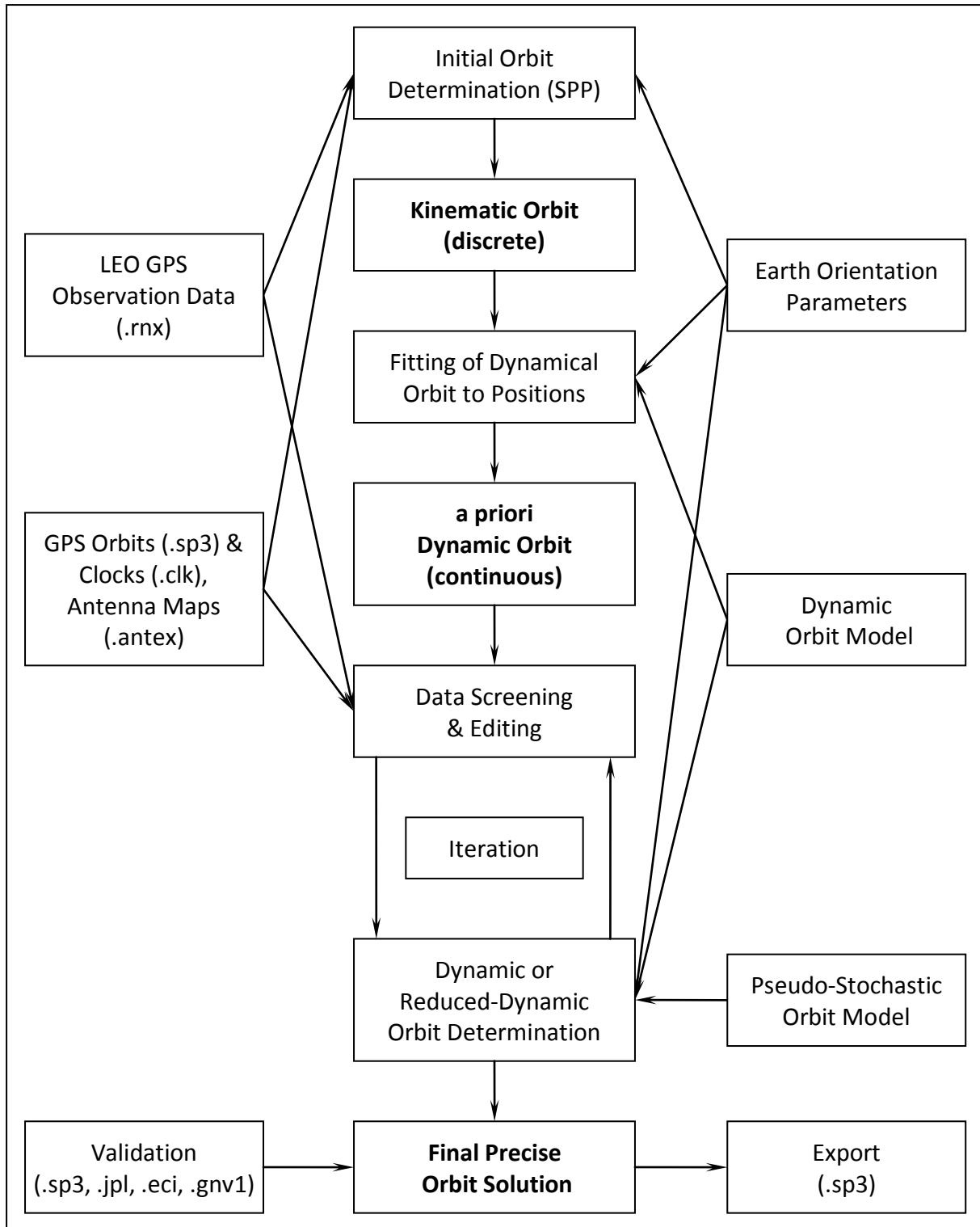


Figure 5.1: The processing scheme for LEO POD with the software *ORBIT*

In summary, the developed software is a comprehensive tool for state of the art precise orbit determination of LEO spacecraft. Figure 5.1 displays the whole processing scheme for LEO POD with the software *ORBIT*. An overview of the graphical interface and of the main functions of the software is given in Appendix A.4.

6 Results for CHAMP and GRACE POD

In this chapter the previously elaborated techniques for precise orbit determination are applied to the CHAMP and GRACE satellites. Furthermore, POD will be demonstrated using different settings for the orbit model, the input data and for data editing. The results will be evaluated with external precise orbit solutions.

6.1 CHAMP POD

In this chapter the achievable accuracy of the established precise orbit determination procedures will be assessed for the CHAMP satellite. This is accomplished by comparison with precise orbit solutions of other institutions. By this means, the applied POD strategies can be evaluated in comparison to other techniques. However, this may not be seen as a rigorous quality assessment, but rather as an exemplary demonstration of the applied POD capabilities. In addition, the impact of some features of the employed POD procedure will be investigated.

The GPS data for CHAMP is publicly available at the Global Environmental and Earth Science Information System (GENESIS) of the JPL [GENESIS, 2009] and at the Information System and Data Center (ISDC) of the GFZ Potsdam [ISDC, 2009]. The GPS measurements are provided in the RINEX format [Gurtner, 1994], with a sample rate of 10 seconds. In addition, these two institutions also provide orbit solutions.

In a first step, purely dynamic POD will be evaluated. As will be shown, dynamic LEO POD is only possible for comparatively short periods of about 1 hour to 90 minutes, which corresponds to not more than one revolution. For longer time intervals the deficiencies of the dynamic force model accumulate rapidly and force the solution to diverge heavily. Nevertheless, for short arcs dynamic POD may be an appealing alternative for applications where empirical parameters are not desirable. Figure 6.1 shows the residuals of a 90 minute orbital arc with respect to a solution of UPC [Ramos-Bosch, 2008b] on 11 July 2006. As for all subsequently presented examples the EIGEN-GL04C gravity field model [Förste *et al.*, 2006], up to degree and order 360, has been employed.

However, according to Figure 6.1, a purely dynamic model can very well serve for precise orbit determination. The residuals of the three components remain at the sub-dm level and the overall accuracy shows an RMS of 6 cm. Therefore, it can be concluded that dynamic LEO POD is in principle possible for periods of up to 90 minutes. For intervals of longer duration purely dynamic orbit determination proved not qualified for POD. However, it must be noted that orbit determination over short data arcs is highly prone to erroneous data or data gaps. The benefits of the averaging effect and the bridging of data gaps become effective only for much longer intervals. Thus, dynamic LEO POD has to be performed with caution.

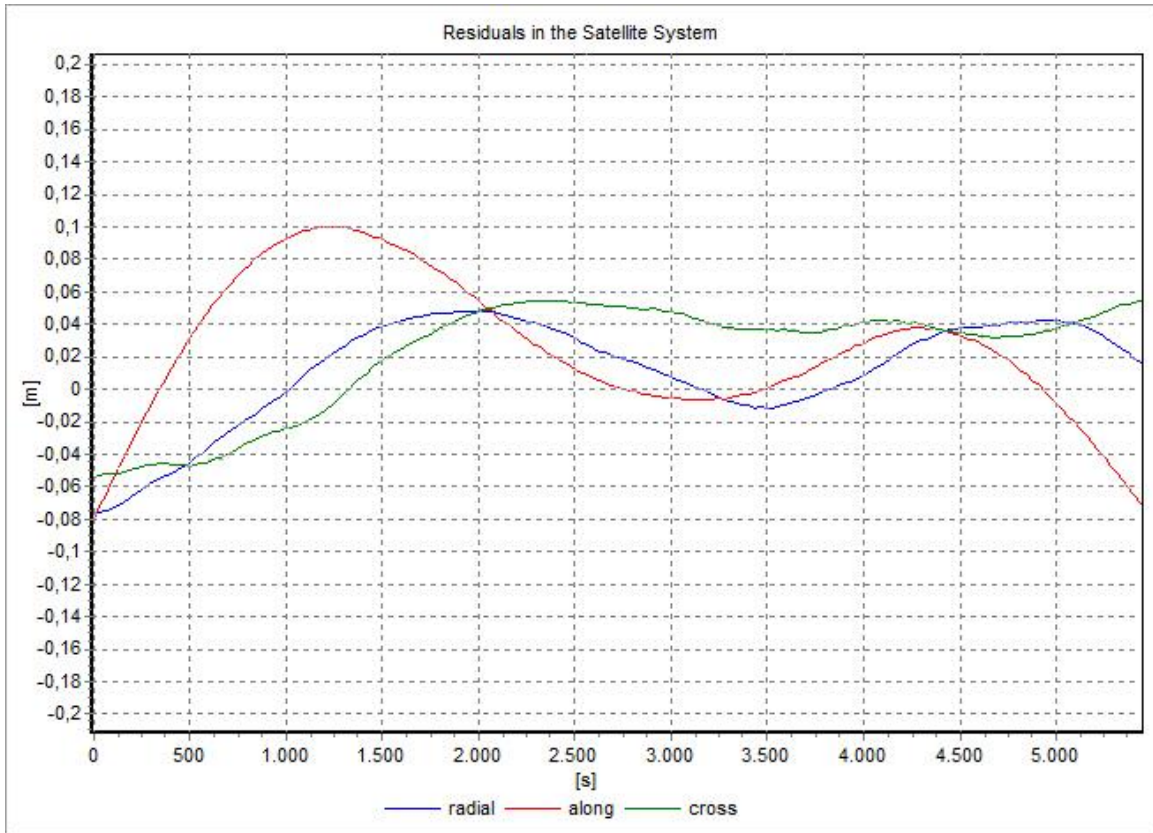


Figure 6.1: CHAMP dynamic orbit solution over 90 minutes (approx. one revolution)
w.r.t UPC (6 cm RMS); $t_0 = 10$ July 2006, 0:00:00

Although dynamic orbits do not fulfil the accuracy requirements for POD, they serve as a basis for reduced-dynamic orbits. Therefore, in order to generate a long orbit which incorporates pseudo-stochastic pulses or piecewise constant accelerations, a dynamic solution of good quality must be available. Figure 6.2 displays the residuals of the dynamic solution with respect to the precise orbit of UPC [Ramos-Bosch, 2008b] over 24 hours. The solution shows an overall deviation of the position of about 5.6 meters RMS. Thus, over long time intervals the dynamic orbit determination delivers a priori solutions of yet very high accuracy. Therefore, it can be concluded that modern dynamic force models for LEO satellites are already very advanced.

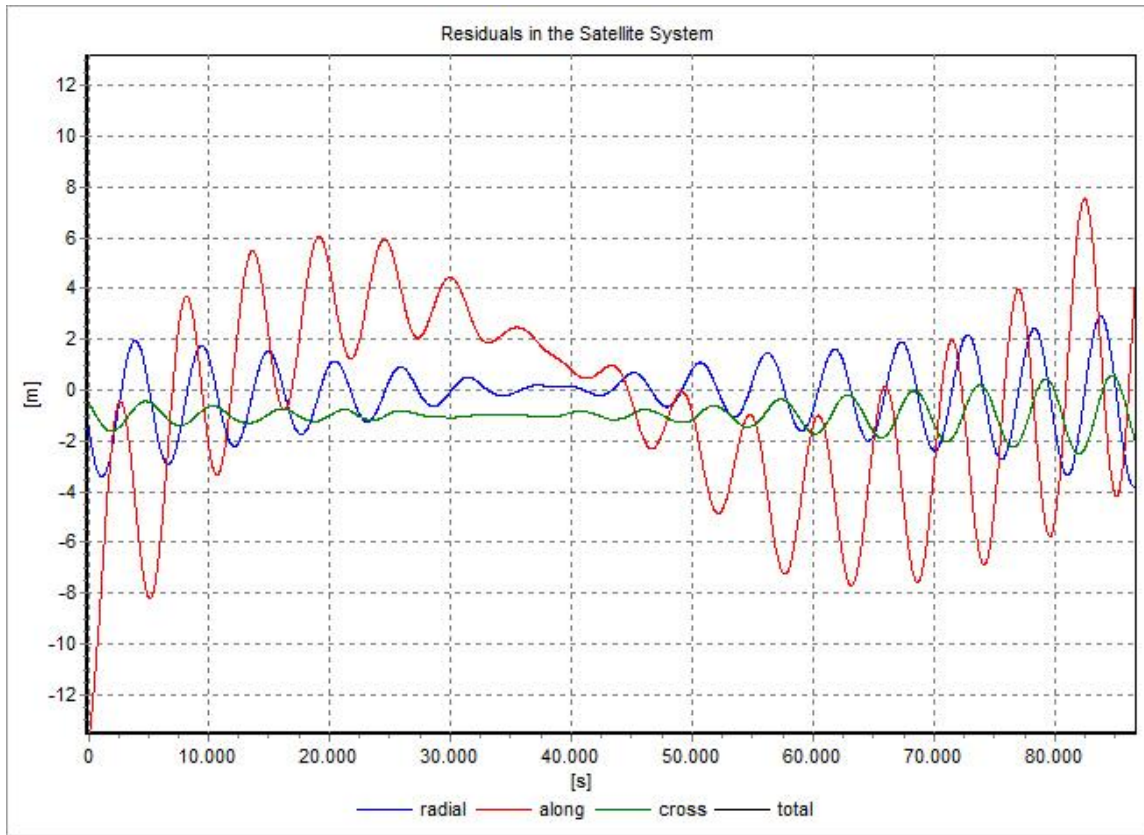


Figure 6.2: CHAMP dynamic orbit solution over 24 Hours w.r.t UPC (5.6 m RMS);
 $t_0 = 10$ July 2006, 0:00:00

In a next step, the quality of the developed reduced-dynamic POD techniques will be investigated. As a basis the more refined method of piecewise constant accelerations is applied. The parametrization, weighting settings and the employed GPS data products are summarized in Table 6.1. The displayed settings have been found to deliver the most accurate results.

Table 6.1: Parametrization, weighting settings and data products for CHAMP POD

Standard Deviation of the Observations		
σ_P	[m]	± 0.50
σ_L	[m]	± 0.03
Data Screening and Editing		
$\sigma_{\Delta P_{IF}}$	[m]	± 0.70
L_ε	[m]	0.03
Elevation cutt-off angle	[°]	5
Data Products		
Ephemeris data		CODE 15 min [CODE, 2009a]
Clock data		CODE High-rate 30 s [CODE, 2009b]
Piecewise constant Accelerations		
Spacing	[s]	300
$\sigma_{a_{Along}}$	[nm/s ²]	± 200
$\sigma_{a_{Radial}}$	[nm/s ²]	± 50
$\sigma_{a_{Cross}}$	[nm/s ²]	± 100

Figure 6.3 and Figure 6.4 show the residuals of a 24 hour arc (10 July 2006) with respect to orbit solutions of the UPC [Ramos-Bosch, 2008b] and JPL [GENESIS, 2009], respectively. Over this period the CHAMP satellite performs approximately 16 revolutions around the Earth. The applied batch orbit estimation is very well suited for overcoming data gaps. However, if these data outages occur at, or close to, the boundaries the bridging might not be optimal. Therefore, in order to generate an orbit solution over a certain period, the orbit is actually calculated over a longer time interval exceeding the desired period. An additional processing of 3 hours at the beginning and end of the period has been found adequate. Thus, to obtain a 24 hour orbit solution the data of 30 hours must be processed. This procedure was performed with the presented orbit solutions.

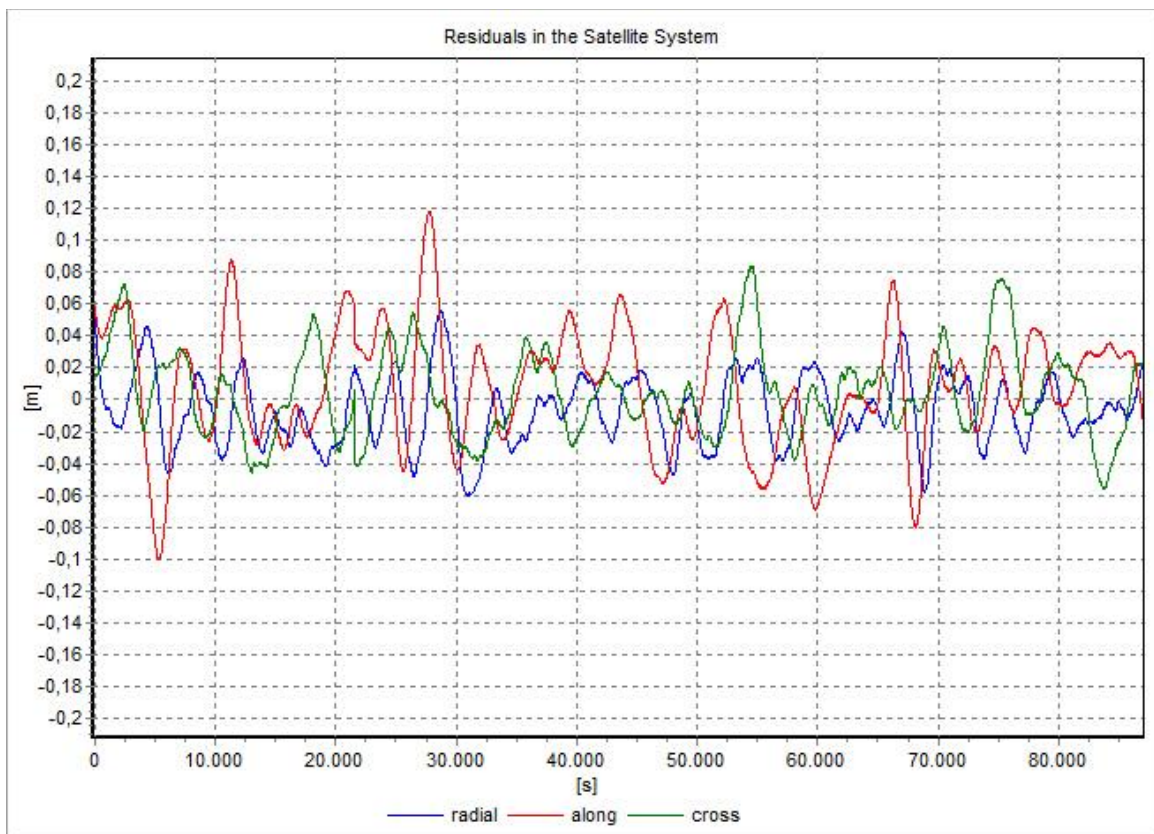


Figure 6.3: CHAMP reduced-dynamic orbit solution with piecewise constant accelerations over 24 hours w.r.t UPC (5 cm RMS);
 $t_0 = 10$ July 2006, 0:00:00

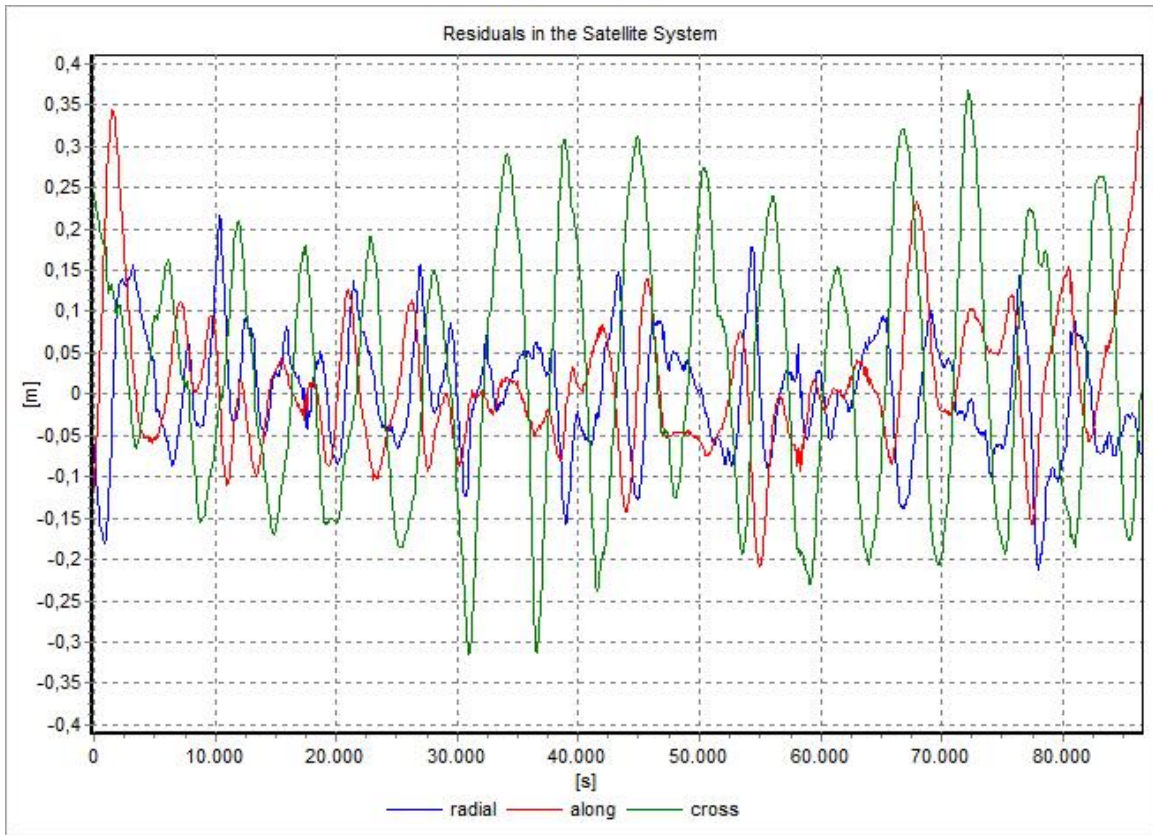


Figure 6.4: CHAMP reduced-dynamic orbit solution with piecewise constant accelerations over 24 hours w.r.t JPL (18 cm RMS);
 $t_0 = 10$ July 2006, 0:00:00

For the concerned orbit over 30 hours a total of 1080 accelerations (360 triples) were introduced and 834 ambiguity parameters had been set up. The GPS data rate of 10 seconds requires the solution of 10800 epoch-wise receiver clock offsets. Together with 9 dynamical parameters an overall number of 12723 unknown parameters were to be solved for. The number of accepted code and phase observations amounted to 44637.

As can be seen in Figure 6.3 and Figure 6.4, the attained orbit solution shows a varying agreement with the two external solutions. While the RMS of the total displacement amounts to just 5 cm with respect to the solution of the UPC, it reaches to 18 cm compared to the JPL orbit. The comparatively weak accordance with the latter solution may be attributed to the fact that the published JPL solutions are not of the utmost accuracy [GENESIS, 2009].

Additionally, CHAMP POD solutions have been compared to precise solutions of the Technical University of Munich (TUM) [Švehla, 2004]. Figure 6.5 shows the comparison of an 24 h orbit on 31 August 2003 with an agreements of 7.5 cm RMS. Thus, it can be concluded, that the applied POD strategy delivers fairly competitive results.

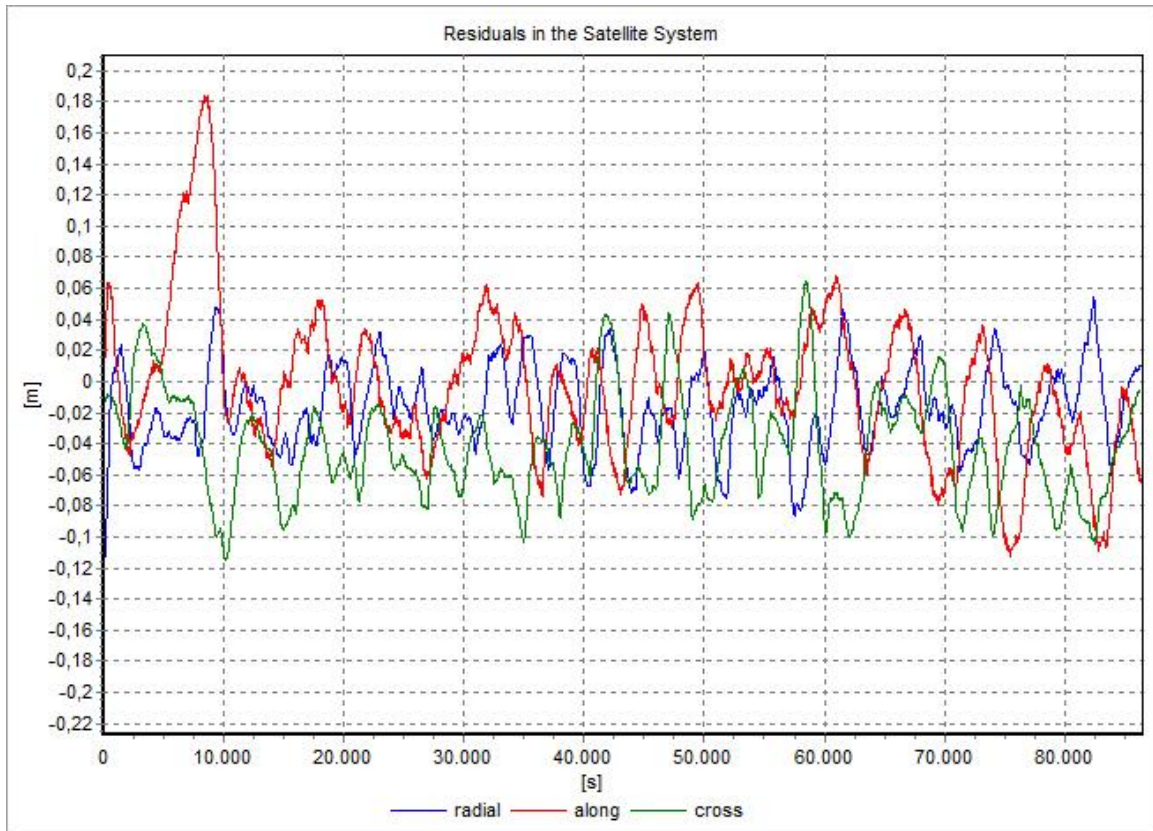


Figure 6.5: CHAMP reduced-dynamic orbit solution with piecewise constant accelerations over 24 hours w.r.t TUM (7.5 cm RMS);
 $t_0 = 31$ August 2003, 0:00:00

The setting of pseudo-stochastic parameters, i.e. their temporal spacing and weighting, is quite critical. It determines the character of the reduced-dynamic solution. Putting weaker constraints on the along-track component of the empirical accelerations has been found appropriate, see Table 6.1. In order to assess the difference between the different kinds of pseudo-stochastic parameters, the trajectory was fitted to the same measurements but employing pulses. The pulses were set up with the same spacing and a corresponding weighting. Figure 6.6 shows the residuals of the orbit using pulses with respect to the solution with piecewise constant accelerations.

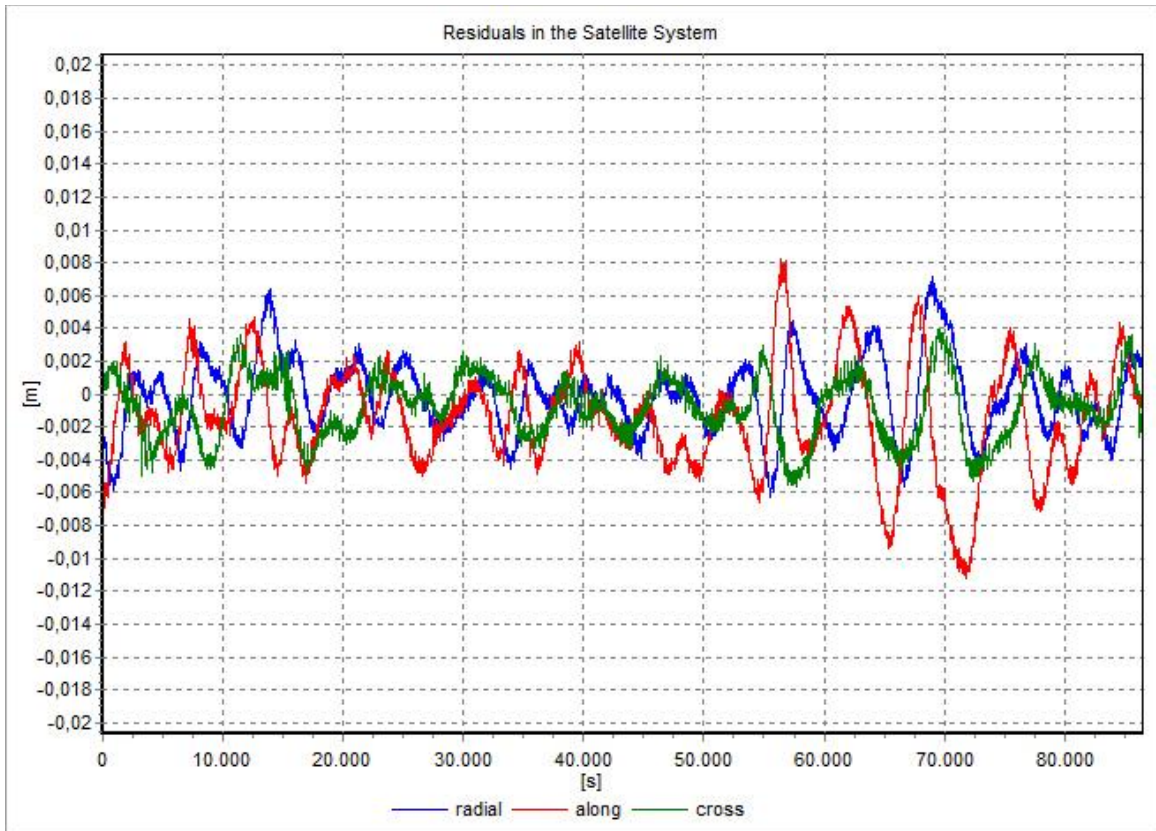


Figure 6.6: CHAMP reduced-dynamic Orbit Solution with instantaneous velocity changes w.r.t solution with piecewise constant accelerations
(2 mm RMS); $t_0 = 10$ July 2006, 0:00:00

The difference in position of only 2 mm RMS of these two types of empirical modeling is very small. Thus, the two methods yield similar orbit accuracies and are both appropriate for precise LEO orbit determination. In both cases the selection of the employed gravity field model is of minor relevance. For most POD applications the series expansion up to degree and order 100 is sufficient. The truncation of higher order terms is easily compensated by the empirical parameters, and thus only marginally affects the positioning of the spacecraft. Figure 6.7 and Figure 6.8 display the estimated pseudo-stochastic parameters.

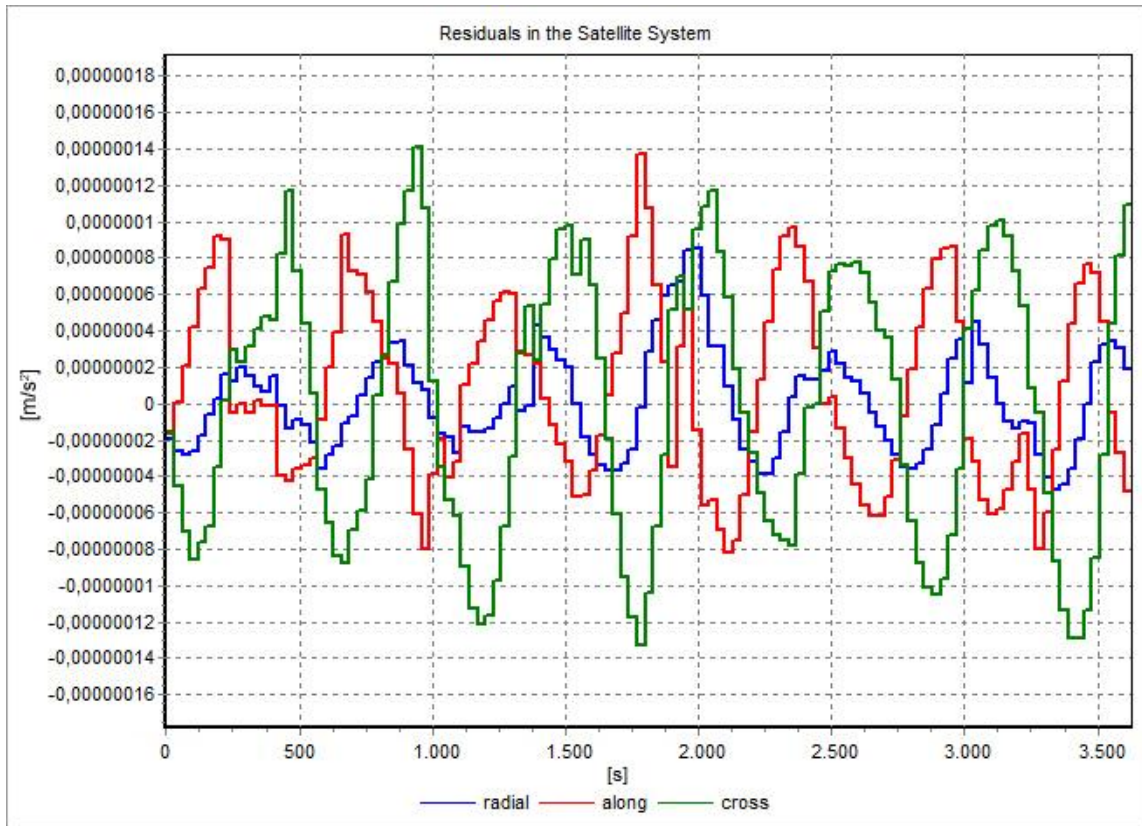


Figure 6.7: The estimated piecewise constant accelerations;
 $t_0 = 10$ July 2006, 0:00:00

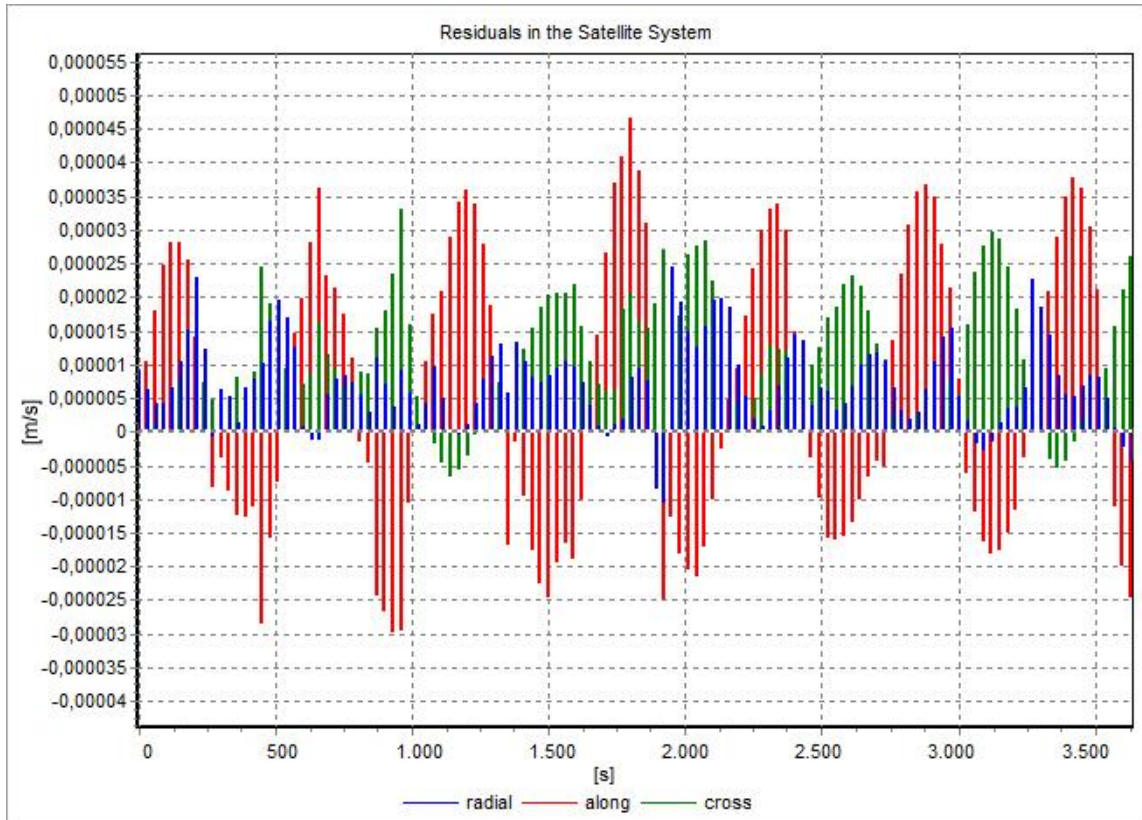


Figure 6.8: The estimated instantaneous velocity changes;
 $t_0 = 10$ July 2006, 0:00:00

For all LEO POD strategies using zero difference GPS observations the use of high-rate GPS clock products is of strong importance. Figure 6.9 demonstrates the difference between the solutions using high-rate (30 seconds) GPS clocks [CODE, 2009b] and GPS clock data with a lower (5 minutes) rate [IGSCB, 2008]. Here, the along-track component is most affected. Thus, the use of high-rate GPS orbit and clock data products is advisable for LEO POD.

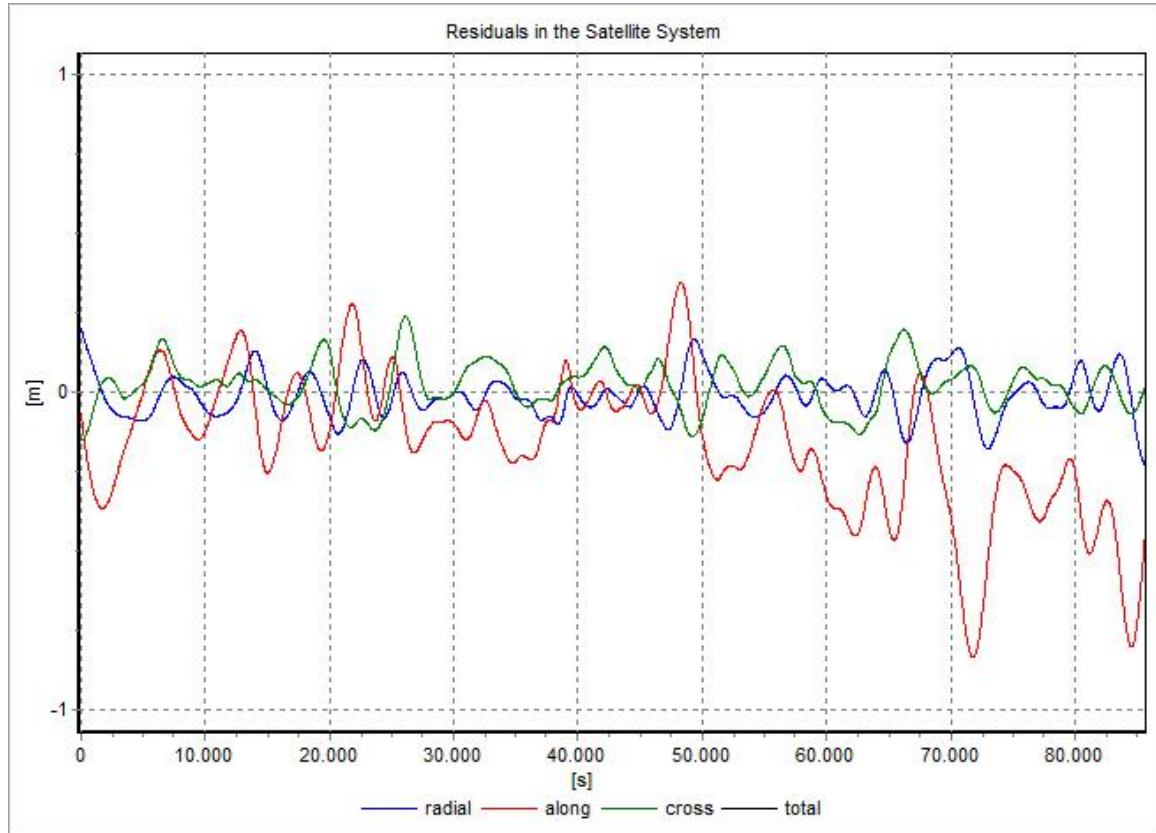


Figure 6.9: The impact of different GPS clock offset data (25 cm RMS);
 $t_0 = 10$ July 2006, 0:00:00

On the other hand, a rather small degradation of the orbit accuracy is encountered by processing the GPS observations at a sample rate of only 30s. The resulting difference is shown in Figure 6.10. Again, the along-track component exhibits the biggest deviation. However, by processing only every third observation epoch the number of observations as well as receiver clock offsets is drastically reduced. Thus, the computation times for data screening and editing and orbit estimation are accordingly much shorter. While an iteration run for a 30h orbit takes typically 15 minutes for processing GPS observations at a 10s sample rate, the calculation is performed in about 5min when using 30s GPS observations. The data screening procedure takes about a third of the computation times. Usually, POD is achieved after 3-4 iteration runs. Therefore, incorporating the GPS measurements at a 30s sample rate may be attractive for many POD applications, yielding considerably faster computation times with only a slight loss of accuracy.

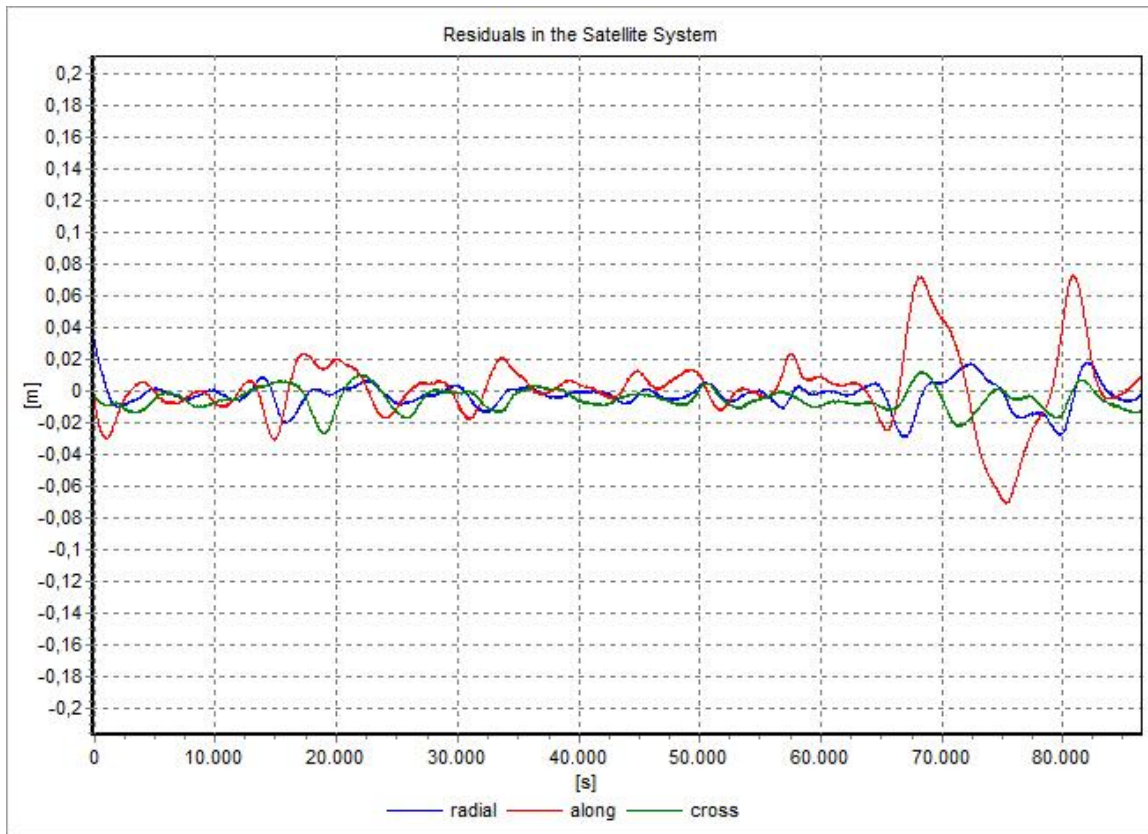


Figure 6.10: The impact of different GPS observation sampling rates (2 cm RMS);
 $t_0 = 10$ July 2006, 0:00:00

In order to demonstrate the influence of the GPS carrier phase measurements, the trajectory has been determined using code data only. Figure 6.11 shows the difference of the orbits using code and phase data and using code data only. By not incorporating the information of the phase measurements the accuracy of the solution was considerably degraded and shows a deviation of 23 cm RMS. However, the computation time is reduced significantly due to the fact that no ambiguity biases are estimated and only about the half of the measurements have to be processed.

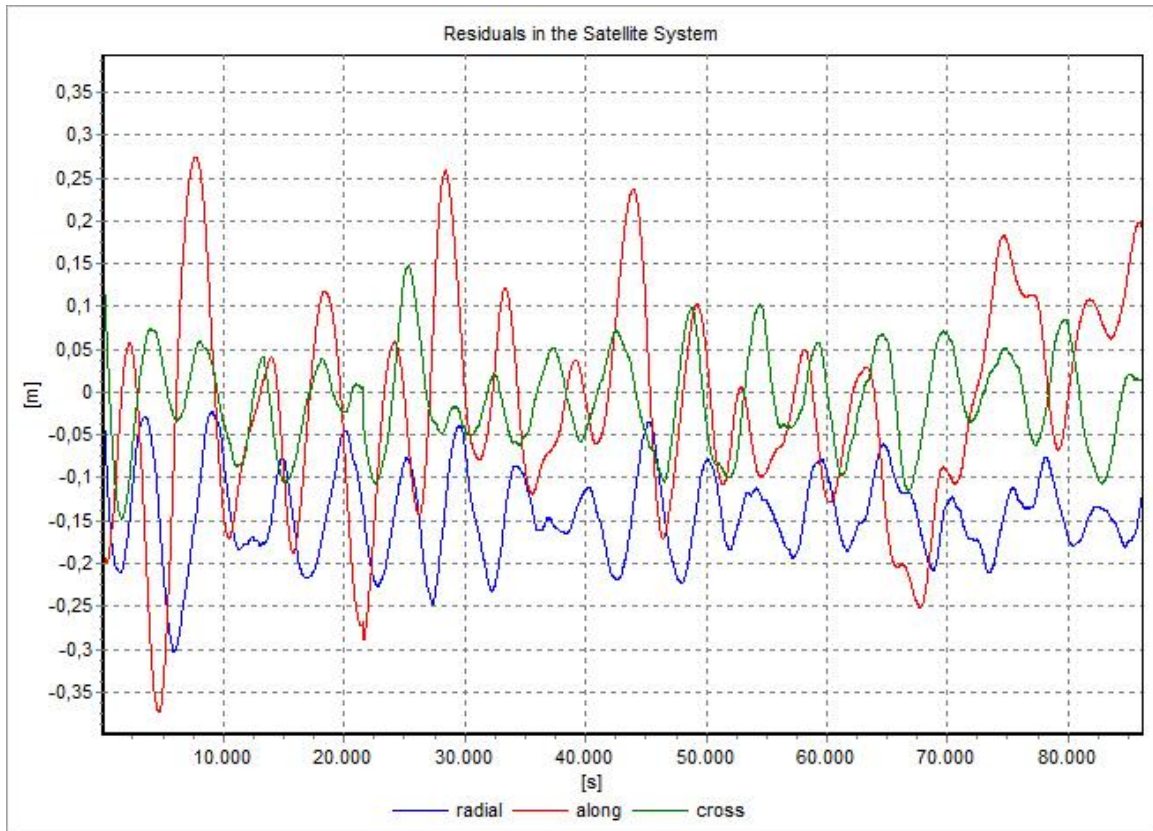


Figure 6.11: Orbit difference between using code plus phase data w.r.t. using code data only (23 cm RMS); $t_0 = 10$ July 2006, 0:00:00

6.2 GRACE POD

In this chapter, the accuracy of single spacecraft POD will be assessed for the GRACE satellites in a similar way as for CHAMP. The GPS data for the GRACE satellites is freely available from the Information System and Data Center (ISDC) of the GFZ Potsdam [ISDC, 2009] and from the Physical Oceanography Distributed Active Archive Center (PODAAC) of the JPL [PODAAC, 2009]. The code and carrier phase measurements are available in the RINEX format [Gurtner, 1994], with a 10 seconds spacing. In addition, precise orbit solutions, generated by the JPL, can be obtained from the two institutions.

As already noted, purely dynamic POD for LEOs with sufficient accuracy is solely possible for periods up to 90 minutes. Figure 6.12 displays a dynamic orbit over 90 minutes for GRACE A on 4 January 2006 with respect to the JPL solution. The achieved solution shows deviations of up to 11 cm compared to the reference.

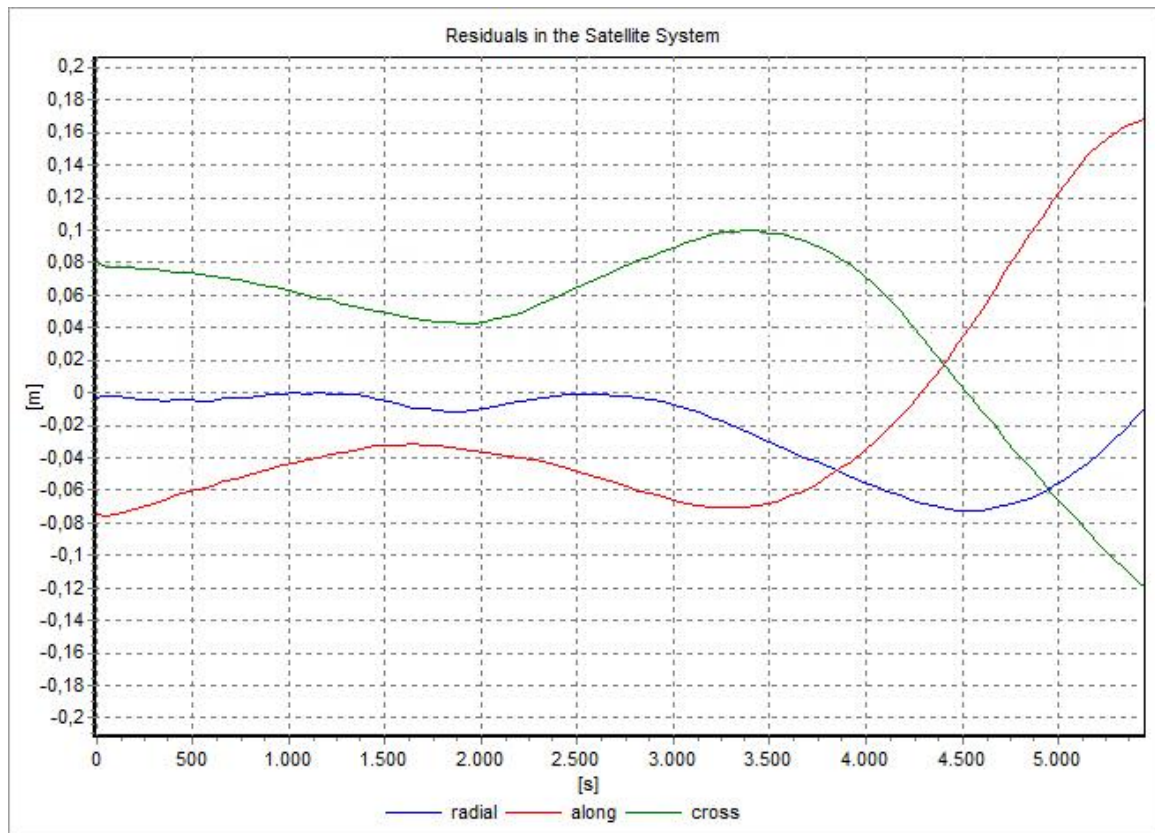


Figure 6.12: GRACE A dynamic orbit solution over 90 minutes (approx. one revolution) w.r.t JPL (11 cm RMS); $t_0 = 4$ January 2006, 0:00:00

The capabilities of reduced-dynamic POD for GRACE will be demonstrated using piecewise constant accelerations. The features, e.g. weighting settings and data screening, of the applied POD technique differ slightly from those for CHAMP and are outlined in Table 6.2.

Table 6.2: Parametrization, weighting settings and data products for GRACE POD

Standard Deviation of the Observations		
σ_P	[m]	± 0.40
σ_L	[m]	± 0.02
Data Screening and Editing		
$\sigma_{\Delta P_{IF}}$	[m]	± 0.40
L_ε	[m]	0.02
Elevation cutt-off angle	[°]	5
Data Products		
Ephemeris data		CODE 15 min [CODE, 2009a]
Clock data		CODE High-rate 30 s [CODE, 2009b]
Piecewise constant Accelerations		
Spacing	[s]	300
$\sigma_{a_{Along}}$	[nm/s ²]	± 100
$\sigma_{a_{Radial}}$	[nm/s ²]	± 25
$\sigma_{a_{Cross}}$	[nm/s ²]	± 50

As specified in Table 6.2, the slightly better performance of the of the GRACE GPS receivers is accounted for in the smaller observation standard deviations and also in the more rigorous settings for data screening.

Figure 6.13 displays the residuals of a 24 hour orbit (4 January 2006) of GRACE A with respect to an orbit solution generated by the JPL. Again, the orbit was actually calculated over a 30 hour period and subsequently truncated to 24 hours. The introduction of empirical accelerations at a 5 minute spacing results in a total of 1080 accelerations. For the respective time interval 693 ambiguity parameters were introduced. Although the data screening was set more rigorous as for CHAMP, the number of ambiguity parameters is usually much less. This can be attributed to the better tracking performance of the receiver. In addition, the number of accepted measurements of 75519 is much higher than for CHAMP. This is mainly due to considerably less multipath effects because of the less complex structure of the GRACE spacecraft [Kroes, 2006].

The RMS of the total position difference with respect to the JPL solution amounts to 4.5 cm, whereas in the radial component the RMS is even at the 2 cm level.

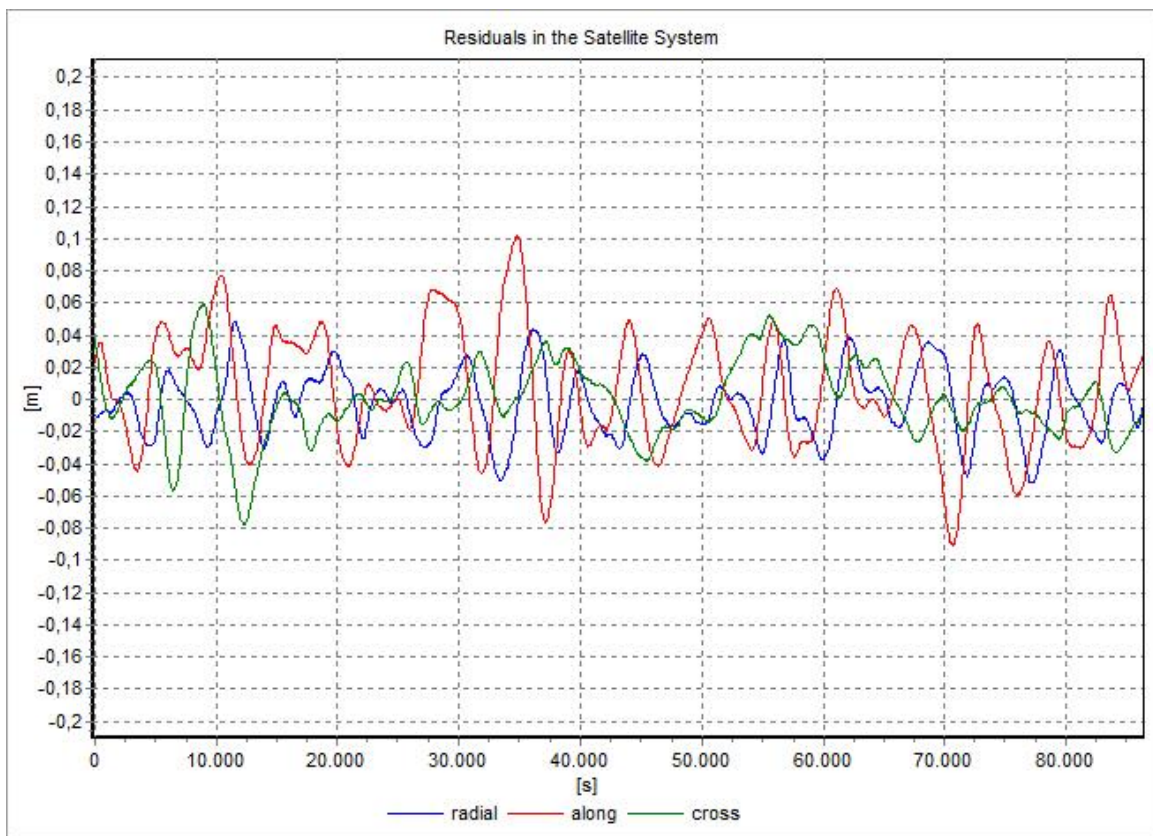


Figure 6.13: GRACE A reduced-dynamic orbit solution with piecewise constant accelerations over 24 hours w.r.t JPL (4.5 cm RMS);
 $t_0 = 4$ January 2006, 0:00:00

Additionally, Figure 6.14 shows the same orbit compared to the solution of the UPC. The attained RMS also amounts to 4.5 cm. In general, for GRACE A the agreement of the position of the generated orbit solution is about the same with respect to the references of the JPL and UPC. The general accuracy of UPC orbits with respect to JPL solutions is reported to be 4 to 5 cm for GRACE A [Ramos-Bosch, 2008b]. Thus, the quality of the generated orbits is quite comparable to these external solutions.

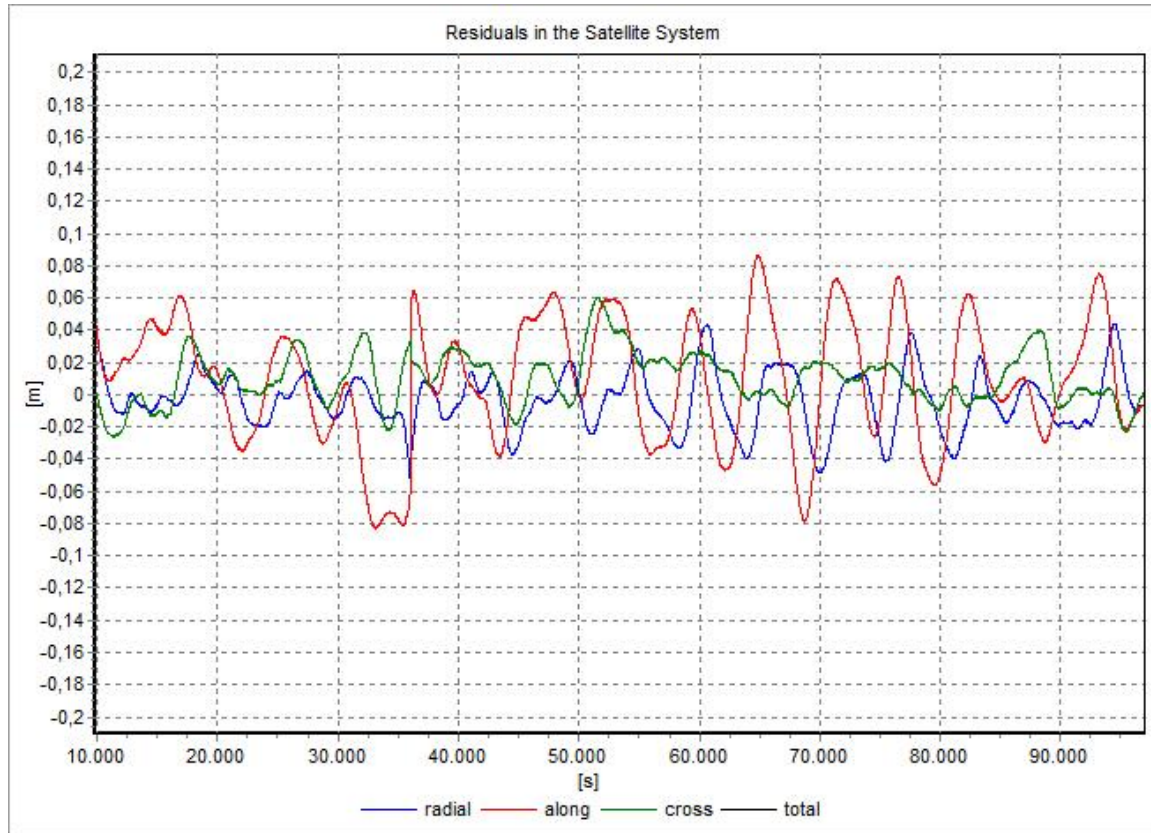


Figure 6.14: GRACE A reduced-dynamic orbit solution with piecewise constant accelerations over 24 hours w.r.t UPC (4.5 cm RMS);
 $t_0 = 4$ January 2006, 0:00:00

The agreement of the solution for GRACE B compared to the JPL orbit is slightly worse for the considered period. Figure 6.15 shows a deviation of 5.5 cm RMS. No orbit solutions of GRACE B from the UPC were available for this period.

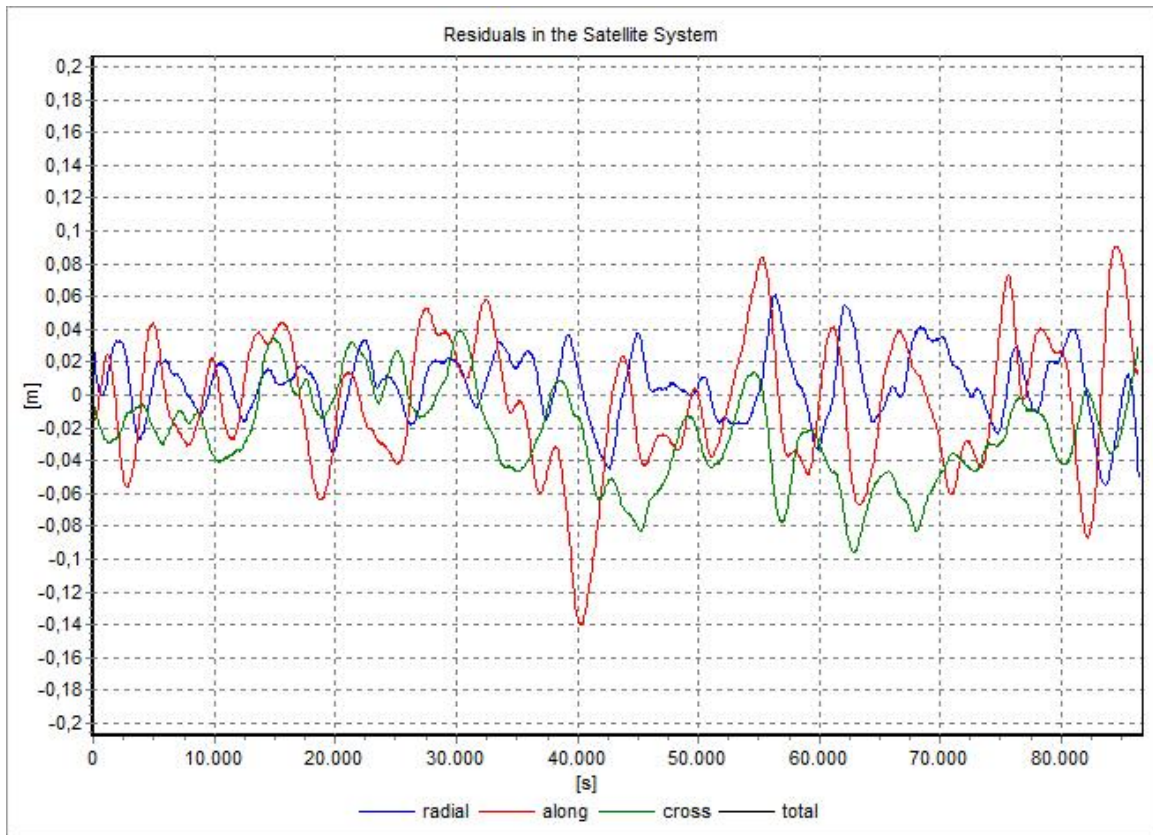


Figure 6.15: GRACE B reduced-dynamic orbit solution with piecewise constant accelerations over 24 hours w.r.t JPL (5.5 cm RMS);
 $t_0 = 4$ January 2006, 0:00:00

Finally, the impact of the number of introduced empirical parameters is assessed. Figure 6.16 displays the difference between a solution using piecewise constant accelerations over 100 seconds with respect to a solution with the accelerations over 300 seconds. Both solutions are adjusted to the same set of observations. The difference of the highly reduced-dynamic orbit solution with respect to the reduced-dynamic solution amounts to 2 cm RMS.

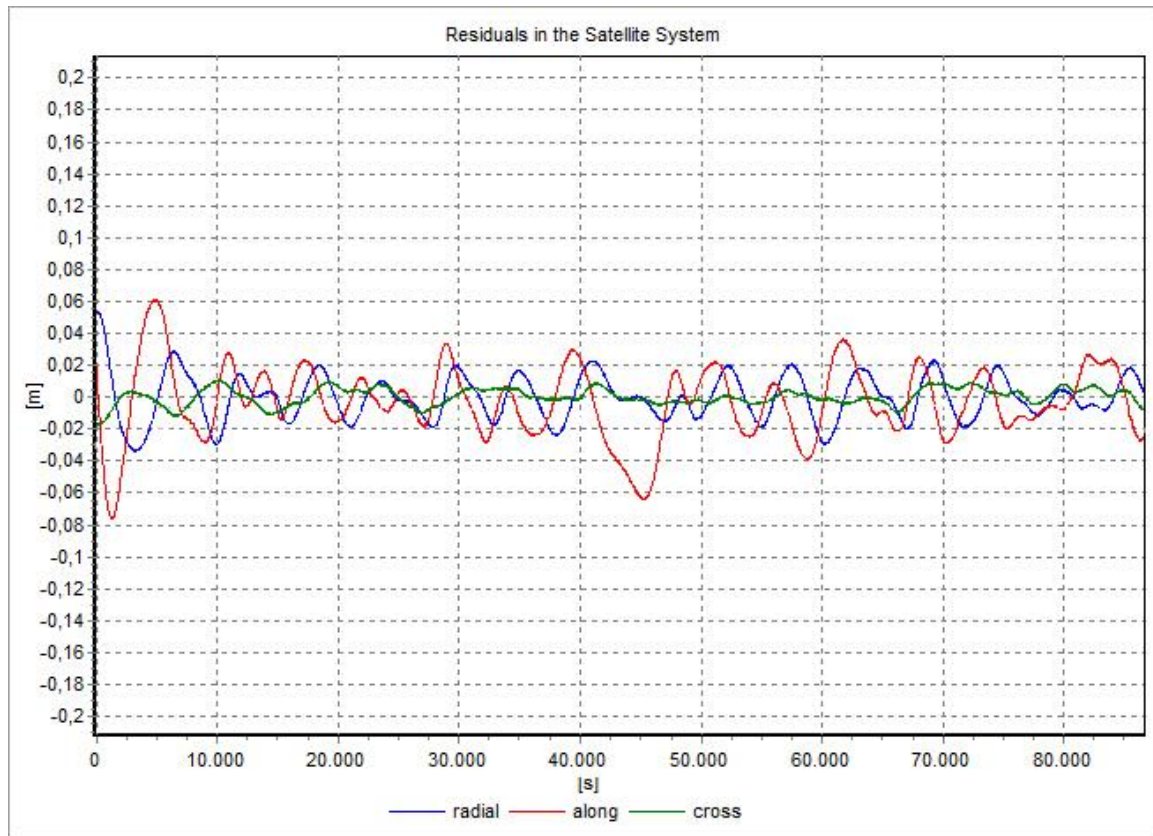


Figure 6.16: The residuals of an orbit solution employing piecewise constant accelerations over 100 seconds with respect to the solution with accelerations over 300 seconds (2.0 cm RMS);
 $t_0 = 4$ January 2006, 0:00:00

The presented results clearly demonstrate that the established strategies are highly qualified for precise LEO orbit determination. Compared to external solutions, position accuracies of about 10 cm RMS and below are attained with all employed techniques. For all tested LEO spacecraft, purely dynamic precise orbit determination could be carried out successfully. However, dynamic POD solutions are limited to orbital lengths of about 90 minutes and care must be taken concerning data reliability. The employment of instantaneous velocity changes or piecewise constant accelerations for reduced-dynamic orbit determination proved highly applicable for LEO POD. The introduction of empirical parameters enables the generation of POD solutions of extremely good quality over much longer time intervals. Orbital arcs of 30 hours or more can be processed without any difficulty, attaining accuracies of up to 5 cm RMS. Thus, the established reduced-dynamic strategies are extremely well suited for LEO POD. In addition, the impact of key features of the POD process has been assessed. As has been demonstrated, if not the most stringent orbit accuracy is required, the orbit solutions can be generated even much faster by introducing the GPS measurements at a lower sampling rate or by using low rate GPS ephemeris and clock data or by using GPS code data only.

7 Conclusion and Outlook

The objective of this work was to establish, implement, test and validate methods for precise orbit determination of satellites in low Earth orbits using GPS. For this purpose a complete standalone software had to be created that generates orbits of LEO satellites. The applied strategies should be efficient, robust, fast and flexible. It was intended to reach an accuracy with respect to solutions of other well-established methods at the sub-dm level. Based on the results that were presented in the previous chapters, all these aims have been achieved. Tested for CHAMP and GRACE, the applied POD strategies attain accuracies well below the dm level compared to external orbit solutions.

The chosen concepts of dynamic and reduced-dynamic orbit determination proved highly adequate for the use of GPS for navigation. The combination of advanced models of spacecraft dynamics and the precision of GPS measurements provides a powerful synergy. The introduction of GPS data in the ionosphere free linear combination at the zero difference level requires a minimum of external data. ZD measurements are very accurate and can be implemented quite simply.

As has been demonstrated, the use of a purely dynamic orbit model is in principle capable for LEO POD. The accuracy of most components of the dynamic force field, especially of recently developed Earth gravity field models [ICGEM, 2009], is very well advanced. However, due to insufficient knowledge of some remaining perturbations, essentially the atmospheric drag, dynamic POD is limited to comparatively short orbital lengths. Orbital arcs over 90 minutes have been found to be the maximum possible length for dynamic POD. Both for CHAMP and GRACE, orbits of 90 minutes can be determined with an accuracy of one decimeter or less with respect to external solutions, see sections 6.1 and 6.2. However, due to this limitation the process of orbit determination becomes severely susceptible to erroneous data or data gaps. Thus, purely dynamic precise orbit determination is possible but not very robust. Adequate quality control of the generated dynamic orbit solutions, e.g. by validation with reduced-dynamic orbits over much longer time intervals, is therefore highly advisable.

The deficiencies of dynamic POD have been successfully overcome by the two presented methods of reduced-dynamic orbit determination. The additional introduction of empirical parameters allows for a simultaneous exploitation of the advantages of the elaborate dynamics and the precision of the GPS measurements. With an optimal number and weighting of the pseudo-stochastic parameters the reduced-dynamic POD methods achieve position agreements of up to 4.5 cm RMS compared to external precise solutions, see sections 6.1 and 6.2. The difference between the two employed techniques of instantaneous velocity changes (pulses) and piecewise constant accelerations is of only very little relevance (2 mm RMS).

The presented algorithms for POD using pulses or piecewise constant accelerations proved to be extremely efficient and yield considerably reduced calculation times and memory requirements. In addition, the widely similar structure of the respective algorithms allows for a rather convenient implementation of both techniques into a computer program. Although the more realistic model of piecewise constant accelerations will be the first choice for most POD applications, the comparison to the pulse model is of scientific interest and useful for quality control. In summary, the presented state-of-the-art techniques for reduced-dynamic POD are highly competitive against other well-established POD strategies. The attained orbit solutions can be used for almost all applications related to POD.

Furthermore, with the highly flexible software the impact of several key features of the POD process has been assessed. It could be shown that the sampling rate of the GPS data (30 s with respect to 10 s) is of only minor importance for the attained orbit accuracies. Here, a further reduction in computation time can be gained. On the other hand, by ignoring the phase measurements and using code data only, the resulting orbit accuracy is severely degraded. A similar loss of accuracy is encountered by employing GPS clock products with a low sampling rate. Nevertheless, for space applications which do not demand the most stringent accuracy but require extremely fast calculation times these strategies might be appealing.

Finally, it has been observed that appropriate GPS data screening and editing is of crucial importance for LEO POD. The established techniques, along with optimal values for the respective thresholds and limits, provide an effective, robust and reliable tool for data screening and editing. Usually, POD is achieved after 3 to 4 iteration runs.

It can be concluded from the results, that the envisaged aim, to establish competitive routines for LEO POD and implement them in a software, has been achieved. However, the accuracy of the orbit solutions can still be further improved. Especially for CHAMP, GRACE and GOCE various additional data is available which would be worthwhile to be introduced. This comprises the data of the attitude sensors, the measurements of the accelerometers and information about thruster firings. Although the concerned satellites are very closely kept to their nominal attitude, the center of mass correction can be performed more accurately and robustly with precise attitude information. The incorporation of accelerometer data might be useful in many ways. The accelerations are measured in the radial, along-track and cross-track components. Thus, these directions very much coincide with the directions of the estimated piecewise constant accelerations. The validation of the estimated with the measured accelerations would yield highly valuable information about the applied parameter constraints. By this means, the necessary amount of empirical parameters and optimal weighting settings can be assessed. Moreover, the accelerometer data can be employed as additionally observational data to further strengthen the orbit accuracy, especially its shape.

The above presented recommendations especially apply for geodetic missions like CHAMP, GRACE and GOCE which carry the according sensor types onboard. However, a large number of spacecraft are equipped with laser retro-reflectors for Satellite Laser Ranging (SLR). Highly accurate ranges between ground stations and the spacecraft are deduced from the two-way travelling time of laser pulses. Again, these measurements may be used for an independent validation of the orbits and as additional measurements.

Regarding the input information, i.e. the force models and the GPS ephemeris and clock data, more or less the most advanced models and data have been employed in this work. However, a refinement of the dynamic model, especially of the atmosphere, would be very much appreciated for LEO POD. Accordingly, advanced spacecraft specific models of the air drag, as well as of the solar radiation pressure, would be very beneficial. On the other hand, the availability of GPS ephemeris and clock data of an ever increasing precision at higher sampling rates is expectable [Bock *et al.*, 2009 and Griffiths and Ray, 2008]. High-rate GPS clock products with a sampling rate of up to 1 Hz would be strongly desirable for precise orbit determination of the GOCE satellite, because the GPS receiver of GOCE collects the data at a sample rate of 1 Hz [Bock *et al.*, 2007].

The established software *ORBIT* provides a profound basis for many kinds of POD and POD related applications. It can be modified very flexibly and its design is suitable for the implementation of various other spaceborne GPS applications.

A very ambitious challenge resides in the precise relative positioning of formation flying spacecraft. The fundamental task is the determination of the relative state between two, or more, spacecraft within a formation. Most prominently, this involves the determination of the baseline between the two satellites of the GRACE mission. Instead of the orbit of a single LEO spacecraft, a baseline in space has to be estimated. In this case, the GPS observations need to be introduced in the doubly differenced mode to accurately resolve the ambiguities. The modeling of the variations of the baseline could be performed using pseudo-stochastic parameters in a similar way as for single LEO POD [Kroes, 2006]. Precise relative spacecraft positioning is a key technology with increasing importance. Some existing space missions, such as GRACE or TerraSAR-X and TanDEM-X [Montenbruck *et al.*, 2007], and many planned or proposed upcoming missions, especially in geodesy [Wiese *et al.*, 2009], require extremely accurate knowledge of the relative position and velocity of the involved satellites.

Eventually, the POD capabilities of the developed software may be extended to POD of GNSS satellites. Here, the measurements of a GPS or another GNSS satellite are attached to a global network of ground stations to estimate the trajectory of the satellite. The involvement of ground stations requires to also account for tropospheric effects. In addition, an adapted force model and procedures for data screening are necessary. However, the main difference between LEO POD and GNSS POD lies in the fact that instead of the motion of a receiver the motion of an emitter has to be estimated. In the case of an emitter, measurements are not made at coincident epochs. Therefore, the estimation of the clock offset of the GNSS satellite has to be treated slightly different.

In summary, the developed methods are highly capable for the precise orbit determination of satellites in a low Earth orbit. The established software is a comprehensive and powerful tool for this application. However, it provides a perfect basis for further space applications and research.

Appendix

A.1 The Light Time Equation

For processing the GPS observation equations as described in section 3.2, the exact emission time and the position and clock offset of the GPS satellite at this epoch is required for all measurements. For any given reception time t_r with the corresponding receiver position $\mathbf{x}_r(t_r)$ and a given trajectory $\mathbf{x}_s(t)$ of the respective GPS satellite, the signal travelling time $\tau(t_r)$, and thus the emission time t_e , are fully determined by assuming the signal travelling with the speed of light c . The emission epoch is thus a function of the (a priori) receiver position and clock offset. The light time equation can be solved iteratively because both the receiver and the GPS satellite are moving much slower than the speed of light. Within the iteration the emission time is always updated with the newly evaluated distance ρ between the receiver and GPS satellite, given by

$$\begin{aligned} t_s^0 &:= t_r \\ t_e^1 &:= t_r - \frac{\rho(t_r, t_e^0)}{c} \\ t_e^1 &:= t_r - \frac{\rho(t_r, t_e^1)}{c} \\ &\vdots \end{aligned} \tag{A.1}$$

with

$$\rho(t_r, t_e^i) = \|\mathbf{x}_r(t_r) - \mathbf{x}_s(t_e^i)\|. \tag{A.2}$$

After sufficient convergence has been reached, the iteration yields the emission time t_e and the signal travelling time $\tau(t_r) = t_r - t_e$. The position and clock offset of the GPS satellite have to be evaluated for t_e , yielding $\mathbf{x}_s(t_e)$ and $\delta s(t_e)$ respectively.

For the solution of the light time equation the signal velocity is throughout assumed to be the speed of light in vacuum. As described in sections 3.2.1 and 3.2.2, this is not precisely the case for GPS observations, due to several delays caused by, e.g., the atmosphere or relativity. However, these delays in time only result in a sub-mm position difference for the GPS satellites, and thus can be neglected. The same holds for the center of mass corrections of the GPS satellite and of the LEO satellite.

A.2 Keplerian Ephemeris Calculation

In the presence of a pointlike mass the orbit of a satellite (of negligible mass) follows an ellipse and can be conveniently described by the Keplerian, or classical, elements [Vallado, 2007]. The six elements are the semimajor axis a , the eccentricity e , the inclination i , the right ascension of the ascending node Ω , the argument of perigee ω and the true anomaly ν , see Figure A.1. Additionally, the time of perifocal passage is denoted as T .

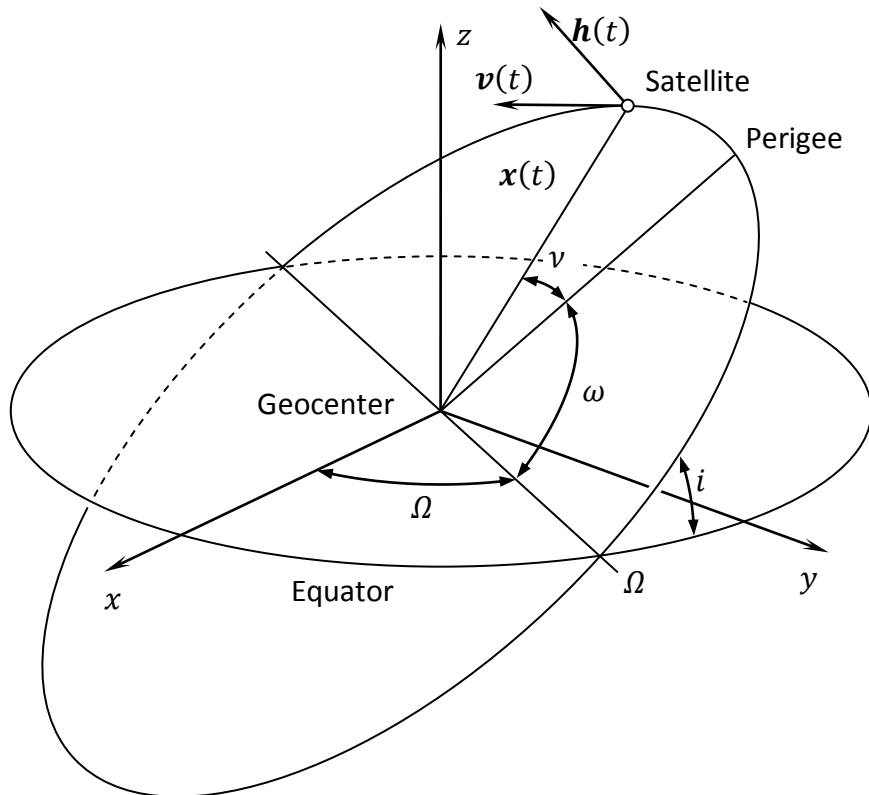


Figure A.1: The Keplerian (or classical) elements

In the following the calculation of the Keplerian elements from the position and velocity of a satellite at a particular epoch and vice versa is given [Battin, 1999].

A.2.1 Keplerian Elements from the Position and Velocity Vectors

Given the position \mathbf{x} and the velocity \mathbf{v} of a spacecraft at epoch t , the orbital plane is assessed by its normal vector \mathbf{h} , given by

$$\mathbf{h} = \mathbf{x} \times \mathbf{v}. \quad (\text{A.3})$$

The vector \mathbf{h} is also defined by the right ascension of the ascending node Ω and the inclination i ,

$$\mathbf{h} = \begin{pmatrix} h_1 \\ h_2 \\ h_3 \end{pmatrix} = h \cdot \begin{pmatrix} \sin i \cdot \sin \Omega \\ -\sin i \cdot \cos \Omega \\ \cos i \end{pmatrix}. \quad (\text{A.4})$$

Therefore, accounting for the quadrant rule, the elements Ω and i can be calculated by

$$\tan \Omega = \frac{h_1}{-h_2}, \quad (\text{A.5})$$

and

$$\tan i = \frac{\sqrt{h_1^2 + h_2^2}}{h_3}. \quad (\text{A.6})$$

To assess the shape and orientation of the ellipse in the orbital plane, the polar equation of the ellipse

$$r = \frac{p}{1 + e \cdot \cos \nu}, \quad (\text{A.7})$$

with the parameter p

$$p = \frac{h^2}{GM_E}, \quad (\text{A.8})$$

has to be rearranged yielding the parameter e_{cv}

$$e_{cv} \doteq e \cdot \cos \nu = \frac{p}{r} - 1. \quad (\text{A.9})$$

Additionally, the equation for the parameter e_{sv} is given by

$$e_{sv} \doteq e \cdot \sin \nu = \sqrt{\frac{p}{GM_E}} \cdot \frac{1}{r} \cdot (\mathbf{x} \cdot \mathbf{v}). \quad (\text{A.10})$$

Now the eccentricity e , the true anomaly ν and the semimajor axis a can be obtained by

$$\begin{aligned} e &= \sqrt{e_{sv}^2 + e_{cv}^2}, \\ \nu &= \tan^{-1} \left(\frac{e_{sv}}{e_{cv}} \right), \\ a &= \frac{p}{1 - e^2}. \end{aligned} \quad (\text{A.11})$$

In a coordinate system that lies in the orbital plane and whose x-axis is pointed towards the ascending node Ω , the position $\mathbf{x}_{\text{Plane}}$ of the satellite is given by the transformation

$$\mathbf{x}_{Plane} = R_1(i) \cdot R_3(\Omega) \cdot \mathbf{x}. \quad (\text{A.12})$$

Expressing this vector in polar coordinates,

$$\mathbf{x}_{Plane} = \begin{pmatrix} x_{P,1} \\ x_{P,2} \\ x_{P,3} \end{pmatrix} = r \cdot \begin{pmatrix} \cos u \\ \sin u \\ 0 \end{pmatrix}, \quad (\text{A.13})$$

yields the polar angle u , which is the sum of the true anomaly v and the argument of perigee ω . Thus, ω is obtained by

$$\omega = u - v, \quad (\text{A.14})$$

where

$$u = \tan^{-1} \left(\frac{x_{P,2}}{x_{P,1}} \right). \quad (\text{A.15})$$

Finally, the time of perifocal passage T is calculated by

$$T = t - \frac{E - e \cdot \sin E}{\sqrt{\frac{GM_E}{a^3}}}, \quad (\text{A.16})$$

where the eccentric anomaly E is given by

$$E = 2 \cdot \tan^{-1} \left(\sqrt{\frac{1-e}{1+e}} \cdot \tan \frac{v}{2} \right). \quad (\text{A.17})$$

A.2.2 Position and Velocity Vectors from the Keplerian Elements

The inverse problem of the Keplerian ephemeris calculation is to find the position and velocity vectors at any epoch t from given Keplerian elements and time of perifocal passage T . Therefore, at first the mean angular motion n has to be calculated by

$$n = \sqrt{\frac{GM_E}{a^3}}. \quad (\text{A.18})$$

The mean anomaly M is defined by

$$M = n \cdot (t - T). \quad (\text{A.19})$$

M is related to the eccentric anomaly E in Kepler's equation, which is given by

$$E - e \cdot \sin E = M . \quad (\text{A.20})$$

Equation (A.20) has to be solved iteratively for E . Now the true anomaly ν and the radial distance r follows as

$$\nu = 2 \cdot \tan^{-1} \left(\sqrt{\frac{1+e}{1-e}} \cdot \tan \frac{E}{2} \right), \quad (\text{A.21})$$

and

$$r = a \cdot (1 - e \cdot \cos E) . \quad (\text{A.22})$$

The quadrant of ν has to be determined from the relations

$$\sin \nu = \frac{a \cdot \sin E \cdot \sqrt{1 - e^2}}{r}, \quad (\text{A.23})$$

and

$$\cos \nu = \frac{a \cdot (\cos E - e)}{r} . \quad (\text{A.24})$$

The position vector of the satellite in the orbital plane can now be calculated from the polar coordinates as

$$\mathbf{x}_{\text{Plane}} = \begin{pmatrix} r \cdot \cos \nu \\ r \cdot \sin \nu \\ 0 \end{pmatrix}. \quad (\text{A.25})$$

The time derivation of the position vector yields the velocity vector, given by

$$\mathbf{v}_{\text{Plane}} = \sqrt{\frac{GM_E}{a \cdot (1 - e^2)}} \cdot \begin{pmatrix} -\sin \nu \\ e + \cos \nu \\ 0 \end{pmatrix}. \quad (\text{A.26})$$

Finally, the two vectors have to be transformed into the inertial coordinate system by

$$\begin{aligned} \mathbf{x} &= R_3(-\Omega) \cdot R_1(-i) \cdot R_3(-\omega) \cdot \mathbf{x}_{\text{Plane}}, \\ \mathbf{v} &= R_3(-\Omega) \cdot R_1(-i) \cdot R_3(-\omega) \cdot \mathbf{v}_{\text{Plane}}. \end{aligned} \quad (\text{A.27})$$

A.3 The partial Derivatives of the dynamic Force Model

The differential equation system (4.38) describing the orbital motion of a spacecraft is a non-linear differential equation system of second order. For its solution with the collocation method a linearized differential equation system must be available. For the linearization the partial derivatives of all force model components with respect to the coordinates of the position x and velocity \dot{x} have to be formed. This also holds for the establishment of the variational equations where the same partial derivatives with respect to the position and velocity but also with respect to dynamical parameters are required. In this section the relevant partial derivatives of the presented force model components with respect to x and \dot{x} , where

$$\boldsymbol{x} = \begin{pmatrix} x \\ y \\ z \end{pmatrix}, \quad (\text{A.28})$$

and

$$\dot{\boldsymbol{x}} = \begin{pmatrix} \dot{x} \\ \dot{y} \\ \dot{z} \end{pmatrix}, \quad (\text{A.29})$$

are given.

Central-Body Term

The most important gravity field component is the central-body term described by (4.35). Its partial derivatives with respect to the position coordinates are given by

$$\begin{aligned} \frac{\partial \ddot{x}}{\partial x} &= -\frac{GM}{r^3} \left(1 - 3 \frac{x^2}{r^2} \right), & \frac{\partial \ddot{x}}{\partial y} &= 3 \frac{GM}{r^5} xy, & \frac{\partial \ddot{x}}{\partial z} &= 3 \frac{GM}{r^5} xz, \\ \frac{\partial \ddot{y}}{\partial x} &= 3 \frac{GM}{r^5} xy, & \frac{\partial \ddot{y}}{\partial y} &= -\frac{GM}{r^3} \left(1 - 3 \frac{y^2}{r^2} \right), & \frac{\partial \ddot{y}}{\partial z} &= 3 \frac{GM}{r^5} yz, \\ \frac{\partial \ddot{z}}{\partial x} &= 3 \frac{GM}{r^5} xz, & \frac{\partial \ddot{z}}{\partial y} &= 3 \frac{GM}{r^5} yz, & \frac{\partial \ddot{z}}{\partial z} &= -\frac{GM}{r^3} \left(1 - 3 \frac{z^2}{r^2} \right). \end{aligned} \quad (\text{A.30})$$

The partial derivatives of the central-body term with respect to the velocity components are zero because the attraction is independent from the motion of the spacecraft. This is the case for all gravitational forces.

The inhomogeneous Earth Gravity Field

According to (4.44), the partial derivatives of the perturbation acceleration of the inhomogeneous gravity field are formed by

$$\frac{\partial \ddot{\mathbf{x}}_{T_e}}{\partial \mathbf{x}_{e,k}} = \frac{\partial}{\partial \mathbf{x}_{e,k}} (D \cdot \nabla_{sphere} T) = \frac{\partial D}{\partial \mathbf{x}_{e,k}} \cdot \nabla_{sphere} T + D \cdot \frac{\partial}{\partial \mathbf{x}_{e,k}} (\nabla_{sphere} T); \quad k = 1, 2, 3 \quad (A.31)$$

with

$$\frac{\partial D}{\partial \mathbf{x}_{e,k}} = \begin{pmatrix} \frac{\partial^2 r}{\partial x_e \partial \mathbf{x}_{e,k}} & \frac{\partial^2 \theta}{\partial x_e \partial \mathbf{x}_{e,k}} & \frac{\partial^2 \lambda}{\partial x_e \partial \mathbf{x}_{e,k}} \\ \frac{\partial^2 r}{\partial y_e \partial \mathbf{x}_{e,k}} & \frac{\partial^2 \theta}{\partial y_e \partial \mathbf{x}_{e,k}} & \frac{\partial^2 \lambda}{\partial y_e \partial \mathbf{x}_{e,k}} \\ \frac{\partial^2 r}{\partial z_e \partial \mathbf{x}_{e,k}} & \frac{\partial^2 \theta}{\partial z_e \partial \mathbf{x}_{e,k}} & \frac{\partial^2 \lambda}{\partial z_e \partial \mathbf{x}_{e,k}} \end{pmatrix}. \quad (A.32)$$

The three matrices $\partial D / \partial \mathbf{x}_{e,k}$ contain the second derivatives of the spherical coordinates with respect to the cartesian coordinates.

Arranged as column vectors, the three terms $\partial(\nabla_{sphere} T) / \partial \mathbf{x}_{e,k}$ can be obtained simultaneously by

$$\left(\frac{\partial}{\partial x_e} (\nabla_{sphere} T) \quad \frac{\partial}{\partial y_e} (\nabla_{sphere} T) \quad \frac{\partial}{\partial z_e} (\nabla_{sphere} T) \right) = \nabla_{sphere} (\nabla_{sphere} T) \cdot D^T \quad (A.33)$$

where

$$\nabla_{sphere} (\nabla_{sphere} T) = \begin{pmatrix} \frac{\partial^2 T}{\partial r^2} & \frac{\partial^2 T}{\partial r \partial \theta} & \frac{\partial^2 T}{\partial r \partial \lambda} \\ \frac{\partial^2 T}{\partial r \partial \theta} & \frac{\partial^2 T}{\partial \theta^2} & \frac{\partial^2 T}{\partial \theta \partial \lambda} \\ \frac{\partial^2 T}{\partial r \partial \lambda} & \frac{\partial^2 T}{\partial \theta \partial \lambda} & \frac{\partial^2 T}{\partial \lambda^2} \end{pmatrix}. \quad (A.34)$$

The matrix contains the second partial derivatives of T with respect to the spherical coordinates which are given by

$$\begin{aligned} \frac{\partial^2 T}{\partial r^2} &= \frac{\mu}{r} \sum_{n=2}^{n_{max}} (n+1)(n+2) \frac{a^n}{r^{n+2}} \sum_{m=0}^n (C_{nm} \cos m\lambda + S_{nm} \sin m\lambda) \cdot P_{nm}(\cos \theta), \\ \frac{\partial^2 T}{\partial \theta^2} &= \frac{\mu}{r} \sum_{n=2}^{n_{max}} \left(\frac{a}{r}\right)^n \sum_{m=0}^n (C_{nm} \cos m\lambda + S_{nm} \sin m\lambda) \cdot \frac{\partial^2 P_{nm}(\cos \theta)}{\partial \theta^2}, \\ \frac{\partial^2 T}{\partial \lambda^2} &= \frac{\mu}{r} \sum_{n=2}^{n_{max}} \left(\frac{a}{r}\right)^n \sum_{m=0}^n m^2 \cdot (-C_{nm} \cos m\lambda - S_{nm} \sin m\lambda) \cdot P_{nm}(\cos \theta), \end{aligned} \quad (A.35)$$

$$\begin{aligned}\frac{\partial^2 T}{\partial r \partial \theta} &= \frac{\mu}{r} \sum_{n=2}^{n_{max}} -(n+1) \frac{a^n}{r^{n+1}} \sum_{m=0}^n (C_{nm} \cos m\lambda + S_{nm} \sin m\lambda) \cdot \frac{\partial P_{nm}(\cos \theta)}{\partial \theta}, \\ \frac{\partial^2 T}{\partial r \partial \lambda} &= \frac{\mu}{r} \sum_{n=2}^{n_{max}} -(n+1) \frac{a^n}{r^{n+1}} \sum_{m=0}^n m \cdot (-C_{nm} \cos m\lambda - S_{nm} \sin m\lambda) \cdot P_{nm}(\cos \theta), \\ \frac{\partial^2 T}{\partial \theta \partial \lambda} &= \frac{\mu}{r} \sum_{n=2}^{n_{max}} \left(\frac{a}{r}\right)^n \sum_{m=0}^n m \cdot (-C_{nm} \cos m\lambda + S_{nm} \sin m\lambda) \cdot \frac{\partial P_{nm}(\cos \theta)}{\partial \theta}.\end{aligned}$$

The derivation of the associated Legendre polynomials and their first and second derivatives can be found in *Swatschka* [2004] and *Hofmann-Wellenhof and Moritz* [2006].

Finally, the partial derivatives of the perturbation acceleration has to be transformed into the inertial reference system according to (4.25) by

$$\mathbf{J}_{ICRF} = \mathbf{U}^T(t) \cdot \mathbf{J}_{ITRF} \cdot \mathbf{U}(t) , \quad (\text{A.36})$$

where

$$\mathbf{J}_{ITRF} = \begin{pmatrix} \frac{\partial \ddot{\mathbf{x}}_{T_e}}{\partial x_e} & \frac{\partial \ddot{\mathbf{x}}_{T_e}}{\partial y_e} & \frac{\partial \ddot{\mathbf{x}}_{T_e}}{\partial z_e} \end{pmatrix} , \quad (\text{A.37})$$

and

$$\mathbf{J}_{ICRF} = \begin{pmatrix} \frac{\partial \ddot{\mathbf{x}}_{T_i}}{\partial x_i} & \frac{\partial \ddot{\mathbf{x}}_{T_i}}{\partial y_i} & \frac{\partial \ddot{\mathbf{x}}_{T_i}}{\partial z_i} \end{pmatrix} . \quad (\text{A.38})$$

Third-Body Perturbations

The partial derivatives of the third-body perturbations (4.47) are given by

$$\begin{aligned}\frac{\partial \ddot{\mathbf{x}}_c}{\partial x} &= -GM_c \cdot \left(\frac{1}{|\mathbf{x}_c - \mathbf{x}|^3} \cdot \begin{pmatrix} 1 \\ 0 \\ 0 \end{pmatrix} - 3 \frac{x_c - x}{|\mathbf{x}_c - \mathbf{x}|^5} \cdot (\mathbf{x}_c - \mathbf{x}) \right) , \\ \frac{\partial \ddot{\mathbf{x}}_c}{\partial y} &= -GM_c \cdot \left(\frac{1}{|\mathbf{x}_c - \mathbf{x}|^3} \cdot \begin{pmatrix} 0 \\ 1 \\ 0 \end{pmatrix} - 3 \frac{y_c - y}{|\mathbf{x}_c - \mathbf{x}|^5} \cdot (\mathbf{x}_c - \mathbf{x}) \right) , \\ \frac{\partial \ddot{\mathbf{x}}_c}{\partial z} &= -GM_c \cdot \left(\frac{1}{|\mathbf{x}_c - \mathbf{x}|^3} \cdot \begin{pmatrix} 0 \\ 0 \\ 1 \end{pmatrix} - 3 \frac{z_c - z}{|\mathbf{x}_c - \mathbf{x}|^5} \cdot (\mathbf{x}_c - \mathbf{x}) \right) .\end{aligned} \quad (\text{A.39})$$

Solid Earth tides

The partial derivatives of the perturbation (4.48) of the mean part of the solid Earth tides is given by

$$\frac{\partial \ddot{\mathbf{x}}_{ST,C}}{\partial x} = -\frac{5x}{|\mathbf{x}|^2} \cdot \ddot{\mathbf{x}}_{ST,C} + \frac{k_2}{2} \cdot \frac{GM_C}{|\mathbf{x}_C|^3} \cdot \frac{a^5}{|\mathbf{x}|^5} \cdot \left\{ \left(3 - 15 \frac{(\mathbf{x} \cdot \mathbf{x}_C)^2}{|\mathbf{x}|^2 \cdot |\mathbf{x}_C|^2} \right) \cdot \begin{pmatrix} 1 \\ 0 \\ 0 \end{pmatrix} - 30 \frac{(\mathbf{x} \cdot \mathbf{x}_C)(x_C - (\mathbf{x} \cdot \mathbf{x}_C) \cdot x)}{|\mathbf{x}|^4 \cdot |\mathbf{x}_C|^4} \cdot \mathbf{x} + 6 \frac{x_C}{|\mathbf{x}_C|^2} \cdot \mathbf{x}_C \right\}, \quad (\text{A.40})$$

$$\frac{\partial \ddot{\mathbf{x}}_{ST,C}}{\partial y} = -\frac{5y}{|\mathbf{x}|^2} \cdot \ddot{\mathbf{x}}_{ST,C} + \frac{k_2}{2} \cdot \frac{GM_C}{|\mathbf{x}_C|^3} \cdot \frac{a^5}{|\mathbf{x}|^5} \cdot \left\{ \left(3 - 15 \frac{(\mathbf{x} \cdot \mathbf{x}_C)^2}{|\mathbf{x}|^2 \cdot |\mathbf{x}_C|^2} \right) \cdot \begin{pmatrix} 0 \\ 1 \\ 0 \end{pmatrix} - 30 \frac{(\mathbf{x} \cdot \mathbf{x}_C)(y_C - (\mathbf{x} \cdot \mathbf{x}_C) \cdot y)}{|\mathbf{x}|^4 \cdot |\mathbf{x}_C|^4} \cdot \mathbf{x} + 6 \frac{y_C}{|\mathbf{x}_C|^2} \cdot \mathbf{x}_C \right\},$$

$$\frac{\partial \ddot{\mathbf{x}}_{ST,C}}{\partial z} = -\frac{5z}{|\mathbf{x}|^2} \cdot \ddot{\mathbf{x}}_{ST,C} + \frac{k_2}{2} \cdot \frac{GM_C}{|\mathbf{x}_C|^3} \cdot \frac{a^5}{|\mathbf{x}|^5} \cdot \left\{ \left(3 - 15 \frac{(\mathbf{x} \cdot \mathbf{x}_C)^2}{|\mathbf{x}|^2 \cdot |\mathbf{x}_C|^2} \right) \cdot \begin{pmatrix} 0 \\ 0 \\ 1 \end{pmatrix} - 30 \frac{(\mathbf{x} \cdot \mathbf{x}_C)(z_C - (\mathbf{x} \cdot \mathbf{x}_C) \cdot z)}{|\mathbf{x}|^4 \cdot |\mathbf{x}_C|^4} \cdot \mathbf{x} + 6 \frac{z_C}{|\mathbf{x}_C|^2} \cdot \mathbf{x}_C \right\},$$

$$\frac{\partial \ddot{\mathbf{x}}_{ST,C}}{\partial \dot{x}} = -\frac{1}{2} C_D \frac{A}{m} \rho \cdot \left(\dot{x} \cdot \frac{\dot{\mathbf{x}}}{|\dot{\mathbf{x}}|} + \begin{pmatrix} 1 \\ 0 \\ 0 \end{pmatrix} \cdot |\dot{\mathbf{x}}| \right),$$

$$\frac{\partial \ddot{\mathbf{x}}_D}{\partial \dot{y}} = -\frac{1}{2} C_D \frac{A}{m} \rho \cdot \left(\dot{y} \cdot \frac{\dot{\mathbf{x}}}{|\dot{\mathbf{x}}|} + \begin{pmatrix} 0 \\ 1 \\ 0 \end{pmatrix} \cdot |\dot{\mathbf{x}}| \right), \quad (\text{A.41})$$

$$\frac{\partial \ddot{\mathbf{x}}_D}{\partial \dot{z}} = -\frac{1}{2} C_D \frac{A}{m} \rho \cdot \left(\dot{z} \cdot \frac{\dot{\mathbf{x}}}{|\dot{\mathbf{x}}|} + \begin{pmatrix} 0 \\ 0 \\ 1 \end{pmatrix} \cdot |\dot{\mathbf{x}}| \right).$$

Atmospheric Drag

The presented model for atmospheric drag (4.52) does not depend on the position of the spacecraft. It only depends on the velocity and on dynamical parameters. The derivatives with respect to the velocity coordinates are given by

$$\frac{\partial \ddot{\mathbf{x}}_D}{\partial \dot{x}} = -\frac{1}{2} C_D \frac{A}{m} \rho \cdot \left(\dot{x} \cdot \frac{\dot{\mathbf{x}}}{|\dot{\mathbf{x}}|} + \begin{pmatrix} 1 \\ 0 \\ 0 \end{pmatrix} \cdot |\dot{\mathbf{x}}| \right),$$

$$\frac{\partial \ddot{\mathbf{x}}_D}{\partial \dot{y}} = -\frac{1}{2} C_D \frac{A}{m} \rho \cdot \left(\dot{y} \cdot \frac{\dot{\mathbf{x}}}{|\dot{\mathbf{x}}|} + \begin{pmatrix} 0 \\ 1 \\ 0 \end{pmatrix} \cdot |\dot{\mathbf{x}}| \right),$$

$$\frac{\partial \ddot{\mathbf{x}}_D}{\partial \dot{z}} = -\frac{1}{2} C_D \frac{A}{m} \rho \cdot \left(\dot{z} \cdot \frac{\dot{\mathbf{x}}}{|\dot{\mathbf{x}}|} + \begin{pmatrix} 0 \\ 0 \\ 1 \end{pmatrix} \cdot |\dot{\mathbf{x}}| \right).$$

Direct Solar Radiation Pressure

Finally, the partial derivatives of the perturbation model of the direct Solar radiation pressure (4.53) are formed by

$$\begin{aligned}\frac{\partial \ddot{\mathbf{x}}_{SR}}{\partial x} &= -\frac{C_{SR} A_e^2 S}{2 c m} \cdot \left(\frac{4}{3} \cdot \frac{\mathbf{x} - \mathbf{x}_S}{|\mathbf{x} - \mathbf{x}_S|^6} \cdot (x - x_S) + \begin{pmatrix} 1 \\ 0 \\ 0 \end{pmatrix} \cdot \frac{1}{|\mathbf{x} - \mathbf{x}_S|^3} \right), \\ \frac{\partial \ddot{\mathbf{x}}_{SR}}{\partial y} &= -\frac{C_{SR} A_e^2 S}{2 c m} \cdot \left(\frac{4}{3} \cdot \frac{\mathbf{x} - \mathbf{x}_S}{|\mathbf{x} - \mathbf{x}_S|^6} \cdot (y - y_S) + \begin{pmatrix} 0 \\ 1 \\ 0 \end{pmatrix} \cdot \frac{1}{|\mathbf{x} - \mathbf{x}_S|^3} \right), \\ \frac{\partial \ddot{\mathbf{x}}_{SR}}{\partial z} &= -\frac{C_{SR} A_e^2 S}{2 c m} \cdot \left(\frac{4}{3} \cdot \frac{\mathbf{x} - \mathbf{x}_S}{|\mathbf{x} - \mathbf{x}_S|^6} \cdot (z - z_S) + \begin{pmatrix} 0 \\ 0 \\ 1 \end{pmatrix} \cdot \frac{1}{|\mathbf{x} - \mathbf{x}_S|^3} \right).\end{aligned}\tag{A.42}$$

A.4 User Interface of the Software *ORBIT*

This section provides an overview of the graphical interface of the main functions of the software *ORBIT*.

Figure A.2 displays the start screen of the program.

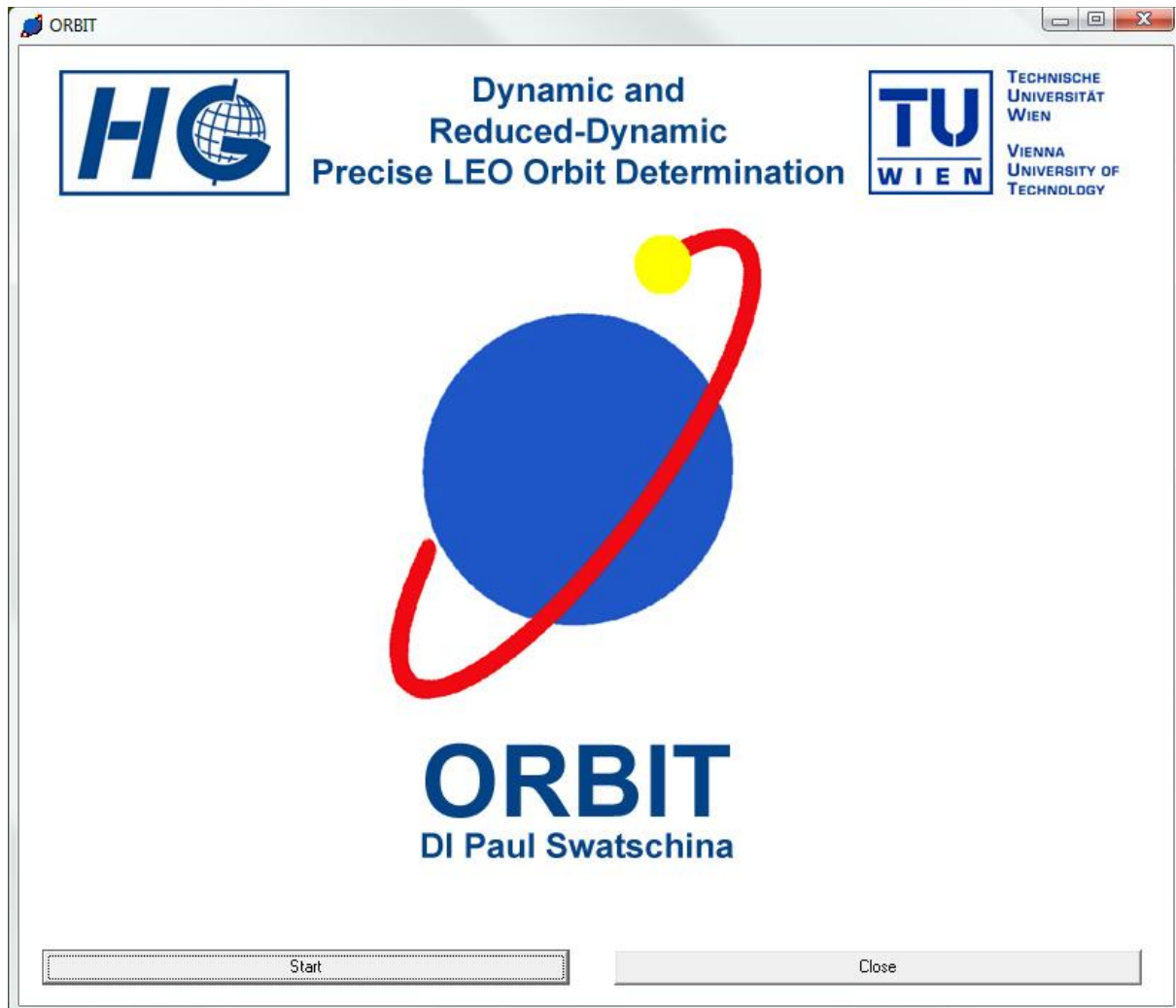


Figure A.2: Welcome screen of the software *ORBIT*

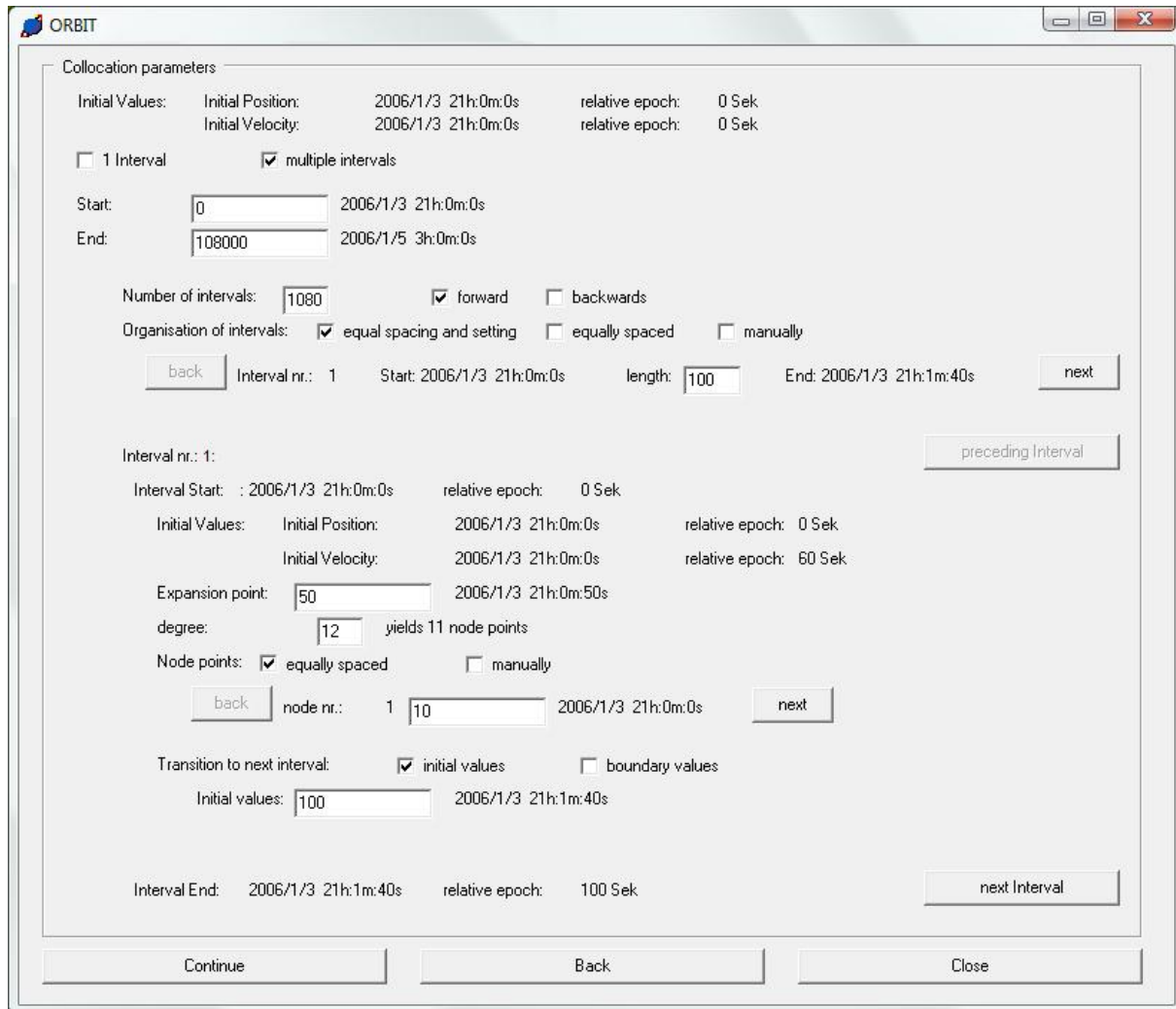


Figure A.3: Definition of the collocation parameters with *ORBIT*

After starting the program, the overall time interval and the collocation parameters have to be defined, see Figure A.3. The definition of the collocation parameters comprises the entry of the number of subintervals, the degree of the polynomials, the distribution of the node points and the expansion point and the transition to the next interval.

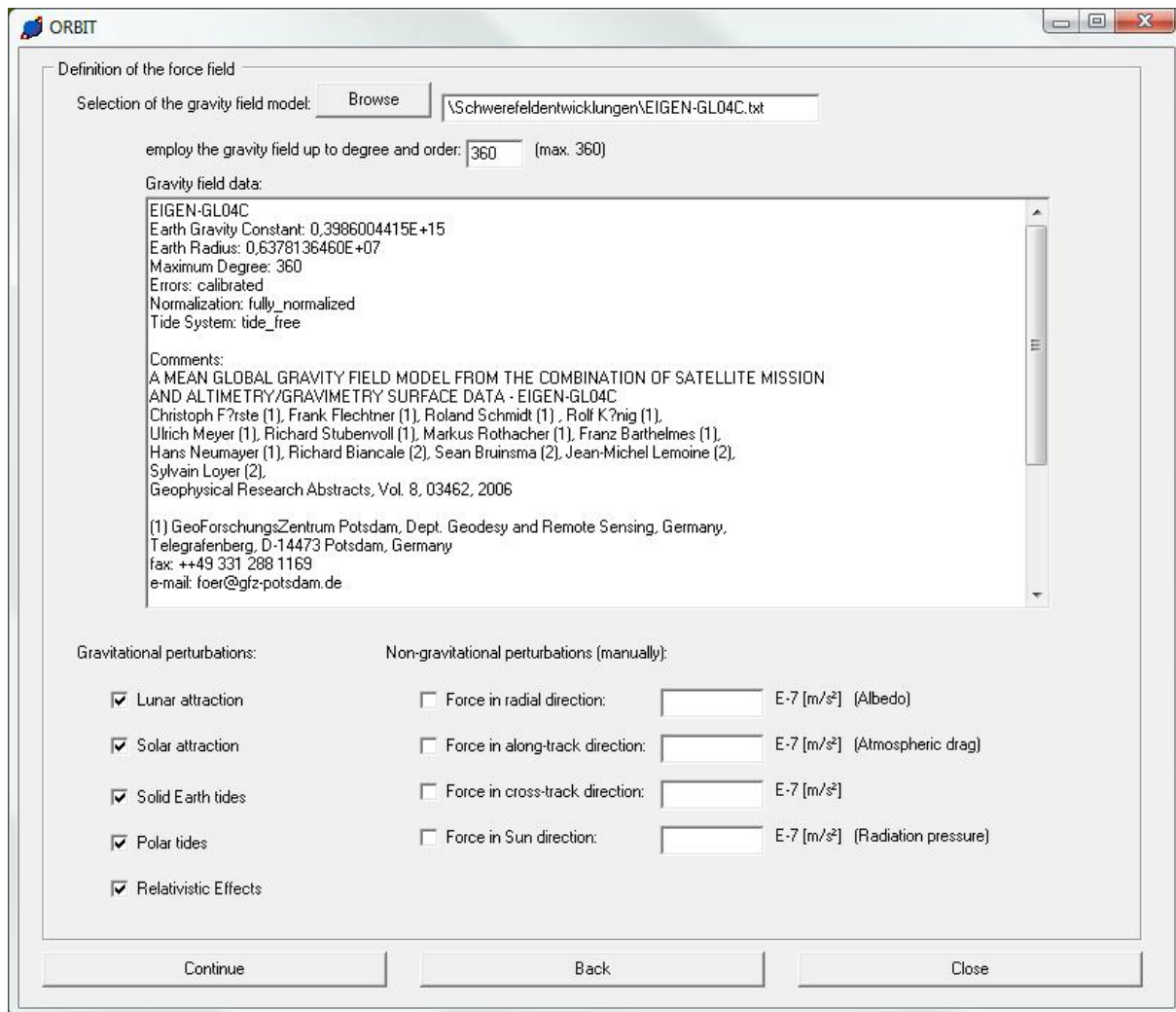


Figure A.4: Definition of the force field with *ORBIT*

Figure A.4 shows the interface for the definition of the force field. Any gravity field model can be chosen and employed up to a user defined degree and order. The gravitational perturbations can be included or excluded individually. The non-gravitational perturbations can be defined manually. The entered values for the non-gravitational forces can be kept fixed or be used as a priori values for the subsequent adjustment.

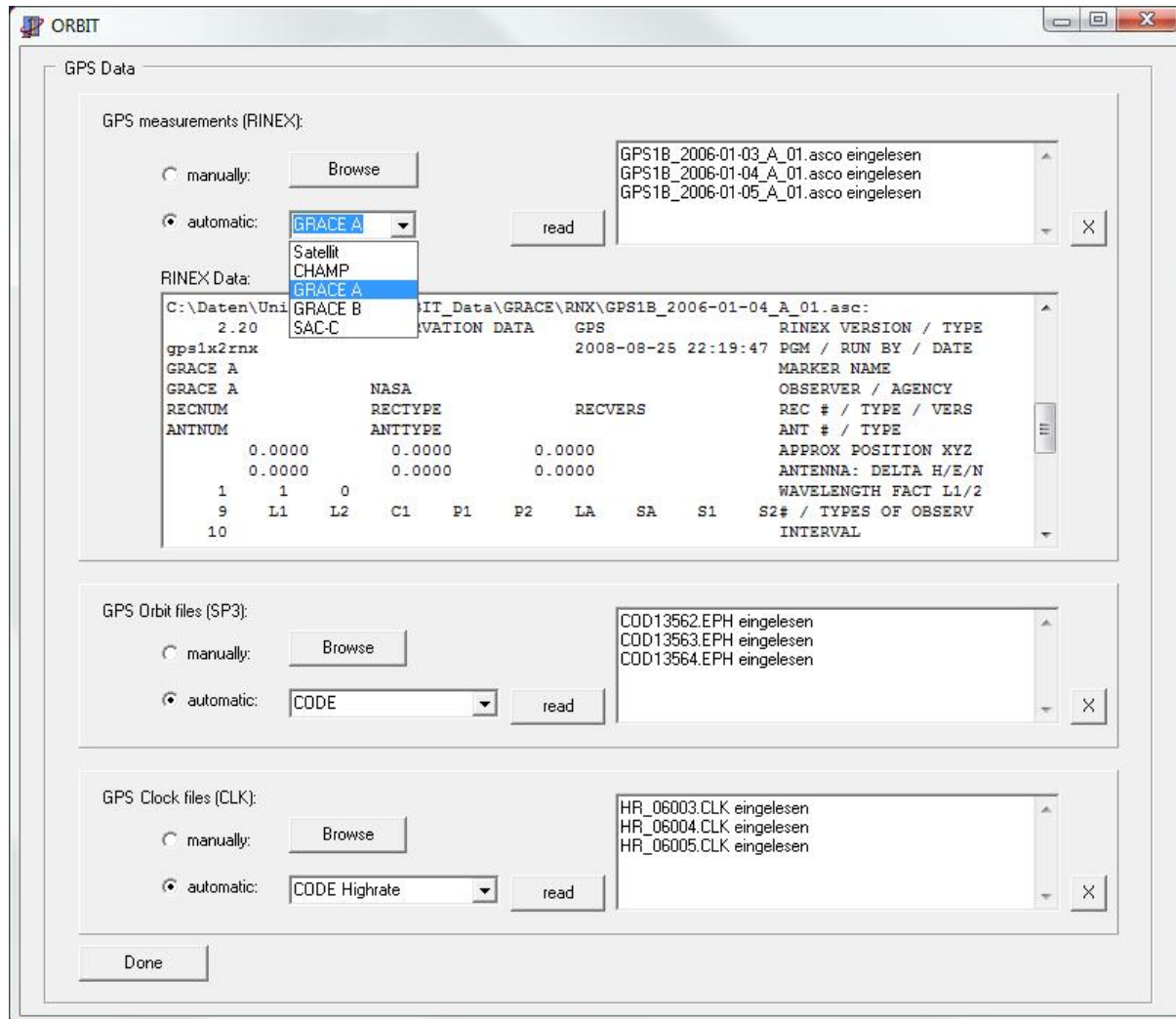


Figure A.5: Import of GPS data with *ORBIT*

In a next step the GPS measurement data has to be imported, see Figure A.5. Therefore, the according satellite and the desired GPS orbit and clock data has to be chosen.

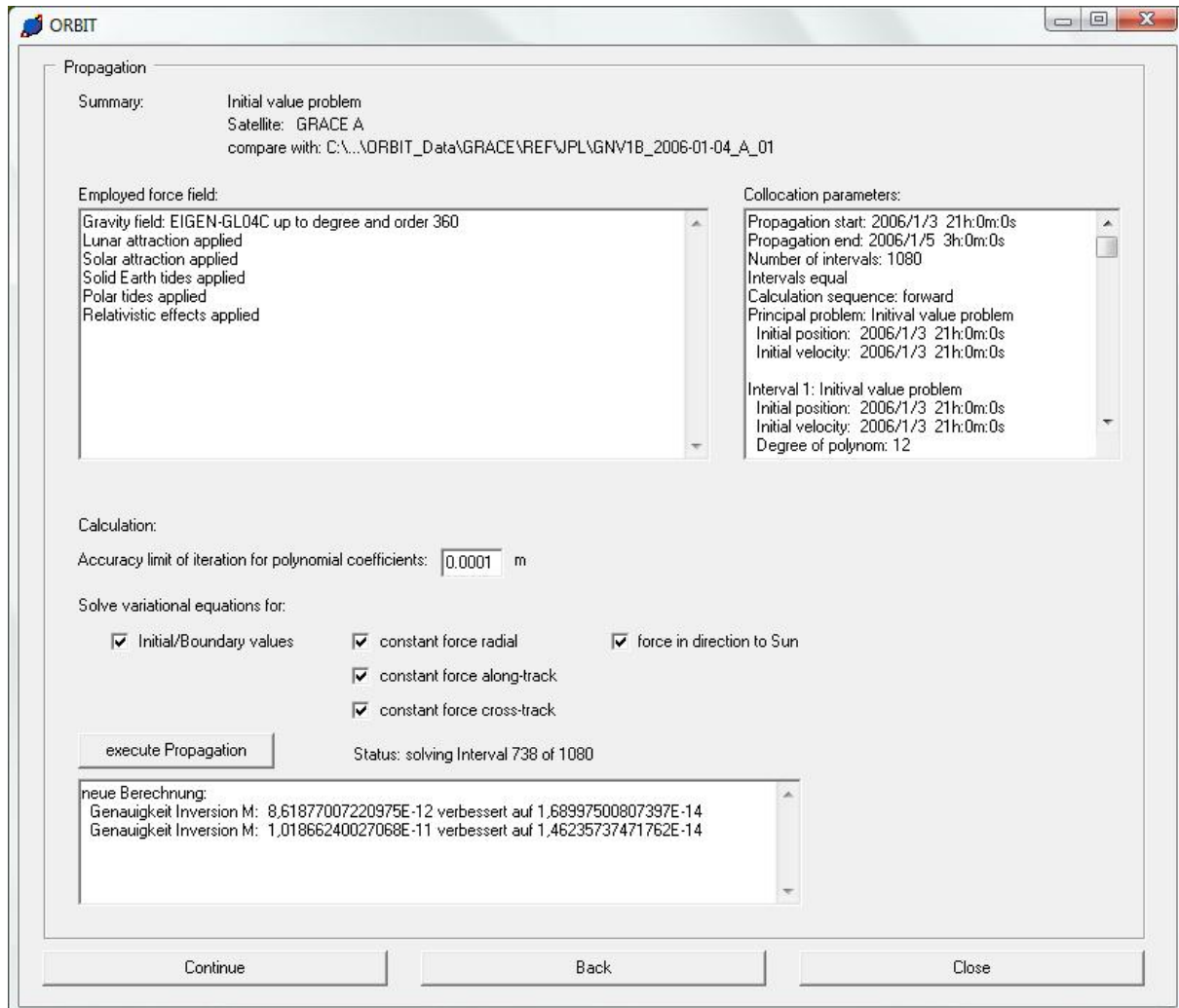


Figure A.6: Propagation settings with *ORBIT*

After the definition of the force field and the collocation parameters and the import of the GPS data, initial orbit determination can be performed, see Figure A.6. Here, it can be defined which variational equations have to be solved along with the propagation of the orbit.

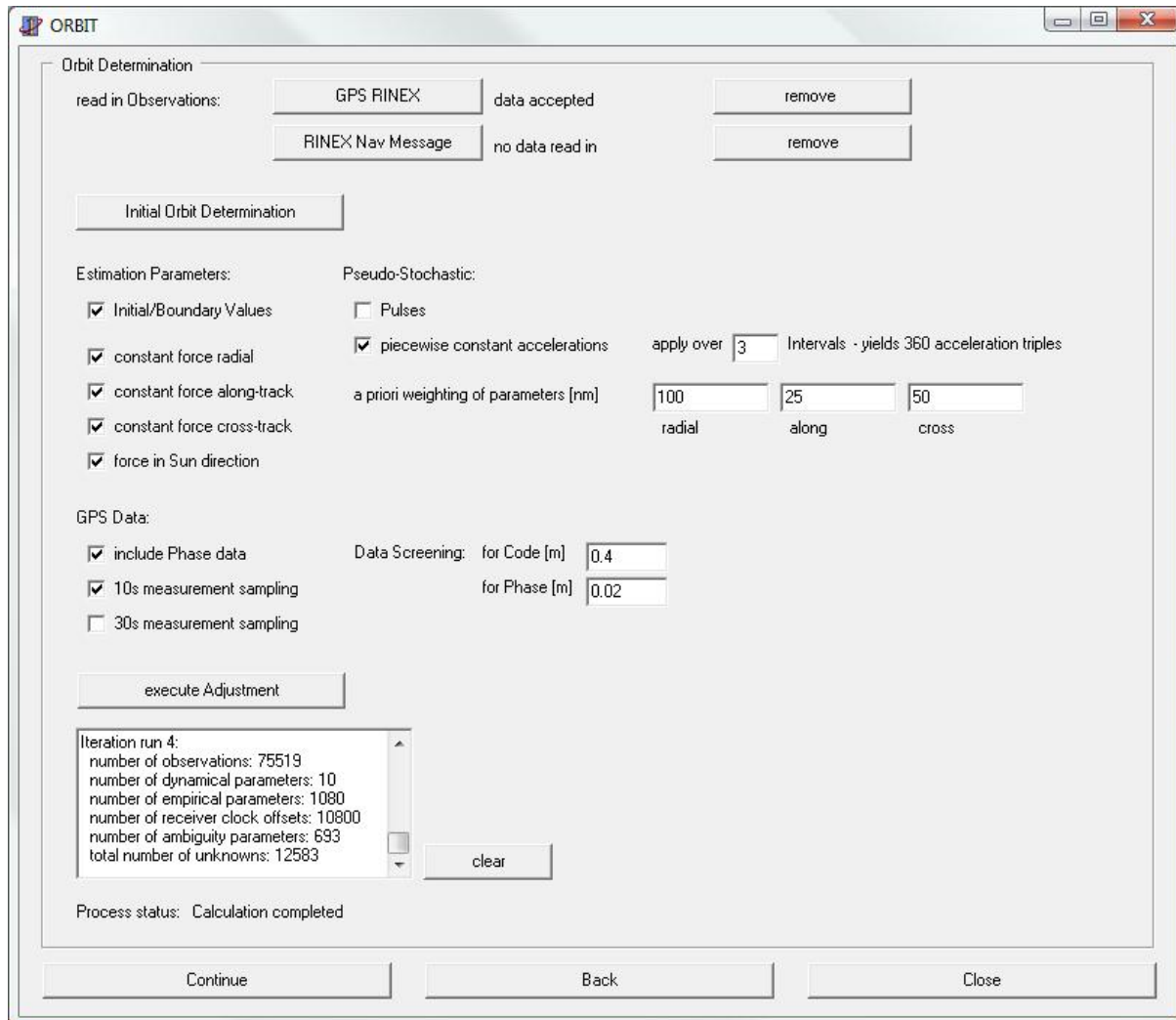


Figure A.7: Orbit determination settings with *ORBIT*

After initial orbit determination, the actual orbit determination can be performed, see Figure A.7. Here, the estimation parameters have to be defined. Additionally, the type of the pseudo-stochastic parameters has to be chosen along with the spacing and weighting of the empirical parameters. Finally, the thresholds for data screening and editing have to be set. After the definition of all these features the adjustment can be executed.

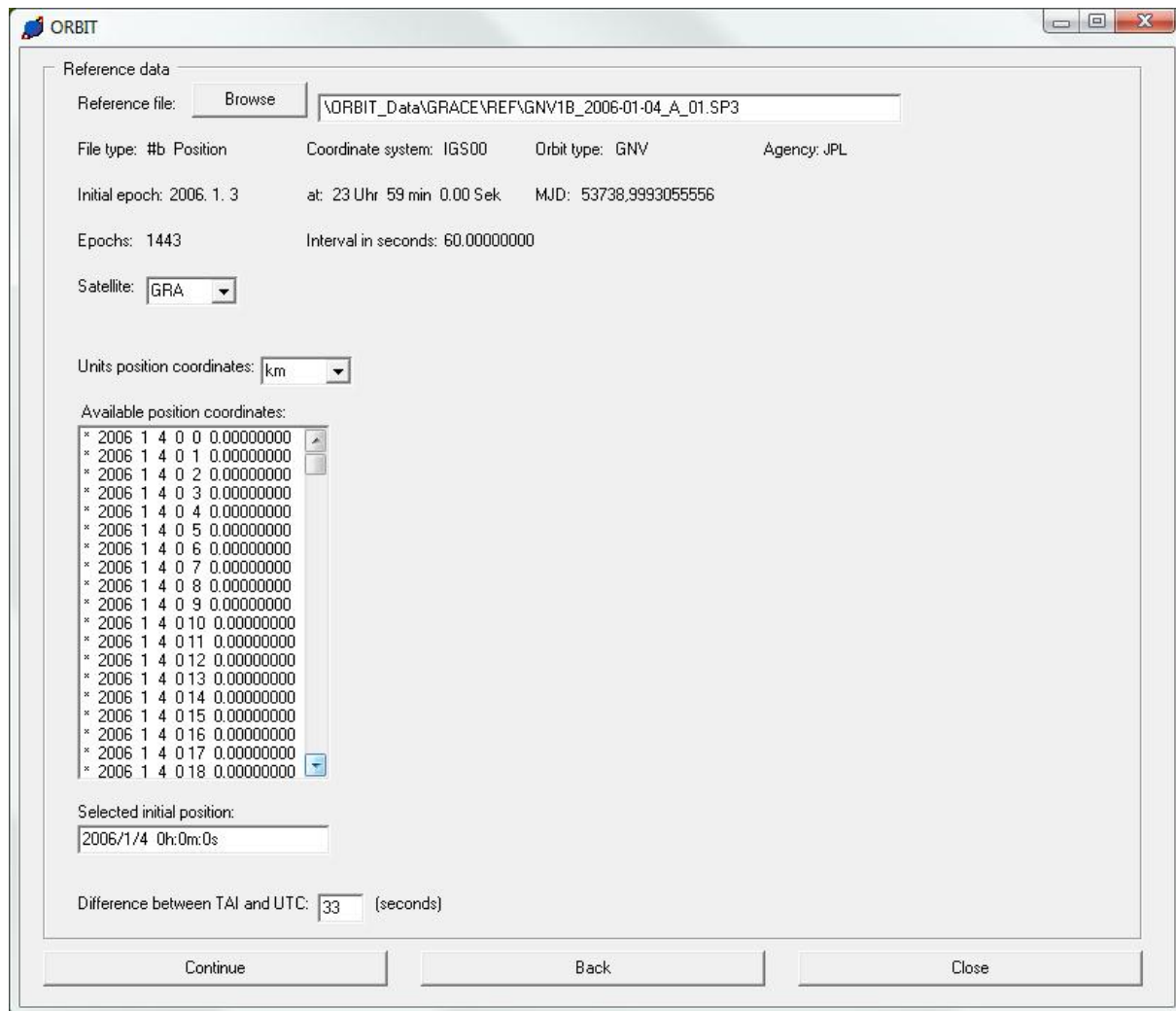


Figure A.8: Definition of the reference orbit solution with *ORBIT*

In order to compare the calculated solution an external solution has to be chosen, see Figure A.8.

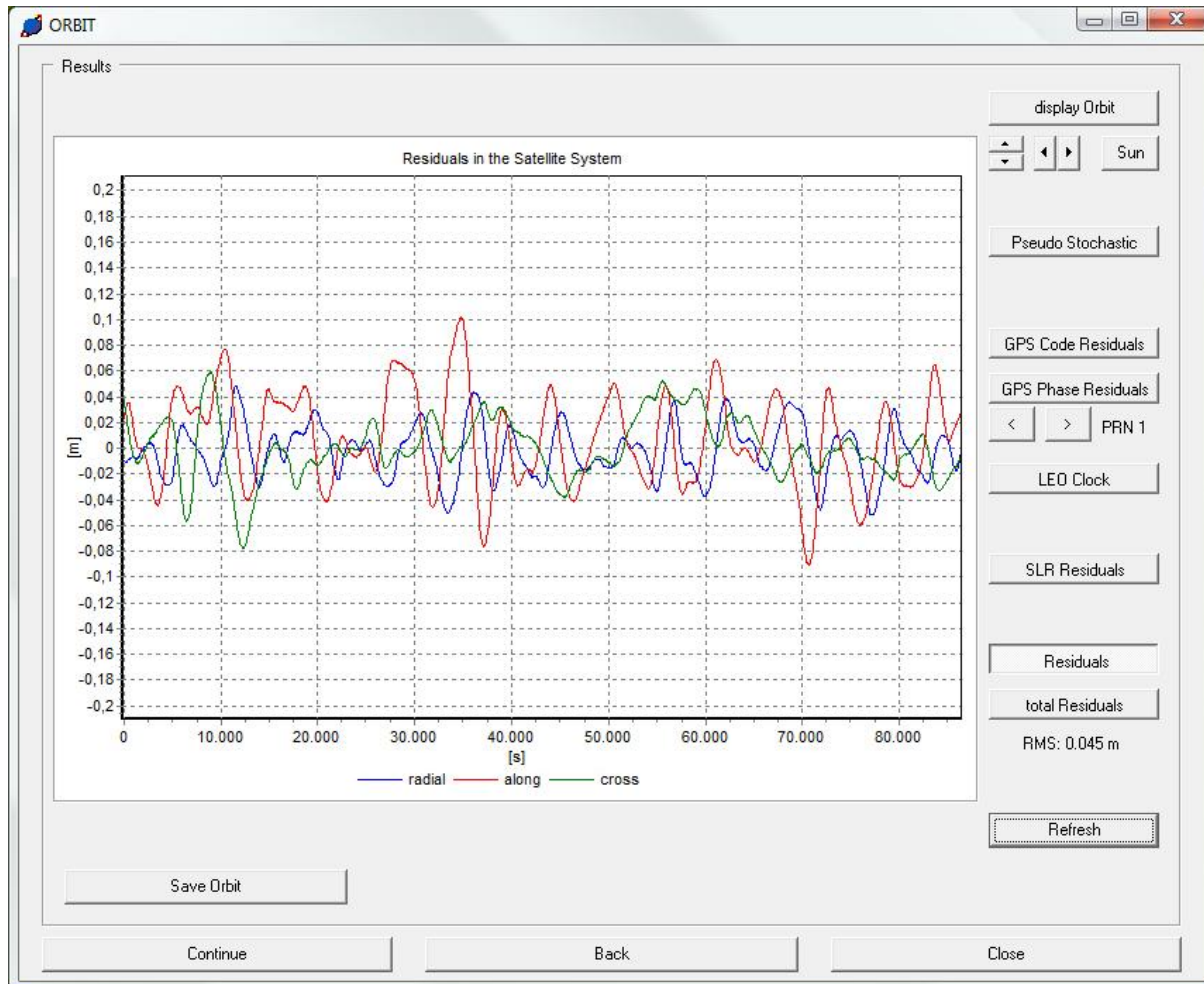


Figure A.9: Display of the attained results with *ORBIT*

Finally, the attained results can be displayed. Besides the residuals of the calculated solution with respect to an external solution (see Figure A.9), also the pseudo-stochastic parameters, the measurement residuals, the receiver clock solution and the orbit itself can be displayed.

In general, the user may switch quite freely between the various interface screens to adjust or change most of the settings and definitions at any time.

Bibliography

- Ashby, N., B. Berdotti (1984), *Relativistic perturbations of an Earth Satellite*, Physical Reviews 52, No. 7, pp. 485 (1984vie).
- Ashby, N. (2007), *Relativity in the Global Positioning System*, Living Reviews in Relativity, 6(1), 2003, revised 2007, online article: <http://www.livingreviews.org/lrr-2003-1>, last access: March 2009.
- Barthelmes F., Ch. Förste (2006), *The ICGEM-format*, GFZ Potsdam, Department 1 - Geodesy and Remote Sensing, http://op.gfz-potsdam.de/grace/results/grav/g005_ICGEM-Format.pdf, last access: April, 2009.
- Bertiger, W.I., Y.E. Bar-Sever, E.J. Christensen, E.S. Davis, J.R. Guinn, B.J. Haines, R.W. Ibanez-Meier, J.R. Jee, S.M. Lichten, W.G. Melbourne, R.J. Muellerschoen, T.N. Munson, Y. Vigue, S.C. Wu, T.P. Yunck, B.E. Schutz, P.A. Abusali, H.J. Rim, M.M. Watkins, and P. Willis (1994), *GPS precise tracking of TOPEX/POSEIDON: results and implication*, Journal of Geophysical Research, 99(C12), 24449–24464.
- Bettadpur, S. (2007), *Gravity recovery and climate experiment product specification document*, GRACE 327-720 (CSR-GR-03-02), Rev. 4.5, February 20, 2007, Center for Space Research, The University of Texas at Austin, USA.
- Beutler, G. (1990), *Numerische Integration gewöhnlicher Differentialgleichungssysteme: Prinzipien und Algorithmen*, Mitteilungen der Satelliten-Beobachtungsstation Zimmerwald Nr. 23, Druckerei der Universität Bern, Switzerland.
- Beutler, G., E. Brockmann, W. Gurtner, U. Hugentobler, L. Mervart, M. Rothacher, A. Verdun (1994), *Extended orbit modeling techniques at the CODE processing center of the international GPS service for geodynamics (IGS): theory and initial results*, Manuscripta Geodaetica, 19, 367–386.
- Beutler, G. (2005), *Methods of Celestial Mechanics*, Springer Verlag, Berlin Heidelberg, Germany, ISBN 3-540-40749-9, 3-540-40750-2.
- Beutler, G., A. Jäggi, U. Hugentobler, and L. Mervart (2006), *Efficient satellite orbit modelling using pseudo-stochastic parameters*, Journal of Geodesy, 80(7), 353-372.
- Blewitt, G. (1991), *Basics of the GPS Technique: Observation Equations*, in Geodetic Applications of GPS, p. 10-54, ed. B. Johnson, Nordic Geodetic Commission, Sweden.

- Bock, H. (2003), *Efficient Methods for Determining Precise Orbits of Low Earth Orbiters using the Global Positioning System*, Geodätisch-geophysikalische Arbeiten in der Schweiz, Vol. 65, Schweizerische Geodätische Kommission.
- Bock, H., U. Hugentobler, A. Jäggi, G. Beutler (2005), *Precise orbit determination for CHAMP using an efficient kinematic and reduced-dynamic procedure*, in Earth Observation with CHAMP - Results from Three Years in Orbit, edited by C. Reigber, H. Lühr, P. Schwintzer and J. Wickert, pp. 157-162, Springer Verlag Berlin Heidelberg, Germany, ISBN: 3-540-22804-7.
- Bock, H., A. Jäggi, D. Švehla, G. Beutler, U. Hugentobler, P. Visser (2007), *Precise orbit determination for the GOCE satellite using GPS*, Advances in Space Research, 39(10), 1638–1647.
- Bock, H., R. Dach, A. Jäggi, G. Beutler (2009), *High-rate GPS clock corrections from CODE: support of 1 Hz applications*, Journal of Geodesy,
- Braasch, M.S. (1995), *Multipath effects*, in Global Positioning System – Theory and Applications – Volume I, edited by B.W. Parkinson and J.J. Spilker, pp. 547–568, American Institute for Aeronautics and Astronautics, Washington, USA, ISBN: 1-563-47106-X.
- Bröderbauer, V. (2009), *Prädiktion von GNSS-Satellitenuhren*, Dissertation in preparation, Technical University of Vienna, Austria.
- Byun, S.H. (2003), *Satellite orbit determination using triple-differences GPS carrier phase in pure kinematic mode*, Journal of Geodesy, 76, 569-585.
- Capderou, M. (2005), *Satellites, Orbits and Missions*, Springer Verlag Paris, France, ISBN: 2-287-59772-7.
- Case, K., G. Kruizinga, and S. Wu (2004), *GRACE Level 1B Data Product User Handbook*, NASA Jet Propulsion Laboratory, JPL Publication D-22027, Pasadena, California, USA.
- CHAMP (2008), *The CHAMP Mission*, GFZ Potsdam Department 1, <http://www-app2.gfz-potsdam.de/pb1/op/champ/>, last access: January 2009.
- CODE (2009a), *CODE 15 min Ephemeris Data*, <ftp://ftp.unibe.ch/aiub/CODE/>, last access: June 2009.
- CODE (2009b), *CODE 30 s Clock Solutions*, <ftp://ftp.unibe.ch/aiub/misc/products/HRRAPCLK>, last access: June 2009.
- Dach, R., U. Hugentobler, P. Fridez, and M. Meindl (Eds.) (2007), *Bernese GPS Software Version 5.0*, Astronomical Institute, University of Bern, Switzerland.
- Dow, J.M., R.E. Neilan, and G. Gendt (2005), *The International GPS Service: Celebrating the 10th anniversary and looking to the next decade*, Advances in Space Research, 36(3), 320–326.

Drinkwater, M., R. Haagmans, D. Muzi, A. Popescu, R. Floberghagen, M. Kern, M. Fehringer (2007), *The GOCE Gravity Mission: ESA's First Core Earth Explorer*, Proceedings of 3rd International GOCE User Workshop, ESA SP-627, pp.1-8, Frascati, Italy, 6-8 Nov. 2006.

Dunn, C., W. Bertiger, Y. Bar-Sever, S. Desai, B. Haines, D. Kuang, G. Franklin, I. Harris, G. Kruizinga, T. Meehan, S. Nandi, D. Nguyen, T. Rogstad, J. Thomas, J. Tien, L. Romans, M. Watkins, S. Wu, S. Bettadpur, and J. Kim (2003), *Instrument of GRACE*, GPS World, February 2003.

Feltens, J. (1991), *Nicht-gravitative Störeinflüsse bei der Modellierung von GPS-Erdumlaufbahnen*, Deutsche Geodätische Kommission, Bayerische Akademie der Wissenschaften, Reihe C, Nr. 371.

Förste, C., F. Flechtner, R. Schmidt, R. König, U. Meyer, R. Stubenvoll, M. Rothacher, F. Barthelmes, K.H. Neumayer, R. Biancale, S. Bruinsma, J. Lemoine (2006), *A mean global gravity field model from the combination of satellite mission and altimetry/gravimetry surface gravity data*, Poster presented at EGU General Assembly 2006, Vienna, Austria, 02-07 April 2006, Geophysical Research Abstracts, Vol. 8, 03462, 2006.

Förste, C., F. Flechtner, R. Schmidt, R. Stubenvoll, M. Rothacher, J. Kusche, K.H. Neumayer, R. Biancale, J. Lemoine, F. Barthelmes, S. Bruinsma, R. König, U. Meyer (2008), *EIGEN-GL05C - A new global combined high-resolution GRACE-based gravity field model of the GFZ-GRGS cooperation*, General Assembly European Geosciences Union (Vienna, Austria 2008), Geophysical Research Abstracts, Vol. 10, Abstract No. EGU2008-A-06944, 2008.

Fu, L., E.J. Christensen, C.A. Yamarone, M. Lefebvre, Y. Ménard, M. Dorrer, and P. Escudier (1994), *TOPEX/POSEIDON mission overview*, Journal of Geophysical Research, 99(C12), 24369–24381.

Gendt, G. (2006), *IGS switch to absolute antenna model and ITRF2005*, IGS Mail No. 5438, <http://igscb.jpl.nasa.gov/mail/igsmai/2006/msg00161.html>, last access: January 2009.

GENESIS (2009), *Global Environmental and Earth Science Information System*, <http://genesis.jpl.nasa.gov/zope/GENESIS>, last access: March 2009.

Gerlach, Ch., N. Sneeuw, P. Visser, D. Švehla (2003), CHAMP gravity field recovery using the energy balance approach, Advances in Geosciences, 1, 73-80.

Gill, E., O. Montenbruck (2004), Comparison of GPS-based Orbit Determination Strategies, paper at 18th International Symposium on Space Flight Dynamics, Munich, Germany, 11-15 Oct. 2004.

GOCE (2008), *The GOCE mission*, European Space Agency, http://www.esa.int/esaLP/ESAYEK1VMOC_LPgoce_0.html, last access: March 2009.

GRACE (2008), *The GRACE Mission*, GFZ Potsdam Department 1, <http://www-app2.gfz-potsdam.de/pb1/op/grace/>, last access: January 2009.

- Griffiths, J., J. Ray (2008), *On the precision and accuracy of IGS orbits*, Journal of Geodesy, 83, 277–287.
- Gurtner, W. (1994), *RINEX: The Receiver-Independent Exchange Format*, GPS World, 5(7), 48-52.
- Haines, B., Y. Bar-Sever, W. Bertiger, S. Desai, P. Willis (2004), *One-Centimeter Orbit Determination for Jason-1: New GPS-Based Strategies*, Marine Geodesy, 27(1-2), 299-318.
- Harris I., W. Priester (1962), *Time-Dependent Structure of the Upper Atmosphere*, NASA TN D-1443, Goddard Space Flight Center, Maryland, USA.
- Hilla, S. (2007), *The Extended Standard Product 3 Orbit Format (SP3-c)*, <http://igscb.jpl.nasa.gov/igscb/data/format/sp3c.txt>, last access: January 2009.
- Hofmann-Wellenhof, B., H. Moritz (2006), *Physical Geodesy*, Second Edition, Springer Verlag, Wien, Austria, ISBN: 3-211-33544-7.
- Hofmann-Wellenhof, B., H. Lichtenegger, E. Wasle (2008), *GNSS – Global Navigation Satellite Systems*, Springer Verlag, Wien, Austria, ISBN: 3-211-73012-5.
- Hugentobler, U., G. Beutler (2003), *Strategies for precise Orbit determination of Low Earth Orbiters using the GPS*, Space Science Reviews, 108(1), 17-26.
- Hugentobler, U. (2004), CODE high rate clocks, IGS Mail No. 4913, <http://igscb.jpl.nasa.gov/mail/igsmai/2004/msg00136.html>, last access: January 2009.
- Hugentobler, U. (2008), *GNSS Bahnbestimmung*, presented at Kolloquium Satelliten-navigation, 17 April 2008.
- IERS (2009), *The International Earth Rotation and Reference Systems Service*, <http://www.iers.org/>, last access: March 2009.
- ICGEM (2009), *International Centre for Global Earth Models*, <http://icgem.gfz-potsdam.de/ICGEM/ICGEM.html>, last access: March 2009.
- IGS Tracking Network (2009), IGS Tracking Network, http://igscb.jpl.nasa.gov/network/net_index.html, last access: January 2009.
- IGSCB (2005), *IGS Products*, <http://igscb.jpl.nasa.gov/components/prods.html>, last access: January 2009.
- IJssel, J. van den, P.N.A.M. Visser, and E.P. Rodriguez (2003), *CHAMP Precise Orbit Determination Using GPS Data*, Advances in Space Research, 31 (8), 1889–1895.
- ISDC (2009), *Information System and Data Center for geoscientific data*, <http://isdc.gfz-potsdam.de/index.php>, last access: March 2009.

ITRF (2009), *The International Terrestrial Reference Frame*, <http://itrf.ensg.ign.fr/>, last access: March 2009.

Jacchia, L. (1971), *Revised Static Models of the Thermosphere and Exosphere with Empirical Temperature Profiles*, SAO Special Report 332, Cambridge, UK.

Jäggi, A., G. Beutler, U. Hugentobler (2005), *Efficient stochastic orbit modeling techniques using least squares estimators*, in a Window on the Future of Geodesy, edited by F. Sanso, pp. 175-180, Springer Verlag Berlin Heidelberg, Germany, ISBN: 3-540-24055-1.

Jäggi, A. (2006), *Pseudo-stochastic Orbit Modeling of Low Earth Satellites using the Global Positioning System*, Dissertation, University of Bern, Switzerland.

Jäggi, A., U. Hugentobler, G. Beutler (2006), *Pseudo-stochastic orbit modeling techniques for low-Earth orbiters*, Journal of Geodesy, 80(1), 47-60.

JASON-1 (2009), Aviso Service for JASON-1, <http://www.aviso.oceanobs.com/>, last access: March 2009.

Kang, Z., B. Tapley, S. Bettadpur, J. Ries, P. Nagel, R. Pastor (2006a), *Precise orbit determination for the GRACE mission using only GPS data*, Journal of Geodesy, 80(6), 322-331.

Kang, Z., B. Tapley, S. Bettadpur, J. Ries, P. Nagel, R. Pastor (2006b), *Precise orbit determination for GRACE using accelerometer data*, Advances in Space Research, 38(9), 2131-2136.

Kirschner, M., O. Montenbruck, S. Bettadpur (2001), *Flight Dynamics Aspects of the GRACE Formation Flying*, paper at 2nd International Workshop on Satellite Constellations and Formation Flying, Haifa, Israel, 19-20 Feb. 2001.

Kouba, J., P. Héroux (2001), *Precise point positioning using IGS orbit and clock products*, GPS Solutions, 5(2), 12–28.

Kouba, J. (2002), *A Guide to Using IGS Products*, Geodetic Survey Division, Natural Resources Canada, Ottawa, Ontario.

Kroes, R. (2006), *Precise Relative Positioning of Formation Flying Spacecraft using GPS*, Vol. 61 of Publications on Geodesy, Nederlandse Commissie voor Geodesie, Delft, The Netherlands.

Kuang, D., Y. Bar-Sever, W. Bertiger, S. Desai, B. Haines, B. Iijima, G. Kruizinga, T. Meehan, L. Romans (2001), *Precise Orbit Determination for CHAMP Using GPS Data from BlackJack Receiver*, presented at the ION National Technical Meeting, Long Beach, California, USA, 22–24 January 2001.

- Kursinski, E.R., G.A. Hajj, J.T. Schofield, R.P. Linfield, and K.R. Hardy (1997), *Observing Earth's atmosphere with radio occultation measurements using the Global Positioning System*, Journal of Geophysical Research, 102(D19), 23429–23466.
- Leick, A. (2004), *GPS Satellite Surveying*, John Wiley and Sons, NJ, USA, ISBN: 0-471-05930-7.
- van Loon, J. (2008), *Functional and stochastic modelling of satellite gravity data*, Vol. 67 of Publications on Geodesy, Nederlandse Commissie voor Geodesie, Delft, The Netherlands.
- Lemoine, F.G., S.C. Kenyon, J.K. Factor, R.G. Trimmer, N.K. Pavlis, D.S. Chinn, C.M. Cox, S.M. Klosko, S.B. Luthcke, M.H. Torrence, Y.M. Wang, R.G. Williamson, E.C. Pavlis, R.H. Rapp, T.R. Olson (1998), *The Development of the Joint NASA GSFC and the National Imagery and Mapping Agency (NIMA) Geopotential Model EGM96*, NASA Technical Paper NASA/TP1998206861, Goddard Space Flight Center, Greenbelt, USA, 1998.
- Luthcke, S.B., N.P. Zelensky, D.D. Rowlands, F.G. Lemoine, and T.A. Williams (2003), *The 1-Centimeter Orbit: Jason-1 Precision Orbit Determination Using GPS, SLR, DORIS, and Altimeter Data*, Marine Geodesy, 26(3-4), 399–421.
- McCarthy, D.D. (Ed.) (1996), *IERS Conventions (1996)*, IERS Technical Note No. 21, Central Bureau of IERS, Observatoire de Paris, France.
- McCarthy, D.D. and G. Petit (Eds.) (2004), *IERS Conventions (2003)*, IERS Technical Note No. 32, Central Bureau of IERS, Observatoire de Paris, France.
- Montenbruck, O. (2000), *Quaternion Representation of BIRD Orientation and Reference System Transformations*, Technical Note TN 00–03, German Space Operations Center.
- Montenbruck, O., E. Gill (2000), *Satellite Orbits*, Springer Verlag, Heidelberg, Germany, ISBN: 3-540-67280-X.
- Montenbruck, O., E. Gill (2002), *Ionospheric Correction for GPS Tracking of LEO Satellites*, The Journal of Navigation, 55, 293–304.
- Montenbruck, O. (2003), *Kinematic GPS positioning of LEO satellites using ionosphere-free single frequency measurements*, Aerospace Science and Technology, 7(5), 396–405.
- Montenbruck, O., and R. Kroes (2003), *In-flight performance analysis of the CHAMP BlackJack GPS Receiver*, GPS Solutions, 7 (2), 74–86.
- Montenbruck, O., E. Gill, R. Kroes (2005a), *Rapid Orbit determination of LEO Satellites using IGS clock and ephemeris products*, GPS Solutions, 9(3), 226–235.
- Montenbruck O., T. van Helleputte, R. Kroes , E. Gill (2005b), *Reduced dynamic orbit determination using GPS code and carrier measurements*, Aerospace Science and Technology, 9(3), 261–271.

- Montenbruck, O., M. Kirschner, S. D'Amico, and S. Bettadpur (2006), *E/i-vector separation for safe switching of the GRACE formation*, Aerospace Science and Technology, 10(7), 628–635.
- Montenbruck, O., M. Markgraf, M. Garcia-Fernandez, A. Helm (2007), *GPS for Microsatellites – Status and Perspectives*, paper at 6th IAA Symposium on Small Satellites for Earth Observation, Berlin, Germany, April 23-26 2007.
- Montenbruck, O., P. Ramos-Bosch (2007), *Precision real-time navigation of LEO satellites using global positioning system measurements*, GPS Solutions, 12(3), 187-198.
- Montenbruck, O., P. van Barneveld, Y. Yoon, P. Visser (2007), *GPS-Based Precision Baseline Reconstruction for the TanDEM-X SAR-Formation*, paper at 20th International Symposium on Space Flight Dynamics, Annapolis, USA, September 24-28 2007.
- Pavlis, N.K., S.A. Holmes, S.C. Kenyon, J.K. Factor (2008), *An Earth Gravitational Model to Degree 2160: EGM2008*, presented at the 2008 General Assembly of the European Geosciences Union, Vienna, Austria, April 13-18, 2008.
- Press, W., B. Flannery, S. Teutscholsky, W. Vertterling (1989), *Numerical Recipes in Pascal*, Cambridge University Press, NY, USA, ISBN: 0-521-37516-9.
- PODAAC (2009), *Physical Oceanography Distributed Active Archive Center* (PO.DAAC), <http://podaac.jpl.nasa.gov/>, last access: March 2009.
- Ramos-Bosch, P. (2008a), *Improvements in autonomous GPS navigation of Low Earth Orbit satellites*, Ph. D. Thesis, Universitat Politecnica de Catalunya, Spain.
- Ramos-Bosch, P. (2008b), *Precise Orbit Solutions for the CHAMP and GRACE satellites*, private communication.
- Ray, J., W. Gurtner (2006), RINEX Extensions to Handle Clock Information, http://igscb.jpl.nasa.gov/igscb/data/format/rinex_clock.txt, last access: January 2009.
- Reigber, C., H. Lühr, P. Schwintzer (Eds.) (2003), *First CHAMP Mission Results for Gravity, Magnetic and Atmospheric Studies*, Springer Verlag, Berlin, Germany, ISBN: 3-540-00206-5.
- Reigber, Ch., H. Jochmann, J. Wünsch, S. Petrovic, P. Schwintzer, F. Barthelmes, K.H. Neumayer, R. König, Ch. Förste, G. Balmino, R. Biancale, J. Lemoine, S. Loyer, F. Perosanz (2004), *Earth Gravity Field and Seasonal Variability from CHAMP*, in: Reigber, Ch., H. Lühr, P. Schwintzer, J. Wickert (Eds.), *Earth Observation with CHAMP - Results from Three Years in Orbit*, p. 25-30, Springer, Berlin, 2004, ISBN: 3-540-22804-7.
- Reigber, C., R. Schmidt, F. Flechtner, R. König, U. Meyer, K.H. Neumayer, P. Schwintzer, S.Y. Zhu (2005), *An Earth gravity field model complete to degree and order 150 from GRACE: EIGEN-GRACE02S*, Journal of Geodynamics, 39(1), 1-10.

- Remondi, B.W. (1991), *NGS second generation ASCII and binary orbit formats and associated interpolation studies*, Proceedings of the 20th General Assembly of the International Union of Geodesy and Geophysics, Vienna, Austria.
- Rim, H.-J., S.-P. Yoon, Y. Kim, and B.E. Schutz (2005), *ICESat precision orbit determination over solar storm period*, Spaceflight Mechanics 2005, edited by D.A. Vallado, M.J. Gabor, and P.N. Desai, Vol. 120, pp. 579–588.
- Rocken, C., R. Anthes, M. Exner, D. Hunt, S. Sokolovskiy, R. Ware, M. Gorbunov, W. Schreiner, D. Feng, B. Herman, Y.-H. Kuo, and X. Zou (1997), *Analysis and validation of GPS/MET data in the neutral atmosphere*, Journal of Geophysical Research, 102(D25), 29849–29866.
- Rogers, R.M. (2007), *Applied Mathematics in integrated Navigation Systems*, Third Edition, American Institute of Aeronautics and Astronautics, VA, USA, ISBN: 1-563-47656-8.
- Rothacher, M., R. Schmid (2006), *ANTEX: The Antenna Exchange Format Version 1.3*, <http://igscb.jpl.nasa.gov/igscb/station/general/antex13.txt>, last access: January 2009.
- SAC-C (2009), *NASA Goddard Space Flight Center – SAC-C Satellite*, http://www.gsfc.nasa.gov/gsfc/service/gallery/fact_sheets/spacesci/sac-c.htm, last access: March 2009.
- Schmid, R., M. Rothacher, D. Thaller, P. Steigenberger (2005), *Absolute phase center corrections of satellite and receiver antennas: Impact on GPS solutions and estimation of azimuthal phase center variations of the satellite antenna*, GPS Solutions, 9(4), 283-293.
- Schmid, R., P. Steigenberger, G. Gendt, M. Ge, M. Rothacher (2007), *Generation of a consistent absolute phase-center correction model for GPS receiver and satellite antennas*, Journal of Geodesy, 81(12), 781-798.
- Schneider, M. (1988), *Satellitengeodäsie*, BI Wissenschaftsverlag, Mannheim, Wien, Zürich, ISBN: 3-527-27712-9.
- Schutz, B.E, H.J. Zwally, C.A. Shuman, D. Hancock, and J.P. DiMarzio (2005), *Overview of the ICESat Mission, Transformations and Standards*, Geophysical Research Letters, 32, L21S01.
- Schwintzer, P., H. Lühr, C. Reigber, L. Grunwaldt, and C. Förste (2002), *CHAMP Reference Systems, Transformations and Standards*, CH-GFZ-RS-002, GFZ Potsdam, Germany, April 2002.
- Seeber, G. (2003), *Satellite Geodesy: Foundations, Methods and Applications*, de Gruyter, Berlin, Germany, ISBN: 3-110-10082-7.
- Springer, T., G. Beutler, M. Rothacher (1999), *A New Solar Radiation Pressure Model for GPS Satellites*, GPS solutions, 2(3), 50-62.

Staudinger, M., G. Navratil (2003), *Ausgleichungsrechnung oder Die Anwendung statistischer Methoden in Vermessungswesen und GIS*, Institute for Geoinformation, Technical University Vienna, Austria.

Švehla, D., M. Rothacher (2002), *Kinematic Orbit Determination of LEOs Based on Zero or Double-difference Algorithms Using Simulated and Real SST GPS Data*, in: Adam, J.; Schwarz, K.-P. (eds.) *Vistas for Geodesy in the New Millennium*, IAG Symposia, Springer, Vol. 125, pp 322-328, ISBN: 3-540-43454-2.

Švehla, D., M. Rothacher (2003), *Kinematic and reduced-dynamic precise orbit determination of low earth orbiters*, Advances in Geosciences, 1, 47–56.

Švehla, D. (2004), *Precise Orbit Solutions for the CHAMP satellite*, private communication.

Švehla, D., M. Rothacher (2005), *Kinematic positioning of LEO and GPS satellites and IGS stations on the ground*, Advances in Space Research, 36(3), 376-381.

Švehla, D., M. Rothacher (2006), *Impact of a LEO Formation and a LEO/GPS Dual Constellation on the IGS Products*, presentation at IGS Workshop, Darmstadt, Germany, May 8-12 2006.

Swatschka, P. (2004), *Bahnintegration tieffliegender Erdsatelliten am Beispiel der Schwerfeldmission CHAMP*, Diploma Thesis, Institute of Geodesy and Geophysics, Technical University Vienna.

Tapley, B.D., D.P. Chambers, S. Bettadpur, J.R. Ries (2003), *Large scale circulation from the GRACE GGM01 Geoid*, Geophysical Research Letters, 30(22), 2163.

Tapley, B.D., B.E. Schutz, G.H. Born (2004a), *Statistical Orbit Determination*, Elsevier Academic Press, MA, USA, ISBN: 0-126-83630-2.

Tapley, B.D., S. Bettadpur, J.C. Ries, P.F. Thompson, M. Watkins (2004b), *GRACE measurements of mass variability in the Earth system*, Science, 305 (5683), 503–505.

Tapley, B.D., J. Ries, S. Bettadpur, D. Chambers, M. Cheng, F. Condi, B. Gunter, Z. Kang, P. Nagel, R. Pastor, T. Pekker, S. Poole and F. Wang (2005), *GGM02 – An improved Earth gravity field model from GRACE*, Journal of Geodesy, 79(8), 467-478.

Tapley, B.D., J. Ries, S. Bettadpur, D. Chambers, M. Cheng, F. Condi, S. Poole (2007), *The GGM03 Mean Earth Gravity Model from GRACE*, Eos Trans. AGU 88(52), Fall Meeting Suppl., Abstract G42A-03, 2007.

Teunissen, PJG., A.Kleusberg (Eds.) (1998), *GPS for Geodesy*, Springer Verlag, Heidelberg, Germany, ISBN: 3-540-63661-7.

Vallado, D.A. (2007), *Fundamentals of Astrodynamics and Applications*, Space Technology Library, Springer, NY, USA, ISBN: 0-387-71831-1.

- Wertz, J. (2001), *Mission Geometry; Orbit and Constellation Design and Management*, Microcosm Press, CA, USA, ISBN: 0-792-37148-8.
- Wickert, J., G. Beyerle, R. König, S. Heise, L. Grunwaldt, G. Michalak, Ch. Reigber, T. Schmidt (2005), *GPS radio occultation with CHAMP and GRACE: A first look at a new and promising satellite configuration for global atmospheric sounding*, Annales Geophysicae, 23, 653-658.
- Wiese, D., W. Folkner, R. Nerem (2009), *Alternative mission architectures for a gravity recovery satellite mission*, Journal of Geodesy, 83(6), 1432-1394.
- Woo, K. (1991), *Optimum semicodeless carrier-phase tracking for L2*, Navigation, 47 (2), 82–99.
- Wu, S.C., T.P. Yunck, C.L. Thornton (1991), *Reduced-dynamic technique for precise orbit determination of low Earth satellites*, Journal of Guidance, Control, and Dynamics, 14(1), 24–30.
- Wu, J.T., S.C. Wu, G.A. Hajj, W.I. Bertiger, and S.M. Lichten (1993), *Effects of antenna orientation on GPS carrier phase*, Manuscripta Geodaetica, 18, 91–98.
- Wu, B.-H., V. Chu, P. Chen, and T. Ting (2005), *FORMOSAT-3/COSMIC science mission update*, GPS Solutions, 9(2), 111–121.
- Xu, G. (2003), *GPS – Theory, Algorithms and Applications*, Springer Verlag, Heidelberg, Germany, ISBN: 3-540-72714-0.
- Zumberge, J., G. Gent (2001), *The Demise of selective availability and implication for the International GPS Service*, Physics and Chemistry of the Earth, 26(A), 637-644.

Curriculum Vitae

- 10/2009: PhD in Surveying Science,
Vienna University of Technology
PhD thesis title: "Dynamic and Reduced-Dynamic Precise Orbit
Determination of Satellites in Low Earth Orbits"
- 06/2004: Vienna University of Technology
Diploma (M.Sc.) in Surveying Science,
Diploma thesis entitled: "Bahnintegration tieffliegender Erdsatelliten am
Beispiel der Erdschwerefeldmission CHAMP"
- 06/1999: Vienna University of Technology
First Diploma Degree
Inscription to "Geodesy and Geophysics"
- 10/1996: Vienna University of Technology
Inscription to "Vermessungswesen/Surveying Science"
- 09/1988-06/1996: Grammar School in Laa/Thaya, Austria
- 09/1984-06/1988: Primary School in Mistelbach, Austria

GEOWISSENSCHAFTLICHE MITTEILUNGEN

Bisher erschienen:

- Heft 1 Kolloquium der Assistenten der Studienrichtung Vermessungswesen. 1970 - 1973, Dezember 1973.
- Heft 2 EGGER-PERDICH-PLACH-WAGEN SOMMERER, Taschenrechner HP 45 und HP 65, Programme und Anwendungen im Vermessungswesen. 1. Auflage, März 1974, Special Edition in English, Juli 1974, 2. verbesserte Auflage, November 1974.
- Heft 3 Kolloquium der Assistenten der Studienrichtung Vermessungswesen 1973 - 1974, September 1974.
- Heft 4 EGGER-PALFINGER-PERDICH-PLACH-WAGEN SOMMERER, Tektronix-Tischrechner TEK 31, Programmhbibliothek für den Einsatz im Vermessungswesen, November 1974.
- Heft 5 K. LEDERSTEGER, Die horizontale Isostasie und das isostatische Geoid, Februar 1975.
- Heft 6 F. REINHART, Katalog von FK4 Horrebow-Paaren für Breiten von +30 bis +60, Oktober 1975.
- Heft 7 Arbeiten aus dem Institut für Höhere Geodäsie, Wien, Dezember 1975.
- Heft 8 Veröffentlichungen des Instituts für Photogrammetrie zum XIII. Internationalen Kongreß für Photogrammetrie in Helsinki 1976, Wien, Juli 1976.
- Heft 9 W. PILLEWIZER, Felsdarstellung aus Orthophotos, Wien, Juni 1976.
- Heft 10 PERDICH-PLACH-WAGEN SOMMERER, Der Einsatz des programmierbaren Taschenrechners Texas Instruments SR-52 mit Drucker PC100 in ingenieurgeodätischen Rechentechnik, Wien, Mai 1976.
- Heft 11 Kolloquium der Assistenten der Studienrichtung Vermessungswesen 1974 - 1976, November 1976.
- Heft 12 Kartographische Vorträge der Geodätischen Informationstage 1976, Wien, Mai 1977.
- Heft 13 Veröffentlichung des Instituts für Photogrammetrie anlässlich des 80. Geburtstages von Prof. Dr.h.c. K. Neumaier, Wien, Januar 1978.
- Heft 14 L. MOLNAR, Self Checking Analytical Relative Orientation and Strip Formation, Wien, Dezember 1978.
- Heft 15 Veröffentlichung des Instituts für Landesvermessung anlässlich des 80. Geburtstages von Prof. Dr. Alois Bavar, Wien, Januar 1979.
- Heft 16 Kolloquium der Assistenten der Studienrichtung Vermessungswesen 1976 - 1978, Wien, November 1979.
- Heft 17 E. VOZIKIS, Die photographische Differentialumbildung gekrümmter Flächen mit Beispielen aus der Architekturbildmessung, Wien, Dezember 1979.
- Heft 18 Veröffentlichung des Instituts für Allgemeine Geodäsie anlässlich des 75. Geburtstages von Prof. Dipl.-Ing. Dr. F. Hauer, Die Höhe des Großglockners, Wien, 1981.

- Heft 19 H. KAGER, Bündeltriangulation mit indirekt beobachteten Kreiszentren, Wien, April 1981.
- Heft 20 Kartographische Vorträge der Geodätischen Informationstage 1980, Wien, Mai 1982.
- Heft 21 Veröffentlichung des Instituts für Kartographie anlässlich des 70. Geburtstages von Prof. Dr. Wolfgang Pillewizer: Glaziologie und Kartographie, Wien, Dezember 1982.
- Heft 22 K. TEMPFLI, Genauigkeitsschätzung digitaler Höhenmodelle mittels Spektralanalyse, Wien, Mai 1982.
- Heft 23 E. CSAPLOVICS, Interpretation von Farbinfrarotbildern, Wien, November 1982.
- Heft 24 J. JANSA, Rektifizierung von Multispektral-Scanneraufnahmen - Entwicklung und Erprobung eines EDV-Programms, Wien, Mai 1983.
- Heft 25 Zusammenfassung der Diplomarbeiten, Dissertationen und Habilitationen an den geodätischen Instituten der TU Wien, Wien, November 1984.
- Heft 26 T. WUNDERLICH, Die voraussetzungsfreie Bestimmung von Refraktionswinkeln, Wien, August 1985.
- Heft 27 G. GERSTBACH (Hrsg.), Geowissenschaftliche/geotechnische Daten in Landinformationssystemen - Bedarf und Möglichkeiten in Österreich, Juni 1986.
- Heft 28 K. NOVAK, Orientierung von Amateuraufnahmen ohne Paßpunkte, Wien, August 1986.
- Heft 29 Veröffentlichung des Instituts für Landesvermessung und Ingenieurgeodäsie, Abt. Ingenieurgeodäsie, anlässlich des 80. Geburtstages von Prof. Dipl.-Ing. Dr. F. Hauer, Wien, Oktober 1986.
- Heft 30 K.-H. ROCH, Über die Bedeutung dynamisch ermittelter Parameter für die Bestimmung von Gesteins- und Gebirgseigenschaften, Wien, Februar 1987.
- Heft 31 G. HE, Bildverbesserung mittels digitaler Filterung, Wien, April 1989.
- Heft 32 F. SCHLÖGELHOFER, Qualitäts- und Wirtschaftlichkeitsmodelle für die Ingenieurphotogrammetrie, Wien, April 1989.
- Heft 33 G. GERSTBACH (Hrsg.), Geowissenschaftliche/geotechnische Daten in Landinformationssystemen - Datenbestände und Datenaustausch in Österreich, Wien, Juni 1989.
- Heft 34 F. HOCHSTÖGER, Ein Beitrag zur Anwendung und Visualisierung digitaler Geländemodelle, Wien, Dezember 1989.
- Heft 35 R. WEBER, Lokale Schwerefeldmodellierung unter Berücksichtigung spektraler Methoden zur Geländereduktion, Wien, April 1990.
- Heft 36 o.Prof. Dr. Hans Schmid zum 70. Geburtstag. Veröffentlichung der Abteilung für Landesvermessung, Wien, Oktober 1990.
- Heft 37 G. GERSTBACH, H. P. HÖLLRIEGL und R. WEBER, Geowissenschaftliche Informationsbörse - Eine Nachlese zu GeoLIS II, Wien, Oktober 1990.
- Heft 38 R. ECKER, Rastergraphische Visualisierungen mittels digitaler Geländemodelle, Wien, August 1991.

- Heft 39 Kartographische Forschungen und Anwendungsorientierte Entwicklungen, herausgegeben von W. Stams und F. Kelnhofer zum 80. Geburtstag von Prof. Dr. W. Pillewizer, Wien, Juli 1991.
- Heft 39a W. RIEGER, Hydrologische Anwendungen des digitalen Geländemodells, Wien, Juli 1992.
- Heft 40 K. STEINNOCHER, Methodische Erweiterungen der Landnutzungsklassifikation und Implementierung auf einem Transputernetzwerk, Wien, Juli 1994.
- Heft 41 G. FORKERT, Die Lösung photogrammetrischer Orientierungs- und Rekonstruktionsaufgaben mittels allgemeiner kurvenförmiger Elemente, Wien, Juli 1994.
- Heft 42 M. SCHÖNER, W. SCHÖNER, Photogrammetrische und glaziologische Untersuchungen am Gásbre (Ergebnisse der Spitzbergenexpedition 1991), Wien, Mai 1996.
- Heft 43 M. ROIC, Erfassung von nicht signalisierten 3D-Strukturen mit Videotheodoliten, Wien, April 1996.
- Heft 44 G. RETSCHER, 3D-Gleiserfassung mit einem Multisensorsystem und linearen Filterverfahren, Wien, April 1996.
- Heft 45 W. DAXINGER, Astrogravimetrische Geoidbestimmung für Ingenieurprojekte, Wien, Juli 1996.
- Heft 46 M. PLONER, CCD-Astrometrie von Objekten des geostationären Ringes, Wien, November 1996.
- Heft 47 Zum Gedenken an Karl Killian "Ingenieur" und "Geodät" 1903-1991, Veröffentlichung der Fachgruppe Geowissenschaften, Wien, Februar 1997.
- Heft 48 A. SINDHUBER, Ergänzung und Fortführung eines digitalen Landschaftsmodells mit multispektralen und hochauflösenden Fernerkundungsaufnahmen, Wien, Mai 1998.
- Heft 49 W. WAGNER, Soil Moisture Retrieval from ERS Scatterometer Data, Wien, Dezember 1998.
- Heft 50 R. WEBER, E. FRAGNER (Editoren), Prof. Bretterbauer, Festschrift zum 70. Geburtstag, Wien, Juli 1999.
- Heft 51 Ch. ÖHRENEDER, A Similarity Measure for Global Image Matching Based on The Forward Modeling Principle, Wien, April 1999.
- Heft 52 M. LECHTHALER, G. GARTNER, Per Aspera ad Astra, Festschrift für Fritz Kelnhofer zum 60. Geburtstag, Wien, Jänner 2000.
- Heft 53 F. KELNHOFER, M. LECHTHALER, Interaktive Karten (Atlanten) und Multimedia - Applikationen, Wien, März 2000.
- Heft 54 A. MISCHKE, Entwicklung eines Videotheodolit-Meßsystems zur automatischen Richtungsmessung von nicht signalisierten Objektpunkten, Wien, Mai 2000.
- Heft 55 Veröffentlichung des I.P.F. anlässlich der Emeritierung von Prof. Dr. Peter Waldhäusl, Wien.
- Heft 56 F. ROTTENSTEINER, Semi-automatic Extraction of Buildings Based on Hybrid Adjustment Using 3D Surface Models and Management of Building Data in a TIS, Wien, Juni 2001.

- Heft 57 D. LEGENSTEIN, Objektrekonstruktion aus perspektiven Bildern unter Einbeziehung von Umrisslinien, Wien, Mai 2001.
- Heft 58 F. KELNHOFER, M. LECHTHALER und K. BRUNNER (Hrsg.), Telekartographie und Location Based Services, Wien, Jänner 2002.
- Heft 59 K. BRETTERRAUER, Die runde Erde eben dargestellt: Abbildungslehre und sphärische Kartennetzentwürfe, Wien, 2002.
- Heft 60 G. GARTNER, Maps and the Internet 2002, Wien 2002.
- Heft 61 L. DORFFNER, Erzeugung von qualitativ hochwertigen 3D Photomodellen für internetbasierte Anwendungen mit besonderem Augenmerk auf Objekte der Nahbereichsphotogrammetrie, Wien, Jänner 2002.
- Heft 62 K. CHMELINA, Wissensbasierte Analyse von Verschiebungsdaten im Tunnelbau, Wien 2002.
- Heft 63 A. NIESSNER, Qualitative Deformationsanalase unter Ausnutzung der Farbinformation, Wien 2002.
- Heft 64 K. BRETTERRAUER, R. WEBER, A Primer of Geodesy for GIS-Users, Wien 2003.
- Heft 65 N. PFEIFER, 3D Terrain Models on the basis of a triangulation, Wien, Jänner 2002.
- Heft 66 G. GARTNER (Hrsg), Lacation Based Services & Telecartography, Wien 2004.
- Heft 67 I. KABASHI, Gleichzeitig-gegenseitige Zenitwinkelmessung über größere Entfernung mit automatischen Zielsystemen, Wien 2004.
- Heft 68 J. BÖHM, Troposphärische Laufzeitverzögerungen in der VLBI, Wien 2004.
- Heft 69 R. WEBER, W. SCHLÜTER, U. SCHREIBER, O. TTOV Evolving Space Geodesy Techniques (EGS XXVII General Assembly, Nice, France, 2002), Wien 2004.
- Heft 70 G. WEINWURM, Amalthea's Gravity Field and its Impact on a Spacecraft Trajectory, Wien 2004.
- Heft 71 Forschungsgruppe Ingenieurgeodäsie, Festschrift anlässlich des 65. Geburtstages von Herrn o.Univ. Prof. Dr.-Ing. Heribert Kahmen, Wien 2005.
- Heft 72 A. REITERER, A Knowledge-Based Decision System for an On-Line Video-Theodolite-Based Multisensor System, Wien 2005.
- Heft 73 M. HABERLER, Einsatz von Fuzzy Methoden zur Detektion konsistenter Punktbewegungen, Wien 2005.
- Heft 74 G. GARTNER, Location Based Services & Telecartography, Proceedings of the Symposium 2005, Wien 2005.
- Heft 75 Th. HOBIGER, VLBI as a tool to probe the ionosphere, Wien 2006.
- Heft 76 E. KLAFFENBÖCK, Troposphärische Laufzeitverzögerung von GNSS-Signalen – Nutzen aktiver Referenzstationsnetze für die Meteorologie, Wien 2006.
- Heft 76a P. J. MENDES-CERVEIRA, Tidal and non-tidal contributions to surface loading processes on station coordinates, Wien 2006.

- Heft 78 G. KOSTOV, G. BOURDA, L. FERNANDEZ, T. KONDO, Research Projects at IGG Reports, Wien 2007.
- Heft 79 J. BÖHM, A. PANY, H. SCHUH (Editors), Proceedings of the 18th European VLBI for Geodesy and Astrometry Working Meeting, 12-13 April 2007, Wien 2007.
- Heft 80 J. BÖHM, Tropospheric Delay Modelling at Radio Wavelengths for Space Geodetic Techniques, Wien 2007.
- Heft 81 G. Retscher, Mobile Multi-sensor Systems for Personal Navigation and Location-based Services, Wien 2007.
- Heft 82 R. HEINKELMANN, Bestimmung des atmosphärischen Wasserdampfes mittels VLBI als Beitrag zur Klimaforschung, Wien 2008.
- Heft 83 F. ROTTENSTEINER, Automatic extraction of buildings from airborne laserscanner data and aerial images, Wien 2008.
- Heft 84 S. TODOROVA, Kombination geodätischer Weltraumverfahren für globale Karten der Ionosphäre, Wien 2009.
- Heft 85 J. WRESNIK, Simulationen für die neue Generation von VLBI-Systemen, Wien 2009.
- Heft 86 A. KARABATIC, Precise Point Positioning (PPP). An alternative technique for ground based GNSS troposphere monitoring, Wien 2011.
- Heft 87 K. TEKE, Sub-daily Parameter Estimation in VLBI Data Analysis, Wien 2011.
- Heft 88 G. THALER, Echtzeit Bahn- und Uhrberechnung der GPS-Satellitenkonstellation basierend auf Beobachtungsdaten des RTIGS-Stationsnetzwerkes, Wien 2013.
- Heft 89 P. SWATSCHEINA, Dynamic and Reduced-Dynamic Precise Orbit Determination of Satellites in Low Earth Orbits, Wien 2012.
- Heft 90 S. BÖHM, Tidal excitation of Earth rotation observed by VLBI and GNSS, Wien 2012.